Numerical Investigations of Cavitation-Induced Tissue Damage

by

Lauren Mancia

A dissertation submitted in partial fulfillment
of the requirements for the degree of
Doctor of Philosophy
(Mechanical Engineering)
in the University of Michigan
2020

Doctoral Committee:

Associate Professor Eric Johnsen, Chair
Professor J. Brian Fowlkes
Professor Karl Grosh
Associate Professor Zhen Xu

Lauren Mancia
lamancha@umich.edu
ORCID iD: 0000-0003-4366-1944

DEDICATION

To all clinicians who value first principles

ACKNOWLEDGMENTS

I am forever grateful to my thesis advisor, Professor Eric Johnsen for his unwavering support of my many research endeavors and career pursuits over the past nine years. It seems unnecessary to describe someone who is currently training 11 doctoral students while leading funded projects on applications ranging from kidney stones to nuclear fusion as a model teacher and scholar, so I'll qualify my gratitude with a story about his mentoring instead. My first exposure to biomedical research was through an ultrasound project in Eric's lab. At the time, I noticed that there was very limited interaction between clinicians and researchers in theoretical and computational fields. I had familiarity with clinical medicine from volunteer work at a local hospice and decided that becoming a clinician myself would be both personally fulfilling and could potentially fill a need for further collaboration between medicine and computational research. To my surprise and immense relief, Eric was extremely supportive of this change in plans, and I transitioned to a terminal Master's degree to apply to medical schools. Lesser people, my former self included, might have held some slight degree of resentment towards a student with five years of fellowship funding who opted for a terminal Master's degree instead of a PhD. Not Eric. Even with no guarantee that I would be able rejoin his lab in the future, he wrote me reference letters, provided interview advice, and was a critical source of encouragement throughout an accelerated premed curriculum and capricious application process. On his reference, I was ultimately accepted at the University of Michigan and rejoined the lab as a MD/PhD student through the Medical Scientist Training Program. I cherish Eric's example of selfless leadership, and I will remember it for the duration of my career.

I am also grateful to the esteemed members of my thesis committee: Prof. Brian Fowlkes, Prof. Karl Grosh, and Prof. Zhen Xu. These accomplished scientists have served as excellent role models, and I feel privileged to have worked with them. I am especially grateful to Prof. Xu and the histotripsy group for their experimental assistance and many insightful discussions at our interdisciplinary cavitation meetings. I am grateful to the gifted experimentalists Prof. Eli Vlaisvljevich and Dr. Jonathan Sukovich for many fruitful collaborative projects on focused ultrasound and bubble dynamics. I also appreciate the contributions of BRC project faculty members Prof. Christian Franck and Prof. David Henann as well as project alumni Prof. Jon Estrada and Dr. Mauro Rodriguez for lending their solid mechanics expertise. I thank Matthew Warnez, Carlos Barajas, and Dr. Renaud Gaudron for their assistance with the numerical methods and constitutive modeling contained in this thesis. Finally, I would like to acknowledge my earliest research mentors: College of Engineering Dean Alec Gallimore and Director of the Program in Technical Communication, Pauline Bary Khan. Their mentorship first inspired my interest in research, and I am very thankful for their gracious support of my subsequent applications to medical school.

I joined this program convinced that clinical experience can inspire basic research, and I have found that it can also be a valuable source of motivation as well. Regular clinical experience was a very welcome complement to the rapid succession of setbacks and successes encountered during this two–year PhD. On this front, I am especially grateful to my clinical preceptor Dr. Geoffrey Siegel, who demonstrated his seemingly boundless patience by welcoming a MSTP student nearly two years removed from M3 clerkships to his clinics and surgeries. Over the past year, he modeled the role of a leader in academic medicine, showing respect for learners at all levels and a genuine interest in medical research– even the ”first principles” basic science research contained in this thesis. I truly appreciate our many interesting discussions about focused ultrasound and its potential clinical relevance to orthopaedic surgery, culminating in what was quite possibly the first computational continuum mechanics abstract accepted for presentation at a clinical oncology meeting. I also thank Jill Hasen, P.A. and the residents I worked with for their patience, their instruction, and their willingness to indulge me with many clinical learning opportunities and conversations about cavitation. I am also grateful to Dr. Michele Caird and Dr. Clifford Craig for their career advice and support of my quest for clinical experience during graduate school.

I have also appreciated the consistent support I received from the Medical Scientist Training Program both as a medical student and while in graduate school. In particular, Professor Ronald Koenig and Justine Hein provided regular guidance and assistance that ensured my transitions from medical school to graduate school and back again were smooth– a truly remarkable feat given my accelerated timeline and nontraditional PhD. I am likewise grateful to staff in the Office of Medical Student Education and to the Mechanical Engineering Graduate Program for their scheduling and administrative assistance.

Finally, I appreciate the support and friendship of my many colleagues in the Auto Lab over the years, especially past and present members of the Scientific Computing and Flow Physics Lab: Pooya, Brandon, Marc, Shahab, Siddhesh, Seth, Phil, Mauro, Suyash, Samuel, Kevin, Griffin, Minki, Michael, Grace, Sonya, and Nick. You have all been exceptional sources of technical insight, intellectual wit, and comic relief. Plus, you have excellent taste in restaurants. I am also thankful for the community of fellow MSTP students I have come to know these past few years as well as for my medical school friends. My family has been a critical source of support and perspective throughout my extended educational journey, and I am deeply grateful for their continued encouragement.

This work was financially supported in part by a Rackham Predoctoral Fellowship, the NSF Graduate Research Fellowship Program, a Summer Biomedical Research Program grant from the University of Michigan Medical School, NIH training grant 5T32GM007863-38 under the University of Michigan MSTP, and ONR grant N00014-17-1-2058 under Dr. Timothy Bentley. Finally, I am grateful for the yearly generosity of U.S. taxpayers, and I hope this work proves worthy of their investment.

TABLE OF CONTENTS

DEDICATION ii
ACKNOWLEDGMENTS iii
LIST OF FIGURES ix
LIST OF TABLES xiv
LIST OF ABBREVIATIONS xv
ABSTRACT xvi

CHAPTER

1 Introduction 1
  1.1 Cavitation and Bubble Dynamics 1
    1.1.1 Nucleation and the Acoustic Cavitation Threshold 2
    1.1.2 Single–Bubble Models in Water and Tissue 4
  1.2 Cavitation in Biomedical Applications 7
    1.2.1 Cavitation–Induced Tissue Damage 8
    1.2.2 Therapeutic Ultrasound Procedures 10
    1.2.3 High Strain Rate Injuries 12
  1.3 Thesis Overview 14
2 Acoustic Measurements of Nucleus Size Distribution at the Cavitation Threshold 17
  2.1 Abstract 17
  2.2 Introduction 17
  2.3 Methods 19
    2.3.1 Single–Bubble Experiments 19
    2.3.2 Single–Bubble Simulations 21
      2.3.2.1 Theoretical Model 21
      2.3.2.2 Problem Setup 23
    2.3.3 Minimum Nucleus Size and Validation Metric 24
  2.4 Results 27
  2.5 Discussion 28
  2.6 Conclusions 28
3 Validation of Histotripsy Single–Bubble Models 29
  3.1 Abstract 29
  3.2 Introduction 30
  3.3 Methods 33
    3.3.1 Single–Bubble Experiments 33
    3.3.2 Theoretical Model 35

3.3.2.1 Compressibility Effects 35
3.3.2.2 Thermal Effects 37
3.3.3 Problem Setup 38
3.3.4 Validation Metric 39
3.4 Results 40
3.4.1 Acoustic Waveform 41
3.4.2 Compressibility Effects 44
3.4.3 Thermal Effects 45
3.5 Discussion 50
3.6 Conclusions 54
4 Acoustic Cavitation Rheometry 55
4.1 Abstract 55
4.2 Introduction 56
4.3 Methods 58
4.3.1 Experiments 58
4.3.2 Theoretical Model and Numerical Methods 59
4.3.3 IMR Approach: Three–Parameter Sweep 61
4.4 Results 62
4.5 Discussion 64
4.5.1 Stress–Free Radius, R_0 64
4.5.2 Shear modulus, G 65
4.5.3 Viscosity, μ 65
4.5.4 Additional Uncertainties 66
4.5.5 Acoustic vs. Laser–Induced Cavitation Data in IMR 67
4.6 Conclusions 67
5 Predicting Tissue Susceptibility to Mechanical Cavitation Damage in Therapeutic Ultrasound 69
5.1 Abstract 69
5.2 Introduction 70
5.3 Theoretical Model 72
5.3.1 Constitutive Model 74
5.3.2 Problem Setup 76
5.4 Results 77
5.4.1 Baseline Case 77
5.5 Parametric Study 85
5.5.0.1 Viscosity 86
5.5.0.2 Shear Modulus 88
5.5.0.3 Waveform Peak Negative Pressure 91
5.5.0.4 Waveform Frequency 93
5.5.0.5 Nucleus Size 96
5.5.1 Elastic–to–Viscous Stress Transition 97
5.6 Discussion 100
5.6.1 Predicting the Elastic–to–Viscous Transition 101
6 Modeling Tissue–Selective Cavitation Damage 106
6.1 Abstract 106

- 6.2 Introduction . . . 107
- 6.3 Methods . . . 110
  - 6.3.1 Theoretical Model . . . 110
  - 6.3.2 Viscoelastic and Acoustic Parameters . . . 114
  - 6.3.3 Problem Setup . . . 116
  - 6.3.4 Stress and Strain Fields . . . 117
- 6.4 Results . . . 118
  - 6.4.1 Radial Dynamics . . . 118
  - 6.4.2 Stress Fields . . . 120
  - 6.4.3 Strain Fields . . . 123
  - 6.4.4 Strain Rate Fields . . . 125
- 6.5 Discussion . . . 127
  - 6.5.1 Mechanical Damage Mechanisms . . . 127
  - 6.5.2 Extent of Tissue Damage . . . 129
- 6.6 Conclusions . . . 133

7 Conclusion . . . 135
- 7.1 Summary . . . 135
- 7.2 Conclusions . . . 136
- 7.3 Future Research Directions . . . 139
  - 7.3.1 Nucleation . . . 139
  - 7.3.2 Bubble Dynamics in Water and Soft Matter . . . 140
  - 7.3.3 Cavitation Damage Mechanisms . . . 141

BIBLIOGRAPHY . . . 142

LIST OF FIGURES

1.1 Experimental determination of the acoustic (intrinsic) cavitation threshold in water with 1.5–MHz high–amplitude ultrasound pulse by Vlaisavljevich et al. (a) Passive cavitation detection signals at increasing ultrasound peak negative pressure (left) with corresponding high–speed optical images of bubbles produced in focal region (right). (b) Experimental plot of cavitation probability in degassed water as a function of peak negative pressure magnitude. The intrinsic cavitation threshold is measured to occur at a cavitation probability of approximately 0.5, corresponding to a peak negative pressure magnitude of approximately 27 MPa. 2
1.2 Comparison of experimental bubble images and single–bubble numerical simulations: (a) Representative images of bubbles produced by high–amplitude ultrasound in agarose tissue phantoms with increasing Young's modulus (E) at two pulse frequencies (500 and 345 kHz). Single–bubble simulations showing expected radius vs. time behavior of bubbles in media with varying (b) Young's modulus (fixed pulse frequency of 345 kHz) and (c) pulse frequency (fixed Young's modulus of 1 kPa). 5
1.3 Further study of cavitation damage mechanisms is needed to better mitigate deleterious effects of cavitation in biomedical contexts. (a) High–speed videography showing formation of temporary cavity (top – bottom) formed by high velocity bullet in ballistic gelatin, (b) Deformation of a brain tissue slice during blast–induced microcavitation (boxed region), (c) Transthoracic echocardiogram image showing cavitation bubbles (yellow arrow) inside the left ventricular cavity in the presence of a mechanical valve 8
1.4 Histotripsy liver ablation in a rodent model. (a) Real-time ultrasound imaging showing creation of a histotripsy lesion in rodent liver, (b) lesion visualized after treatment on MRI, (c) gross lesions in rodent livers, (d) pathology slide showing sharp boundaries between fractionated tissue and healthy surrounding tissue. 11

2.1 (Reproduced from Chapter 2) (a) Radius vs. time measurements from 88 separate experiments. The clustering of experimental data sets is a consequence of aligning all data such that the maximum radii occur at $t = 0$. A single data set is shown in black with spatial resolution error bars. (b) All data sets scaled by maximum radius and collapse time. 20
2.2 (a) Simulation R_{max} as a function of nucleus size. (b) A representative data set shown in black. The simulation (blue trace) initialized with R_0 indicated by solid red point in (a) optimizes the normalized rms error between experiment and simulation nearest neighbors (red open points). 24

2.3 Aggregate experimental data sets from Fig. 1. Shaded region is bounded by the simulations initialized with the smallest and largest nucleus sizes. The dark red trace is the simulation corresponding to the mean nucleus size. The dashed blue line is the simulation initialized with R_0^*. 26
2.4 Nucleus size distribution fitted to lognormal pdf (red). 27

3.1 Experimental data sets containing radius vs. time measurements from 88 separate experiments. Three representative data sets are identified in black with error bars corresponding to limits in spatial resolution of the experiments. 34
3.2 Three representative experimental data sets are shown as black solid markers: $R_{max}^{\mu-\sigma}$ (squares), R_{max}^{μ} (diamonds), and $R_{max}^{\mu+\sigma}$ (circles). The traces through each data set are optimal simulations with nearest neighbor points identified by open markers. 40
3.3 Inference of acoustic driving pressure: (Panel 1) Representative experimental data set with spatial resolution error bars (top) and raw histotripsy waveform with a peak pressure of -24 MPa (bottom). (Panel 2) Smooth curve fit through bubble radius vs. time data set using cubic splines method. (Panel 3) Assume curve fit solves the Rayleigh–Plesset equation and solve Eq. 3.7 for p_f. Solution is shown as dashed black line over the raw waveform, and the inset shows a detail of the peak negative pressure portion of the waveform. (Panel 4) Scale p_f to match known peak negative (threshold) pressure (yellow dashed line), and fit scaled p_f with a continuous analytic pulse, p_{ac} (Eq. 3.8, black solid line). (Panel 5) Use p_{ac} to obtain numerical radius vs. time solutions. 41
3.4 (a) Radius vs. time simulations obtained with the cold fluid assumption for thermal effects and the Rayleigh–Plesset (RP), Keller–Miksis with pressure (KMP), and Keller–Miksis with enthalpy (KME) models for compressibility all initialized with a fixed R_0 of 3 nm. (b) The same models initialized with the optimized R_0 for each of three representative data sets: $R_{max}^{\mu-\sigma}$ (squares), R_{max}^{μ} (diamonds), and $R_{max}^{\mu+\sigma}$ (circles). The optimized R_0 values and NRMSE organized by data set and compressibility model are shown in Table 3.2. 45
3.5 Optimized R_0 distributions (top row) and normalized rms error (NRMSE) distributions (bottom row) obtained by applying a cold fluid assumption with each compressibility model to 88 experimental data sets. 46
3.6 (a) Radius vs. time simulations obtained with the KMP equation for compressibility effects and the adiabatic polytropic approximation (Adi), isothermal polytropic approximation (Iso), cold fluid assumption (Cold), and full thermal (Full) models all initialized with a fixed R_0 of 3 nm. (b) The same models initialized with the optimized R_0 for each of three representative data sets: $R_{max}^{\mu-\sigma}$ (squares), R_{max}^{μ} (diamonds), and $R_{max}^{\mu+\sigma}$ (circles). The optimized R_0 values and NRMSE organized by data set and thermal model are shown in Table 3.3. 47
3.7 Optimized R_0 distribution (top row), and NRMSE distribution (bottom row) obtained by applying the KMP equation for compressibility effects with the (a) adiabatic polytropic approximation, (b) isothermal polytropic approximation, and (c) full thermal models for bubble contents to 88 experimental data sets. The cold fluid assumption distributions are shown in Fig.3.5(b). 48

3.8 Raw histotripsy waveform (gray) with overlay showing scaled waveform inferred from experimental data (dashed yellow) as well as the rising portion of analytic waveforms with fitting parameters $\eta = 3.7$ (black), 1.5 (green), and 29 (blue). Inset shows finer detail of boxed region. 53

4.1 Scaled radius vs. time data adapted from Wilson et al. for 19 experiments in 0.3% (open markers) agarose gel and 21 experiments in 1% (filled markers) agarose gel. . . 59
4.2 Dimensional radius vs. time data for 19 experiments in 0.3% agarose gel. The best fit simulation for a representative experimental data set (filled squares) is shown in black. 61
4.3 Stress–free radius, R_0 distribution for experiments in 0.3% and 1% agarose gels. . . . 62
4.4 Shear modulus, G distribution for experiments in 0.3% and 1% agarose gels. 63
4.5 Viscosity, μ distribution for experiments in 0.3% and 1% agarose gels. 63

5.1 Radial (τ_{rr}) and polar ($\tau_{\theta\theta} = -\tau_{rr}/2 = \tau_{\phi\phi}$) stresses and strains on a wedge of tissue during bubble growth (left) and collapse (right) 73
5.2 Schematic illustrating bubble radius and material coordinates in undeformed and deformed configurations. 75
5.3 Time history of the bubble radius (top) driven by a single negative histotripsy cycle (bottom) for the baseline case. 77
5.4 Top: Color plot shows temporal and spatial evolution of the total (viscous + elastic) radial stress distribution in the tissue for the baseline case. Solid lines correspond to stresses experienced as a function of time along Lagrangian trajectories starting 1 to 200 m from the bubble nucleus, with stress magnitude along each trajectory indicated by arrows at right. Vertical dashed lines correspond to stresses in the surroundings at fixed times given below. Bottom: Bubble color plots show stresses at fixed times between 5 and 41 s, with traces indicating the magnitudes of compressive stresses (solid blue) and tensile stresses (dashed red) as a function of distance from the bubble wall. 79
5.5 Same as for Fig. 5.4, but for viscous stresses, τ_{rr}^{V}. 81
5.6 Same as for Fig. 5.4, but for elastic stresses, τ_{rr}^{E} 82
5.7 Radial strains versus time following Lagrangian trajectories (left) and at Eulerian points (right). Distances correspond to the different initial distances of the particles from the origin (Lagrangian) and to the initial distances from the maximum radius (Eulerian). 83
5.8 Time history of bubble radius for media of different viscosities ($\mu = 1$, 5, 15, 50 and 100 mPa.s). 86
5.9 Maximum compressive (left) and tensile (right) stresses versus initial distance from the bubble nucleus in media of different viscosities ($\mu = 1$, 5, 15, 50 and 100 mPa.s). The elastic–to–viscous transitions are circled on the compressive stress traces. 87
5.10 Maximum compressive Hencky strain versus distance from the bubble nucleus in media of different viscosities ($\mu = 1$, 5, 15, 50 and 100 mPa.s). 87
5.11 Time history of bubble radius for media of different shear moduli ($G = 0$, 1, 2.5, 10, 100 and 1000 kPa). 89

5.12 Maximum compressive (left) and tensile (right) stresses as a function of initial distance from the bubble nucleus for media of different shear moduli (G = 0, 1, 2.5, 10, 100 and 1000 kPa). Elastic-to-viscous transitions are circled on compressive stress traces. 89
5.13 Maximum compressive Hencky strain as a function of distance from the bubble nucleus in media of different shear moduli (G = 0, 1, 2.5, 10, 100 and 1000 kPa). 90
5.14 Time history of the bubble radius for different peak negative pressures (p_A= 20, 30, 40, 50 and 60 MPa). 91
5.15 Maximum compressive (left) and tensile (right) stresses as a function of initial distance from the bubble nucleus for different peak negative pressures (p_A= 20, 30, 40, 50 and 60 MPa). Elastic-to-viscous transitions are circled on compressive stress traces. 92
5.16 Maximum compressive Hencky strain as a function of distance from the bubble nucleus for different peak negative pressures (p_A= 20, 30, 40, 50 and 60 MPa). 92
5.17 Time history of the bubble radius for different frequencies (ω = 0.5, 0.7, 1.0, 3.0 and 5.0 MHz) 93
5.18 Maximum compressive (left) and tensile (right) stresses as a function of distance from the bubble nucleus for different frequencies (ω = 0.5, 0.7, 1.0, 3.0 and 5.0 MHz). Elastic-to-viscous transitions are circled on compressive stress traces. 94
5.19 Maximum compressive Hencky strain as a function of distance from the bubble nucleus for different frequencies (ω = 0.5, 0.7, 1.0, 3.0 and 5.0 MHz). 94
5.20 Time history of the bubble radius for different initial bubble radii (R_0 = 2.5, 5.0, 10, 100, 1000 and 10,000 nm). 95
5.21 Maximum compressive (left) and tensile (right) stresses as a function of initial distance from the bubble nucleus for different initial bubble radii (R_0 = 2.5, 5.0, 10, 100, 1000 and 10,000 nm). Elastic-to-viscous transitions are circled on compressive stress traces. 95
5.22 Maximum compressive Hencky strain as a function of distance from the bubble nucleus for different initial bubble radii (R_0 = 2.5, 5.0, 10, 100, 1000 and 10,000 nm). . . 96
5.23 Elastic-to-viscous compressive stress transition distance x_{EV} as a function of viscosity for G = 0.5, 2.5 and 5 kPa (left) and of shear modulus for μ = 15, 20 and 25 mPas (right). 98
5.24 Elastic-to-viscous compressive stress transition distance xEV as a function of peak negative pressure for ω = 0.8, 1.0, and 3.0 MHz (left) and of waveform frequency for p_A = 20, 30 and 40 MPa (right). 98
5.25 Schematic illustrating three likely time points for mechanical tissue damage during a single cycle of bubble growth and collapse. The dominant mechanisms acting at points R_1, R_2 and R_3 are given in Table 5.2. 99
5.26 Scaled elastic–to–viscous compressive stress transition distance as a function of the dimensionless elastic–to–viscous forces ratio, ξ. 103

6.1 Histotripsy liver lesions with preserved vessels (a,c,d) and bile ducts (b,e). Results show (a) arterial phase MR image of patent artery (red arrow) in ablation zone (arrow heads), (b) liver-specific contrast MR image with patent bile ducts (green arrows) in ablation zone (arrow heads). H&E slides of (c) portal vein (black arrows), (d) intact artery wall (blue arrows), and (e) bile ducts (white arrows) with adjacent necrosis (arrow heads) in ablation zone. 109
6.2 Analytic waveform (black dotted trace) over a representative experimental waveform (solid blue trace); both have a frequency of 1 MHz. 114
6.3 Simulated radius as a function of time traces for (a) 0.5 MHz, (b) 1 MHz, and (c) 3 MHz waveforms in tissues with properties given in Table 1. 119
6.4 Total deviatoric radial stress fields developed in liver (a) and HCC (b) exposed to 1 MHz waveform. White region corresponds to tissue deformation with respect to distance from the bubble nucleus as a function of time. Black lines correspond to Lagrangian paths taken by particles starting 20, 50, and 100 μm from the bubble nucleus. Plots (c) and (d) show the numerical magnitudes of total stress along the Lagrangian paths shown in (a) and (b), respectively. 120
6.5 Maximum von Mises stress surrounding bubble as a function of initial distance from the bubble nucleus for different tissues exposed to (a) 0.5 MHz, (b) 1 MHz, and (c) 3 MHz waveforms. 121
6.6 Total radial strain along the Lagrangian paths starting 20, 50, and 100 μm from the bubble nucleus in (a) liver and (b) HCC exposed to a 1 MHz waveform. 123
6.7 Maximum von Mises strain surrounding bubble as a function of initial distance from the bubble nucleus for different tissues exposed to (a) 0.5 MHz, (b) 1 MHz, and (c) 3 MHz waveforms. Vertical lines indicate the distance at which strain first attenuates below the ultimate true strain of liver, hepatic artery, gallbladder, and stomach. 124
6.8 Total radial strain rate along the Lagrangian paths starting 20, 50, and 100 μm from the bubble nucleus in (a) liver and (b) HCC exposed to a 1 MHz waveform. 125
6.9 Maximum von Mises strain rate surrounding bubble as a function of initial distance from the bubble nucleus for different tissues exposed to (a) 0.5 MHz, (b) 1 MHz, and (c) 3 MHz waveforms. Inset figures show enlargement of strain rate traces in the boxed region. Vertical lines indicate the distance at which strain first attenuates below the ultimate true strain of liver, hepatic artery, gallbladder, and stomach. 126
6.10 Von Mises stress as a function of scaled distance from maximum bubble radius for different initial radii in (a) liver ($R_{max}/R_0 = 4.4 \times 10^4, 2.4 \times 10^4, 264, 55$) and (b) hepatic artery ($R_{max}/R_0 = 2.4 \times 10^4, 1.3 \times 10^4, 140, 31$) under 1 MHz forcing. 133

LIST OF TABLES

2.1 Constant Parameters 23

3.1 Constant Parameters 36
3.2 Normalized rms error associated with the cold fluid assumption combined with each of three compressibility models. Models are applied to three representative data sets shown in Fig. 3.4: $R_{max}^{\mu-\sigma}$ (squares), R_{max}^{μ} (diamonds), and $R_{max}^{\mu+\sigma}$ (circles). Mean optimized R_0 in nanometers is indicated in parentheses. 47
3.3 NRMSE obtained using the KMP equation and each model for thermal effects. Models are applied to three representative data sets: $R_{max}^{\mu-\sigma}$ (squares), R_{max}^{μ} (diamonds), and $R_{max}^{\mu+\sigma}$ (circles) maximum radii. Mean optimized R_0 in nanometers is indicated in parentheses. 49
3.4 Mean NRMSE of each model for radial dynamics and bubble contents. Mean optimized R_0 in nanometers indicated in parentheses. 50

4.1 Weighted mean and standard deviation of inferred properties for 0.3% and 1% agarose specimens using three–parameter sweep (mean ± standard deviation) 63

5.1 Magnitude of maximum strain experienced by a particle starting at the wall of the bubble nucleus. The absolute maximum strains occur when the bubble reaches its maximum radius, and relative maximum strains occur at minimum bubble radius. . . . 84
5.2 Mechanical damage mechanisms during a single cycle of bubble growth and collapse for nuclei sizes < 10 nm. 99

6.1 Tissue viscoelastic and acoustic properties, taken from the literature 113
6.2 Parameters fixed for all simulations 116
6.3 Strain–related damage extent, x_D and maximum radii, R_{max} in microns for different waveform frequencies 129

LIST OF ABBREVIATIONS

CRT cavitation rheology technique

IMR inertial microcavitation–based high strain–rate rheometry

ESWL extracorporeal shock wave lithotripsy

HIFU high intensity focused ultrasound

NRMSE normalized root mean squared error

ABSTRACT

Cavitation occurs when a sufficient pressure rarefaction causes explosive growth of material defects or nuclei into larger cavities (bubbles) which can damage their surroundings. Specifically, high stresses, strains and strain rates are induced locally during bubble growth and are further concentrated during bubble collapse. Although cavitation in water has received significant attention, cavitation dynamics in tissue remain poorly understood. Cavitation–induced tissue damage can occur in high strain rate injuries and can be controlled for therapeutic purposes in focused ultrasound procedures. An improved understanding of cavitation damage mechanisms could inform the development of new damage metrics for injury diagnostics and focused ultrasound treatment planning. However, experimental studies of cavitation in tissue face limitations in spatial and temporal resolution. Numerical bubble dynamics models offer insight into highly localized and transient cavitation damage mechanisms but have historically neglected non–Newtonian effects such as viscoelasticity that are essential to understanding the physics of cavitation in tissue.

This work investigates cavitation–induced tissue damage using numerical simulations of bubble dynamics validated with experimental data obtained by collaborating research groups. We first introduce a single–bubble model for cavitation in water exposed to a time–varying tensile pressure waveform with an amplitude equal to the experimental threshold for acoustic cavitation. Simulation results are then validated using experimental measurements of bubble radius as a function of time for bubbles generated at threshold. A method is presented that combines single–bubble experimental data and simulations to infer the distribution of nuclei sizes at the acoustic cavitation threshold in water. The size distribution obtained is lognormal with a mean nucleus radius of 2.88 nm. This approach is subsequently extended to validate a bubble dynamics model for viscoelastic media using experiments performed in agarose gel. We obtain distributions for agarose properties including pore size, shear modulus, and viscosity using experiments performed at various gel concentrations. The general applicability of these results to high strain rate material characterization is addressed.

The validated model is used to investigate tissue damage in focused ultrasound procedures by quantifying stress, strain, and strain rate fields developed around an ultrasound–nucleated cavitation bubble. A dimensionless parameter combining tissue and waveform characteristics is derived that dictates the dominant damage mechanism (strain vs. strain rate) as a function of distance from the bubble nucleus. These results motivate the proposal of a strain–based damage metric which can explain experimental observations of tissue–selective ablation in intrinsic threshold histotripsy treatments. The metric predicts single–bubble damage zones with radii of 30 to 500 microns determined by tissue mechanical properties and histotripsy sonication parameters. Simulation results are consistent with observed histology of histotripsy–treated *ex vivo* tissue samples. The implications of these results for selective focused ultrasound ablation of solid tumors are discussed.

CHAPTER 1

Introduction

The following chapter begins with a general overview of acoustic cavitation and bubble dynamics in water and tissue. A discussion of nucleation and the acoustic cavitation threshold is provided. An introduction to popular single–bubble numerical models follows. Subsequently, cavitation is discussed in the context of biomedical applications. Cavitation–induced tissue damage mechanisms are described, and a more detailed discussion of cavitation damage incurred during therapeutic ultrasound procedures and high strain rate injuries follows. The chapter concludes with a thesis overview highlighting key contributions to the field.

1.1 Cavitation and Bubble Dynamics

Acoustic cavitation is defined by (Leighton, 2012) as the creation of surfaces in a material as well as the expansion, contraction, and distortion of preexisting cavities in response to acoustic energy. In this work, acoustic cavitation is said to occur when a preexisting, stabilized nucleus in liquid or soft matter is exposed to a sufficient pressure rarefaction, causing it to grow into a larger cavity or bubble. A bubble grows rapidly and then violently collapses to a radius that is typically smaller than the nucleus. Bubble collapse generates localized high temperatures and pressures; it can also lead to microjet formation and shockwave emission (Brennen, 2014). Bubbles can undergo multiple cycles of growth and collapse in response to the continuous input of acoustic energy, or they can undergo a single cycle of explosive growth and violent implosion under the inertia of the surrounding medium (Miller *et al.*, 1996). The following subsections describe the growth of

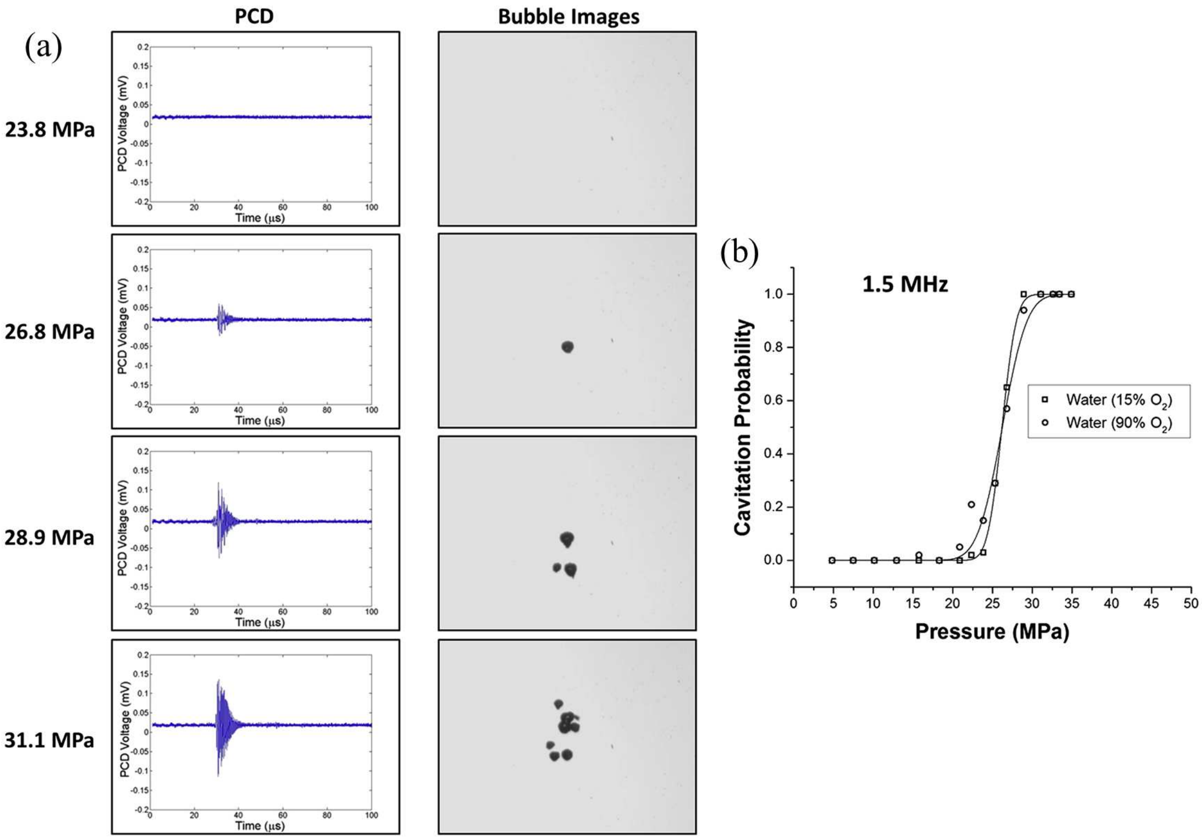

Figure 1.1: Experimental determination of the acoustic (intrinsic) cavitation threshold in water with 1.5–MHz high–amplitude ultrasound pulse by Vlaisavljevich *et al.* (2015b). (a) Passive cavitation detection signals at increasing ultrasound peak negative pressure magnitude (left) with corresponding high–speed optical images of bubbles produced in focal region (right). (b) Experimental plot of cavitation probability in degassed water as a function of peak negative pressure. The intrinsic cavitation threshold is measured to occur at a cavitation probability of approximately 0.5, corresponding to a peak negative pressure magnitude of approximately 27 MPa.

nuclei at the acoustic cavitation threshold and provide an overview of single–bubble models for the dynamic behavior of bubbles in water and tissue.

1.1.1 Nucleation and the Acoustic Cavitation Threshold

In an idealized liquid without nuclei present, “homogeneous” cavitation occurs when the liquid ruptures under a tensile (negative) pressure exceeding its tensile strength. Classical nucleation theory predicts that the homogeneous cavitation threshold in water is approximately −134 MPa at 25°C (Fisher, 1948). The theoretical tensile strength of water has also been calculated from the

Van der Waals and Berthelot equations of state, giving values of −100 MPa and −486 MPa, respectively at 27°C (Benson & Gerjuoy, 1949). These significant discrepancy in these values reflects the "tight" ordering of constituent molecules assumed by the Berthelot equation of state. Experimental techniques that approach homogeneous cavitation conditions have inferred cavitation thresholds in water of −60 MPa using a microfluidic channel (Ando *et al.*, 2012) and of −140 MPa inferred using ultraclean inclusions of water in quartz (Zheng *et al.*, 1991). Most direct measurements of cavitation thresholds are substantially lower due to nuclei and impurities that reduce the effective tensile strength of water (Mørch, 2007). Cavitation in the presence of nuclei is termed "heterogeneous" and is more commonly encountered in practice. In heterogeneous cavitation, nuclei are believed to arise from microscopic gas bubbles stabilized by a thin coating of organic impurity, by gas trapped in the crevices of tiny solid particles or 'motes', or by gas trapped in tiny surface imperfections in the liquid container (Leighton, 2012). Another possibility is cavitation arising from ion–stabilized nanoscale nuclei or "bubbstons" (Bunkin & Bunkin, 1992), with ions arising from self–ionization or from soluble ions in the liquid.

Theories that account for the existence of nuclei predict cavitation thresholds much closer to acoustic measurements of the cavitation threshold (Crum, 1979; Sukop & Or, 2005). Some authors have suggested that acoustic methods are measuring the onset of heterogeneous cavitation in a subpopulation of these nuclei rather than a true homogeneous threshold (Maxwell *et al.*, 2013; Sankin & Teslenko, 2003; Mancia *et al.*, 2020). Despite variation in water purity and experimental setup, acoustic threshold measurements are fairly reproducible, ranging from -21 MPa to -27 MPa near room temperature (Herbert *et al.*, 2006; Maxwell *et al.*, 2013; Greenspan, 1967; Wurster *et al.*, 1994). The acoustic cavitation threshold is often defined as the peak negative pressure at which the probability of cavitation detection is 0.5, and is related to the initiation of cloud cavitation in ultrasound experiments. For example, Figure 1.1 illustrates how the acoustic cavitation threshold (also called the 'intrinsic' threshold) is determined experimentally in water. In this case, the cavitation threshold is measured to occur at peak negative pressure of approximately -27 MPa. High reproducibility of threshold measurements suggests that nuclei giving rise to acoustic cavitation are consistent and ubiquitous in water (Maxwell *et al.*, 2013; Borkent *et al.*, 2007; Ando *et al.*, 2012; Azouzi *et al.*, 2013; Davitt *et al.*, 2010). The subpopulation of threshold nuclei are also believed to be intrinsic to other liquids (Bader *et al.*, 2019; Bunkin & Bunkin, 1992) and even to soft matter (Mancia *et al.*, 2020) and tissue (Maxwell *et al.*, 2013), leading authors to call this measurement that intrinsic threshold. Despite experimental evidence of their existence, nuclei responsible for this intrinsic cavitation threshold are poorly characterized. Attempts to directly measure nucleus sizes are complicated by limitations in experimental spatial resolution (Reuter *et al.*, 2019; Liu & Brennen, 1998; Billet, 1986) and difficulty tracking individual bubbles from their points of inception (Maxwell *et al.*, 2013; Sankin & Teslenko, 2003). More information about the cavitation nuclei present in a given material is needed to develop methods for cavitation control in naval applications (Chatterjee & Arakeri, 1997), materials science (Chikina & Gay, 2000; Wilkerson & Ramesh, 2016; Singh *et al.*, 2016; Guan *et al.*, 2013), and biomedical applications (Maxwell *et al.*, 2013; Vlaisavljevich *et al.*, 2016a, 2014, 2015b; Salzar *et al.*, 2017), which will subsequently be discussed in greater detail.

1.1.2 Single–Bubble Models in Water and Tissue

Numerical models for studying cavitation in tissue provide a valuable adjunct to experiments for several reasons. Cavitation nuclei exposed to high–amplitude ultrasound forcing can grow from nanometers to hundreds of microns in size and then collapse to nanometer sizes within time spans of hundreds of microseconds. Experiments face limitations in spatial and temporal resolution that make this complete cycle of bubble growth and collapse difficult to observe and measure. Opaque tissues also limit optical access (Adams *et al.*, 2017). In the study of damage mechanisms, stresses and strains are often too transient and localized to be measured directly (Vlaisavljevich *et al.*, 2016c). Numerical approaches offer a means to quantify bubble radius vs. time behavior as well as the possibility of calculating proposed damage mechanisms (mechanical stress, strain, and strain rate) (Mancia *et al.*, 2017; Estrada *et al.*, 2018). Although cavitation damage applications often involve large groups or clouds of bubbles, single bubble models can offer useful insight

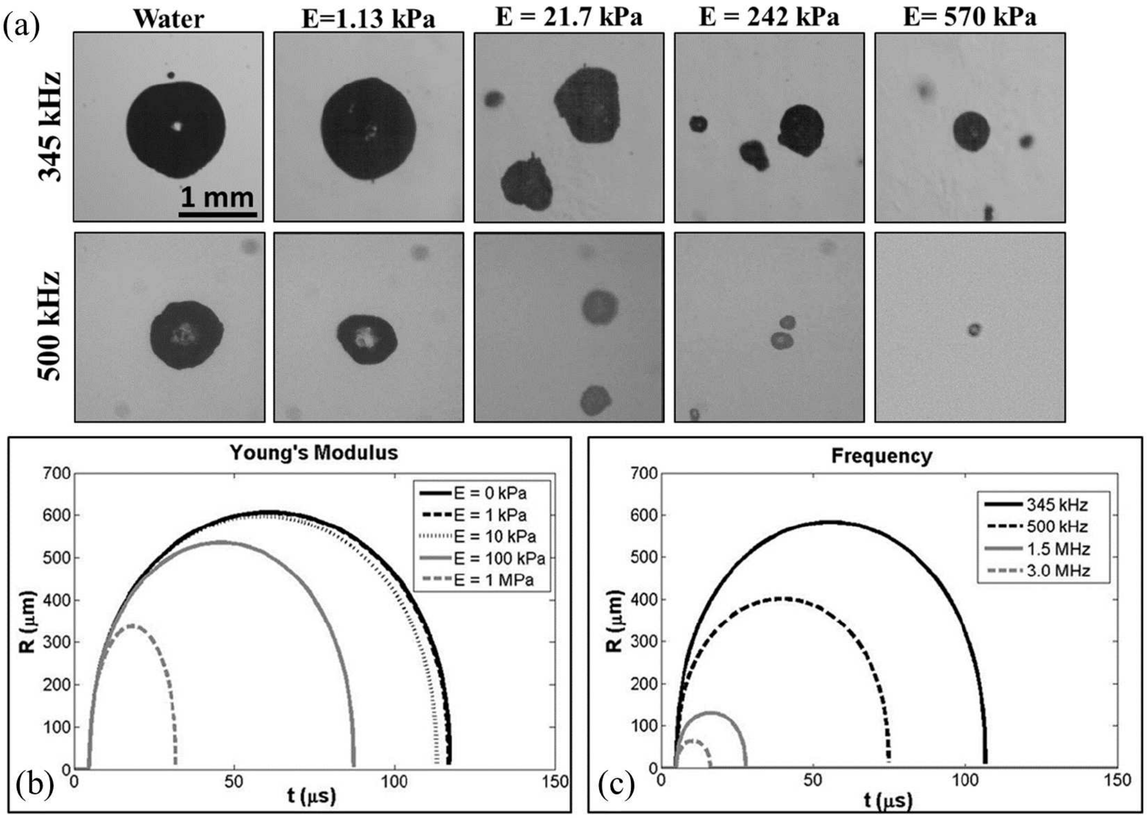

Figure 1.2: Comparison of experimental bubble images and single–bubble numerical simulations Vlaisavljevich *et al.* (2015a): (a) Representative images of bubbles produced by high–amplitude ultrasound in agarose tissue phantoms with increasing Young's modulus (E) at two pulse frequencies (500 and 345 kHz). Single–bubble simulations showing expected radius vs. time behavior of bubbles in media with varying (b) Young's modulus (fixed pulse frequency of 345 kHz) and (c) pulse frequency (fixed Young's modulus of 1 kPa).

into basic physics without extensive computational resources. These models have also remained a popular starting point for developing cavitation damage metrics (Bader & Holland, 2016; Apfel & Holland, 1991) and can inform the development of higher fidelity modeling approaches (Rodriguez & Johnsen, 2019).

There has been considerable interest in modeling cavitation in water given its relevance to naval and machinery applications (Brennen, 2014). Forms of the Rayleigh–Plesset (Plesset, 1949) equation for bubble dynamics in water have been validated by experiments in sonoluminescence (Ketterling & Apfel, 1998) and laser cavitation (Lam *et al.*, 2016). Similar models have been adopted for acoustic cavitation (Leighton, 2012), including bubble dynamics under high–amplitude ultrasound forcing. Available single–bubble models make varying assumptions regarding radial dynamics and thermal effects. For instance, the Keller–Miksis (Keller & Miksis, 1980) and Gilmore–Akulichev (Gilmore, 1952; Akulichev, 1967; Church, 1989) equations include higher order compressibility effects believed to be more important in cases of large–amplitude bubble oscillation (Vokurka, 1986). Similarly, although many authors adopt a polytropic approximation for the pressure inside the bubble (Vlaisavljevich *et al.*, 2014, 2015b,a, 2016c; Bader & Holland, 2016; Mancia *et al.*, 2017), more detailed treatments of thermal effects which consider heat transfer across the bubble wall (Prosperetti *et al.*, 1988; Kamath *et al.*, 1993) have also been used. Some authors have chosen a simplified version of the complete thermal model which considers temperature variation inside the bubble while assuming the surrounding medium remains at a constant temperature (i.e. the cold–medium assumption) (Prosperetti, 1991; Estrada *et al.*, 2018; Mancia *et al.*, 2019). Despite multiple studies comparing experiments and modeling results (Vlaisavljevich *et al.*, 2014, 2015b,a, 2016c), there is limited quantitative validation of models for bubble dynamics subjected to high–amplitude ultrasound forcing. Single–bubble numerical simulations typically provide mostly qualitative insight into experimental trends. For example, Figure 1.2 shows that numerical results are consistent with experimental observations of decreasing bubble size with increasing pulse frequency and Young's modulus (Vlaisavljevich *et al.*, 2015a). However, recently developed experimental methods (Wilson *et al.*, 2019) have enabled the measurement of single–bubble radius vs. time data from ultrasound–nucleated bubbles. Rigorous comparison of new experimental data to the results of bubble dynamics simulations is necessary to inform the implementation of computationally efficient models with quantifiable accuracy.

Tissue and other soft matter present further challenges for cavitation modeling, particularly regarding the selection of an appropriate constitutive model and any associated material properties. A variety of viscoelastic constitutive models have been adapted to the study of cavitation with the intention of modeling bubble dynamics in tissue, including the Maxwell (Allen & Roy, 2000a), Kelvin-Voigt (Yang & Church, 2005), Oldroyd (Allen & Roy, 2000b) and Zener or standard linear solid (Warnez & Johnsen, 2015) models. More recently, viscoelastic models with non-linear elasticity (Gaudron *et al.*, 2015; Estrada *et al.*, 2018) have higher fidelity given their basis in finite–strain theory. These models are believed to more adequately represent the large deformations encountered in the nanometer–to–micron–scale bubble growth observed in histotripsy (Mancia *et al.*, 2017). Modeling cavitation in tissue also requires knowledge of material properties. Although the physical properties of water are generally well–characterized, soft materials are often inhomogeneous, highly compliant (Arora *et al.*, 1999), and their properties depend on strains (deformations) and strain rates (deformation rates) (Brujan & Vogel, 2006). Furthermore, the properties of biological materials can change significantly outside of their in vivo environments (Zimberlin *et al.*, 2010), necessitating minimally invasive measurement techniques. One approach for measuring soft material properties is the cavitation rheology technique (CRT). CRT involves creating a cavity in soft material and measuring the critical pressure of mechanical instability. The critical pressure is directly related to the material's elastic modulus (Zimberlin *et al.*, 2007). More recently, the inertial microcavitation–based high strain–rate rheometry (IMR) method (Estrada *et al.*, 2018) has been proposed as a minimally invasive means of measuring soft material properties at the high strain rates relevant to cavitation. Further study of material characterization under cavitation–relevant conditions is essential to the development of accurate models for bubble dynamics in biological tissue and other soft matter.

1.2 Cavitation in Biomedical Applications

Early studies of cavitation concerned primarily hydrodynamics and turbomachinery applications (Brennen, 2014), but the more recent study of cavitation in viscoelastic media has been motivated by problems of biomedical relevance (Brujan, 2010). Cavitation in human tissue can have both traumatic and therapeutic effects. This work considers a bubble directly in a bulk viscoelastic medium, rather than a contrast agent with a shell. The following subsections describe cavitation–induced tissue damage and discuss the significance of cavitation to high strain rate injuries and therapeutic ultrasound procedures.

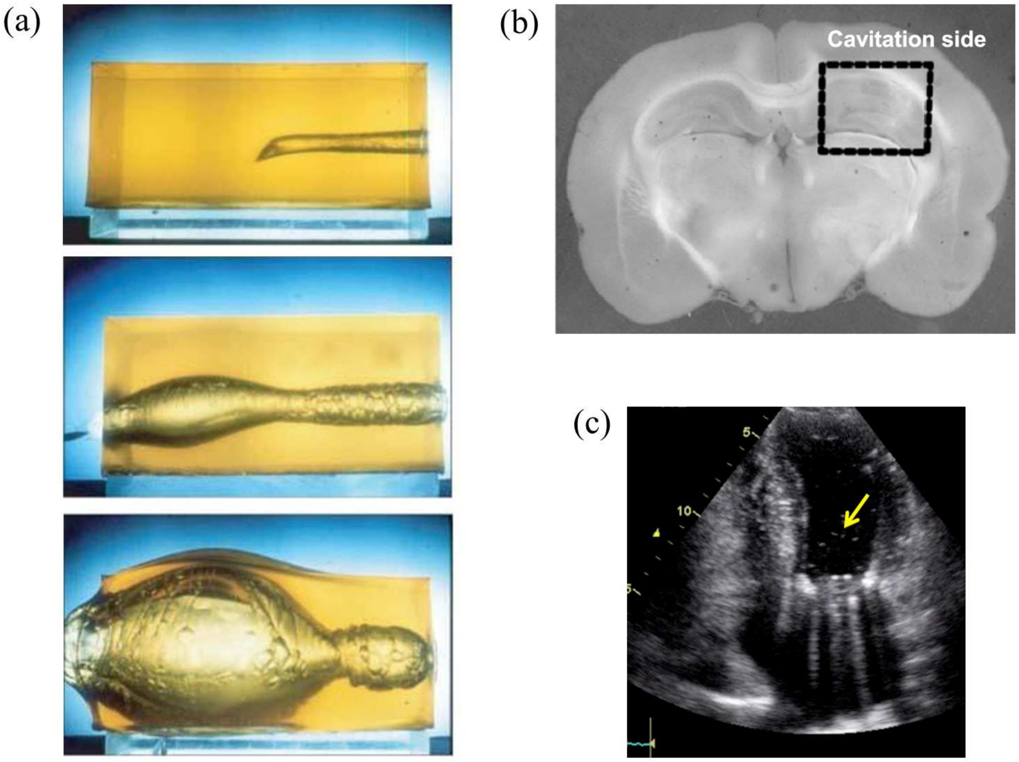

Figure 1.3: Further study of cavitation damage mechanisms is needed to better mitigate deleterious effects of cavitation in biomedical contexts. (a) High–speed videography showing formation of temporary cavity (top – bottom) formed by high–velocity bullet in ballistic gelatin Russell *et al.* (2014), (b) Deformation of a brain tissue slice during blast–induced microcavitation (boxed region) Canchi *et al.* (2017), (c) Transthoracic echocardiogram image showing cavitation bubbles (yellow arrow) inside the left ventricular cavity in the presence of a mechanical valve Lancellotti *et al.* (2016).

1.2.1 Cavitation–Induced Tissue Damage

Cavitation is relevant to high velocity rifle wounds (Brennen, 2015; Russell *et al.*, 2014), particularly for understanding the dynamics of the temporary cavity. In addition, blast waves can give rise to microbubbles in tissue which contribute to traumatic brain injuries (Franck, 2017; Goeller *et al.*, 2012; Canchi *et al.*, 2017)., and cavitation can cause hemolysis as blood flow decelerates immediately before and after valve closure (Rambod *et al.*, 1999; Lancellotti *et al.*, 2016). In these examples of deleterious cavitation (summarized in Figure 1.3), knowledge of cavitation damage mechanisms can be used to develop mitigation strategies. Mitigation and avoidance of cavitation damage is also important to ensure the safe use of microbubble contrast agents for diagnostic ultrasound (Blomley *et al.*, 2001) and encapsulated bubbles for targeted drug delivery (Crum *et al.*, 2010). In other contexts, cavitation–induced tissue damage is used for targeted tissue ablation and erosion. For example, cavitation damage has long been studied in the context of laser surgery (Vogel *et al.*, 1996). Additionally, high–amplitude ultrasound procedures including extracorporeal shock wave lithotripsy (ESWL) (Coleman & Saunders, 1993), histotripsy (Khokhlova *et al.*, 2015), and High Intensity Focused Ultrasound (HIFU) (Dubinsky *et al.*, 2008) have increased interest in the tissue damage mechanisms most relevant to acoustic cavitation (Coleman & Saunders, 1993). These therapeutic applications require a thorough understanding and quantification of cavitation damage mechanisms in order to plan and guide treatments that target pathological tissue and avoid collateral damage.

While cavitation damage to (hard) solids in water is reasonably well understood (Brennen, 2014), cavitation damage to soft materials is less well understood because additional physics must be considered. For example, tissue elasticity and possibly relaxation can introduce previously absent damage mechanisms (e.g. resistance to elastic deformations leading to cell rupture) and enhance others (e.g. more significant heating leading to cell denaturation because of higher viscous/thermal transport properties). A variety of cavitation damage mechanisms are believed to contribute to tissue destruction. In particular, the violent implosion of bubbles during inertial cavitation is associated with multiple effects. Bubble collapse concentrates high temperatures and pressures; it can also result in the emission of destructive shock wave emission or microjet formation (Brennen, 2014). Microjetting occurs when a bubble imploding asymmetrically near a boundary produces a water jet. These jets are capable of eroding metal (Coleman *et al.*, 1987; Miller *et al.*, 1996). The concentration of energy at bubble collapse can also indirectly lead to cell death through the generation of free radicals and sonochemicals (Riesz & Kondo, 1992), though this is believed to be a minor contribution to overall cell damage (Miller *et al.*, 1996). More recently, studies of histotripsy tissue ablation have found that tissue mechanical properties correlate with resistance to cavitation damage (Vlaisavljevich *et al.*, 2013a; Xu & Bigelow, 2011; Cooper *et al.*, 2004). In particular, *ex vivo* tissue samples with higher stiffness, higher average density, lower average water content, and higher ultimate strength were observed to be less susceptible to histotripsy perforation. These findings suggest that mechanical damage mechanisms (e.g. stress, strain, strain rate) are likely sources of tissue damage in cavitation–based ultrasound therapies. Experiments also found that resistance to cavitation damage had a stronger correlation with tissue ultimate strength than ultimate strain (Vlaisavljevich *et al.*, 2013a). This finding implies that stress is a key source of mechanical cavitation damage in tissue; however, available experimental techniques are unable to measure stress fields at the time and length scales relevant to cavitation (Vlaisavljevich *et al.*, 2016c). Numerical simulations can quantify the stress, strain, and strain rate fields developed during cavitation bubble growth and collapse. Cavitation modeling also permits the study of these damage mechanisms under a variety of sonication conditions, facilitating the optimization of treatment parameters. Further study and validation of models for cavitation in tissue are necessary for the development of tissue damage metrics to permit treatment planning and ensure safety.

1.2.2 Therapeutic Ultrasound Procedures

Therapeutic ultrasound includes varying modalities with a wide range of bioeffects, and cavitation bioeffects in particular remain poorly understood (Zhou, 2015). Ultrasonic physiotherapy first developed in the 1930s is now used for a variety of indications including pain relief, wound healing, tendinosis, and fracture healing (Watson, 2008); however, the precise mechanisms for achieving these therapeutic effects remain unknown. Although hyperthermia was originally thought to be the primary mechanism of action in ultrasound physiotherapy treatments, emerging evidence suggests cavitation is the more likely mechanism in soft tissue treatments (Zhou, 2015). In addition, extracorporeal shock wave lithotripsy (ESWL) is a first line treatment for uncomplicated renal and proximal ureteral calculi (Donaldson *et al.*, 2015), but this noninvasive treatment is not applicable in all settings and carries some risk of collateral damage to renal tissue. Ultrasound–mediated drug and gene delivery could enable localized release of chemotherapy agents (Schroeder *et al.*, 2009)

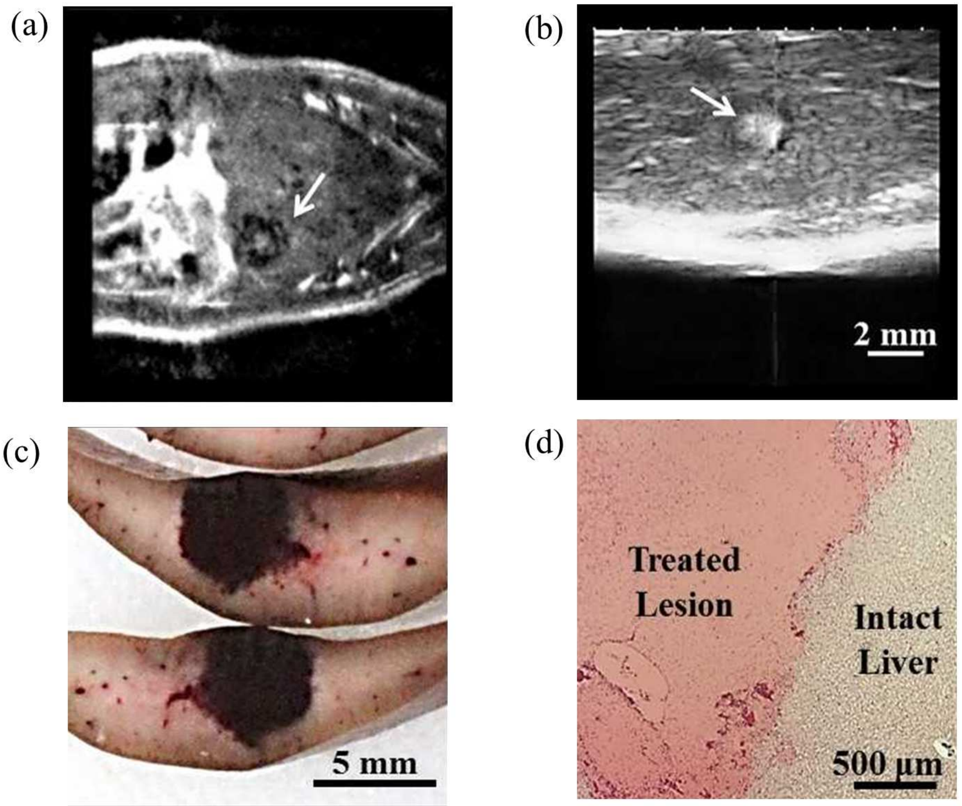

Figure 1.4: Histotripsy liver ablation in a rodent model Vlaisavljevich *et al.* (2016b). (a) Real-time ultrasound imaging showing creation of a histotripsy lesion in rodent liver, (b) lesion visualized after treatment on MRI, (c) gross lesions in rodent livers, (d) pathology slide showing sharp boundaries between fractionated tissue and healthy surrounding tissue.

and drug transport across the blood brain barrier (Kinoshita *et al.*, 2006). Cavitation is believed to be the primary mediator of targeted drug and gene transport in these cases, but further study is needed to ensure efficient drug delivery and to avoid collateral damage before these therapies can be offered to patients (Paliwal & Mitragotri, 2006). High intensity focused ultrasound (HIFU) and histotripsy are developing procedures for targeted, noninvasive ablation of pathological tissue and are promising treatments for benign and malignant tumors. Given the often transient and stochastic nature of cavitation as well as uncertainties regarding its effects on cells and tissues, further study of cavitation control and cavitation bioeffects is needed to ensure the safety and efficacy of these developing therapeutic ultrasound applications (Zhou, 2015).

Tissue ablation in HIFU is achieved primarily through thermal necrosis, but cavitation at the focus can contribute to its therapeutic effects (Coussios *et al.*, 2007) and could even be used to improve treatment efficiency (Miller & Song, 2003). In contrast, histotripsy is a non–thermal focused ultrasound procedure that relies on targeted cavitation to homogenize soft tissue into acellular debris (Xu *et al.*, 2005a; Parsons *et al.*, 2006a; Roberts *et al.*, 2006) (Fig. 1.4). Histotripsy applications include treatment of prostate pathology, solid tumors, venous thromboembolism, cardiac defects, and kidney stones (Khokhlova *et al.*, 2015; Roberts, 2014). Successful tissue fractionation requires the formation of a dense cloud of cavitation bubbles at the treatment focus (Parsons *et al.*, 2007; Xu *et al.*, 2005a). Understanding the mechanisms for cloud formation and maintenance as well as the dynamics of cavitation bubbles within the cloud is necessary to advance this technology, and these topics have been the subject of multiple experimental studies (Vlaisavljevich *et al.*, 2015b,a, 2016a). However, given that histotripsy bubbles are believed to grow explosively from nanometer–scale nuclei in a time span of microseconds(Xu *et al.*, 2005a), experimental studies face limitations in spatial and temporal resolution (Vlaisavljevich *et al.*, 2016c). The stochastic nature of cavitation inception also makes advances in cavitation control essential to ensuring the safety of histotripsy treatments. Previous authors have suggested that characterization of cavitation nuclei in tissue is particularly important for achieving this aim (Maxwell *et al.*, 2013). In addition, experimental studies suggest that histotripsy can be tissue–selective (Vlaisavljevich *et al.*, 2013a,c; Khokhlova *et al.*, 2015). However, a more precise understanding of cavitation damage in different tissues and the development of reliable damage metrics will be needed to design tissue–selective treatments.

1.2.3 High Strain Rate Injuries

Blast events leading to traumatic brain injury (TBI) (Rosenfeld *et al.*, 2013; Eskridge *et al.*, 2012), rupture of tympanic membranes and hollow viscera, pulmonary barotrauma, and other injuries (DePalma *et al.*, 2005) currently account for the majority of combat injuries and deaths (Eskridge *et al.*, 2012). These injuries remain challenging to study as they occur on a wide range of spatial and temporal scales (Gupta & Przekwas, 2015) and there is a lack of standardized methods to simulate field conditions in experiments (Sundaramurthy *et al.*, 2012). Furthermore, such injuries are often difficult to characterize because standardized clinical coding taxonomies fail to account for combat–specific injuries (Eskridge *et al.*, 2012). Given these limitations in experimental and clinical approaches, physics–based models for tissue response in blast injuries can inform the development of new diagnostic metrics (Franck, 2017; Bar-Kochba *et al.*, 2016) as well as protective countermeasures and mitigation strategies (Gupta & Przekwas, 2015; Stuhmiller *et al.*, 1996).

Cavitation can be a direct source of injury in these events, such as when a blast wave transmitted through the skull gives rise to microcavitation and consequent TBI (Goeller *et al.*, 2012). However, even in the absence of direct cavitation–induced damage, blast injuries are associated with high strain rate ($> 10^3$) loading of tissue. Cavitation provides a useful context in which to study tissue response to these extreme conditions (Estrada *et al.*, 2018; Mancia *et al.*, 2019). For example, studies of microcavitation–induced tissue damage (Mancia *et al.*, 2019, 2017; Bailey *et al.*, 2003b) have motivated the design of small–scale platforms that model the failure response of soft solids (Milner & Hutchens, 2019). Such studies have also led to the development of novel techniques for characterizing soft matter (Estrada *et al.*, 2018). Biological materials are known to behave differently under high strain rates (Shunmugasamy *et al.*, 2010), and material characterization should account for these differences. The inertial microcavitation–based rheometry (IMR) method used high–speed videography and cavitation modeling to infer material properties of polyacrylamide gels (Estrada *et al.*, 2018). While promising, this method has currently only been tested in polyacrylamide using laser–induced cavitation bubbles. Agarose–based media are more widely used as tissue phantoms than polyacrylamide (Culjat *et al.*, 2010). Furthermore, laser cavitation introduces the complexities of plasma formation and optical breakdown at the site of cavitation; these effects can alter local material properties before radius vs. time data is obtained (Brujan & Vogel, 2006). Thus, further study of the IMR method is needed, particularly with application to new materials and with alternative sources of cavitation data.

1.3 Thesis Overview

The objective of this thesis is to use validated single–bubble numerical models for material characterization under cavitation conditions and for the study of cavitation–induced tissue damage mechanisms. The results are applicable to the characterization of tissue–like media at high strain rates and to the development of damage metrics for focused ultrasound treatments. Key contributions to the field are summarized below:

1. We present a novel approach for using single–bubble experiments and simulations to measure the size distribution of nanoscale cavitation nuclei present at the acoustic threshold (Chapter 2, (Mancia *et al.*, 2020)). Cavitation nuclei are found to follow a lognormal size distribution typical of heterogeneous cavitation in other contexts and with a mean radius consistent with first principles estimates for ion-stabilized nanoscale nuclei. These findings support the hypothesis that self–ionization of water is responsible for the persistent difference between acoustic measurements and theoretical estimates of the homogeneous cavitation threshold in water. Furthermore, this work supports the value of the acoustic cavitation threshold and the associated nucleus size distribution as intrinsic material properties that characterize liquids and soft matter.

2. Radius vs. time measurements for single historipsy–nucleated bubbles in water are used to objectively compare a variety of bubble dynamics modeling assumptions (Chapter 3, (Mancia *et al.*, 2020b)). We justify a popular analytic approximation of the histotripsy waveform. Notably, we find that even modeling approaches with significant assumptions regarding compressibility and thermal effects are quite adequate for simulating the majority of histotripsy single–bubble behavior. In particular, we show that all models are applicable at maximum bubble radius, which is considered a key damage metric. Our validation of these simplified models stands to improve the computational efficiency of bubble cloud models.

3. We demonstrate the inertial microcavitation–based high strain–rate rheometry (IMR) method

for characterization of agarose gel using acoustic cavitation data (Chapter 4, (Mancia *et al.*, 2020c)). Our approach is able to infer material properties such as pore size, shear modulus, and viscosity for the 0.3% and 1% agarose gel specimens in an efficient and cost–effective manner. This work justifies use of a new source of cavitation data: Use of radius vs. time measurements from acoustic rather than laser–induced cavitation experiments. Our findings are valuable because acoustic cavitation experiments are less likely to alter material properties than laser–induced cavitation experiments, and acoustic cavitation is a closer analogue to blast injuries. We also show that cavitation–based material characterization can be applied to agarose, a more complex material than polyacrylamide that is more widely used as a tissue phantom.

4. We use a validated single–bubble model to study the effects of tissue properties and waveform parameters on the bubble dynamics of a nucleus subjected to a single negative histotripsy-relevant cycle and calculate stress, strain, and strain rate fields in a tissue–like viscoelastic medium (Chapter 5, (Mancia *et al.*, 2017)). We find that all field quantities are maximized at the bubble wall and attenuate with increasing distance from the bubble, a result consistent with observed sharp boundaries of the histotripsy ablation zone. Furthermore, stress is found to be of two distinct origins: viscous and elastic. Stress contributions decrease at different rates with elastic stresses dominating near the bubble wall and viscous stresses dominating farther away. We identify the critical distance beyond which the maximum compressive stress is of viscous rather than elastic origin. Our scaling analysis demonstrates that a fundamental relationship exists between the scaled transition location and the dimensionless elastic–to–viscous forces ratio.

5. We model bubble dynamics in a variety of tissues with literature–sourced viscoelastic and acoustic properties to investigate potential mechanisms for tissue–selective cavitation damage (Chapter 6, (Mancia *et al.*, 2019)). We compare calculated von Mises strain fields to available ultimate true strain data to estimate the predicted strain–related damage extent in

different tissues. We show that the distinct viscoelastic properties of each tissue affect the magnitudes of stress, strain, and strain rate more significantly with increasing distance from the bubble. Our findings support the hypothesis that differential tissue mechanical responses could be used to design tissue–selective treatments. Modeling results are also consistent with experiments demonstrating resistance to ablation in stiffer tissues, smaller lesion size associated with higher frequency waveforms, and sharp boundaries of the histotripsy ablation zone. Our approach to quantifying damage extent can inform the design of treatments that are selective to pathological tissue and spare critical anatomic structures.

CHAPTER 2

Acoustic Measurements of Nucleus Size Distribution at the Cavitation Threshold

This chapter is adapted from Mancia *et al.* (2020).

2.1 Abstract

The homogeneous cavitation threshold is an intrinsic material property of practical importance in a variety of applications requiring cavitation control, but acoustic threshold measurements in pure water differ from those predicted by classical nucleation theories. This persistent discrepancy is explained by combining novel methods for nucleating single bubbles at threshold with numerical modeling to obtain a nucleus size distribution consistent with first-principles estimates for ion–stabilized nucleii. We identify acoustic cavitation at threshold as a subtype of heterogeneous cavitation that is nevertheless reproducible and could offer a new means of material characterization.

2.2 Introduction

Homogeneous cavitation occurs when a medium ruptures under a tensile (negative) pressure exceeding its tensile strength (Leighton, 2012). Acoustic measurements of the homogeneous cavitation threshold in water range from −21 to −27 MPa at room temperature (Herbert *et al.*, 2006;

Davitt *et al.*, 2010; Greenspan & Tschiegg, 1982), which are of significantly smaller magnitude than values predicted by classical homogeneous nucleation theories (Debenedetti, 1996) and measured using microfluidic techniques (Ando *et al.*, 2012). This discrepancy could be due to impurities (Davitt *et al.*, 2010; Azouzi *et al.*, 2013) or vessel surface defects (Fisher, 1948). Self–ionization of water is a proposed source of ion impurities that destabilize water to cavitation (Davitt *et al.*, 2010). Alternatively, these ions could stabilize preexisting nanoscale gas bubbles against dissolution (producing *bubbstons*) (Bunkin & Bunkin, 1992; Sankin & Teslenko, 2003). This latter hypothesis in particular suggests that acoustic methods could be measuring the onset of heterogeneous cavitation in a subpopulation of stabilized, nanoscale nuclei rather than a genuine homogeneous threshold (Maxwell *et al.*, 2013; Sankin & Teslenko, 2003). Nevertheless, the reproducibility of acoustic threshold measurements in water of variable purity implies that this subpopulation of nuclei is highly consistent (Maxwell *et al.*, 2013; Borkent *et al.*, 2007; Ando *et al.*, 2012), *ubiquitous* in water (Azouzi *et al.*, 2013; Davitt *et al.*, 2010), and *intrinsic* to a variety of liquids (Bader *et al.*, 2019; Bunkin & Bunkin, 1992). Despite such robust experimental evidence of their existence, these nuclei remain poorly characterized.

Attempts to experimentally measure the size of cavitation nuclei are complicated by spatial resolutions limited to micron–sized bubbles (Reuter *et al.*, 2019; Liu & Brennen, 1998; Billet, 1986) that are not observed in the filtered, ultrapure water samples used in previous acoustic threshold measurements (Herbert *et al.*, 2006). Attempts to use fundamental thermodynamics (Bunkin & Bunkin, 1992) or nucleation theories to predict a critical or lower–bound cavitation nucleus size at a given temperature (Davitt *et al.*, 2010; Azouzi *et al.*, 2013) provide no information about the distribution of nuclei that occurs in more practical settings, and failure to account for variation of nucleus size within a cloud of acoustically–generated bubbles risks neglecting important physics (Wang, 1999). Prior work in heterogeneous cavitation suggests that nucleus sizes follow a lognormal (Ben-Yosef *et al.*, 1975; Ando *et al.*, 2011) or Weibull (Wienken *et al.*, 2006) distribution, but it is not clear that these distributions are applicable to nanoscale nuclei. Finally, previous acoustic methods used to infer a stabilized nanoscale nucleus size for water and other liquids have been limited by the inability to track bubbles from their point of inception (Maxwell *et al.*, 2013; Sankin & Teslenko, 2003). Previous authors have also calculated nucleus size by adapting homogeneous nucleation theory to acoustic cavitation, assuming spontaneous generation of gas bubbles under energetically–favorable conditions (Church, 2002). Such methods can only infer a critical or mean nucleus size that gives rise to bubble growth at the measured threshold pressure. To date, no study has both distinguished acoustic cavitation at threshold as a highly reproducible subtype of heterogeneous cavitation and provided measured cavitation statistics for the distribution of preexisting nuclei this implies.

Macroscopic cavitation activity in a variety of disciplines is likely affected by such a nucleus size distribution. The nuclei population is known to determine the onset of ultrasound–induced cavitation in water (Brotchie *et al.*, 2009; Bader *et al.*, 2019) and soft matter (Maxwell *et al.*, 2013; Vlaisavljevich *et al.*, 2016a, 2014, 2015b) in biomedical applications. Cavitation inception in blast traumatic brain injuries (Salzar *et al.*, 2017) and hydrodynamic applications (Chatterjee & Arakeri, 1997) is also thought to involve preexisting nuclei. Moreover, assumptions about the characteristics of initial cavities or defects in adhesives (Chikina & Gay, 2000), metals (Wilkerson & Ramesh, 2016), and amorphous solids (Singh *et al.*, 2016; Guan *et al.*, 2013) are needed to predict cavitation failure of these materials. Given the stochastic nature of cavitation phenomena, the ability to characterize and potentially control the nuclei population in a given medium would be useful in all of these settings (Brotchie *et al.*, 2009; Maxwell *et al.*, 2013; Chatterjee & Arakeri, 1997). This Chapter presents measurements of nanoscale cavitation nuclei in water, specifically, a complete size distribution of nuclei induced to grow at the acoustic cavitation threshold.

2.3 Methods

2.3.1 Single–Bubble Experiments

Our measurements are made by combining a unique ultrasound system capable of producing a single cavitation bubble at threshold (Wilson *et al.*, 2019) with validated numerical modeling (Estrada

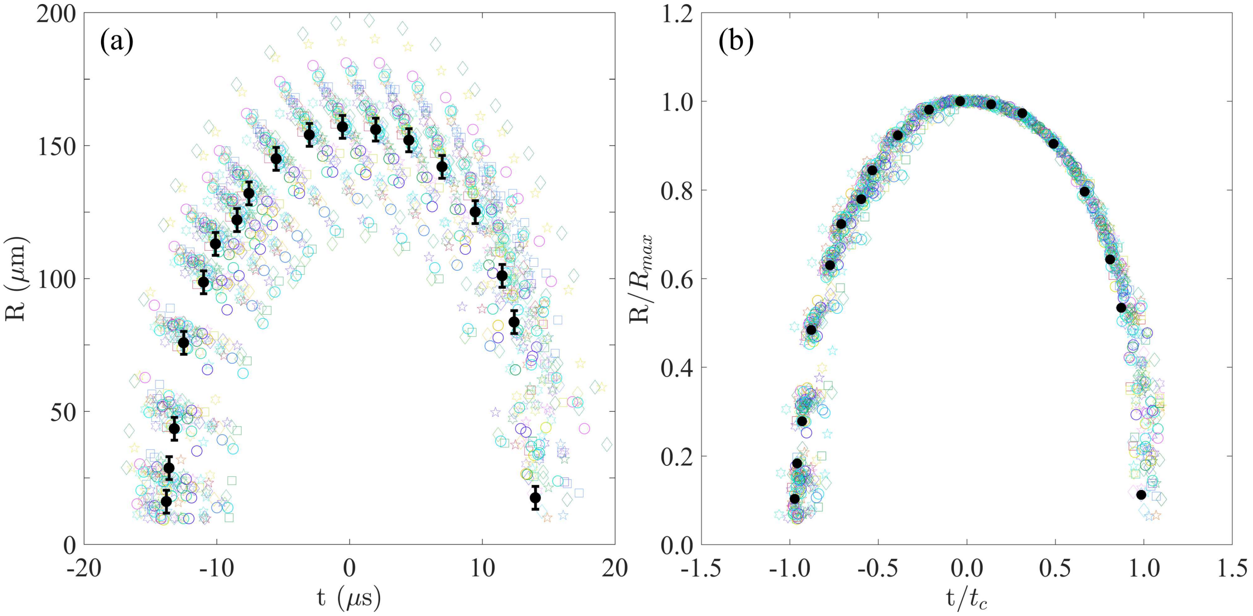

Figure 2.1: (Reproduced from Chapter 2) (a) Radius vs. time measurements from 88 separate experiments. The clustering of experimental data sets is a consequence of aligning all data such that the maximum radii occur at $t = 0$. A single data set is shown in black with spatial resolution error bars. (b) All data sets scaled by maximum radius and collapse time.

et al., 2018). These numerical and experimental methods were previously used in a study comparing laser– to ultrasound–generated cavitation in water and gels (Wilson *et al.*, 2019). Here, we leverage the data sets from those experiments in water. In brief, water is deionized, filtered to 2 μm, and degassed to 4 kPa. Experiments use a spherical acoustic array containing 16 focused transducer elements with a central frequency of 1 MHz that is capable of generating a single cavitation bubble with a well–characterized pressure waveform. Such control ensures that energy input to grow the bubble is known for a given nucleus size. Single bubbles are nucleated with a probability of 0.5 using a 1.5–cycle acoustic pulse which has a single rarefactional pressure half–cycle with an amplitude of −24 MPa. This value is consistent with that obtained by previous authors using highly purified water (Herbert *et al.*, 2006). Images of the bubbles through a single cycle of growth and collapse are obtained using a high–speed camera with a multi–flash–per–camera–exposure technique (Wilson *et al.*, 2019). This technique generates images of nested, concentric bubbles which are differentiated using brightness thresholding and edge detection. Bubble radii are measured at individual flash points by applying a least squares circle fit to their detected boundaries. For all experiments, spatial resolution is limited to ±4.3 μm, and temporal resolution to ±1.25 μs.

Aggregate radius vs. time data sets for 88 acoustically–nucleated single–bubble experiments in water are shown in Figure 2.1(a). Although all of the bubbles represented in the curves in Fig. 2.1(a) were generated under equivalent experimental conditions, significant differences between individual experiments are evident. Black points are a single representative data set, and error bars correspond to uncertainty associated with limitations in spatial resolution. Given that most of the other data sets fall outside of these error bars, it can be concluded that error associated with limitations in spatial resolution does not explain the data spread. Figure 2.1(b) shows that the data sets collapse when scaled by the measured maximum radius and collapse time, $t_c = 0.92 R_{max} \sqrt{\rho_\infty / P_\infty}$, where R_{max} is the maximum bubble radius of a given data set, ρ_∞ is liquid density, and P_∞ is the far–field liquid pressure (both constants given in Table 2.1). Thus, all experiments are governed by the same physics with exceedingly small uncertainty once appropriate scaling addresses uncertainties in initial conditions. In particular, the energy delivered by the ultrasound pulse to the nucleus grows the bubble as the bubble expands to maximum radius against its surroundings. That initial energy is proportional to the nucleus volume and ultrasound pressure amplitude. Given the negligible error in pressure amplitude measurement and its consistency with previous studies (Davitt *et al.*, 2010), we submit that the data spread is due to different nanoscale nucleus sizes corresponding to each experiment.

2.3.2 Single–Bubble Simulations

2.3.2.1 Theoretical Model

We simulate the dynamics of a single spherical, homobaric air bubble in water. To account for near–field compressibility effects, radial bubble dynamics are described by the Keller–Miksis equation (Keller & Miksis, 1980):

$$\left(1-\frac{\dot{R}}{c_\infty}\right)R\ddot{R}+\frac{3}{2}\left(1-\frac{\dot{R}}{3c_\infty}\right)\dot{R}^2=\frac{1}{\rho_\infty}\left(1+\frac{\dot{R}}{c_\infty}+\frac{R}{c_\infty}\frac{d}{dt}\right)\left[p_B-\left(p_\infty+p_f(t)\right)-\frac{2\sigma}{R}-4\mu\frac{\dot{R}}{R}\right], \quad (2.1)$$

where R is the bubble radius, c_∞ and ρ_∞ are the constant sound speed and density of the medium, respectively. The surface tension, σ and viscosity, μ are constants for water at 25 °C. These parameters and others that remain constant for all simulations are given in Table 3.1.

Heat transfer effects are considered by solving for temperature fields inside and outside of the bubble. The time derivative of the internal bubble pressure, $p_B(t)$ couples the Keller–Miksis equation (Eq. 5.1) to the energy equation for air inside the bubble:

$$\dot{p}_B=\frac{3}{R}\left((\kappa-1)K\left.\frac{\partial T}{\partial r}\right|_R-\kappa p_B\dot{R}\right) \quad (2.2)$$

$$\frac{\kappa}{\kappa-1}\frac{p_B}{T}\left[\frac{\partial T}{\partial t}+\frac{1}{\kappa p_B}\left((\kappa-1)K\frac{\partial T}{\partial r}-\frac{r\dot{p}_B}{3}\right)\frac{\partial T}{\partial r}\right]=\dot{p}_B+\frac{1}{r^2}\frac{\partial}{\partial r}\left(r^2K\frac{\partial T}{\partial r}\right), \quad (2.3)$$

where $T(r,t)$ is the temperature field of air inside the bubble, which has a ratio of specific heats κ. The air has a thermal conductivity given by $K = K_AT + K_B$, where constants K_A and K_B were determined empirically for air (Prosperetti *et al.*, 1988). The initial pressure inside the bubble is $p_B(0) = p_\infty + 2S/R$. A boundary condition is prescribed for the center of the bubble: $\nabla T = 0$ at $r = 0$. The bubble wall boundary condition is simplified to $T(R) = T_\infty$ under the assumption that the water remains at its constant ambient temperature through the single cycle of bubble growth and collapse considered in each experiment (Prosperetti, 1991; Estrada *et al.*, 2018).

The far–field pressure is the sum of the ambient pressure, p_∞ and time–varying incident pulse,

Table 2.1: Constant Parameters

Parameter	Value
p_A	24 MPa
f	1 MHz
n	3.7
δ	5 μs
σ	72 mN/m
c_∞	1496 m/sec
ρ_∞	1000 kg/m^3
p_∞	101.325 kPa
T_∞	25 °C
κ	1.4
K_A	5.28×10^{-5} W/mK^2
K_B	1.165×10^{-2} W/mK

$p_f(t)$:

$$p_f(t) = \begin{cases} p_A \left(\frac{1+\cos[\omega(t-\delta)]}{2}\right)^n, & |t-\delta| \leq \frac{\pi}{\omega}, \\ 0, & |t-\delta| > \frac{\pi}{\omega}. \end{cases} \tag{2.4}$$

The pressure amplitude, $p_A = -24$ MPa and frequency, $f = 1$ MHz ($\omega = 2\pi f$) are approximated from experimental waveform measurements while the time delay, $\delta = 5$ μs and fitting parameter, n are chosen as in previous studies (Vlaisavljevich *et al.*, 2014; Mancia *et al.*, 2017).

2.3.2.2 Problem Setup

The equations are nondimensionalized (Warnez & Johnsen, 2015) using the initial bubble radius, R_0, water density, ρ_∞, equilibrium pressure of the bubble contents, $p_0 = p_\infty + 2S/R$, and far–field temperature, T_∞ to define a characteristic speed, $u_c = \sqrt{p_0/\rho_\infty}$ and dimensionless parameters: Reynolds number, $\mathrm{Re} = \rho_\infty u_c R_0/\mu$, Weber number, $\mathrm{We} = p_0 R_0/2S$, dimensionless sound speed, $C = c_\infty/u_c$, and $\chi = T_\infty K_M/p_0 R_0 u_c$. A variable–step, variable–order solver based on numerical differentiation formulas (MATLAB *ode15s*) is used for numerical time marching (Shampine & Reichelt, 1997; Shampine *et al.*, 1999). Equations are integrated over a dimensional time span of $t = [0, 50]$ in microseconds; results are then time–shifted so that the maximum bubble radius occurs

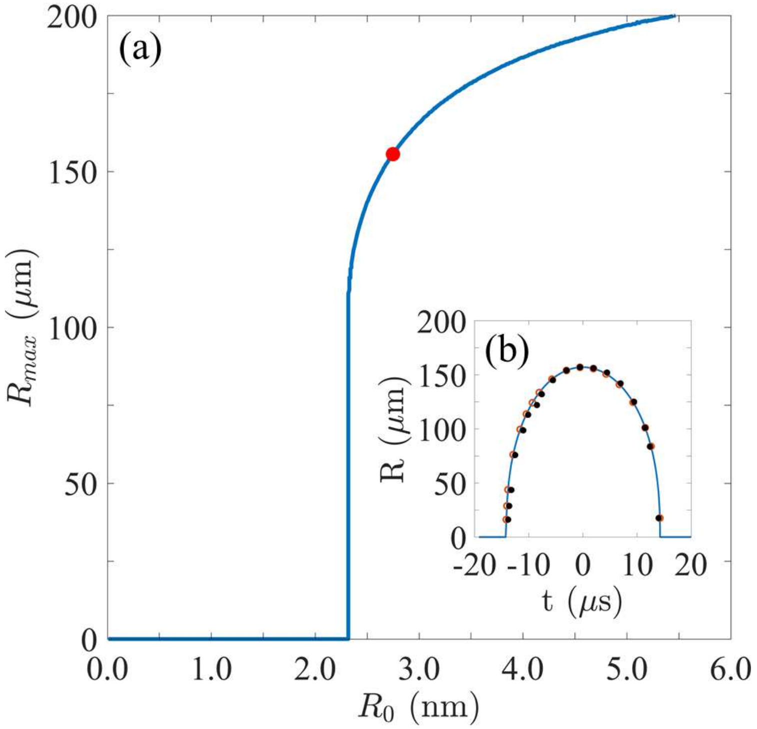

Figure 2.2: (a) Simulation R_{max} as a function of nucleus size. (b) A representative data set shown in black. The simulation (blue trace) initialized with R_0 indicated by solid red point in (a) optimizes the normalized rms error between experiment and simulation nearest neighbors (red open points).

at $t = 0$. Using numerical methods described by (Warnez & Johnsen, 2015), the spatial derivatives in the energy equation are discretized on a mesh of $N_s + 1$ points in r-space (Prosperetti *et al.*, 1988) inside the bubble and computed using a spectral collocation method (Warnez & Johnsen, 2015). Results are sufficiently converged when simulations use $N_s = 30$ points inside the bubble. A more detailed treatment of the derivation and numerical implementation of this model can be found in the literature (Prosperetti *et al.*, 1988; Kamath *et al.*, 1993; Barajas & Johnsen, 2017; Warnez & Johnsen, 2015).

2.3.3 Minimum Nucleus Size and Validation Metric

To construct the nucleus size distribution, we hypothesize that cavitation nuclei exist as stabilized nanobubbles (Maxwell *et al.*, 2013; Sankin & Teslenko, 2003) and seek to determine the minimum nucleus size, R_0^* required for cavitation growth at a given threshold pressure. Based on past work on the acoustic cavitation threshold (Maxwell *et al.*, 2013; Vlaisavljevich *et al.*, 2015b, 2016a), the threshold pressure is fixed at its measured value of −24 MPa for all simulations. Figure 2.2(a) shows the simulation maximum bubble radius as a function of nucleus size under this tensile pressure. Bubble growth is negligible until a minimum nucleus size of $R_0^* = 2.32$ nm is reached. Because the time of the tensile pulse is much longer than the timescale of the bubble, the quasistatic assumption holds, and the minimum nucleus size can be calculated from the Blake threshold (Leighton, 2012). The minimum pressure amplitude needed to cause explosive growth of a bubble with initial radius R_0 is given by:

$$P_B = P_0 + \frac{8\sigma}{9}\sqrt{\frac{3\sigma}{2(P_0 + 2\sigma/R_0)R_0^3}}, \tag{2.5}$$

where P_B is the Blake threshold, $P_0 = 101325$ Pa is the ambient pressure of the surrounding fluid, and $\sigma = 0.072$ N/m is the surface tension of water at 25°C. Assuming $2\sigma/R_0 \gg P_0$ for these nanoscale nuclei gives rise to a simplified expression for R_0:

$$R_0 = \frac{4\sigma}{3\sqrt{3}}\left(\frac{1}{P_B - P_0}\right). \tag{2.6}$$

In the present case, the Blake threshold pressure is equivalent to the measured threshold pressure: $P_B = 24$ MPa. Substituting the other physical constants into Eq. 2.6 gives $R_0 = 2.32$ nm $= R_0^*$, which is the minimum bubble radius that will grow when exposed to the measured Blake threshold pressure (Walton & Reynolds, 1984). For comparison, previous studies estimate the minimum radii of stabilized nanoscale nuclei to be approximately 2.0 nm (Bunkin & Bunkin, 1992) from first principles and 2.5 nm (Maxwell *et al.*, 2013) from bubble dynamics simulations. In contrast, critical nucleus volumes obtained using homogeneous nucleation theories correspond to radii of 1.3 nm (Davitt *et al.*, 2010) and 0.88 nm (Azouzi *et al.*, 2013) at 300 K.

The complete nucleus size distribution is created by varying the R_0 used to initialize simula-

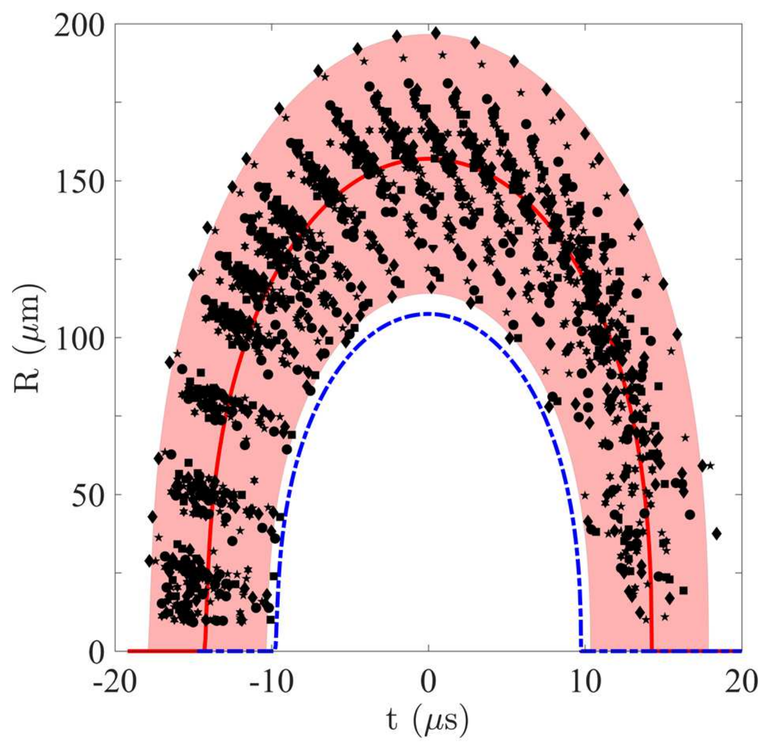

Figure 2.3: Aggregate experimental data sets from Fig. 1. Shaded region is bounded by the simulations initialized with the smallest and largest nucleus sizes. The dark red trace is the simulation corresponding to the mean nucleus size. The dashed blue line is the simulation initialized with R_0^*.

tions over a range of 2.32 – 6.00 nm for each experimental data set. A nearest neighbors algorithm with a standardized Euclidean distance metric is then used to identify simulation points closest to experimental data points. The nucleus distribution consists of R_0 values that optimize the normalized root–mean–squared (rms) error between individual data points of a given experimental realization and their simulation nearest neighbors. The average normalized rms error for these data sets is 0.98 (with 1.00 implying a perfect fit). Figure 2.2(b) shows the representative data set from Figure 2.1. The simulation initialized with $R_0 = 2.78$ nm (indicated by the red point in Figure 2.2(a)) optimizes the normalized rms error between the experimental data (black points) and the nearest neighbors on the simulation trace (red open points). In this case, the normalized rms error is 0.98, which is equivalent to the mean error for all data sets. This procedure is followed for each data set to obtain R_0 values optimizing the normalized rms error.

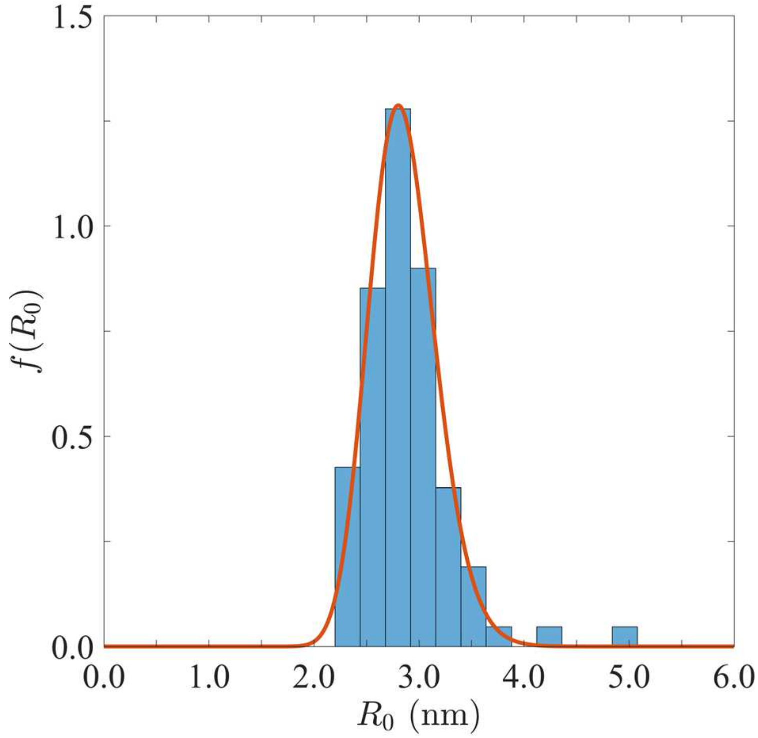

Figure 2.4: Nucleus size distribution fitted to lognormal pdf (red).

2.4 Results

Figure 2.3 illustrates how simulations initialized with different nucleus sizes effectively bound the experimental data sets. Aggregate experimental data from Figure 2.1 are shown in black, and the shaded region is bounded by simulations initialized with the smallest nucleus size, $R_0 = 2.33$ nm and the largest nucleus size, $R_0 = 4.99$ nm that optimize the normalized rms error. The dark red trace is the simulation initialized with the mean nucleus size of 2.88 nm, and the blue dashed trace is the simulation initialized with the predetermined, lower–bound nucleus, $R_0^* = 2.32$ nm. The nucleus size distribution is best approximated by a lognormal probability distribution function (pdf), outlined in red in Figure 4.3, which has $\sigma = 0.11$ and $\mu = 1.0$. This finding is consistent with previous use of a lognormal distribution to model equilibrium bubble sizes for polydisperse flow based on measured bubble populations in a water tunnel and ocean water (Ben-Yosef *et al.*, 1975; Ando *et al.*, 2011).

2.5 Discussion

The nucleus size distribution is consistent with previous studies which estimated the sizes of ion–stabilized nuclei to be between 2 and 4 nm (Sankin & Teslenko, 2003; Bunkin & Bunkin, 1992), and support the hypothesis that hydronium ions (e.g. those produced during self–ionization of water) are the ubiquitous impurity responsible for the discrepancy between acoustically–measured and theoretical homogeneous cavitation thresholds (Davitt *et al.*, 2010). The lognormal pdf parallels size distributions measured for larger cavitation bubbles in settings of heterogeneous cavitation (Ben-Yosef *et al.*, 1975; Ando *et al.*, 2011), and nuclei measured in this study are at least 1 nm larger than critical nuclei obtained using classical nucleation theories. These findings suggest that acoustic methods, even in highly purified water, are measuring a threshold for heterogeneous rather than homogeneous cavitation. However, consistency in measurements (Herbert *et al.*, 2006; Davitt *et al.*, 2010; Greenspan & Tschiegg, 1982) distinguishes cavitation at the acoustic threshold in a medium as a reflection of the nucleii population intrinsic to that medium. Although water is the only medium considered in this study, the methods presented here could be readily extended to predict the intrinsic nucleus size distributions characteristic of other liquids and soft materials, thus offering a new avenue for achieving cavitation control in biomedical, manufacturing, and naval applications.

2.6 Conclusions

In summary, this work presents a new approach for using single–bubble experiments and simulations to measure the size distribution of nanoscale cavitation nucleii present at the acoustic threshold. Recognizing that the leading–order experimental uncertainty lies in the initial nucleii population, the inverse problem for the nucleus size distribution is solved with a single–bubble numerical model. The nucleus size distribution obeys a lognormal pdf ranging from 2.33 to 4.99 nm with a mean of 2.88 nm.

CHAPTER 3

Validation of Histotripsy Single–Bubble Models

This chapter is adapted from Mancia *et al.* (2020b).

3.1 Abstract

A variety of approaches have been used to model the dynamics of a single histotripsy–nucleated bubble. Until recently, the lack of single–bubble experimental radius vs. time data for bubble dynamics under a well–characterized driving pressure has limited model validation efforts. This study uses radius vs. time measurements of single historipsy–nucleated bubbles in water (Wilson *et al.*, 2019) to quantitatively compare a variety of bubble dynamics modeling approaches, including compressible and incompressible models for radial dynamics as well as adiabatic and isothermal polytropic approximations, a cold fluid assumption, and a full thermal model for heat transfer effects. A popular analytic approximation for the histotripsy waveform is inferred directly from the experimental radius vs. time and cavitation threshold data. We then compare distributions of a calculated validation metric obtained for each model applied to 88 experimental data sets. It is shown that there is minimal distinction ($< 1\%$) among the modeling approaches for compressibility and thermal effects considered in this study. These results suggest that even simplified models which minimize parametric uncertainty and resource demands can accurately simulate the majority of histotripsy single–bubble behavior, including points at and near the maximum bubble radius. Additional sources of parametric and model–based uncertainty are discussed.

3.2 Introduction

High–amplitude ultrasound therapies such as high intensity focused ultrasound (HIFU) and histotripsy are promising noninvasive treatments with a variety of clinical applications including treatment of solid tumors, prostate pathologies, and biofilm infections (Khokhlova *et al.*, 2015; Roberts, 2014; Bigelow *et al.*, 2018). Acoustic cavitation, the explosive growth and violent collapse of microbubbles in response to acoustic forcing, is a known source of mechanical tissue damage during these treatments. In HIFU treatments, acoustic absorption causes tissue heating and subsequent thermal necrosis. Cavitation in the focal region can contribute to mechanical tissue damage but is generally believed to be a secondary mechanism (Coussios *et al.*, 2007). In contrast, histotripsy is a non–thermal focused ultrasound procedure that relies on targeted cavitation to homogenize soft tissue into acellular debris (Xu *et al.*, 2004, 2005a; Parsons *et al.*, 2006a; Roberts *et al.*, 2006). Successful tissue fractionation in histotripsy requires the formation of a dense cloud of cavitation bubbles at the treatment focus (Parsons *et al.*, 2007; Xu *et al.*, 2005a). The mechanisms for cloud formation and maintenance as well as the dynamics of cavitation bubbles within the cloud have been the subject of multiple experimental studies (Vlaisavljevich *et al.*, 2014, 2015b,a, 2016c). Given that histotripsy bubbles are believed to grow explosively from nanometer–scale nuclei within tens of microseconds (Maxwell *et al.*, 2013), experimental studies face limitations in temporal and spatial resolution as well as difficulties observing cavitation events in real tissues (Mancia *et al.*, 2017; Vlaisavljevich *et al.*, 2016c).

Numerical models for bubble dynamics under histotripsy forcing have been used to provide physical insight at time and length scales that are beyond current experimental resolution. Most modeling efforts to date have attempted to simulate the dynamics of a single histotripsy bubble (Mancia *et al.*, 2019, 2017; Bader, 2018a,b; Bader & Holland, 2016). These basic models offer the advantage of capturing fundamental bubble dynamics while using minimal computational resources. Demonstrating the adequacy of basic models could also simplify efforts to determine model parameters which are challenging to measure. For example, a study characterizing polyacrylamide gel under cavitation–relevant conditions found that a finite–deformation Kelvin–Voigt model was equivalent or superior to the more complex standard nonlinear solid model, which required consideration of non–equilibrium shear modulus as an additional unknown (Estrada *et al.*, 2018). Moreover, identifying the essential physics needed to accurately model single bubbles remains an important step for advancing the development of higher–order methods (Rodriguez & Johnsen, 2019) and bubble cloud models (Maeda & Colonius, 2019; Ma *et al.*, 2018; Fuster & Colonius, 2011) representative of histotripsy treatments. These methods require extensive computational resources and are not yet suitable for real–time treatment monitoring (Rossinelli *et al.*, 2013). Ultimately, treatment planning and monitoring will rely on efficient algorithms capable of predicting the onset of cavitation and on quantifying the extent of cavitation–induced tissue damage even in the simple case of a single, spherical bubble (Mancia *et al.*, 2019). At present, however, the most widely used single–bubble models for dynamic cavitation during histotripsy treatments require further validation to inform cloud cavitation models.

At present, variable models for bubble radial dynamics or compressibility, bubble contents or thermal effects, and driving pressure have been used in histotripsy simulations. Histotripsy bubble dynamics models use forms of the Rayleigh–Plesset equation that have been validated by experiments in sonoluminescence (Ketterling & Apfel, 1998) and laser cavitation (Lam *et al.*, 2016), but it is unclear if similar models can accurately predict the dynamics of single bubbles nucleated by high–amplitude ultrasound pulses. For radial dynamics, the Keller–Miksis (Keller & Miksis, 1980) and Gilmore–Akulichev equations (Gilmore, 1952; Akulichev, 1967; Church, 1989) are popular alternatives to the Rayleigh–Plesset (Plesset, 1949) equation given their inclusion of weak compressibility effects. Some authors have claimed that the Gilmore model is needed in cases of large amplitude bubble oscillations (Vokurka, 1986), while others argue that enthalpy formulations of the Keller–Miksis equation are more accurate (Prosperetti & Lezzi, 1986). Treatments of thermal effects have also varied considerably, with most studies adopting a polytropic approximation for gas pressure inside the bubble (Vlaisavljevich *et al.*, 2014, 2015b,a, 2016c; Bader & Holland, 2016; Mancia *et al.*, 2017). A more complete treatment of thermal effects (Prosperetti *et al.*, 1988) has been used previously to study the effect of water temperature on the histotripsy intrinsic threshold (Vlaisavljevich *et al.*, 2016a). More recently, a study of tissue–selective effects in histotripsy (Mancia *et al.*, 2019) used a simplified version of this model considering temperature variation inside the bubble while assuming surroundings remain at a constant temperature (i.e. the cold–medium assumption) (Prosperetti, 1991; Estrada *et al.*, 2018). However, histotripsy is considered a nonthermal therapy (Roberts *et al.*, 2006), so it is also reasonable to assume isothermal conditions (Mancia *et al.*, 2017). Model forcing waveforms have included a Gaussian pulse envelope (Maxwell *et al.*, 2013) and half–cycle tensile pulses (Vlaisavljevich *et al.*, 2014, 2015b,a, 2016c; Mancia *et al.*, 2017, 2019) which are scaled by the peak negative pressure. A complete histotripsy waveform has also been used in bubble dynamics simulations (Bader & Holland, 2016), though this approach is not necessarily superior due to uncertainty in the acoustic field at the instant and location of cavitation inception.

Comparisons between histotripsy experiments and modeling results have featured in studies of the intrinsic cavitation threshold (Vlaisavljevich *et al.*, 2014, 2015b), bubble behavior (Vlaisavljevich *et al.*, 2015a, 2016c), and cavitation–induced tissue damage (Mancia *et al.*, 2017, 2019). To date, these comparisons have been general and largely qualitative. Even a recent study comparing maximum radii obtained in histotripsy bubble behavior experiments with model–predicted maximum radii (Bader & Holland, 2016) is limited by its use of experimental radius vs. time data which includes cloud cavitation events (Vlaisavljevich *et al.*, 2015a). Robust quantitative validation of single–bubble models requires experimental observation and measurement of a single histotripsy–nucleated bubble from inception through collapse. Only recently have advances in experimental methods (Wilson *et al.*, 2019; Sukovich *et al.*, 2020) offered the possibility of validating existing single–bubble models for acoustic cavitation dynamics under histotripsy–type forcing. Validation of models for single–bubble dynamics in histotripsy has been limited by a lack of information about the driving pressure due to the presence of many bubbles distorting the acoustic field. The development of a single–cycle waveform (Wilson *et al.*, 2019) and use of specialized high–speed videography permits, for the first time, a validation of histotripsy single–bubble modeling assumptions.

This study presents a quantitative comparison of different histotripsy modeling approaches to experimental radius vs. time data obtained from single–bubble nucleation events in water (Wilson *et al.*, 2019). First, we introduce single–bubble experiments in brief and provide an overview of models for compressibility and thermal effects used to simulate histotripsy bubble dynamics. Subsequently, we validate a common analytic approximation of the histotripsy waveform and apply the methods and validation metric presented in a study of cavitation nuclei (Mancia *et al.*, 2020) to evaluate select models for compressibility and thermal effects assuming that the primary parametric uncertainty for acoustic cavitation in water lies in the initial radius or intrinsic nucleus size. Representative radius vs. time experimental data sets are used for comparison to simulation results obtained with different models. Finally, we discuss a quantitative summary of initial radius statistics and validation metrics for each treatment of compressibility and thermal effects. Remaining parametric and model–based uncertainties in simulating single–bubble dynamics in histotripsy are described.

3.3 Methods

3.3.1 Single–Bubble Experiments

Experimental data was first presented in a study comparing laser and acoustic cavitation in gels and water, and further details regarding experimental methods can be found in this original work (Wilson *et al.*, 2019). Water used in experiments was deionized, filtered to 2 μm, and degassed to 4 kPa. Experiments were performed in a spherical acoustic array containing 16 focused transducer elements with a central frequency of 1 MHz. Single bubbles were nucleated using a 1.5–cycle histotripsy pulse with a single rarefactional pressure half–cycle. Images of the bubbles through a single cycle of growth and collapse were obtained using a high–speed camera with a multi–flash–per–camera–exposure technique (Sukovich *et al.*, 2020). Steps were taken to minimize the likelihood of nucleating multiple bubbles at the focal site, including an empirical threshold study

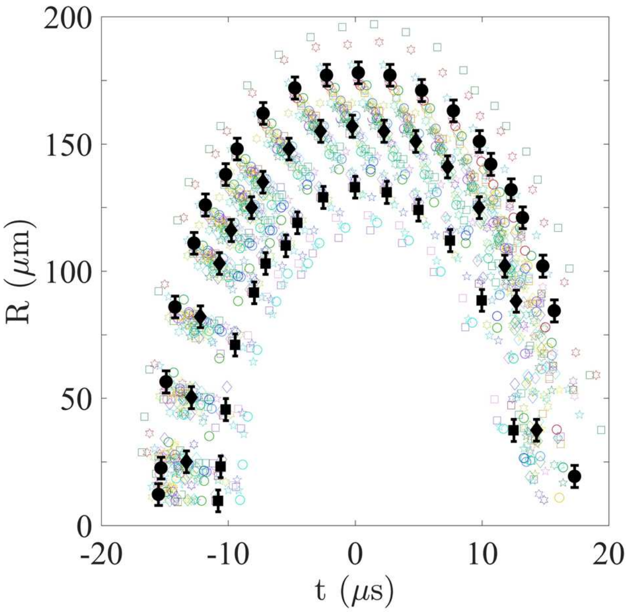

Figure 3.1: Experimental data sets containing radius vs. time measurements from 88 separate experiments. Three representative data sets are identified in black with error bars corresponding to limits in spatial resolution of the experiments.

performed prior to experiments. This was accomplished by varying the acoustic rarefactional pressure such that the probability of generating cavitation at the focus was 50%, which resulted in a peak pressure of approximately −24 MPa. Figure 3.1 is adapted from a study of the acoustic cavitation threshold (Mancia *et al.*, 2020) that presented a method for obtaining nucleus size distributions. It shows radius vs. time data for the 88 acoustically–nucleated single–bubble experiments in water. The clustering of experimental data sets during the growth phase is a consequence of aligning all data sets such that the maximum radius occurs at $t = 0$. Each data set is comprised of 15 – 25 data points. Black filled markers with error bars identify three representative radius vs. time data sets selected because they have maximum radii near the mean maximum radius, R^{μ}_{max}, of all data sets and approximately one standard deviation larger and smaller than this value, $R^{\mu\pm\sigma}_{max}$. The magnitudes of spatial and temporal resolution uncertainties in the experiments were 4.3 microns (indicated with black error bars) and ≤1.25 microseconds, respectively.

3.3.2 Theoretical Model

This study considers several approaches to modeling the dynamics of a single, spherical homobaric histotripsy bubble in water. Bubbles are assumed to arise from preexisting or intrinsic nuclei (Mancia *et al.*, 2020). The following subsections present a series of three models for compressibility effects and four models for thermal effects. Discussion of the derivation and wider applicability of each modeling approach can be found in the cited literature.

3.3.2.1 Compressibility Effects

Radial dynamics of a histotripsy bubble can be modeled using a variety of approaches which differ in their considerations of liquid compressibility and, consequently, acoustic radiation losses from the bubble. We consider three models for bubble radial dynamics which take the following general form:

$$\left(1-\frac{\dot{R}}{c_\infty}\right)R\ddot{R}+\frac{3}{2}\left(1-\frac{\dot{R}}{3c_\infty}\right)\dot{R}^2=\frac{1}{\rho_\infty}\left(1+\frac{\dot{R}}{c_\infty}+\frac{R}{c_\infty}\frac{d}{dt}\right)(\Psi(t,R)-p_{ac}(t)),$$

$$\Psi(t,R)=\begin{cases} p-p_\infty,\ c_\infty\to\infty, & \text{Rayleigh–Plesset} \\ p-p_\infty, & \text{Keller–Miksis with Pressure} \\ h_B, & \text{Keller–Miksis with Enthalpy,} \end{cases} \quad . \tag{3.1}$$

where $\Psi(t,R)$ includes three different treatments of compressibility: Rayleigh–Plesset, Keller–Miksis with pressure, and Keller–Miksis with enthalpy. All models depend on pressure evaluated at the bubble wall: $p = p_B - \frac{2S}{R} - 4\mu\frac{\dot{R}}{R}$, where the internal bubble pressure, p_B is defined in the subsequent section on thermal effects. The Keller-Miksis with enthalpy formulation also depends on enthalpy evaluated at the bubble wall, h_B:

$$h_B=\frac{n}{n-1}(p_\infty+B)\left[\left(\frac{p+B}{p_\infty+B}\right)^{\frac{n-1}{n}}-1\right]. \tag{3.2}$$

Constant parameters n and B for the modified Tait equation of state are defined for water as in (Prosperetti & Lezzi, 1986). These constants as well as the density, ρ_∞, static fluid pressure, p_∞,

Table 3.1: Constant Parameters

Parameter	Value	Parameter	Value
p_∞^0	101.325 kPa	D_M	1.41×10^{-7} m^2/s
c_∞	1497 m/s	B	304.91 MPa
T_∞	25 °C	n	7.15
S	0.072 N m	p_A	−24 MPa
μ	0.001 Pa s	η	3.7
κ	1.4	f	1 MHz
C_p	4181 J/kgK	δ	5 µs
K_A	5.28×10^{-5} W/mK^2		
K_B	1.165×10^{-2} W/mK		
K_M	0.55 W/mK		

constant sound speed, c_∞, surface tension, S, and viscosity, μ, of surrounding water are given in Table 3.1. The acoustic forcing pressure, $p_{ac}(t)$, experienced by a single bubble in the focal region is described by Eq. 3.8, and its determination is discussed in the Results section. The Rayleigh–Plesset equation (Rayleigh, 1917; Plesset, 1949) is incompressible while both the Keller–Miksis with pressure and Keller–Miksis with enthalpy equations assume first–order compressibility effects. The Keller–Miksis in pressure model was previously shown to be slightly inferior to its enthalpy formulation (Prosperetti & Lezzi, 1986). The same study suggested that the Gilmore (Gilmore, 1952) and Herring (Herring, 1941) models are also inferior to the Keller–Miksis with enthalpy formulation, so they will not be considered here. A distinguishing feature of the Gilmore equation is its inclusion of a pressure–dependent speed of sound, which in theory makes it applicable at larger Mach numbers ($\dot{R}/c < 2.2$) than the constant sound speed Keller–Miksis equations ($\dot{R}/c < 1$) (Zilonova *et al.*, 2018). In practice, however, the Mach numbers reached by the histotripsy bubble wall remain well within the range of validity for Keller–Miksis models until the instant of bubble collapse to a nanoscale minimum radius. Limitations in simulating the complex physics at histotripsy bubble collapse are inherent to all available lower–order models and will be addressed in the Discussion.

3.3.2.2 Thermal Effects

Four approaches for evaluating the energy balance inside and outside of a histotripsy bubble are considered: isothermal and adiabatic polytropic approximations, the cold fluid assumption, and a complete heat transfer model. Bubble contents are frequently assumed to be homobaric and to behave as an ideal gas producing an internal pressure that can be modeled with a polytropic equation (Noltingk & Neppiras, 1950b; Akulichev, 1967; Keller & Miksis, 1980; Apfel, 1981):

$$p_B = p_0\left(\frac{R_0}{R}\right)^{3\kappa}, \ \kappa = \begin{cases} 1, & \text{Isothermal} \\ 1.4, & \text{Adiabatic,} \end{cases} \tag{3.3}$$

where $p_0 = p_\infty + 2S/R_0$ is the initial pressure inside the bubble, and the constant κ is equal to 1 in the isothermal case and to the ratio of specific heats for air ($\kappa = 1.4$) in the adiabatic case. Both conditions have been assumed in histotripsy simulations (Vlaisavljevich *et al.*, 2015b,a, 2016c), but the isothermal assumption has been shown to more closely approximate the results of a more complete heat transfer model (Mancia *et al.*, 2017). Heat transfer effects can be included following the approaches described in (Prosperetti *et al.*, 1988; Kamath *et al.*, 1993; Barajas & Johnsen, 2017; Warnez & Johnsen, 2015) by solving energy equations inside and outside the bubble. In this case, the radial dynamics equations given in the previous section are coupled to the energy equation for air inside the bubble via the time derivative of the internal bubble pressure, p_B:

$$\dot{p}_B = \frac{3}{R}\left((\kappa-1)K\left.\frac{\partial T}{\partial r}\right|_R - \kappa p_B \dot{R}\right), \tag{3.4}$$

$$\frac{\kappa}{\kappa-1}\frac{p_B}{T}\left[\frac{\partial T}{\partial t} + \frac{1}{\kappa p_B}\left((\kappa-1)K\frac{\partial T}{\partial r} - \frac{r\dot{p}_B}{3}\right)\frac{\partial T}{\partial r}\right] = \dot{p}_B + \frac{1}{r^2}\frac{\partial}{\partial r}\left(r^2 K\frac{\partial T}{\partial r}\right), \tag{3.5}$$

where $T(r,t)$ is the temperature field of air inside the bubble. Air in the bubble has a ratio of specific heats $\kappa = 1.4$, and its thermal conductivity is given by $K = K_A T + K_B$ where K_A and K_B are empirically determined constants (Prosperetti *et al.*, 1988). The energy balance introduces an additional equation, $\Phi(T_M)$ which is a function of the surrounding liquid temperature, $T_M(t, r)$:

$$\Phi(T_M) = \begin{cases} T_M(R) = T_\infty, & \text{Cold Fluid} \\ \frac{\partial T_M}{\partial t} + \frac{R^2 \dot{R}}{r^2} \frac{\partial T_M}{\partial r} = D_M \nabla^2 T_M + \frac{12\mu}{\rho_\infty C_p} \left(\frac{R^2 \dot{R}}{r^3} \right)^2, & \text{Full Thermal.} \end{cases} \tag{3.6}$$

Equation 3.6 takes one of two forms corresponding to either a cold fluid assumption or a model incorporating full thermal effects. The cold fluid model follows a common simplification introduced by (Prosperetti, 1991) which assumes surrounding liquid remains at a constant ambient temperature, T_∞. This model is particularly appropriate for water given its large heat capacity. In the model including full thermal effects, the energy equation for bubble surroundings is solved. This equation requires knowledge of the specific heat, C_p, thermal diffusivity, $D_M = K_M/(\rho_\infty C_p)$, and thermal conductivity, K_M, of surrounding liquid. These constants are given for water in Table 3.1. Boundary conditions are prescribed for the center of the bubble and far from the bubble: $\nabla T = 0$ at $r = 0$ and $T_M \to T_\infty$ as $r \to L$, where $L \gg R$ is the arbitrary boundary of the domain. Boundary conditions at the bubble–liquid interface couple the internal bubble temperature to the temperature field in the surroundings: $T_M(r, t)$: $T|_{r=R} = T_M|_{r=R}$ and $K_{r=R} \frac{\partial T}{\partial r}|_{r=R} = K_M \frac{\partial T_M}{\partial r}|_{r=R}$.

3.3.3 Problem Setup

The equations are nondimensionalized using the initial bubble radius, R_0, water density, ρ_∞, and far–field temperature T_∞ (Warnez & Johnsen, 2015). The equilibrium pressure of the bubble contents, $p_0 = p_\infty + 2S/R_0$, is used to define a characteristic speed, $u_c = \sqrt{p_0/\rho_\infty}$, and dimensionless parameters: Reynolds number, $\mathrm{Re} = \rho_\infty u_c R_0/\mu$, Weber number, $\mathrm{We} = p_0 R_0/2S$, dimensionless sound speed, $C = c_\infty/u_c$, Fourier number, $F_0 = D_M/u_c R_0$, Brinkman number, $Br = u_c^2/C_p T_\infty$, and $\chi = T_\infty K_M/p_0 R_0 u_c$. A variable–step, variable–order solver based on numerical differentiation formulas (MATLAB *ode15s*) is used for numerical time marching (Shampine & Reichelt, 1997; Shampine *et al.*, 1999). Equations are integrated over a dimensional time span of $t = [0, 50]$ in microseconds; results are then time–shifted so that the maximum bubble radius occurs at $t = 0$.

Using numerical methods described by (Warnez & Johnsen, 2015), the spatial derivatives in the energy equation are discretized on a mesh of $N_s + 1$ points in r-space (Prosperetti *et al.*, 1988) inside and outside of the bubble and computed using a spectral collocation method (Warnez & Johnsen, 2015). Results are sufficiently converged when simulations use $N_s = 30$ points inside and outside of the bubble. A more detailed treatment of the derivation and numerical implementation of this model can be found in the literature (Prosperetti *et al.*, 1988; Kamath *et al.*, 1993; Barajas & Johnsen, 2017; Warnez & Johnsen, 2015).

3.3.4 Validation Metric

The validation procedure used to compare models for compressibility and thermal effects has been described previously (Mancia *et al.*, 2020). This previous study identified the radius used to initialize simulations (nucleus size, R_0) as the greatest source of parametric uncertainty in single–bubble experiments. For each experimental data set, numerical simulations are performed for a series of R_0 values with the intent of finding the R_0 that produces the best fit of simulation to data. The lower bound R_0 for all simulations was shown to be 2.32 nm from first principles (Mancia *et al.*, 2020). The simulation points closest to experimental points in each data set are then identified using a nearest neighbors algorithm with a standardized Euclidean distance metric. A nucleus size distribution is constructed for each modeling approach using R_0 values that optimize the normalized root–mean–squared (rms) error between the simulation nearest neighbors and corresponding experimental points in each data set. The normalized rms error validation metric ranges from $-\infty$ (worst fit) to 1.00 (optimal fit), with most values falling between 0.88 and 0.99 in the present study. This procedure is illustrated in Figure 3.2, where three representative experimental data sets are shown as black solid markers. The traces through each data set are optimized simulations obtained using the Keller–Miksis equation with pressure and the cold fluid assumption. Nearest neighbor points on each simulation trace are identified with open markers. For the previously introduced $R_{max}^{\mu-\sigma}$ (squares), R_{max}^{μ} (diamonds), and $R_{max}^{\mu+\sigma}$ (circles) data sets, the optimal normalized rms errors (with corresponding optimal R_0 for this model) are 0.969 (2.42 nm), 0.979 (2.78 nm), and 0.984

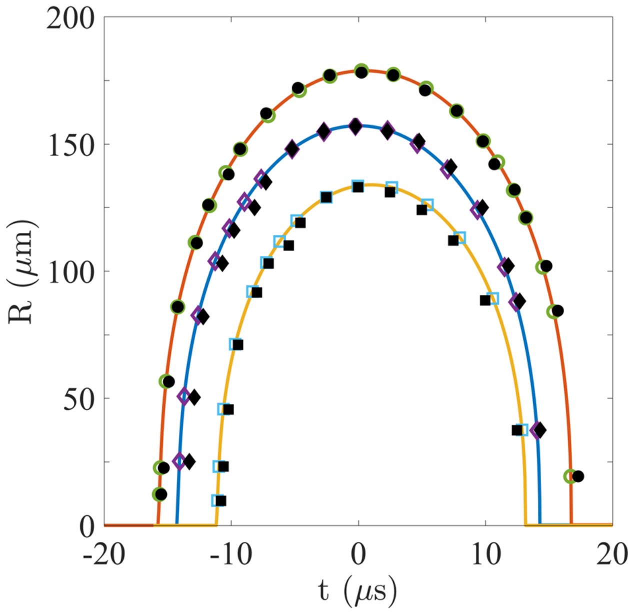

Figure 3.2: Three representative experimental data sets are shown as black solid markers: $R_{max}^{\mu-\sigma}$ (squares), R_{max}^{μ} (diamonds), and $R_{max}^{\mu+\sigma}$ (circles). The traces through each data set are optimal simulations with nearest neighbor points identified by open markers.

(3.52 nm), respectively.

3.4 Results

Experimental bubble radius vs. time measurements are first used to infer the acoustic forcing experienced by a single bubble in the focal region. Subsequently, numerical simulations are performed combining each of three modeling approaches for compressibility effects (Eq. 3.1) with each of four different models for thermal effects (Eqs. 3.3 – 3.6). To review, for compressibility effects, we consider the Rayleigh–Plesset equation, Keller–Miksis equation with pressure, and Keller–Miksis equation with enthalpy. Thermal effects are modeled using adiabatic and isothermal polytropic approximations, the cold fluid assumption, and a full thermal model. For quantitative comparison of these different modeling approaches, we present the optimized normalized rms error distributions and R_0 distributions obtained by applying the models to each of the 88 experimental data sets.

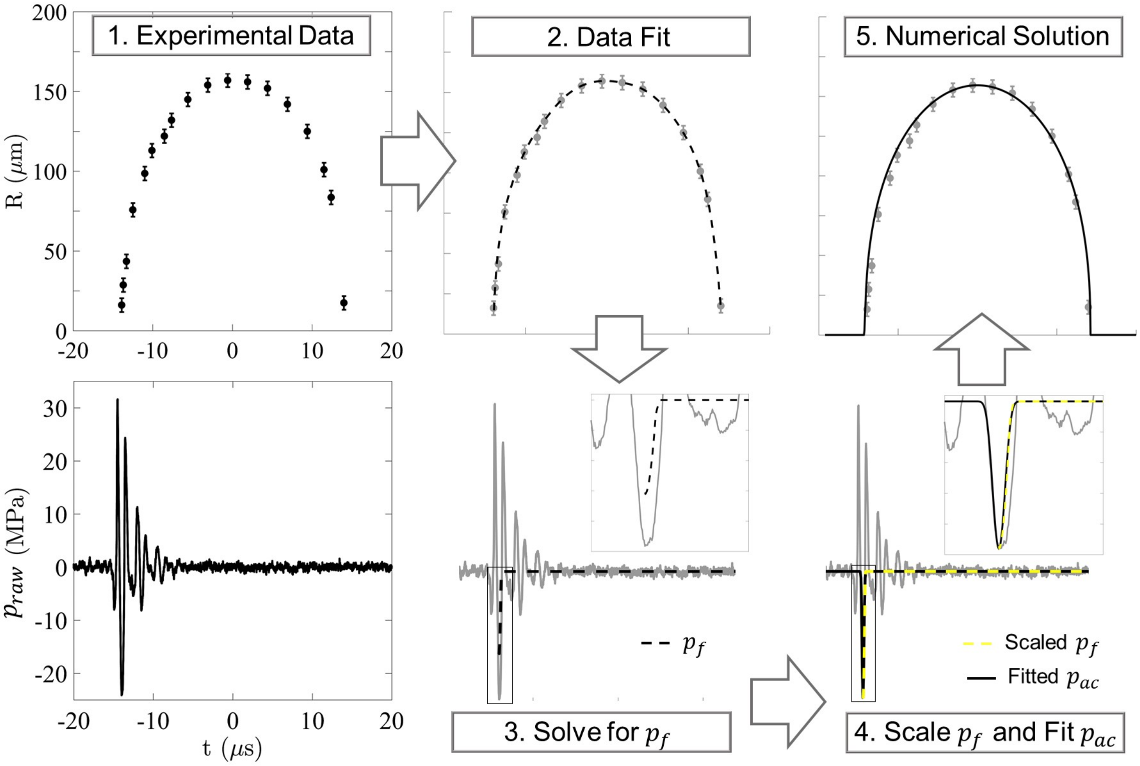

Figure 3.3: Inference of acoustic driving pressure: (Panel 1) Representative experimental data set with spatial resolution error bars (top) and raw histotripsy waveform with a peak pressure of −24 MPa (bottom). (Panel 2) Smooth curve fit through bubble radius vs. time data set using cubic splines method. (Panel 3) Assume curve fit solves the Rayleigh–Plesset equation and solve Eq. 3.7 for p_f. Solution is shown as dashed black line over the raw waveform, and the inset shows a detail of the peak negative pressure portion of the waveform. (Panel 4) Scale p_f to match known peak negative (threshold) pressure (yellow dashed line), and fit scaled p_f with a continuous analytic pulse, p_{ac} (Eq. 3.8, black solid line). (Panel 5) Use p_{ac} to obtain numerical radius vs. time solutions.

3.4.1 Acoustic Waveform

Histotripsy transducers produce nonlinear oscillatory waveforms with high–amplitude tensile and compressive components. Precise measurement of the forcing pressure as a function of time is challenging because these high–amplitude pressure waves ultimately produce destructive cavitation at the hydrophone tip (Vlaisavljevich *et al.*, 2015b; Bader & Holland, 2016). Additionally, existing bubbles and intervening material can distort the original waveform. Given these challenges, various representations of a histotripsy forcing waveform have been used in simulations. For example, a study of the cavitation threshold in tissues used a Gaussian pulse envelope (Maxwell *et al.*, 2013). An averaged waveform constructed from measured shock scattering histotripsy pulses was also used in bubble dynamics simulations (Bader & Holland, 2016). In addition, multiple previous studies have adopted a half–cycle tensile pulse fitted to the peak negative pressure portion of a raw histotripsy waveform (Vlaisavljevich *et al.*, 2014, 2015b,a, 2016c; Mancia *et al.*, 2017, 2019; Bader, 2018a). It is not obvious on first inspection that this tensile half–cycle is representative of the acoustic forcing experienced by a single cavitation bubble in the focal region; however, a strong case for the validity of this approximation can be made using the single–bubble data now available and the concept of a cavitation threshold.

The procedure for inferring the acoustic forcing waveform in histotripsy simulations is outlined in Fig. 3.3. The setup begins with a representative bubble radius vs. time data set and the measured histotripsy forcing waveform shown in panel one. This raw waveform was deduced from voltage measurements made with a fiber-optic hydrophone at a pressure of −18 MPa (to avoid hydrophone damage) and exhibits electrical noise and nonlinear distortion. Under the constraint of producing single bubbles, the peak negative pressure in the focal region is equal to the experimentally–determined cavitation threshold of −24 MPa. The raw waveform shown in Panel 1 of Fig. 3.3 has been scaled accordingly. Assuming that each bubble radius vs. time data set solves a Rayleigh–Plesset–type equation, the data set is fitted with a smooth curve to obtain a hypothetical $R(t)$ solution (dashed black line in Panel 2 of Fig. 3.3). A cubic splines method is used for the data fit to ensure continuity of the first and second derivatives of R, which are computed using central differences. One can then infer the acoustic forcing by solving for the forcing term in the Rayleigh–Plesset form of Eq. 3.1:

$$p_f(t) = p - \rho_\infty \left(R\ddot{R} + \frac{3}{2}\dot{R}^2 \right) - p_\infty. \tag{3.7}$$

The p_f solution obtained using Eq. 3.7 is shown in Panel 3 of Fig. 3.3 as the black dashed trace overlay on the raw waveform. As seen in the inset showing finer detail of the boxed region, the peak of the p_f trace aligns with the peak negative pressure segment of the measured histotripsy pulse but is clearly of lower amplitude. The discrepancy between the amplitudes of the measured waveform and p_f solution is in part due to the cubic splines data fit for R beginning at the first measured data point. The absence of radius vs. time data during early growth effectively assumes that the bubble grows from a 10–micron nucleus. However, multiple studies have suggested that true threshold nuclei are on the order of nanometers (Maxwell *et al.*, 2013; Vlaisavljevich *et al.*, 2015b, 2016a), and nucleus size is a key parametric uncertainty (Mancia *et al.*, 2020). Instead, as in the case of the raw waveform, one can confidently take the peak negative pressure of the waveform to be equivalent to the measured acoustic cavitation threshold of −24 MPa. It is thus reasonable to scale the p_f solution such that its maximum tension is equal to this measured threshold. Panel 4 of Fig. 3.3 shows the yellow dashed trace corresponding to linear scaling of the p_f solution. The scaled p_f solution is then readily fit by a popular approximation for histotripsy forcing, p_{ac}, shown in Panel 4 of Figure 3.3 as the solid black trace and expressed analytically below:

$$p_{ac}(t) = \begin{cases} p_A \left(\frac{1+cos[\omega(t-\delta)]}{2}\right)^{\eta}, & |t-\delta| \leq \frac{\pi}{\omega}, \\ 0, & |t-\delta| > \frac{\pi}{\omega}. \end{cases} \tag{3.8}$$

The measured peak pressure corresponds to $p_A = -24$ MPa in this analytic expression while the frequency, f, of the experimental waveform appears as $\omega = 2\pi f$ ($f = 1$ MHz) in Eq. 3.8. The parameter δ is an arbitrary time delay, typically taken to be 5 μs. The dimensionless fitting parameter η is typically chosen to match the curvature of the peak tensile portion of a measured histotripsy waveform. Previous studies have used this analytic expression with $\eta = 3.7$ (Mancia *et al.*, 2017, 2019; Vlaisavljevich *et al.*, 2015b,a, 2016a,c), a value deduced from a series of experimental waveforms with frequencies ranging from 0.345–3.0 MHz (Vlaisavljevich *et al.*, 2015b). The rising portion of the analytic waveform with $\eta = 3.7$ fits the scaled p_f with an accuracy $> 99.9\%$. Thus, our p_f solution inferred independently from experimental radius vs. time data and scaled to threshold amplitude is consistent with a popular analytic approximation of the histotripsy waveform, supporting the validity of this analytic waveform for histotripsy simulations. The raw waveform is noticeably broader than both the p_f solution and the fitted p_{ac} waveform. This likely reflects nonlinear broadening of the waveform that reaches the hydrophone tip, which could be more significant than broadening of the driving pressure experienced by an individual nucleus in the focal region. The experimental histotripsy waveform capable of producing a single bubble at threshold is highly reproducible with negligible shot–to–shot variability, but a relatively wide range of η produce analytic waveforms that fit the scaled p_f solution obtained from radius vs. time data with an accuracy of at least 99.8% (See Discussion). Given relative insensitivity of numerical results to changes in η, nucleus size is considered the primary source of parametric uncertainty in simulations. Nucleus size is inferred by iterating over the initial radius used for simulations until a best fit simulation is found (Panel 5 of Fig. 3.3). This procedure was reviewed in Sect. 3.3.4.

3.4.2 Compressibility Effects

Radial dynamics of a histotripsy bubble are modeled using the Rayleigh–Plesset equation (RP), the Keller–Miksis equation with pressure (KMP), and the Keller–Miksis equation with enthalpy (KME) forms of Eq. 3.1. The radius vs. time behavior produced by each radial dynamics model combined with the cold fluid assumption for a fixed 3.00 nm initial radius is shown in Fig. 3.4(a). Consistent with expectations, the RP form results in a larger maximum radius due to the absence of compressive damping. The KMP and KME forms both exhibit compressive damping and differ from each other to a lesser degree, with the enthalpy form achieving a negligibly smaller maximum radius than the pressure form. Figure 3.4(b) shows the optimized radius vs. time simulations obtained with each model by iterating R_0 for three representative data sets. The normalized rms error (NRMSE) and optimized R_0 obtained for each compressibility model applied to these data sets are shown in Table 3.2. The numerical radius vs. time results obtained with each model show good agreement with experimental data sets and considerable overlap with each other when initialized with an optimized R_0. The radial dynamics models differ most when applied to the $R_{max}^{\mu-\sigma}$ data set. The NRMSE ranges from 0.950 for the Rayleigh–Plesset model applied to the $R_{max}^{\mu-\sigma}$ data set to 0.984 for the Keller–Miksis models applied to the $R_{max}^{\mu+\sigma}$ data set. The best agreement between experiment and simulation is achieved for the $R_{max}^{\mu+\sigma}$ data set regardless of the model used. Use of

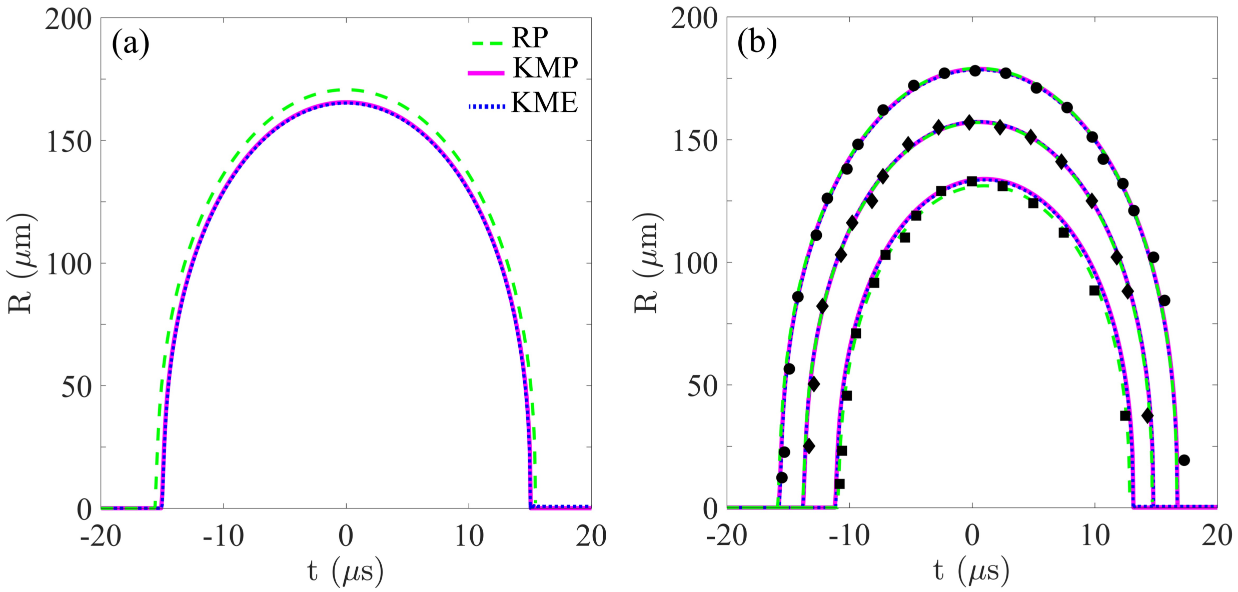

Figure 3.4: (a) Radius vs. time simulations obtained with the cold fluid assumption for thermal effects and the Rayleigh–Plesset (RP), Keller–Miksis with pressure (KMP), and Keller–Miksis with enthalpy (KME) models for compressibility all initialized with a fixed R_0 of 3 nm. (b) The same models initialized with the optimized R_0 for each of three representative data sets: $R_{max}^{\mu-\sigma}$ (squares), R_{max}^{μ} (diamonds), and $R_{max}^{\mu+\sigma}$ (circles). The optimized R_0 values and NRMSE organized by data set and compressibility model are shown in Table 3.2.

KMP or KME results in better agreement with experiments than using the RP form. The KMP model is slightly superior to KME for the $R_{max}^{\mu-\sigma}$ and R_{max}^{μ} data sets, though the KME model achieves agreement of 0.95 or greater in more data sets than KMP. The optimized R_0 values are smallest for RP and larger for the two compressible models. Complete distributions of the normalized rms error and optimized R_0 for 88 data sets obtained using the cold fluid assumption with each of the compressibility models are shown in Fig. 3.5. The NRMSE and optimized R_0 distributions for each model and all data sets show considerable overlap.

3.4.3 Thermal Effects

The gaseous contents of a histotripsy bubble are modeled using the adiabatic polytropic approximation (Adi, Eq. 3.3, $\kappa = 1.4$), the isothermal polytropic approximation (Iso, Eq. 3.3, $\kappa = 1$), the cold fluid assumption (Cold, Eqs. 6.3 – 3.6), and the full thermal model (Full, Eqs. 6.3 – 3.6). The radius vs. time behavior produced by each thermal model combined with the KMP equation for a

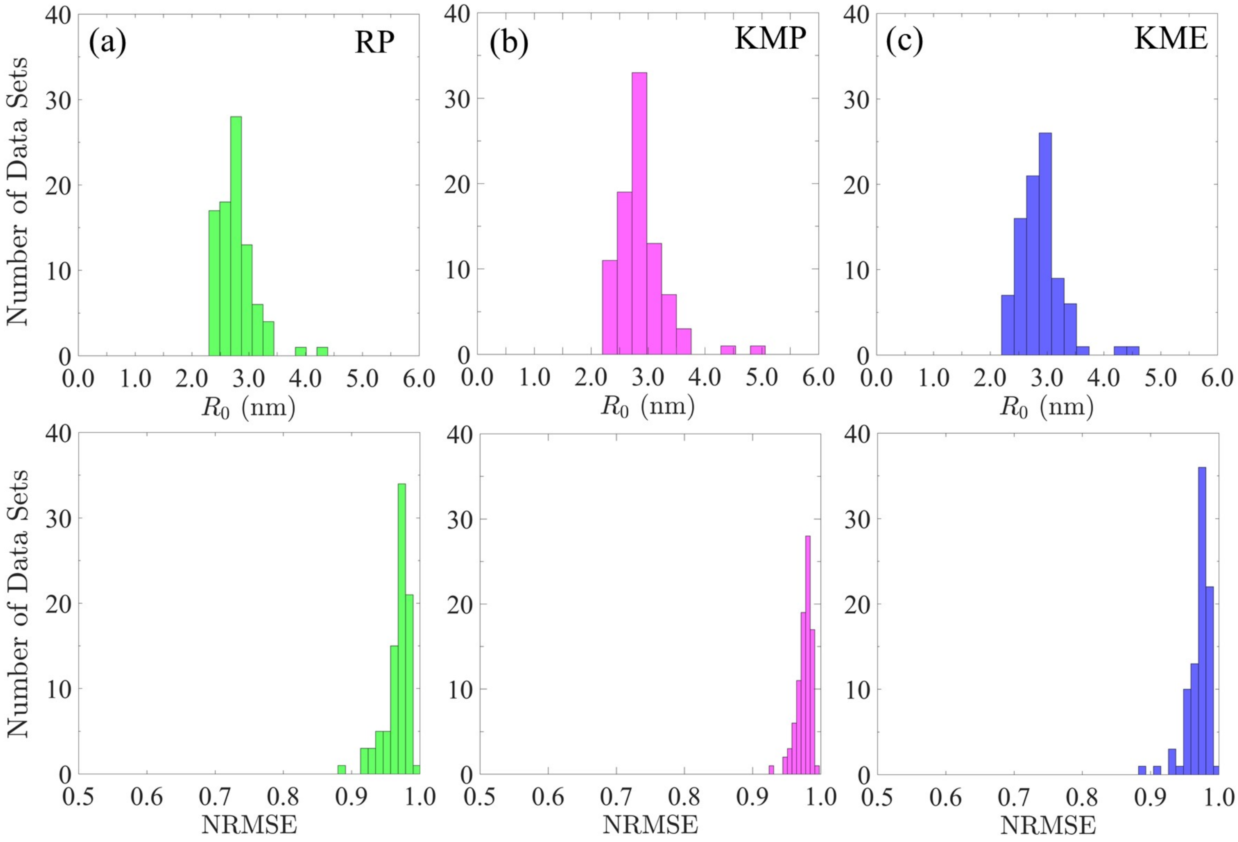

Figure 3.5: Optimized R_0 distributions (top row) and normalized rms error (NRMSE) distributions (bottom row) obtained by applying a cold fluid assumption with each compressibility model to 88 experimental data sets.

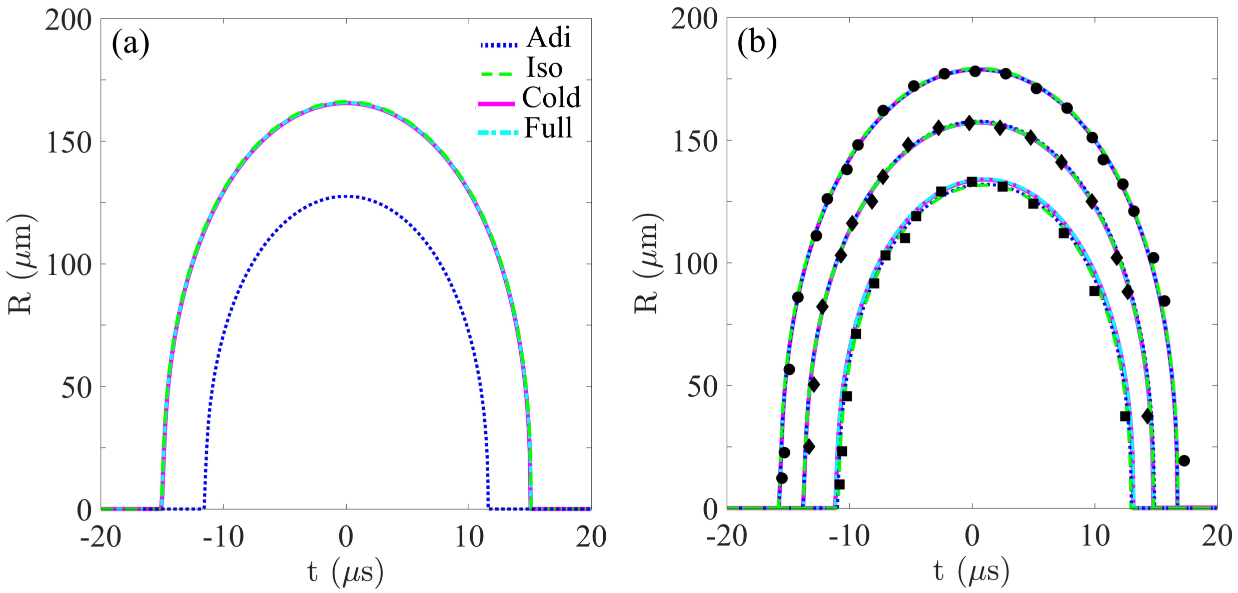

Figure 3.6: (a) Radius vs. time simulations obtained with the KMP equation for compressibility effects and the adiabatic polytropic approximation (Adi), isothermal polytropic approximation (Iso), cold fluid assumption (Cold), and full thermal (Full) models all initialized with a fixed R_0 of 3 nm. (b) The same models initialized with the optimized R_0 for each of three representative data sets: $R_{max}^{\mu-\sigma}$ (squares), R_{max}^{μ} (diamonds), and $R_{max}^{\mu+\sigma}$ (circles). The optimized R_0 values and NRMSE organized by data set and thermal model are shown in Table 3.3.

fixed 3.00 nm initial radius is shown in Fig. 3.6(a). As noted previously (Mancia *et al.*, 2017), there is minimal distinction between the isothermal polytropic, cold fluid assumption, and full thermal models. The most noticeable distinction is seen in the adiabatic polytropic case, which results in a significantly smaller maximum bubble radius for any given initial radius. Fig. 3.6(b) shows optimized radius vs. time simulations for each thermal model coupled to the KMP equation for three representative data sets. The NRMSE and optimized R_0 obtained with each model applied to these

Table 3.2: Normalized rms error associated with the cold fluid assumption combined with each of three compressibility models. Models are applied to three representative data sets shown in Fig. 3.4: $R_{max}^{\mu-\sigma}$ (squares), R_{max}^{μ} (diamonds), and $R_{max}^{\mu+\sigma}$ (circles). Mean optimized R_0 in nanometers is indicated in parentheses.

	Compressibility Models		
Data Set	Rayleigh–Plesset	KM with Pressure	KM with Enthalpy
$R_{max}^{\mu-\sigma}$	0.950 (2.39)	0.969 (2.42)	0.965 (2.45)
R_{max}^{μ}	0.973 (2.69)	0.979 (2.78)	0.974 (2.80)
$R_{max}^{\mu+\sigma}$	0.982 (3.30)	0.984 (3.52)	0.984 (3.52)

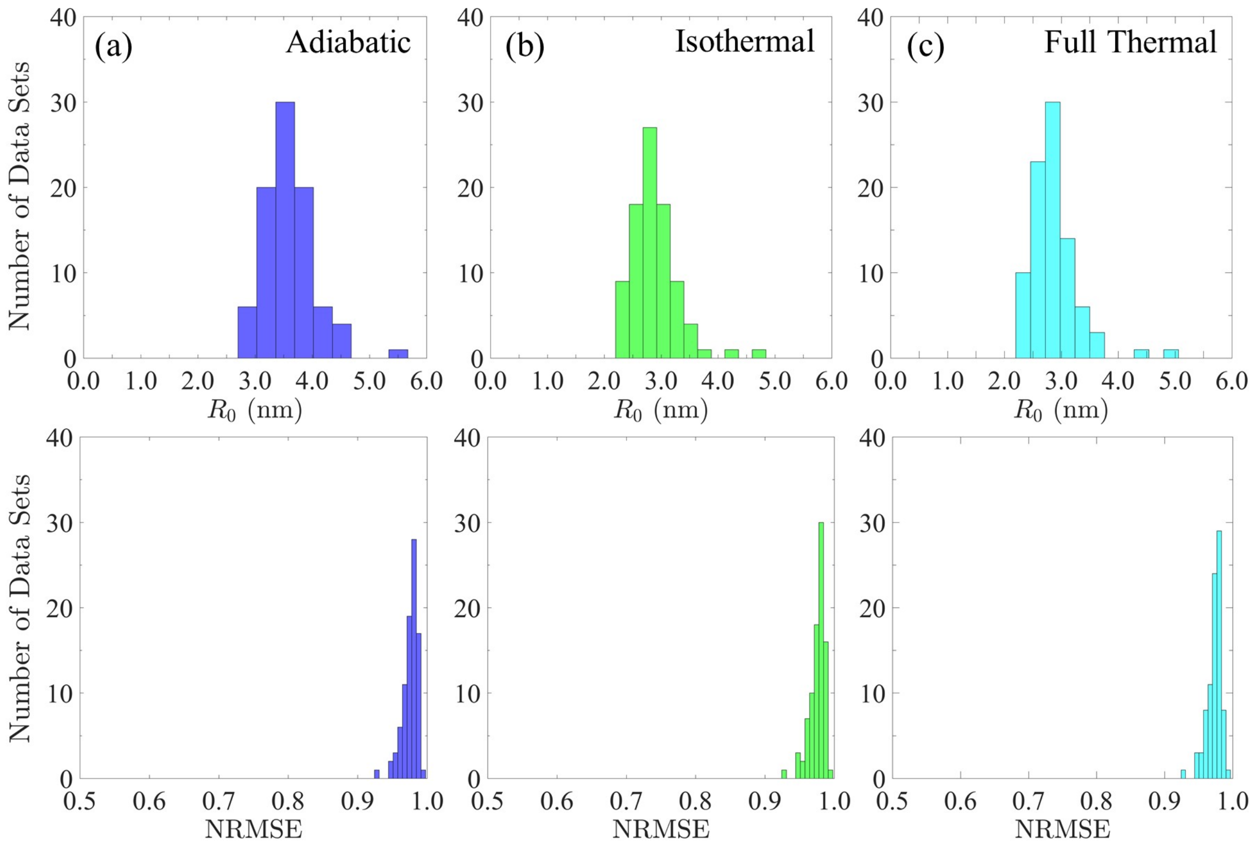

Figure 3.7: Optimized R_0 distribution (top row), and NRMSE distribution (bottom row) obtained by applying the KMP equation for compressibility effects with the (a) adiabatic polytropic approximation, (b) isothermal polytropic approximation, and (c) full thermal models for bubble contents to 88 experimental data sets. The cold fluid assumption distributions are shown in Fig.3.5(b).

data sets are shown in Table 3.3. The numerical results obtained with each model show good agreement with experimental data sets, and the radius vs. time traces overlap noticeably for all but the adiabatic polytropic approximation case. As was seen in the compressibility models,differences in thermal models are most apparent when applied to the $R_{max}^{\mu-\sigma}$ data set. The NRMSE ranges from 0.961 for the full thermal model applied to the $R_{max}^{\mu-\sigma}$ data set to 0.984 for the adiabatic polytropic and cold fluid models applied to the $R_{max}^{\mu+\sigma}$ data set. As in the previous section, the best agreement between experiment and simulation is achieved for the $R_{max}^{\mu+\sigma}$ data set regardless of model. There are minimal differences in the NRMSE achieved with either the polytropic approximation or the cold fluid assumption. The optimized R_0 values are nearly 1 nm larger for the adiabatic polytropic approximation than for any other model, and the other models have near identical optimized R_0 values for the three data sets. The complete distributions of the NRMSE and optimized R_0 for 88 data sets obtained using the KMP equation and each thermal model are shown in Fig. 3.7. Only the distributions for the polytropic approximation and full thermal models are shown in Fig. 3.7 because the cold fluid assumption case appears in Fig. 3.5(b). The NRMSE distributions for each model are similar, with NRMSE > 0.9 for all cases. The optimized R_0 distributions are also similar for the isothermal polytropic, cold fluid, and full thermal cases but with a noticeable shift to larger R_0 values for the adiabatic polytropic case.

Table 3.3: NRMSE obtained using the KMP equation and each model for thermal effects. Models are applied to three representative data sets: $R_{max}^{\mu-\sigma}$ (squares), R_{max}^{μ} (diamonds), and $R_{max}^{\mu+\sigma}$ (circles) maximum radii. Mean optimized R_0 in nanometers is indicated in parentheses.

	Bubble Contents Models			
Data Set	Adiabatic Polytropic	Isothermal Polytropic	Cold Fluid	Full Thermal
$R_{max}^{\mu-\sigma}$	0.969 (3.06)	0.969 (2.42)	0.969 (2.42)	0.961 (2.44)
R_{max}^{μ}	0.979 (3.53)	0.979 (2.78)	0.979 (2.78)	0.974 (2.78)
$R_{max}^{\mu+\sigma}$	0.984 (4.43)	0.983 (3.51)	0.984 (3.52)	0.982 (3.52)

Table 3.4: Mean NRMSE of each model for radial dynamics and bubble contents. Mean optimized R_0 in nanometers indicated in parentheses.

	Compressibility Models		
Thermal Models	Rayleigh–Plesset	KM with Pressure	KM with Enthalpy
Adiabatic Polytropic	0.967 (3.49)	0.976 (3.63)	0.974 (3.65)
Isothermal Polytropic	0.967 (2.77)	0.975 (2.88)	0.967 (2.89)
Cold Fluid	0.967 (2.77)	0.976 (2.88)	0.970 (2.89)
Full Thermal	0.967 (2.76)	0.973 (2.88)	0.967 (2.88)

3.5 Discussion

In an effort to validate histotripsy single–bubble modeling approaches, three models for compressibility effects and four models for thermal effects were applied to single–bubble radius vs. time measurements in water. The resulting mean NRMSEs and mean optimized initial radius sizes obtained from the 88 experimental data sets with each combination of modeling approaches are summarized in Table 3.4. Notably, all modeling approaches achieve mean NRMSEs that are 0.967 or greater, and our results demonstrate a less than 1% distinction between models for single–bubble compressibility and thermal effects. Mean optimized initial radius sizes range from 2.76 nm to 3.65 nm, which are consistent with estimates for intrinsic nucleus sizes predicted previously (Mancia *et al.*, 2020; Vlaisavljevich *et al.*, 2015b; Maxwell *et al.*, 2013). Given an appropriate choice of initial radius, all modeling approaches considered in this study appear to achieve a similar degree of fidelity. Differences in mean R_0, while statistically significant, agree to within a tenth of a nanometer in all approaches except those that include an adiabatic polytropic approximation. The significantly larger optimized R_0 values obtained with the adiabatic polytropic approximation reflect this model's idealized neglect of heat transfer. Consistency among models employing the isothermal polytropic approximation, cold fluid assmption, and full thermal model suggest that these are relatively interchangeable. We advocate preferencing the isothermal polytropic approximation or cold fluid assumption over the adiabatic approximation given their consistency with the more complete physics included in the full thermal model. Greater guidance regarding best practices for modeling single–bubble dynamics in histotripsy will require considering the limitations of available data and models as well as the significance of parametric uncertainties during the bubble lifespan.

During bubble growth, model validation is limited by an absence of experimental measurements at nucleation and the onset of rapid bubble expansion. Although there is robust experimental evidence that histotripsy bubbles arise from preexisting, nanoscale nuclei (Mancia *et al.*, 2020; Vlaisavljevich *et al.*, 2015b; Maxwell *et al.*, 2013), the specific nucleus sizes are well below the spatial resolution of available measurement techniques. Given this expected scale of nucleus sizes, model limitations most pronounced during bubble growth include the neglect of differences between local surface tension at the bubble wall and its bulk value in surrounding water as well as possible interactions between nuclei and ions or impurities in the water (Azouzi *et al.*, 2013). The initial bubble radius or nucleus size, R_0, is thus a key parametric uncertainty in all of the models presented and must be inferred in an iterative fashion to initialize simulations. The resulting R_0 distributions are consistent with physical expectations that models accounting for thermal losses and acoustic damping will predict relatively larger R_0 values. For example, compressible models both predict significantly larger R_0 values than the incompressible RP equation. Additionally, the adiabatic polytropic approximation, which assumes no heat transfer, predicts significantly larger R_0 values than the isothermal polytropic, cold fluid, and full thermal models.

Model validation in late collapse is similarly limited by an absence of experimental measurements. Perhaps the greatest challenge to the modeling approaches considered in this study and to lower–order models in general is observations of bubble breakup at collapse in histotripsy experiments (Duryea *et al.*, 2015). Bubble behavior at the instant of collapse is thus beyond the scope of the present study, but there are promising model considerations that could be justified when more data becomes available. For example, bubbles often lose spherical symmetry near collapse (Ohl *et al.*, 1998), and consideration of more complex bubble geometries will be necessary for the prediction and modeling of bubble breakup. Although future experimental work could potentially justify alternative treatments of bubble geometry, the incomplete understanding of bubble collapse physics in histotripsy remains a universal limitation of existing single–bubble models.

The compressibility and thermal effects considered in this study are relevant throughout the bubble lifespan. In fact, the minimal distinction ($< 1\%$) seen among modeling approaches is likely explained by the absence of experimental data for the earliest stages of bubble growth and the latest stages of bubble collapse, when acoustic damping and thermal losses become most significant. Future experimental studies during these times could ultimately justify alternatives to the models for compressibility and thermal effects presented here. For example, as mentioned previously, bubble wall velocity at the instant of collapse can exceed the range of validity for weakly compressible KMP and KME models and potentially favor use of the Gilmore equation for radial dynamics (Zilonova *et al.*, 2018). Similarly, although the full thermal model provides a relatively complete treatment of heat transfer in bubble dynamics, even this approach neglects the dependence of thermal damping on driving frequency, nonuniform internal gas pressure, and the possibility of a nonconstant polytropic exponent (Prosperetti, 1977, 1984). In addition, mass transfer effects are expected to be small because the mass boundary layer thickness remains small relative to the bubble radius throughout bubble expansion (Barajas & Johnsen, 2017); however, these effects are also most significant during early bubble growth and late collapse (Bader, 2018a; Barajas & Johnsen, 2017) when experimental data is most lacking.

The driving pressure remains a source of model–based uncertainty deserving of further attention. We inferred the driving waveform from the experimental radius vs. time data by solving an inverse problem for p_f (Eq. 3.7), scaling the resulting waveform to have an amplitude equal to the measured acoustic cavitation threshold, and fitting a symmetric analytic pulse, p_{ac} (Eq. 3.8), to this scaled p_f. The measured histotripsy waveform, scaled p_f, and the rising portion of analytic pulses with select fitting parameters (η = 3.7, 1.5, 29) are shown in Figure 3.8. There is minimal distinction in these waveforms at a timescale comparable to the lifespan of the bubble; however, the measured waveform appears noticeably broader than the other waveforms in the inset. This apparent broadening of the measured waveform relative to scaled p_f could be explained by nonlinear distortion of the acoustic waveform. Specifically, nuclei in the focal region are expected to experience forcing that differs from the measured pulse reaching the hydrophone. The inset also shows

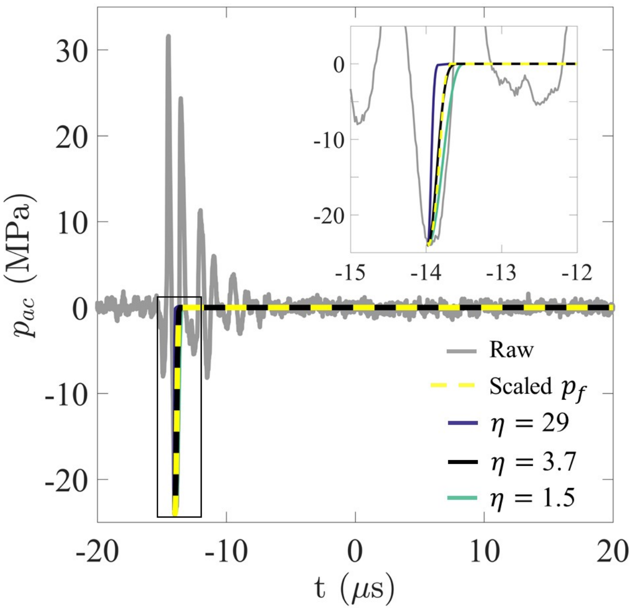

Figure 3.8: Raw histotripsy waveform (gray) with overlay showing scaled waveform inferred from experimental data (dashed yellow) as well as the rising portion of analytic waveforms with fitting parameters η = 3.7 (black), 1.5 (green), and 29 (blue). Inset shows finer detail of boxed region.

how the fitting parameter η affects the shape of the analytic pulse (Eq. 3.8). Excellent agreement between the scaled p_f waveform and the rising portion of p_{ac} with $\eta = 3.7$ is evident. In contrast, the rising portions of analytic pulses with $\eta = 1.5$ and $\eta = 29$ differ from the p_{ac} solution to the same degree: 0.1%. These results suggest that the analytic pulses with a wide range of η values could be valid alternatives to the highly nonlinear measured waveform, but the precise relationship between these approximations and the measured waveform will require clarification with future experiments.

Although the physical properties of water in Table 3.1 are potential sources of parametric uncertainty throughout bubble growth and collapse, water is well–characterized under the room temperature conditions of the experiments, and minor variation in these parameters has a negligible effect on bubble dynamics (Mancia *et al.*, 2019). Uncertainty in physical properties is a more significant consideration in tissue and other inhomogeneous materials, suggesting that simplified models (e.g. RP equation, polytropic approximations) could be useful in providing a limiting case solution when there is incomplete knowledge of these parameters. Likewise, all single–bubble models presented offer a resource–sparing, computationally–efficient alternative to higher–order methods. Despite some persistent model–based and parametric uncertainties most pronounced during early bubble growth and late bubble collapse, the consistency between single–bubble experiments and single–bubble modeling approaches supports the potential value of these models for high–throughput parameter studies. In particular, for an assumed nucleus size, our methods provide a rapid first–order approximation of maximum bubble radius, a key histotripsy damage metric (Mancia *et al.*, 2017, 2019; Bader & Holland, 2016)

3.6 Conclusions

Radius vs. time measurements for historipsy–nucleated bubbles in water (Wilson *et al.*, 2019) are used to objectively compare a variety of bubble dynamics modeling approaches, including the Rayleigh–Plesset equation and Keller–Miksis equations with pressure and enthalpy for compressibility effects as well as adiabatic and isothermal polytropic approximations, a cold fluid assumption, and a full thermal model for thermal effects. Single–bubble experimental data is used to justify a popular analytic approximation of the histotripsy waveform. We compared the optimized initial radius and associated NRMSE distributions obtained with each model applied to 88 data sets and found that present single–bubble models are validated without significant distinction for the vast majority of histotripsy bubble growth and collapse in water. The minimal distinction ($< 1\%$) seen among modeling approaches is largely due to the absence of experimental data for the earliest stages of bubble growth and the latest stages of bubble collapse, when acoustic damping and thermal losses become most significant. However, the regime of model validity notably includes maximum bubble radius, a key candidate for histotripsy damage metrics (Mancia *et al.*, 2017, 2019; Bader & Holland, 2016), suggesting this important quantity and other general features of histotripsy bubble dynamics can be adequately predicted with low–fidelity modeling approaches that require minimal computational resources. Future experimental measurements during early bubble growth and late bubble collapse could more definitively inform model choice.

CHAPTER 4

Acoustic Cavitation Rheometry

This Chapter is adapted from Mancia *et al.* (2020c).

4.1 Abstract

The inertial microcavition–based high strain–rate rheometry (IMR) method [Estrada *et al., J. Mech. Phys. Solids*, 2018, **112**, 291–317] can noninvasively measure local material properties of soft materials at high strain rates relevant to blast injuries and focused ultrasound procedures. While promising, this method has currently only been tested in polyacrylamide using laser–induced cavitation bubbles. The applicability of this approach to other materials has not been shown. Furthermore, laser cavitation introduces the complexities of plasma formation and optical breakdown at the site of cavitation; effects which can alter local material properties before radius vs. time data is obtained. In the present study, we demonstrate the IMR method using acoustic cavitation data obtained from single–bubble experiments performed in agarose. Material properties including pore size, shear modulus, and viscosity are inferred for 0.3% and 1% agarose gel specimens. The resulting parameter distributions are consistent with available measurements of agarose properties and with expected trends related to gel concentration and high strain rate loading. Our findings support the general IMR approach for material characterization and suggest that use of acoustic cavitation data is advantageous in some circumstances.

4.2 Introduction

Characterization of soft materials such as polymers, hydrogels, biological tissues, and tissue phantoms is important to a variety of engineering and biomedical applications (Chaudhuri *et al.*, 2016; Lee & Mooney, 2012; Storrie & Mooney, 2006; Solomon & Jindal, 2007). These materials are challenging to characterize given their inhomogeneity, high compliance (Arora *et al.*, 1999), and the time and length scale dependence of their properties (Brujan & Vogel, 2006). For example, classical methods for measuring bulk material properties are limited by their neglect of specimen microstructure and the technical challenges of specimen preparation (Hu *et al.*, 2012). Specimen preparation concerns are particularly relevant to biological materials because their properties can change significantly outside of their in vivo environments (Zimberlin *et al.*, 2010), making minimally invasive measurement techniques especially important for these specimens. Nanoscale indentation (Hu *et al.*, 2010, 2012) and microbead rheology (Mason & Weitz, 1995) techniques, while suitable for complex materials at microscopic length scales, require expensive equipment and complex data analysis strategies (Hu *et al.*, 2012; Córdoba *et al.*, 2012).

Recently, cavitation–based rheometry techniques capable probing local material properties of inhomogeneous specimens using relatively simple and inexpensive setups (Zimberlin *et al.*, 2007; Estrada *et al.*, 2018) have shown promise for soft material characterization. The first of these methods, cavitation rheology technique (CRT), involves creating a cavity in soft material via air injection and measuring the critical pressure of mechanical instability. The critical pressure is directly related to the material's elastic modulus. CRT has been successfully applied to the measurement of eye vitreous (Zimberlin *et al.*, 2010), eye lens (Cui *et al.*, 2011), skin (Chin *et al.*, 2013), and polymer (Bentz *et al.*, 2016) properties. This method is minimally invasive, cost–effective, efficient, and applicable at microscopic length scales; however, injection must be slow enough for a quasi–static assumption to hold (Zimberlin *et al.*, 2007; Estrada *et al.*, 2018). Thus, CRT has limited applicability to soft material characterization at high strain rates most relevant to blast injury diagnostics and mitigation (Nyein *et al.*, 2010; Ramasamy *et al.*, 2011), focused ultrasound ablation (Mancia *et al.*, 2019), and laser surgery (Brujan & Vogel, 2006; Vogel *et al.*, 2008). The development of inertial microcavitation–based high strain–rate rheometry (IMR) was motivated by these applications (Estrada *et al.*, 2018). This technique uses high–speed videography to track the radius vs. time behavior of a bubble produced via inertial cavitation, then compares recorded radius measurements with numerical simulations that permit inference of a constitutive model and viscoelastic parameters (Estrada *et al.*, 2018). Although IMR requires more resources and training than CRT, it has the powerful advantage of measuring local material properties at high strain rates ($> 10^3$ s^{-1}).

The IMR technique was first demonstrated with laser cavitation data, but the authors note that any input of energy capable of creating the pressure differential needed to induce inertial cavitation in the medium can be used to obtain radius vs. time measurements (Estrada *et al.*, 2018). Laser cavitation is initiated when the rapid concentration of high temperatures and pressures generated during laser plasma formation triggers explosive expansion (Vogel *et al.*, 2008). In contrast, ultrasound generates cavitation when a sufficient acoustic rarefaction causes some preexisting defect or nucleus in a material to grow explosively into a larger cavity. Ultrasound–induced cavitation is not complicated by the plasma formation and laser–induced material rupture, making it more relevant to focused ultrasound applications and potentially more analogous to blast injury mechanics. However, given the technical difficulty of generating single bubbles with high–amplitude ultrasound, only recent developments in experimental technique have permitted a rigorous comparison of single–bubble dynamics generated via laser vs. ultrasound (Wilson *et al.*, 2019).

This work provides a proof of concept demonstration of the IMR method with acoustic– rather than laser–induced cavitation data and uses it to infer material properties of 0.3% and 1% agarose gel specimens first studied by (Wilson *et al.*, 2019). Agarose properties including pore size, shear modulus, and viscosity are inferred using a combination of ultrasound–induced cavitation radius vs. time measurements and a numerical model for single bubble dynamics in a finite–deformation Kelvin–Voigt material. Our parameter distributions are subsequently compared to previously inferred average values (Wilson *et al.*, 2019) and to available measurements of agarose material properties. We discuss additional sources of uncertainty to explore in future work and conclude with a comparison of IMR applied with acoustic vs. laser–induced inertial cavitation data.

4.3 Methods

4.3.1 Experiments

The experimental methods for generating single bubbles via high–amplitude ultrasound were described previously (Wilson *et al.*, 2019), and we use the 19 data sets in 0.3% agarose and the 21 data sets in 1% agarose from that study. To summarize, the gel specimens are prepared according to the procedure described in (Vlaisavljevich *et al.*, 2015b) with the modification that gels are allowed to solidify at 17.8 °C rather than 4 °C. Experiments were performed in a open–topped, spherical acoustic array that was 10–cm in diameter and populated with 16 focused transducer elements with a center frequency of 1 MHz. A 5.8–cm–diameter opening at the top of the transducer permitted insertion of the gel specimens. Bubbles were nucleated using a 1.5–cycle acoustic pulse containing a single rarefactional pressure half–cycle −24 MPa. For each experiment, bubbles were nucleated at least 5 mm away from previous cavitation sites, and specimens had specific acoustic impedance close to that of water (within 5%) to ensure samples could be regarded as infinite relative to the bubbles. Bubbles are imaged through a single cycle of growth and collapse using a camera with a fixed frame rate of 400 kHz. The multi–flash–per–camera–exposure technique (Wilson *et al.*, 2019) generated images of nested, concentric bubbles which are differentiated using brightness thresholding and edge detection. Bubble radii are measured at individual flash points by applying a circle fit to their detected boundaries. For all experiments, the magnitude of the spatial resolution uncertainty is ≤4.3 μm while temporal resolution uncertainty is ≤1.25 μs.

The scaled radius vs. time data for all experiments is shown in Figure 4.1, where the open markers correspond to the 0.3% gel data and the filled markers correspond to the 1% gel data. As in previous studies (Mancia *et al.*, 2020; Wilson *et al.*, 2019; Estrada *et al.*, 2018), the scaling is by maximum bubble radius, R_{max} and collapse time, t_c. As noted in a previous study of cavitation

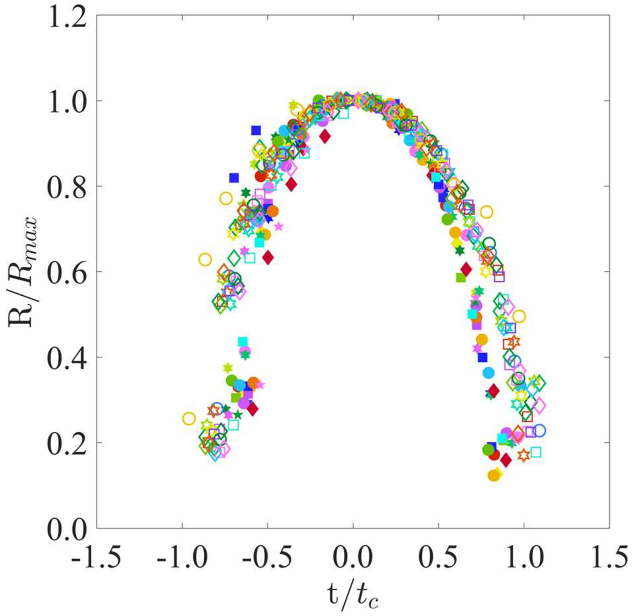

Figure 4.1: Scaled radius vs. time data adapted from Wilson et al. for 19 experiments in 0.3% (open markers) agarose gel and 21 experiments in 1% (filled markers) agarose gel.

nuclei sizes in water (Mancia *et al.*, 2020), this data collapse with appropriate scaling suggests that all experiments are governed by the same physics. In the present case, however, there are significant uncertainties in both the initial conditions as well as the local material response and viscoelastic parameters of the gel specimens.

4.3.2 Theoretical Model and Numerical Methods

Numerical simulations are based on a theoretical model for cavitation in a finite–deformation Kelvin–Voigt material that has been used in multiple prior studies of ultrasound–induced cavitation (Mancia *et al.*, 2019; Wilson *et al.*, 2019; Bader, 2018a; Mancia *et al.*, 2017; Vlaisavljevich *et al.*, 2016a,c, 2015b) and will thus only be described briefly here. Simulations model a spherical homobaric microbubble subjected to a tensile half–cycle experimental waveform with an amplitude of −24 MPa. The Keller–Miksis equation (Keller & Miksis, 1980) is used to model bubble radial dynamics, and the energy equation is solved inside the bubble. The gel surrounding the bubble remains at a constant ambient temperature of 25 °C, and the interface between the bubble and surrounding gel is assumed to be impervious to gas. These assumptions have been used in previous studies (Prosperetti, 1991; Prosperetti *et al.*, 1988; Kamath *et al.*, 1993; Warnez & Johnsen, 2015) and are acceptable for modeling the single cycles of bubble growth and collapse measured in the experiments (Warnez & Johnsen, 2015; Mancia *et al.*, 2017; Barajas & Johnsen, 2017).

The selection of an appropriate viscoelastic constitutive model for the gel specimens is nontrivial but can be further elucidated with rigorous application of the IMR approach (Estrada *et al.*, 2018). For this proof of concept study, we assume that both gel specimens behave as finite–deformation Kelvin–Voigt materials. First derived by Gaudron et al. (Gaudron *et al.*, 2015) and subsequently used for polyacrylamide characterization in the IMR study (Estrada *et al.*, 2018), the model is favored for high–amplitude ultrasound simulations given the typically large bubble growth observed in these cases (Mancia *et al.*, 2019, 2017; Vlaisavljevich *et al.*, 2016c). The integral of the deviatoric contribution of the stresses in the surrounding medium is given by:

$$J = \frac{4\mu\dot{R}}{R} + \frac{G}{2}\left[5 - 4\left(\frac{R_0}{R}\right) - \left(\frac{R_0}{R}\right)^4\right],$$

where R is the time–dependent bubble radius, and R_0 is the stress–free bubble radius which is equivalent to the initial radius in all simulations. The stress–free radius has potential physical significance to agarose which will be discussed in Sect. 4.5.1. Viscoelastic parameters of the gel specimens include a shear modulus, G and viscosity, μ. The above constitutive equation thus contains three key parametric uncertainties. Physical parameters for water and air are assumed constant for all simulations and are the same as those given in (Wilson *et al.*, 2019; Mancia *et al.*, 2020) with the exception of quantities to be inferred: R_0, G, and μ. We adopt a previously presented nondimensionalization for the resulting system of ODEs and PDE (Barajas & Johnsen, 2017). Numerical time marching is achieved using a variable–step, variable–order solver based on numerical differentiation formulas (MATLAB *ode15s*) (Shampine & Reichelt, 1997; Shampine *et al.*, 1999). Spatial derivatives in the energy equation are computed using second–order central differences (Estrada *et al.*, 2018; Barajas & Johnsen, 2017).

4.3.3 IMR Approach: Three–Parameter Sweep

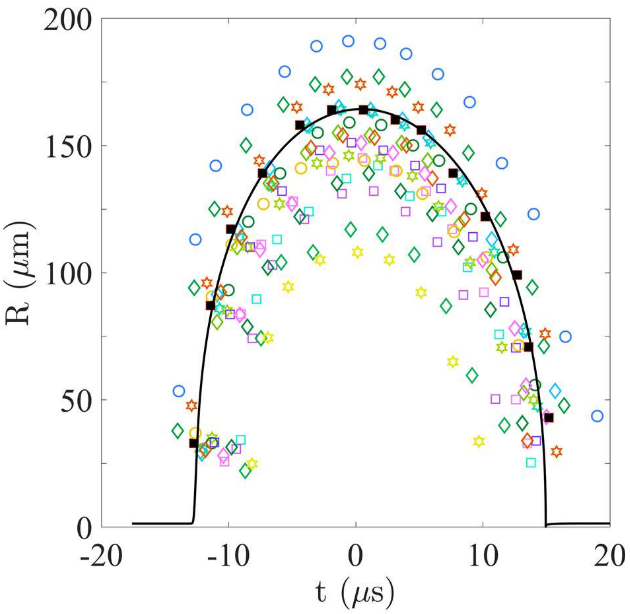

Figure 4.2: Dimensional radius vs. time data for 19 experiments in 0.3% agarose gel. The best fit simulation for a representative experimental data set (filled squares) is shown in black.

We use the IMR approach to infer the initial radius of a cavitation bubble, R_0 and, assuming the material behaves as a finite–deformation Kelvin–Voigt material (Estrada *et al.*, 2018), the gel shear modulus, G and viscosity, μ. The coupling of each experimental realization to these three parameters is achieved with numerical simulations of single–bubble dynamics. We perform a series of simulations for each experimental radius vs. time data set with a 3–parameter fit over R_0, G, and μ using a previously presented normalized root mean squared (rms) error metric to quantify each fit (Mancia *et al.*, 2020). To review, the normalized rms error is calculated between the radius vs. time data points from a given experiment and their nearest neighbor points on a simulation trace. This error metric ranges from $-\infty$ (poorest fit) to 1.0 (best fit). For example, Fig. 4.2 shows the 19 individual radius vs. time data sets for 0.3% gel. The black trace is the simulation initialized with an R_0, G, and μ that best fits a representative data set (black squares). For this representative case, $R_0 = 1.4\ \mu$m, $G = 8.5$ kPa, and $\mu = 0.088$ Pa.s, and the normalized rms error is 0.98. Normalized rms error for the 0.3% gel cases ranged from 0.95 to 0.99 with a mean of 0.98. For the 1% gel,

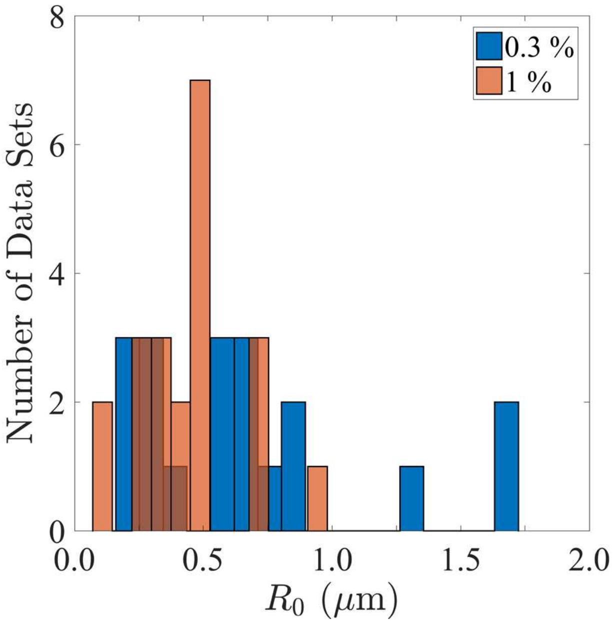

Figure 4.3: Stress–free radius, R_0 distribution for experiments in 0.3% and 1% agarose gels.

normalized error ranged from 0.95 to 0.99 with a mean of 0.98.

4.4 Results

The three–parameter sweep over stress–free radius, shear modulus, and viscosity is performed using the 19 individual radius vs. time data sets for 0.3% agarose gel and using the 21 data sets for 1% gel. Distributions are shown for each parameter of interest: R_0 (Fig. 4.3), G (Fig. 4.4), and μ (Fig. 4.5), and their mean values weighted by normalized rms error are summarized in Table 4.1. The optimized R_0 values for 0.3% gel have a broader distribution (0.22–1.72 μm) and larger mean (0.68 μm) than in the 1% (0.11–0.98 μm and 0.44 μm). In contrast, optimized G values obtained via the three–parameter sweep have relatively narrow distributions in both gel concentrations with a fitted G range of 8.1–9.9 kPa in the 0.3% gel and of 11–18 kPa in the 1% gel. All G values are larger in the 1% gel than in the 0.3% gel. The optimized viscosity, μ has a broad distribution in both gel concentrations with a range of 0.033–0.14 in the 0.3% gel and a range of 0.080–0.175 in the 1% gel. Although the μ values are shifted to higher values in the 1% there is considerable overlap between the distributions.

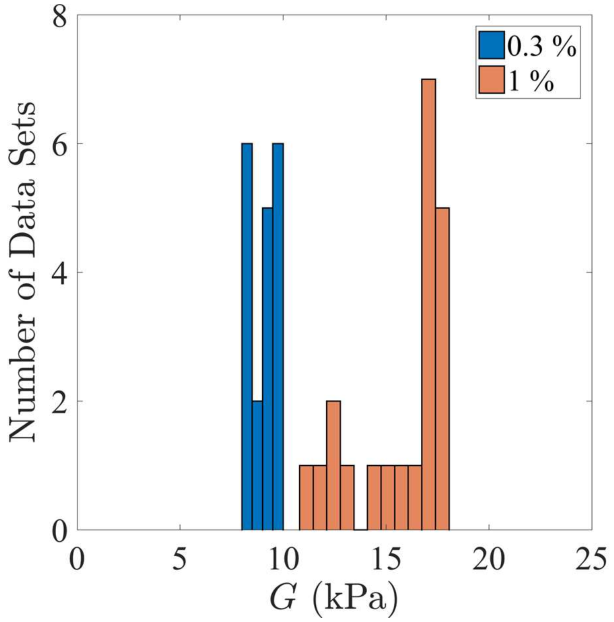

Figure 4.4: Shear modulus, G distribution for experiments in 0.3% and 1% agarose gels.

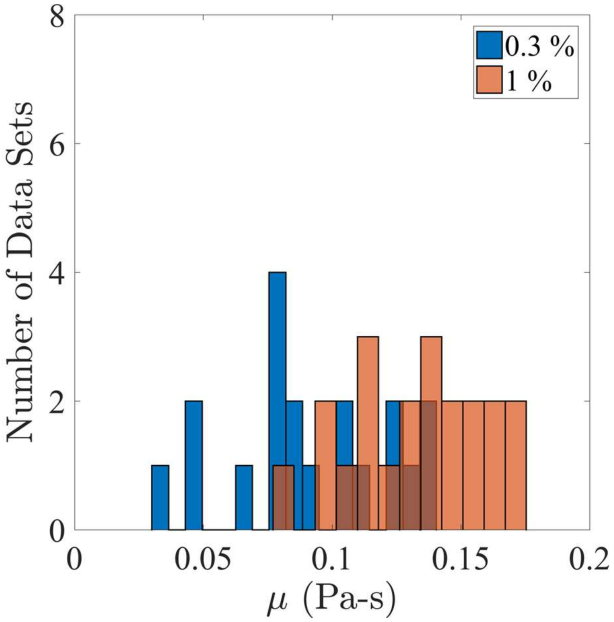

Figure 4.5: Viscosity, μ distribution for experiments in 0.3% and 1% agarose gels.

Table 4.1: Weighted mean and standard deviation of inferred properties for 0.3% and 1% agarose specimens using three–parameter sweep (mean ± standard deviation)

Gel Concentration	R_0 (μm)	G (kPa)	μ (Pa-s)
0.3 %	0.68 ± 0.45	9.0 ± 0.62	0.092 ± 0.031
1 %	0.44 ± 0.20	16 ± 2.3	0.13 ± 0.026

4.5 Discussion

4.5.1 Stress–Free Radius, R_0

Our use of acoustic rather than laser–induced cavitation experiments requires the additional consideration of an unknown stress–free radius, R_0, which is equivalent to the initial radius in our simulations. Numerous studies have suggested that cavitation bubbles in high–amplitude ultrasound arise from preexisting nuclei (Mancia *et al.*, 2020; Wilson *et al.*, 2019; Bader *et al.*, 2019; Vlaisavljevich *et al.*, 2016c,a, 2015b, 2014; Maxwell *et al.*, 2013). The parameter sweep approach and bubble dynamics model presented here was previously used to infer the nucleus size distribution at the acoustic cavitation threshold in water (Mancia *et al.*, 2020). In the setting of agarose gels and other soft matter, the physical significance of the initial radius parameter is less clear, but acoustic cavitation in soft materials likely originates from preexisting defects which act as stress risers and are analogous to cavitation nuclei in liquids (Guan *et al.*, 2013; Wilson *et al.*, 2019). Wilson et al. first hypothesized that stress–free radii could be related to agarose porosity (Wilson *et al.*, 2019). They found a correlation between measured agarose pore size (Narayanan *et al.*, 2006) and initial radii they estimated for representative data sets from agarose gel specimens of varying concentration. Using only maximum radii of three data sets per gel specimen, they inferred nuclei sizes of approximately 1.4 μm in 0.3% gel and 0.25 μm in 1% gel. These estimates are consistent with previous measurements (Narayanan *et al.*, 2006) and fall nearly within a single standard deviation of our mean inferred R_0 values using all data sets. Moreover, atomic force microscopy measurements of mean agarose pore sizes (Pernodet *et al.*, 1997), when extrapolated to smaller gel concentrations, are within a standard deviation of our mean estimates. This study also observed our trends of larger mean pore size and broader pore size distributions with decreasing gel concentration.

4.5.2 Shear modulus, G

Shear modulus can also be inferred given an assumed material model, which we take to be a finite–deformation Kelvin–Voigt medium in this study. Vlaisavljevich et al. measured the Young's moduli for agarose gels with a parallel–plate rheometer (Vlaisavljevich *et al.*, 2015b), and these moduli were subsequently used as physical parameters for simulations of cavitation in agarose gels (Wilson *et al.*, 2019; Vlaisavljevich *et al.*, 2015b). Agarose is considered nearly incompressible (Normand *et al.*, 2000), so these values can be readily converted to mean shear moduli of 0.38 kPa for 0.3% gel and 7.2 kPa for 1% gel. Notably, these measurements were performed on gross specimens under quasistatic conditions. Local shear moduli inferred from inertial cavitation experiments are expected to be larger given the stiffening behavior observed in gels subjected to high strain rates (Wang *et al.*, 2016; Kwon & Subhash, 2010). Application of IMR to polyacrylamide specimens using laser–induced cavitation data also measured shear moduli that were at least two times larger than quasistatic measurements (Estrada *et al.*, 2018). Consistent with these observations, our parameter sweep infers local mean shear moduli that are $>$ 8 kPa larger than the quasistatic measurements. There are currently no measurements of agarose shear moduli at the time and length scales relevant to acoustic cavitation, so our values can provide a useful reference point for future studies of high strain rate phenomena in gel media.

4.5.3 Viscosity, μ

Viscosity of the gel specimens is the final uncertainty considered in our three–parameter sweep. Wilson et al. proposed using an agarose viscosity of 0.115 for 0.3%, 1%, 2.5%, and 5% gel specimens (Wilson *et al.*, 2019). Although they admit this value is somewhat arbitrary, it was found to result in a relationship between initial radii and gel concentration that followed the same approximate scaling as agarose pore size and gel concentration. As noted by previous authors (Movahed *et al.*, 2016), there are currently no measured values of agarose viscosity relevant to cavitation conditions. Past studies of ultrasound–induced cavitation in agarose have assumed water viscosity (0.001 Pa.s) (Vlaisavljevich *et al.*, 2015b) or considered a range of viscosities (0.001 – 10 Pa.s) (Movahed *et al.*, 2016) to account for this otherwise unknown quantity. Meanwhile, shear wave elastography techniques have been used to infer gel viscosity under more typical conditions. For example, a prior study assuming a Kelvin–Voigt type material model measured a viscosity of 0.22 Pa.s for an agar–gelatin phantom at 400 kHz (Catheline *et al.*, 2004). This measurement is of the same order of magnitude as our inferred viscosity values. However, still assuming a Kelvin–Voigt model, other authors measured a viscosity of 1 Pa.s under ballistic loading of a 10 wt% ballistic gelatin block (Liu *et al.*, 2014). Larger viscosity values of 5 to 900 Pa.s have also been measured for agar under frequencies ranging from 20 to 200 Hz (Nayar *et al.*, 2012). In part given this wide variation in measurements, Movahed et al. conclude that a single viscosity parameter cannot fully describe dissipative behavior of the gels but that the effective viscosity of agarose should be assumed to be larger than that of water (Movahed *et al.*, 2016). Our findings support the use of viscosity values on the order of 0.1 Pa.s for agarose gels, which is also consistent with the polyacrylamide viscosities (0.101 Pa.s and 0.118 Pa.s) measured by the IMR method using laser–induced cavitation data (Estrada *et al.*, 2018).

4.5.4 Additional Uncertainties

The primary aim of this work is to demonstrate application of the IMR method using acoustic cavitation data; however, consideration of additional parametric and modeling uncertainties beyond the three parameters inferred here could improve the accuracy and utility of this approach for material characterization. First, the choice of constitutive model for soft materials is nontrivial and deserving of future dedicated studies. We use the finite–deformation Kelvin–Voigt model in this work in part because it demonstrates the success of even a simple two–parameter model in fitting the data sets. It is also a popular choice for modeling cavitation in soft matter (Mancia *et al.*, 2019, 2017; Vlaisavljevich *et al.*, 2016c) and was found to be the best–fit material model for polyacrylamide gel in the original IMR study (Estrada *et al.*, 2018). Additional uncertainty remains in the acoustic forcing waveform chosen for our numerical simulations. The precise, time–

dependent acoustic forcing experienced by bubbles in the focal region cannot be directly measured due to damaging cavitation at the hydrophone tip. Our analytic approximation is successful in high–amplitude ultrasound contexts (Mancia *et al.*, 2020) largely because the resonant frequency of the bubble is much less than the driving frequency of the waveform (1 MHz). Although waveform frequency and peak negative pressure can be measured with high confidence, future experiments could clarify specific waveform characteristics at cavitation foci within the material.

4.5.5 Acoustic vs. Laser–Induced Cavitation Data in IMR

This work demonstrates that the IMR method can be applied using radius vs. time data from ultrasound–nucleated cavitation bubbles. Use of acoustic cavitation measurements removes the uncertainties associated with laser–material interactions and optical breakdown. Acoustic cavitation also has direct relevance to ultrasound applications and could more closely approximate cavitation phenomena in blast injuries. Laser cavitation measurements are still advantageous in avoiding uncertainties associated with the acoustic forcing waveform and with the likely stochastic distribution of preexisting cavitation nuclei. Laser experiments can also extract more radius vs. time data per experiment because bubbles nucleated by high–amplitude ultrasound tend to break into smaller bubbles before any rebounds are observed (Duryea *et al.*, 2015). However, it is conceivable that the advantages and disadvantages of each method could ultimately prove complementary. For instance, a combined approach could involve use of laser–induced cavitation data to determine cavitation–relevant material parameters, followed by use of acoustic cavitation data to determine local waveform characteristics.

4.6 Conclusions

This work presents a proof of concept demonstration of agarose gel characterization using the IMR method (Estrada *et al.*, 2018) with acoustic cavitation data. We use a parameter sweep approach to infer material properties including pore size, shear modulus, and viscosity for the 0.3% and 1%

agarose gel specimens first studied by Wilson *et al* (Wilson *et al.*, 2019). As in the original IMR study, parameters are inferred using a combination of cavitation radius vs. time measurements and a numerical model for single bubble dynamics in a finite–deformation Kelvin–Voigt material. Our resulting parameter distributions show trends and mean values that are consistent with available measurements of agarose properties, thus supporting the feasibility of using acoustic cavitation data in future IMR applications.

CHAPTER 5

Predicting Tissue Susceptibility to Mechanical Cavitation Damage in Therapeutic Ultrasound

This Chapter is adapted from Mancia *et al.* (2017).

5.1 Abstract

Histotripsy is a developing focused ultrasound procedure that uses cavitation bubbles to mechanically homogenize soft tissue. To better understand the mechanics of damage, a numerical model of single bubble dynamics was used to calculate stress, strain, and strain rate fields produced by a cavitation bubble exposed to a tensile histotripsy pulse. The explosive bubble growth and its subsequent collapse was shown to depend on the properties of the surrounding material and on the histotripsy pulse. Stresses on the order of 10^{12} MPa were observed close to the bubble wall but attenuate by 4-6 orders of magnitude within 50 microns from the bubble wall, with at least two orders of magnitude attenuation occurring within the first 10 microns from the bubble. Elastic stresses were found to dominate close to the bubble wall while viscous stresses tended to persist farther into the surroundings. A nondimensional parameter combining tissue, waveform and bubble properties was identified, which dictates the dominant stress (viscous vs. elastic) as a function of distance from the bubble nucleus. Characteristic times were identified in a given cycle of bubble growth and collapse at which mechanical damage is likely to occur and identify dominant mechanisms acting at each time.

5.2 Introduction

High-intensity ultrasound pulses produce rapid pressure changes in tissue, thus giving rise to cavitation. As they grow and collapse, bubbles forming in low-pressure regions can cause damage to surrounding tissue. Acoustic cavitation dynamics in soft tissue has been a subject of growing interest following the development of non-invasive, focused ultrasound therapies. Treatments such as Shock-Wave Lithotripsy (SWL) and histotripsy directly rely on cavitation. In SWL, the erosive effect of collapsing bubbles contributes to fractionating kidney stones (Bailey *et al.*, 2003a). Histotripsy is a noninvasive focused ultrasound procedure that uses cavitation generated by high-amplitude ultrasound pulses to mechanically destroy soft tissue (Parsons *et al.*, 2006b; Roberts *et al.*, 2006; Xu *et al.*, 2005b). Experimental studies of histotripsy-induced cavitation in tissue phantoms and animal models have illustrated the influence of tissue mechanical properties such as elasticity on the cavitation threshold (Vlaisavljevich *et al.*, 2014, 2015b) and bubble growth (Vlaisavljevich *et al.*, 2015a). At present, however, the mechanisms responsible for tissue damage observed in histotripsy and other cavitation-inducing ultrasound treatments remain difficult to quantify. There is strong evidence that stiffer tissues are more resistant to cavitation damage. However, the mechanics of cell-bubble interactions and the influence of material properties, e.g. shear modulus, viscosity, ultimate stress/strain are less clear (Vlaisavljevich *et al.*, 2013b). An improved understanding of cavitation-induced tissue damage mechanisms will facilitate the development of effective means of planning and monitoring therapeutic ultrasound procedures, as well as improve the treatment's safety and efficacy (Miller *et al.*, 2012). Understanding the influence of tissue properties on damage could enable optimization of treatment parameters for different tissues, which would be particularly important for the development of self-limiting and vessel-sparing clinical applications (Vlaisavljevich *et al.*, 2013b).

Multiple mechanisms for cavitation-induced damage during ultrasound procedures have been proposed, including shock waves and high temperatures at bubble collapse, as well as re-entrant jets produced during aspherical bubble collapse (Nyborg *et al.*, 2002). Experimental observations

(De *et al.*, 2007; Vlaisavljevich *et al.*, 2016c) indicate that local deformations in the vicinity of histotripsy bubbles can be considerable, occur rapidly and depend on the material properties. It is thus reasonable to hypothesize that cavitation-induced mechanical loading is a potential tissue damage mechanism in histotripsy. Correlations between high tensile strength and resistance to tissue damage also suggest that stress in particular contributes to tissue rupture in histotripsy (Vlaisavljevich *et al.*, 2013b). However, experimental measurements of local, highly transient, cavitation-induced stresses and strains are difficult to obtain due to limited spatiotemporal resolution and optical access. To bypass these challenges, a spherical bubble dynamics are numerically modeled in a soft material (Warnez & Johnsen, 2015), thus quantifying localized stress and strain distributions in simulated tissues exposed to histotripsy pulses.

Deformations produced in viscoelastic media by single cavitation bubbles exposed to harmonic forcing have been computed previously (Church & Yang, 2006). The current study is unique in providing independent consideration of different tissue mechanical properties and waveform characteristics on several proposed damage mechanisms (stresses, finite strains, and strain rates) developed during cavitation under histotripsy forcing. Stress and strain fields are considered in different reference frames to facilitate experimental comparisons. The focus is to quantify proposed damage mechanisms to identify specific contributors to tissue damage and provide a theoretical basis for the development and enhancement of damage metrics. Furthermore, recent experimental investigations of cells (neurons) exposed to large compressive strains at high rates demonstrated that a critical strain threshold must be met to produce cell death, but that the extent of cell death depends on strain rate (Bar-Kochba *et al.*, 2016). The present work presents a means of identifying the relative influence of strain (dominated by tissue elasticity) vs. strain rate (proportional to tissue viscosity) as a function of distance from the bubble wall, which could provide a more detailed prediction of the of lesion morphology in different tissue types. The numerical methods in this study were previously used to complement experimental investigations of histotripsy-induced cavitation thresholds (Vlaisavljevich *et al.*, 2014, 2015b) bubble growth (Vlaisavljevich *et al.*, 2015a), and cell-bubble interactions (Vlaisavljevich *et al.*, 2016c). After describing the theoretical model and problem setup, methods for calculating field quantities are introduced. Next, the results of a simulation parameter study are shown to illustrate the influence of tissue (viscosity, shear modulus, nucleus size) and waveform (amplitude, frequency) properties on stress and strain developed in the tissue. Finally, a relationship is identified between the dominant contribution to viscous vs. elastic stress and distance from the bubble nucleus.

5.3 Theoretical Model

Early theoretical models were developed to study bubbles driven hydrodynamically (Plesset, 1949) and acoustically (Noltingk & Neppiras, 1950a) in liquids. More recently, non-Newtonian models have been used to investigate cavitation in viscoelastic materials representative of polymer gels (Shima & Tsujino, 1982) and soft biological tissue (Brujan, 2010). Several constitutive models have been adapted to the study of cavitation with the intention of mimicking the dynamics of bubbles in soft tissue, including Maxwell (Allen & Roy, 2000a), Kelvin-Voigt (Yang & Church, 2005), Oldroyd (Allen & Roy, 2000b) and Zener (Hua & Johnsen, 2013) models. The present study simulates the dynamics of a single, spherical bubble in a compressible Kelvin-Voigt-based viscoelastic solid with nonlinear elasticity (Gaudron *et al.*, 2015), which accounts for the reference configuration of the tissue. Our model includes a hyperelastic term derived from finite-strain theory to adequately represent the large deformations encountered in the nanometer to micron-scale bubble growth observed in histotripsy.

This study considers a spherical, homobaric bubble in an infinite, homogenous viscoelastic medium. To account for acoustic radiation losses, the bubble dynamics are described by the Keller-Miksis (1980) equation:

$$\left(1-\frac{\dot{R}}{c_\infty}\right)R\ddot{R}+\frac{3}{2}\left(1-\frac{\dot{R}}{3c_\infty}\right)\dot{R}^2=\frac{1}{\rho_\infty}\left(1+\frac{\dot{R}}{c_\infty}+\frac{R}{c_\infty}\frac{d}{dt}\right)\left[p_B-\left(p_\infty+p_f\left(t+\frac{R}{c_\infty}\right)\right)-\frac{2S}{R}+J\right], \tag{5.1}$$

where R is the bubble radius, c_∞ and ρ_∞ are the constant sound speed and density of the medium, S is the surface tension. The far-field pressure is the sum of the ambient pressure, p_∞ and time-

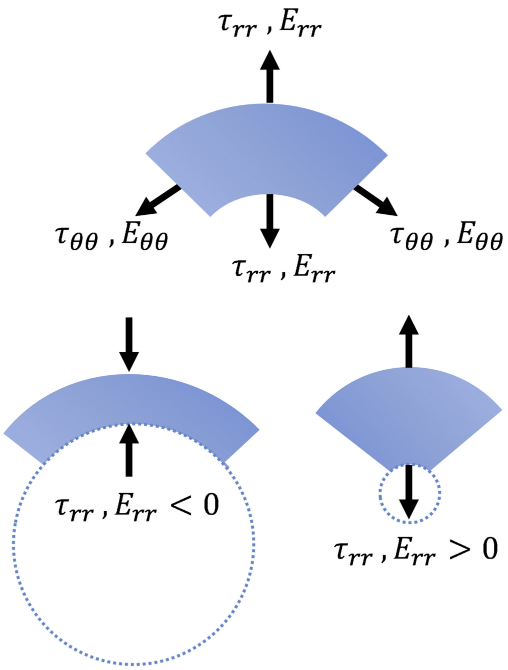

Figure 5.1: Radial (τ_{rr}) and polar ($\tau_{\theta\theta} = -\tau_{rr}/2 = \tau_{\phi\phi}$) stresses and strains on a wedge of tissue during bubble growth (left) and collapse (right)

varying ultrasound forcing, $p_f(t)$ (Eq. (5.8)). The pressure of the non-condensable air inside the bubble is given by the polytropic relationship $p_B = p_0(R_0/R)^{3\kappa}$, where $p_0 = p_\infty + 2S/R_0$ is the pressure inside the bubble at equilibrium. Gas inside the bubble is assumed to behave isothermally with a polytropic coefficient $\kappa = 1$, which is expected to be an accurate representation of the heat transfer. For simplicity, the tissue-bubble boundary is assumed to be impervious to gas, and vapor inside the bubble is neglected. These assumptions could potentially under-predict the bubble size (Harvey *et al.*, 1944); however, this error is expected to be minor because the mass boundary layer thickness is small relative to the bubble radius throughout bubble expansion (Barajas & Johnsen, 2017). The integral of deviatoric stresses in the surrounding tissue is

$$J = 2\int_R^\infty \frac{\tau_{rr} - \tau_{\theta\theta}}{r} dr, \tag{5.2}$$

where r is the radial distance from the origin, and τ_{rr} and $\tau_{\theta\theta}$ are the radial and polar stress components, respectively.

5.3.1 Constitutive Model

A Kelvin-Voigt-based constitutive model relates the deviatoric stress, $\boldsymbol{\tau}$, and strain, $\mathbf{E}$, tensors in the surrounding tissue whose coordinates span $r \in [R, L]$, where L is the arbitrary size of the domain. In this formulation, the stress at any field coordinate r in the surroundings is the sum of viscous and elastic contributions,

$$\tau_{rr} = \tau_{rr}^{V} + \tau_{rr}^{E} = -4\mu\frac{R^2\dot{R}}{r^3} + \frac{2G}{3}\left[\left(\frac{r_0}{r}\right)^4 - \left(\frac{r}{r_0}\right)^2\right], \tag{5.3}$$

where μ is the viscosity, G is the (linear) shear modulus and the original and current radial coordinates are related via

$$r_0(r,t) = \sqrt[3]{r^3 - R^3 + R_0^3}. \tag{5.4}$$

For an incompressible near field with spherical symmetry, $\tau_{\theta\theta} = -\tau_{rr}/2 = \tau_{\phi\phi}$. By convention, a negative stress at any point in the surroundings represents compression of the corresponding material element, and a positive stress represents tension ("stretching"). Figure 5.1 shows a schematic of the radial stresses and strains on a wedge of tissue during bubble growth and bubble collapse. The shape of the wedge changes as the bubble deforms the surrounding medium, but its mass and volume are conserved. Derived using continuum mechanics formalism, this model ensures that finite deformations $r(r_0, t)$ about the original configuration r_0 is accurately represented during bubble oscillations. Figure 5.2 illustrates the configuration of the bubble and surrounding medium before and after deformation. Labeled coordinates correspond to the variables related by Eqs. 5.3 and 5.4. Evaluating Eq. 5.3 at the bubble wall yields the following constitutive expression in the Keller-Miksis equation:

$$J = -\frac{4\mu\dot{R}}{R} - \frac{G}{2}\left[5 - 4\left(\frac{R_0}{R}\right) - \left(\frac{R_0}{R}\right)^4\right]. \tag{5.5}$$

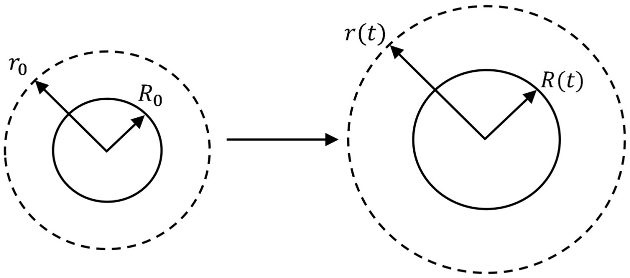

Figure 5.2: Schematic illustrating bubble radius and material coordinates in undeformed and deformed configurations.

Strain fields in the surrounding tissue are computed using the Hencky (or true) strain definition,

$$\begin{aligned} E_{rr}(r,t) &= \frac{2}{3}\log\left(1 - \frac{R^3 - R_0^3}{r^3}\right), \\ E_{\theta\theta}(r,t) &= -\frac{1}{3}\log\left(1 - \frac{R^3 - R_0^3}{r^3}\right), \end{aligned} \tag{5.6}$$

to describe tissue deformation in successive increments of classical engineering strain (Xiao, 2005), and the strain corresponds to the summation of incremental increases in displacement divided by length in the current configuration. The true strain definition is chosen because it most closely approximates the smooth increases in strain observed in experimental studies of cell-bubble interactions (Vlaisavljevich *et al.*, 2016c). This definition has also been favored for measurements of vascular tissue properties because it provides a more direct measure of a material's instantaneous response to applied stress (Khanafer *et al.*, 2013). Strain rates are calculated by taking the material derivative of the strain, where $u_r = \frac{R^2\dot{R}}{r^2}$ is the radial velocity component:

$$\begin{aligned} \frac{DE_{rr}}{Dt} &= \frac{\partial E_{rr}}{\partial t} + u_r\frac{\partial E_{rr}}{\partial r} = -2\frac{R^2\dot{R}}{r^3}, \\ \frac{DE_{\theta\theta}}{Dt} &= \frac{\partial E_{\theta\theta}}{\partial t} + u_r\frac{\partial E_{\theta\theta}}{\partial r} = \frac{R^2\dot{R}}{r^3}. \end{aligned} \tag{5.7}$$

Like the stresses, the radial and polar strains differ by a factor of −2, as do the corresponding strain rates.

5.3.2 Problem Setup

Viscoelastic parameters within the range of values previously studied in histotripsy experiments in tissues (Maxwell *et al.*, 2013; Wells Jr & Merrill, 1962; Diamond, 1999; Duck, 2013) and tissue phantoms (Vlaisavljevich *et al.*, 2015b,a) are considered: $\mu = 1 - 100$ mPa.s, $G = 1 - 1000$ kPa. Other tissue parameters are fixed: $\rho_\infty = 1000$ kg/m^3, $S = 72$ mN.m and $c_\infty = 1497$ m/s, corresponding to values in water at 25°C.

As in our past studies, cavitation is expected to be produced by a single negative histotripsy cycle, given analytically by:

$$p_f(t) = \begin{cases} p_A \left(\frac{1+cos[\omega(t-\delta)]}{2}\right)^n, & |t-\delta| \leq \frac{\pi}{\omega}, \\ 0, & |t-\delta| > \frac{\pi}{\omega}. \end{cases} \tag{5.8}$$

This work investigates the dependence of the bubble dynamics on the pressure amplitude $p_A = 20 - 60$ MPa and "frequency" $\omega = 0.5 - 5$ MHz corresponding to this single cycle; the time delay is $\delta = 5$ μs and $n = 3.7$ is a fitting parameter chosen to match the shape and duration of a typical histotripsy cycle.

Using the characteristic velocity $u = \sqrt{p_\infty/\rho_\infty}$, density and the initial radius for non-dimensionalization, the following dimensionless parameters govern the problem: Reynolds ($\rho_\infty u R_0/\mu$), Weber ($\rho_\infty u^2 R_0/S$), Cauchy ($\rho_\infty u^2/G$) and Mach (u/c_∞) numbers, as well as the polytropic index κ, dimensionless amplitude p_A/p_∞ and frequency $\omega R_0/u$. The resulting dimensionless system of differential equations is numerically integrated using the MATLAB stiff ODE solver *ode15s* (Shampine & Reichelt, 1997). Our subsequent parametric study will consider the effects of varying μ, G, p_A, ω and R_0.

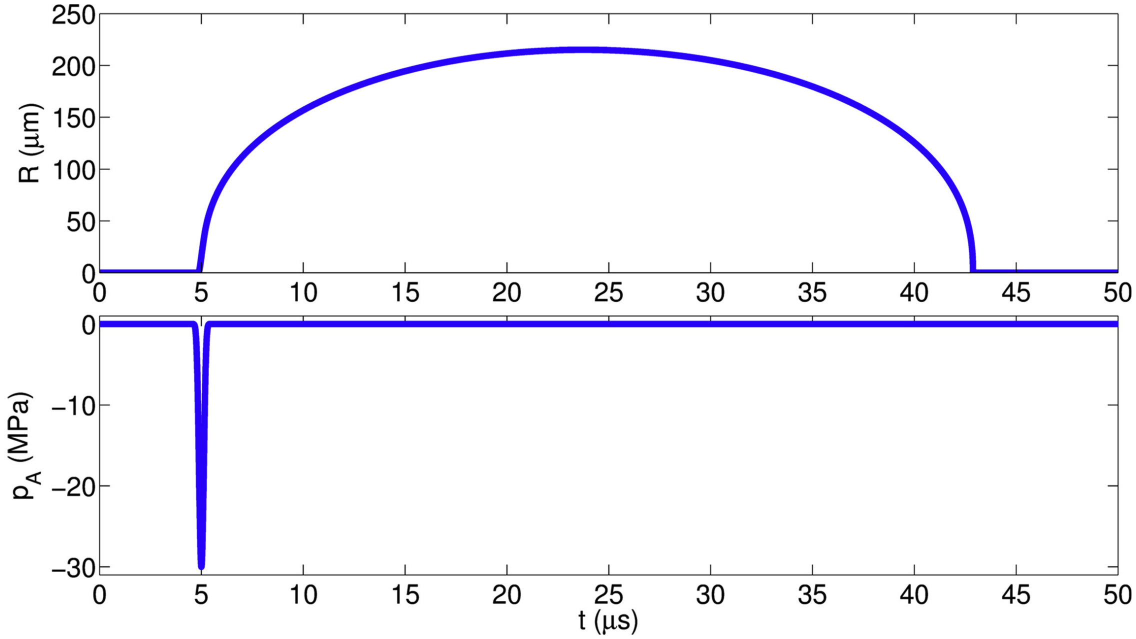

Figure 5.3: Time history of the bubble radius (top) driven by a single negative histotripsy cycle (bottom) for the baseline case.

5.4 Results

5.4.1 Baseline Case

Our baseline case consists of a tissue with $\mu = 15$ mPa.s and $G = 2.5$ kPa, initial nucleus size $R_0 = 5$ nm based on experimentally inferred nuclei sizes, (Maxwell *et al.*, 2013; Vlaisavljevich *et al.*, 2015c), and waveform with amplitude $p_A = -30$ MPa and frequency $\omega = 1$ MHz. This baseline is chosen because it is within the parameter range of our previous studies (Vlaisavljevich *et al.*, 2015b, 2014, 2016a, 2015b, 2016c) and illustrates a transition from strain-dominated to strain rate-dominated mechanical effects. Figure 5.3 shows the time history of the bubble radius and driving pressure. The large peak negative pressure of the histotripsy pulse causes a large expansion phase to a maximum radius of 200 μm, followed by a violent collapse to a minimum radius < 5 nm, which dissipates the energy primarily via compressibility. A single, low-amplitude rebound back to initial bubble radius is resolved, though not evident on the scale of this plot. A detailed study of minimum bubble radius lies beyond the present scope as histotripsy bubbles display more complex behavior at collapse, such as break-up (Duryea *et al.*, 2015); the present focus is on the dynamics until just before collapse.

The spatio-temporal evolution of the total radial stress in the tissue is shown in Fig. 5.4. In addition to the color maps, the time evolution of stresses along Lagrangian trajectories starting at different initial distances from the bubble wall and the radial stress distribution at fixed times are included. The tissue experiences large negative stresses near the bubble wall at the start of growth as the tissue is radially compressed. The highest stresses occur when the bubble reaches its maximum radius and the surrounding tissue is under maximal compression. The total radial stress is not symmetric in time about the maximum radius, illustrated by the large tensile (positive) stresses at collapse as the shrinking bubble releases the compressed tissue to assume its original configuration. Stress magnitudes are greatest near the bubble wall and rapidly attenuate farther into the medium such that it is negligible within 200 μm from the bubble wall. The stresses persisting deeper in the tissue are small ($<$ 0.01 MPa), compared to those within 1 μm of the bubble wall, which can exceed 100 MPa. The highest stresses are so localized to the bubble wall that they are better appreciated in the Lagrangian trajectories where the spherical coordinate system moves with the tissue as it deforms over time. The stresses are computed from Eq. 5.3 along trajectories $r(t)$ for particles starting at different initial locations, r_0. Such a particle could, for instance, represent a cell, whose stress one is interested in monitoring. As the bubble grows and collapses, the Lagrangian points oscillate with the surroundings. By mass conservation, the distance between the Lagrangian trajectories decreases when the bubble grows, and vice-versa during collapse. A particle in the tissue starting 1 μm from the bubble nucleus experiences smoothly increasing compressive stress in the radial direction, with a maximum compressive stress of -70 MPa at maximum radius. A nearly instantaneous peak in tensile stress of 155 MPa occurs at minimum radius. For particles starting $10-50\,\mu$m from the bubble wall, the compressive stress at maximum radius and the tensile stress at collapse are significantly attenuated. The stress profile for a particle starting 10 μm from the bubble wall shows a peak in compressive stress at the onset of growth also present but not clearly visible in the 1 μm trace due to early explosive growth. Further growth is restricted by tissue stiffness, and

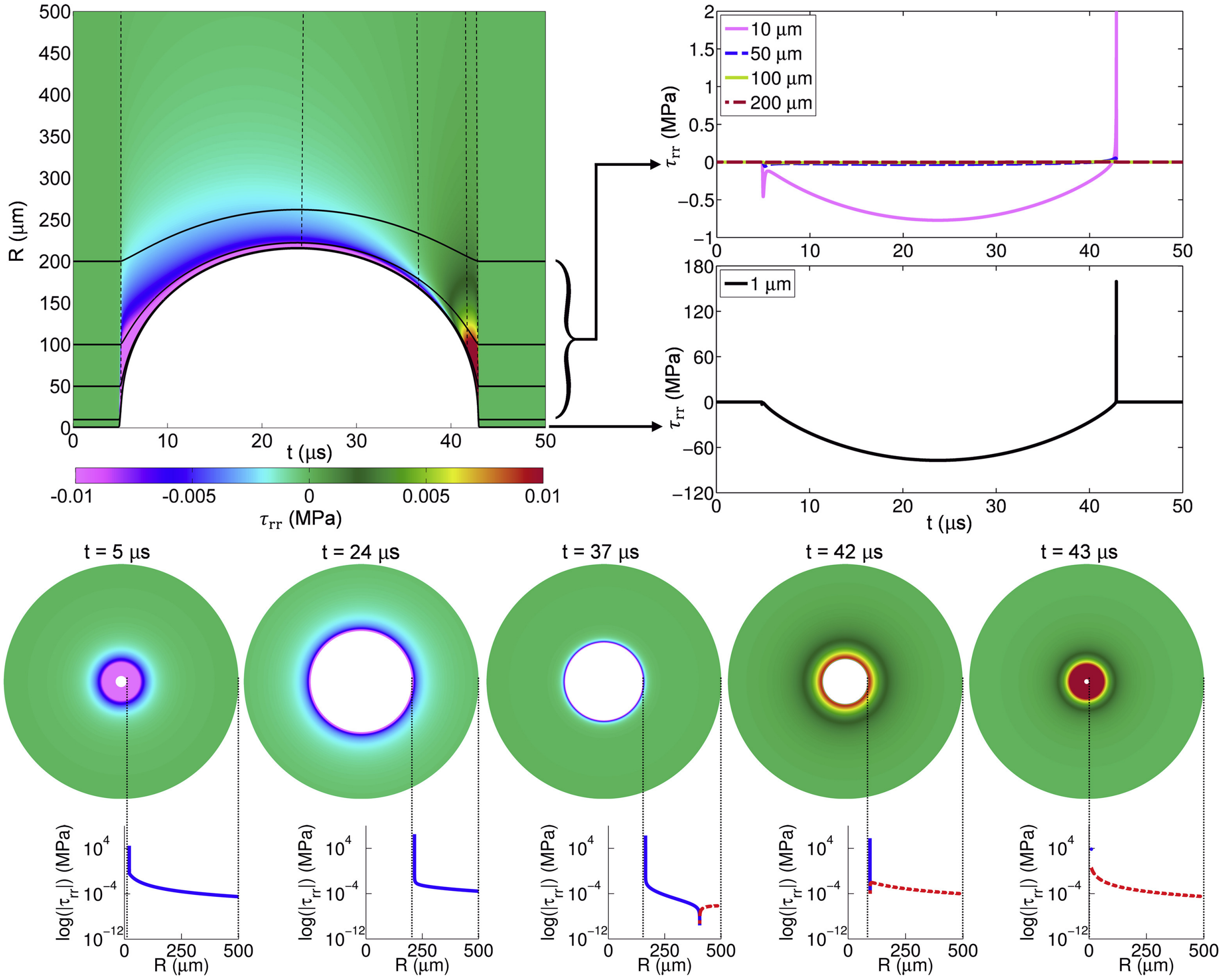

Figure 5.4: Top: Color plot shows temporal and spatial evolution of the total (viscous + elastic) radial stress distribution in the tissue for the baseline case. Solid lines correspond to stresses experienced as a function of time along Lagrangian trajectories starting 1 to 200 m from the bubble nucleus, with stress magnitude along each trajectory indicated by arrows at right. Vertical dashed lines correspond to stresses in the surroundings at fixed times given below. Bottom: Bubble color plots show stresses at fixed times between 5 and 41 s, with traces indicating the magnitudes of compressive stresses (solid blue) and tensile stresses (dashed red) as a function of distance from the bubble wall.

slowed subsequent growth produces a smoothly increasing compressive stress in surroundings. As in the 1 μm case, particles initially 10 μm from the bubble nucleus experience a near instantaneous peak in tensile stress at collapse; however, the magnitude of maximum tensile stress is reduced to 2 MPa at the greater distances. Particles starting 50−200 μm from the bubble nucleus also experience decreasing stress magnitudes. At 50 μm from the bubble wall, the instantaneous peak tensile stress at collapse has largely attenuated and reaches 0.050 MPa, while the compressive stress at maximum radius is −0.054 MPa. There is a further dramatic decrease in stress magnitude experienced by cells 200 microns from the nucleus. Considering that most ruptured tissues have an ultimate tensile strength greater than 0.05 MPa (Vlaisavljevich *et al.*, 2013b), an order of magnitude comparison suggests that radial tensile stress capable of rupturing most tissues is confined to a radius < 50 microns witin a nucleation site, which is consistent with observations of sharp lesion boundaries in previous experimental studies of histotripsy (Roberts *et al.*, 2006).

The susceptibility of tissue to histotripsy-induced damage depends on the tissue's mechanical properties (Vlaisavljevich *et al.*, 2013b). Furthermore, the stress in a viscoelastic tissue depends on strain and strain rate. However, the influences of individual tissue properties on susceptibility to damage is less clear. Thus, separating the stress into its viscous and elastic components is useful for postulating how potential stress-related damage mechanisms depend on tissue properties. The time evolution of the viscous and elastic radial stress distributions in the tissue for the baseline case is shown in Figs. 5.5 and 5.6, respectively. Viewing each component separately indicates that the extrema observed in the total radial stress field originate from different mechanisms. The sharp instantaneous peaks in total stress at early growth and late collapse are due to viscous contributions. Viscous stresses dissipate the kinetic energy of the surroundings into heat as follows:

$$\phi = \underline{\boldsymbol{\tau}} : \boldsymbol{\nabla}\boldsymbol{u} = 12\mu\left(\frac{R^2\dot{R}}{r^3}\right)^2 = -3\frac{R^2\dot{R}}{r^3}\tau^V_{rr}. \tag{5.9}$$

Dissipation increases with increasing tissue viscosity, which in turn limits bubble growth and decreases the velocity of the bubble wall just before collapse. The more gradually increasing stresses

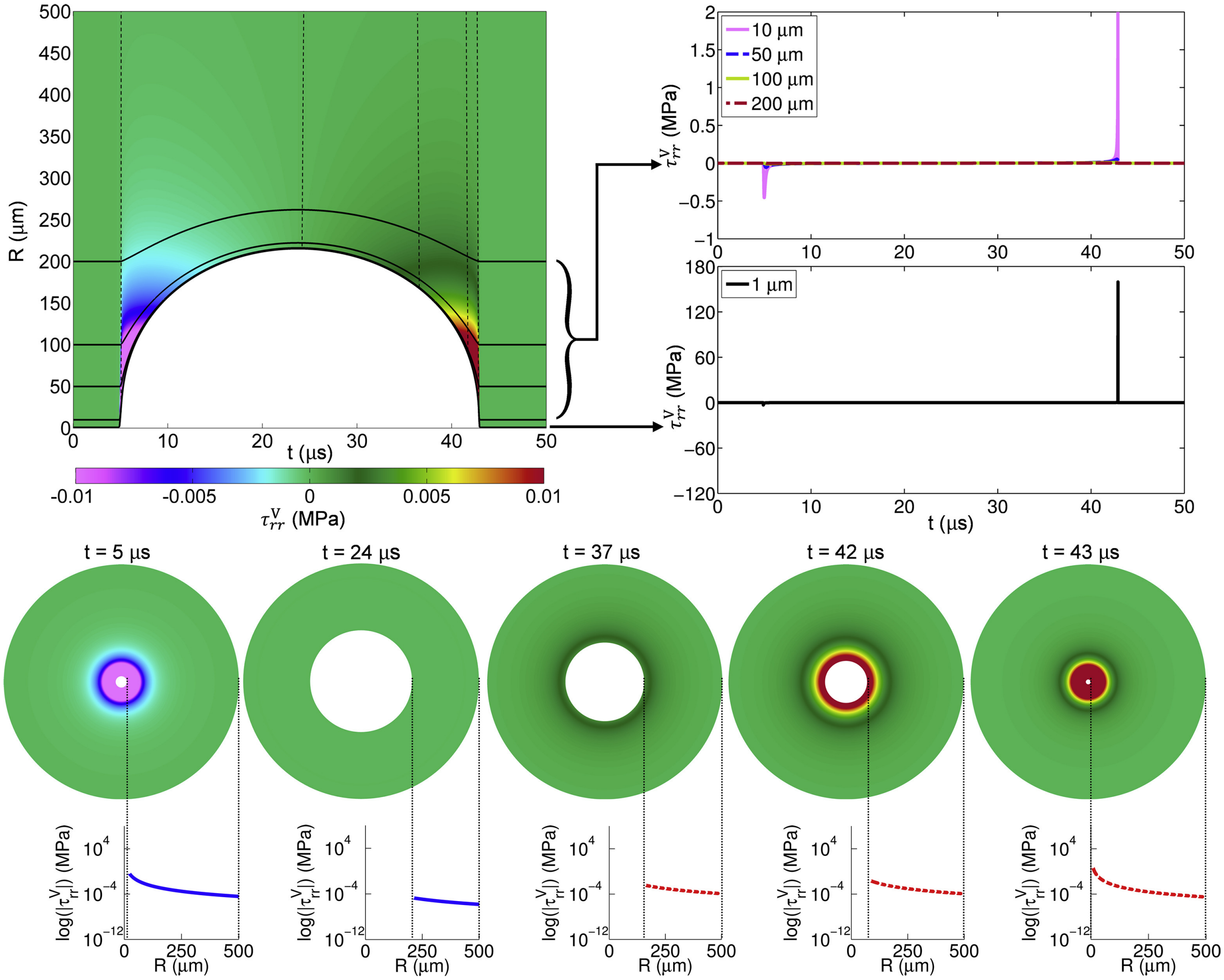

Figure 5.5: Same as for Fig. 5.4, but for viscous stresses, τ_{rr}^{V}.

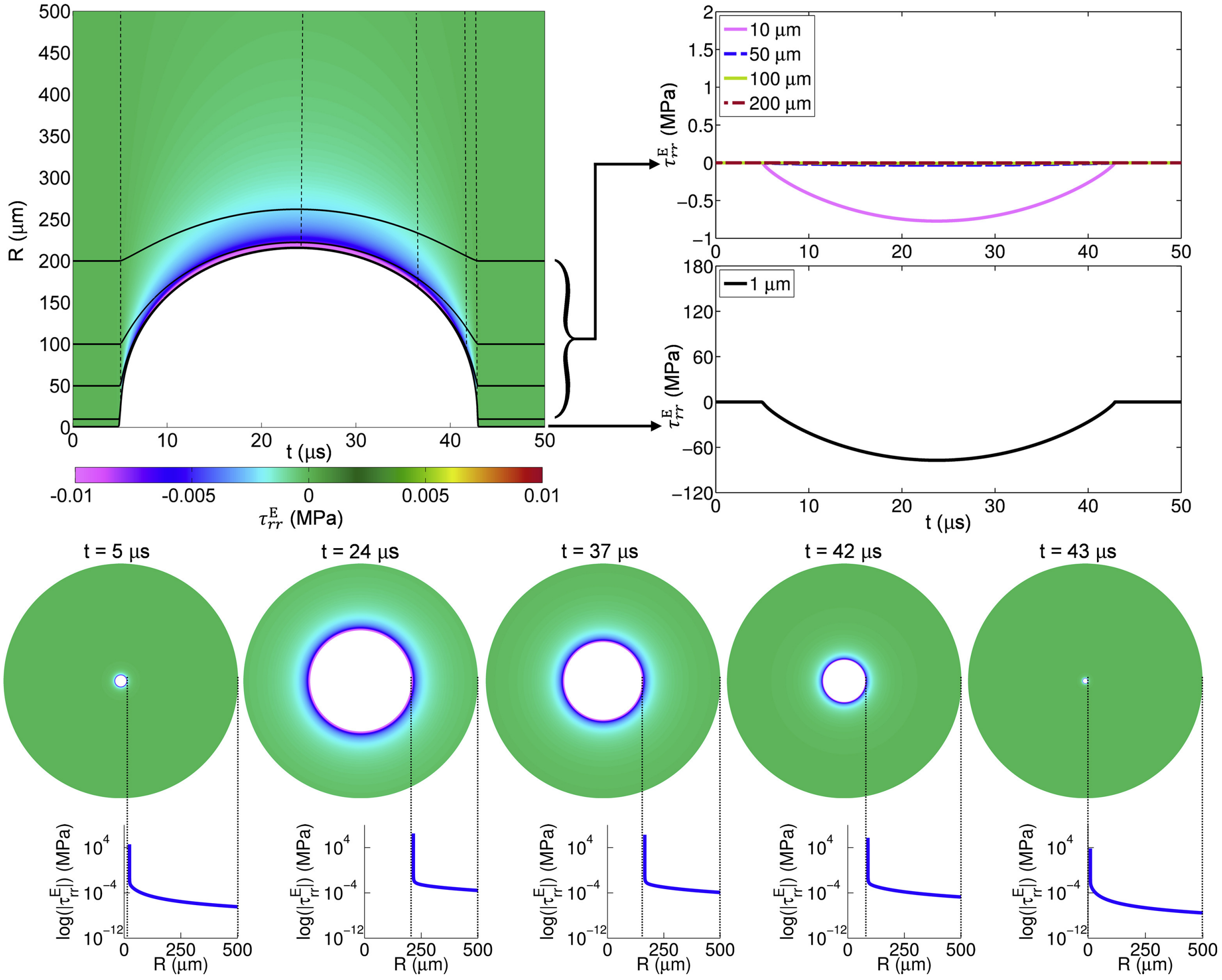

Figure 5.6: Same as for Fig. 5.4, but for elastic stresses, τ_{rr}^{E}

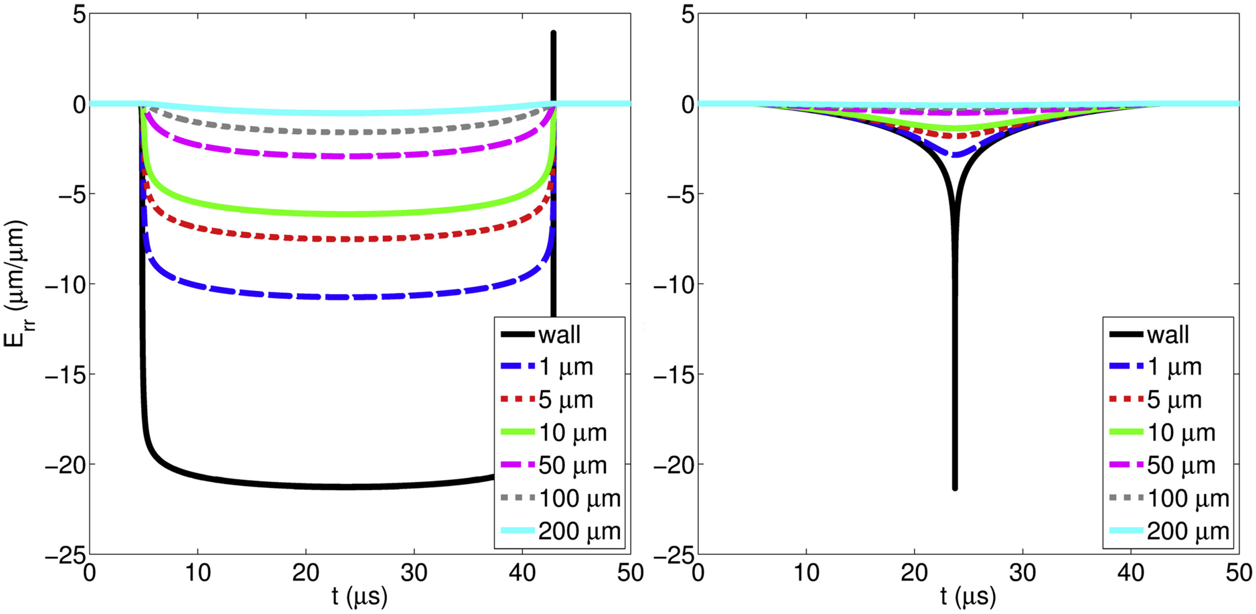

Figure 5.7: Radial strains versus time following Lagrangian trajectories (left) and at Eulerian points (right). Distances correspond to the different initial distances of the particles from the origin (Lagrangian) and to the initial distances from the maximum radius (Eulerian).

at maximum radius are purely elastic and are only compressive since the bubble does not reach a radius much smaller than its initial value of 5 nm. Since viscous stresses at the bubble wall are proportional to $\dot{R}/R$, the stress is compressive (negative) at early growth and tensile at collapse (positive). Otherwise, viscous stresses are negligible.

The stresses correspond to different deformation modes: as evidenced by Eq. 6.6, elastic stresses are proportional to strains (deformation from the initial configuration) while viscous stresses are proportional to strain rates (velocity differentials). Strains and the corresponding rates are quantities that can be measured in experiments without *a priori* knowledge of the constitutive model that describes a particular tissue. Figure 5.7 shows the temporal evolution of Hencky radial strains based on Lagrangian and Eulerian (calculated with respect to a fixed coordinate system) viewpoints. The seemingly larger values in the Lagrangian viewpoint are due to the diverging geometrical field during bubble growth: by conservation of mass, particles starting at a given distance from the bubble end up closer to the bubble wall during expansion. Both plots indicate that strains remain concentrated near the bubble wall and attenuate rapidly with increasing depth into the surrounding tissue. Large radial strains that persist to greater depths in the tissue are compressive

Table 5.1: Magnitude of maximum strain experienced by a particle starting at the wall of the bubble nucleus. The absolute maximum strains occur when the bubble reaches its maximum radius, and relative maximum strains occur at minimum bubble radius.

Location	Direction	Deformation	Expression
Maximum Radius	Radial	Compression	$E_{rr}(R_{max}) \rightarrow 2\log(R_{max}/R_0)$
	Polar	Tension	$E_{\theta\theta}(R_{max}) \rightarrow \log(R_{max}/R_0)$
Minimum Radius	Radial	Tension	$E_{rr}(R_{min}) \rightarrow 2\log(R_0/R_{min})$
	Polar	Compression	$E_{\theta\theta}(R_{min}) \rightarrow \log(R_0/R_{min})$

and occur when maximum bubble radius is reached. Lagrangian particles experience radial compressive strains that smoothly increase to a maximum at maximum radius. The Eulerian strains progressively increase as maximum radius is reached, but are less than 1.0 μm/μm until the bubble radius reaches approximately 150 μm. As the bubble reaches its maximum radius (and approaches the position of the fixed Eulerian point), the strains achieve a maximum and then decrease rapidly with distance from that point. Strain magnitude varies significantly with distance from the bubble in each depiction. In the Lagrangian depiction, radial compressive strains experienced by particles starting within 50 μm from the nucleus are high, e.g., -10.7 μm/μm starting at 1 μm from the nucleus wall. Radial compressive strain experienced by particles starting 200 μm from the nucleus is significantly lower at -0.50 μm/μm. In the Eulerian depiction, maximum compressive stresses achieve the same value of -21.3 μm/μm at the bubble wall at maximum radius, but maximum compressive strains are -2.8 μm/μm at 1 μm and -0.1 μm/μm at 200 μm from the maximum bubble radius. For comparison, tissue measurements suggest that the ultimate fractional tensile strain of tissues ruptured by histotripsy ranges from 0.43 μm/μm for small intestine to 1.5 μm/μm for uterine wall (Vlaisavljevich *et al.*, 2013b).

The largest strains are experienced by particles starting at the bubble wall when the bubble reaches its maximum and minimum radii; exact expressions for the maximum radial compressive, polar tensile, radial tensile and polar compressive strains are summarized in Table 5.1. First, when the bubble achieves its maximum radius, radial strain at the bubble wall is compressive and polar strain at the bubble wall is tensile, corresponding to the maximum radial compressive and polar tensile stresses. In contrast, the largest radial tensile and polar compressive strains occur when the bubble collapses to its minimum radius, $R_{min} < R_0$. At this instant, the tissue is fully released from the compressive radial strain that occurred during bubble growth and the strain changes direction. These strains occur over an exceedingly short time and attenuate much more rapidly into surrounding tissue than the strains generated at maximum bubble radius. As seen in Fig. 5.7, Lagrangian particles starting as close as 1 μm from the bubble nucleus experience negligible radial tensile strain at bubble collapse. The highest strain rates occur at instants of initial bubble growth and late collapse, with maximum values ranging from 10^5 s^{-1} for a Lagrangian particle starting at a distance of 200 μm from the bubble wall to 10^8 s^{-1} at a distance of 1 micron from the bubble wall. The highest strain rates coincide with the peaks in radial tensile stress and strain that occur at the bubble wall just before and at R_{min}.

5.5 Parametric Study

The effects of tissue (viscosity, shear modulus) and waveform (negative pressure, frequency) properties, as well as initial bubble radius, on maximum radial stresses and strains experienced by a Lagrangian particle (e.g., a cell) are evaluated. The Lagrangian viewpoint is of practical relevance since it enables one to determine the loads experienced by a cell, initially at some distance from the nucleation site, over the course of bubble growth and collapse. In all following maximum stress (Figs. 5.9, 5.12, 5.15, 5.18, 5.21) and strain (Figs. 5.10, 5.13, 5.16, 5.19, 5.22) figures, the horizontal axis gives the starting point of a particle within 50 μm from the bubble nucleus, with 500 sample points. The vertical axis shows the highest magnitude of total stress (combined elastic and viscous) or strain experienced by a cell that starts at a given distance from the nucleus. Due to their typically distinct origins, maximum compressive and tensile stresses are considered separately. As a reference, a water case in which viscosity and shear modulus are fixed at $\mu = 1$ mPa.s and $G = 0$ Pa is used when tissue material properties are varied. Results are shown for radial stresses and strains; tissue is also experiencing polar stresses and strains, of opposite sign and half the magnitude.

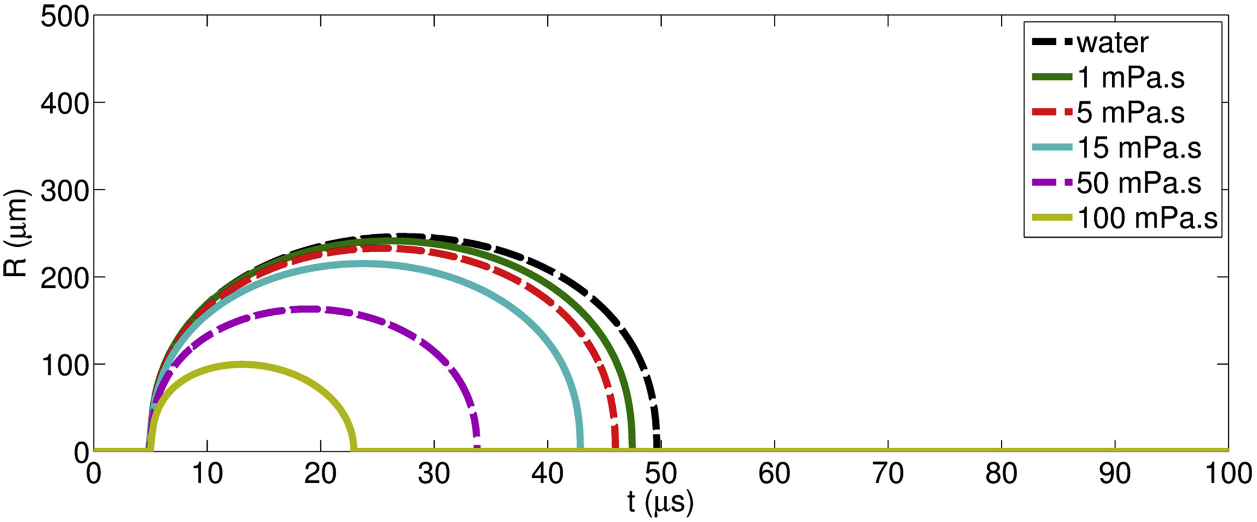

Figure 5.8: Time history of bubble radius for media of different viscosities (μ = 1, 5, 15, 50 and 100 mPa.s).

5.5.0.1 Viscosity

Figures 5.8, 5.9 and 5.10 show the time history of the bubble radius, maximum radial compressive/tensile stress and maximum radial compressible (Hencky) strain experienced by Lagrangian particles starting at different distances from the bubble for $\mu = 1, 5, 15, 50$, and 100 mPa.s, fixing shear modulus ($G = 2.5$ kPa) and other parameters at their baseline values. Equivalently, this corresponds to varying the Reynolds number while holding all other dimensionless parameters fixed.

Increased viscous resistance impedes bubble growth, as evidenced by the reduction of the maximum bubble radius at higher viscosities. As the viscosity is increased, the collapse phase (from R_{max} to R_{min}) becomes longer than the growth phase from a stationary nucleus of radius R_0 to R_{max}). This asymmetry originates from the dissipative nature of viscous effects. For a given viscosity, the maximum tensile stress (produced at collapse) smoothly and monotonically decreases with initial distance. However, slightly lower tensile stress is achieved in the 100 mPa.s medium than in the 50 mPa.s medium. This behavior is again due to increased viscous dissipation, which gives rise to lower velocities at collapse and thus smaller tensile stresses. At sufficiently high viscosities, the maximum compressive stress exhibits a “kink” – a discontinuous slope – highlighted on the

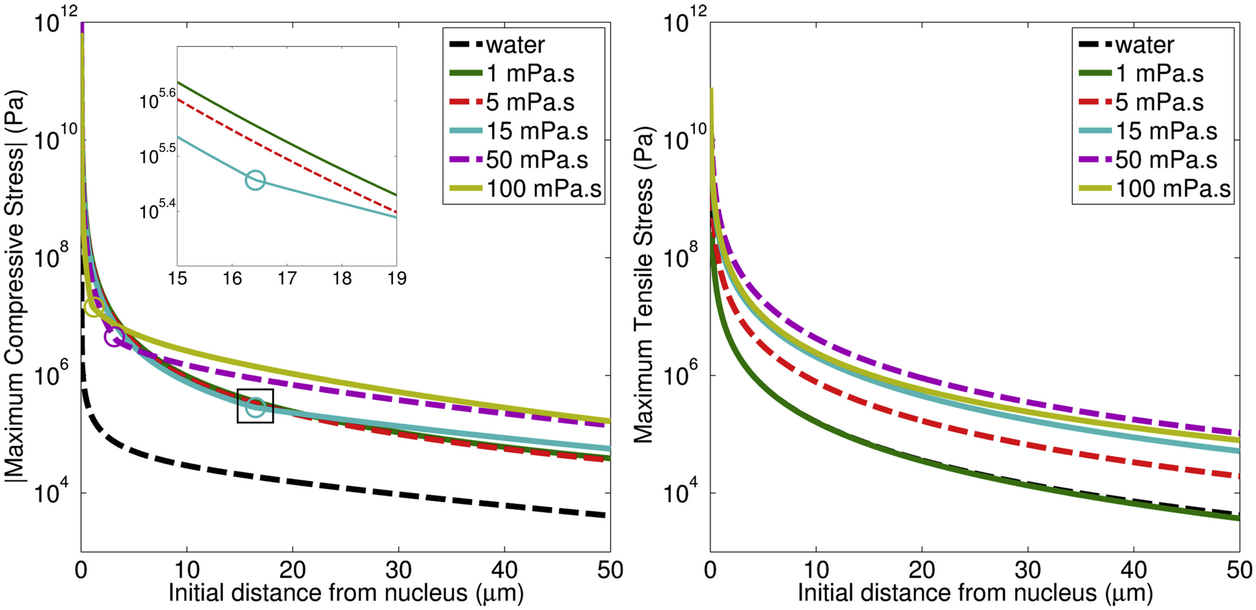

Figure 5.9: Maximum compressive (left) and tensile (right) stresses versus initial distance from the bubble nucleus in media of different viscosities (μ = 1, 5, 15, 50 and 100 mPa.s). The elastic–to–viscous transitions are circled on the compressive stress traces.

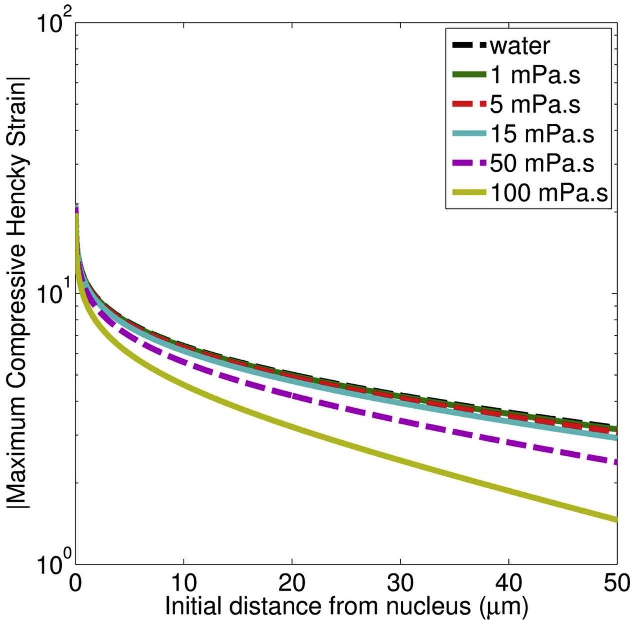

Figure 5.10: Maximum compressive Hencky strain versus distance from the bubble nucleus in media of different viscosities (μ = 1, 5, 15, 50 and 100 mPa.s).

plot by filled circles. This point corresponds to the initial distance of the “cell” from the origin at which the absolute maximum compressive stress transitions from elastic to viscous over the course of the simulation. The absolute maximum compressive stress is of elastic origin and occurs at the bubble wall when the bubble reaches its maximum radius. As initial distance into the tissue is increased, this elastic stress decreases according to the second term in Eq. 5.3. In contrast, a maximum in viscous compressive stress occurs at the bubble wall when growth is initiated; the viscous compressive stress decreases according to the first term in Eq. 5.3. Increasing viscosity enhances the importance of viscous stresses relative to their elastic counterparts in two important ways: the coefficient weighing viscous contributions (μ) is increased compared to that weighing elastic contributions (G), and the maximum radius is reduced. As a result, the attenuation of elastic stresses for particles starting farther away from the bubble is greater than that for viscous stresses. At larger viscosities ($15 - 100$ mPa.s), viscous stresses at the onset of bubble growth exceed elastic stresses achieved at maximum bubble radius closer to the bubble wall. As a reflection of differences in maximum bubble radii as viscosity is increased, compressive strain consistently decreases, thus restricting growth and producing smaller compressive strains. Media with viscosities between $1 - 15$ mPa.s (including water), exhibit similar maximum bubble radii and hence compressive strains of similar magnitude.

5.5.0.2 Shear Modulus

Figures 5.11, 5.12 and 5.13 show the time history of the bubble radius, maximum radial compressive/tensile stress and maximum radial compressible (Hencky) strain experienced by Lagrangian particles starting at different distances away from the bubble for $G = 0$, 1, 2.5, 10, 100 and 1000 kPa, fixing viscosity ($\mu = 15$ mPa.s) and other parameters at their baseline values. Equivalently, this corresponds to varying the Cauchy number while holding all other dimensionless parameters fixed.

Increased tissue stiffness reduces bubble growth, as evidenced by the smaller maximum radii and shorter collapse time (from R_{max} to R_{min}) achieved at higher shear modulus. Contrary to vis-

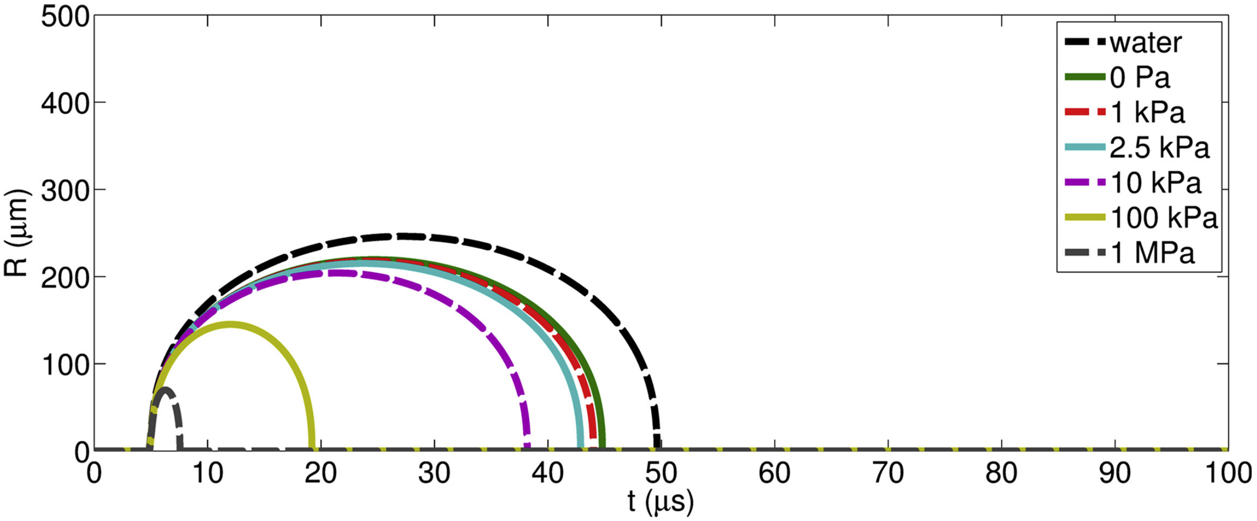

Figure 5.11: Time history of bubble radius for media of different shear moduli (G = 0, 1, 2.5, 10, 100 and 1000 kPa).

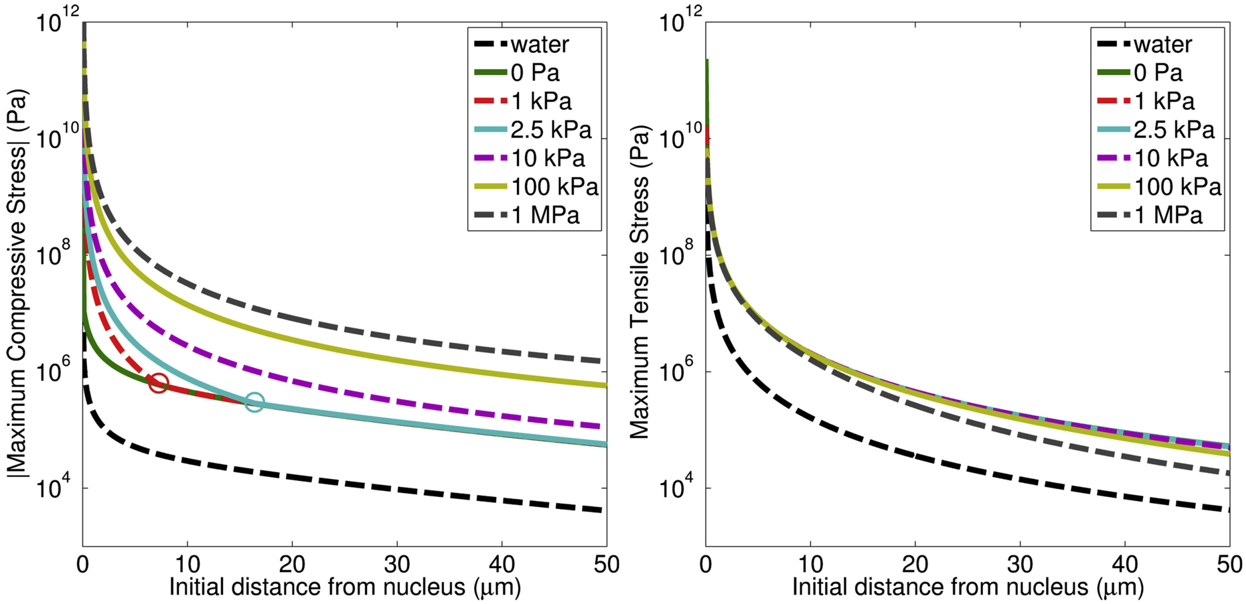

Figure 5.12: Maximum compressive (left) and tensile (right) stresses as a function of initial distance from the bubble nucleus for media of different shear moduli (G = 0, 1, 2.5, 10, 100 and 1000 kPa). Elastic-to-viscous transitions are circled on compressive stress traces.

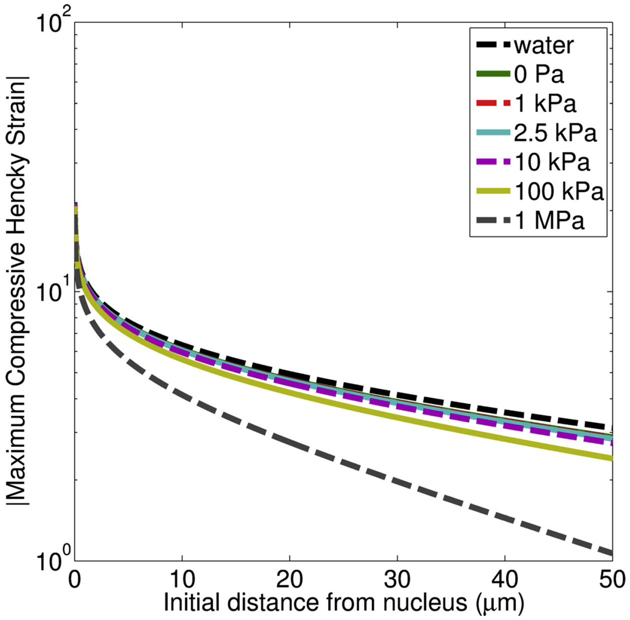

Figure 5.13: Maximum compressive Hencky strain as a function of distance from the bubble nucleus in media of different shear moduli (G = 0, 1, 2.5, 10, 100 and 1000 kPa).

cosity, elasticity is a restoring force with no direct dissipative effects. Symmetry between growth and collapse phases are thus not affected by elasticity. The dominance of elastic stress close to the bubble wall is evident when cases of nonzero shear moduli are compared to the water. The maximum compressive stress increases with increasing shear modulus, while the maximum tensile stress and compressive strain decrease with increasing modulus. As in the previous section, a “kink” is observed in the $G = 1$ kPa and $G = 2.5$ kPa traces for maximum compressive stress, marking the locations at which the dominant stress contribution changes from elastic to viscous. Decreasing the shear modulus reduces the relative importance of elastic contributions compared to viscous stresses. The maximum tensile stress experienced by particles in the tissue exhibits only limited dependence on the shear modulus for $G < 100$ kPa, which is expected since this quantity depends on viscous stresses and since the bubble radius histories are similar. For larger G, smaller maximum tensile stresses are achieved. Again, differences in compressive strain developed at all distances from the bubble are due to differences in maximum bubble radius. Maximum compressive strain shows a relatively weak dependence on shear modulus in low elasticity media ($G < 100$ kPa), and as shear modulus increases, compressive strain decreases.

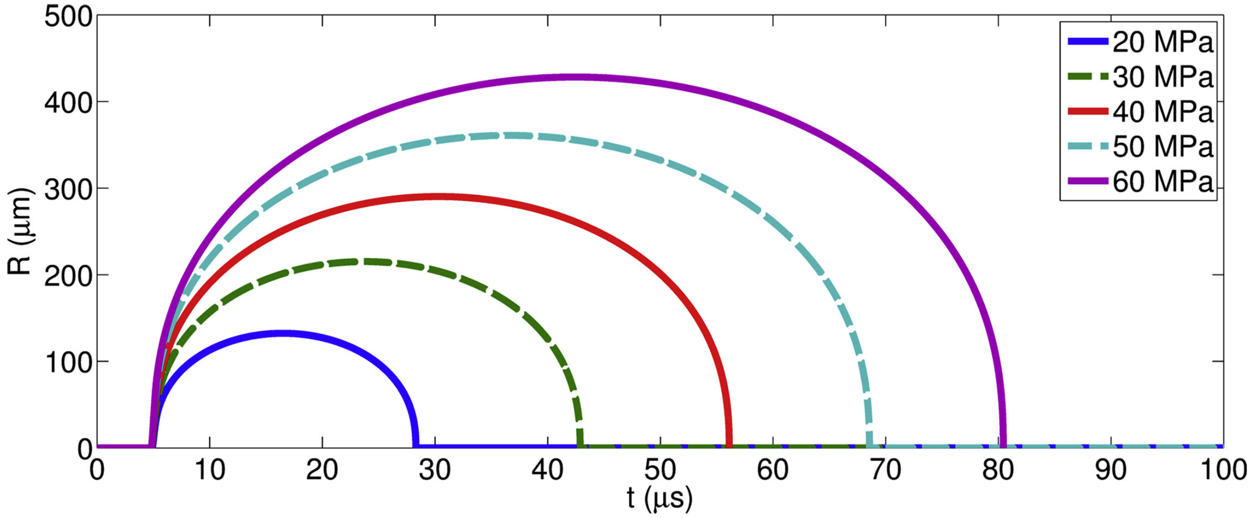

Figure 5.14: Time history of the bubble radius for different peak negative pressures (p_A= 20, 30, 40, 50 and 60 MPa).

5.5.0.3 Waveform Peak Negative Pressure

Figures 5.14, 5.15 and 5.16 show the time history of the bubble radius, maximum radial compressive/tensile stress and maximum radial compressible (Hencky) strain experienced by Lagrangian particles starting different distances away from the bubble for p_A = 20, 30, 40, 50 and 60, holding all other properties constant. Equivalently, this corresponds to varying the nondimensional pressure amplitude holding all other dimensionless parameters fixed.

Increasing the peak negative pressure enhances the bubble growth: the maximum radius and time at collapse (time interval from the beginning of the growth to R_{min}) increases linearly with pressure amplitude. Maximum compressive and tensile stresses, as well as maximum compressive (Hencky) strains, are largest at the bubble wall and monotonically decrease with increasing initial distance. Kinks in the maximum compressive stress are observed in the 20, 30 and 40 MPa traces. This finding indicates that waveform parameters can also affect the origin (elastic vs. viscous) of stresses at different distances from the bubble wall, likely through their effects on R_{max}. When peak negative pressure is varied, the stress behavior is a consequence of the qualitatively similar bubble dynamics at each pressure, by contrast to changes in material properties, which can produce changes in bubble radius histories that are not simply proportional to the altered parameter.

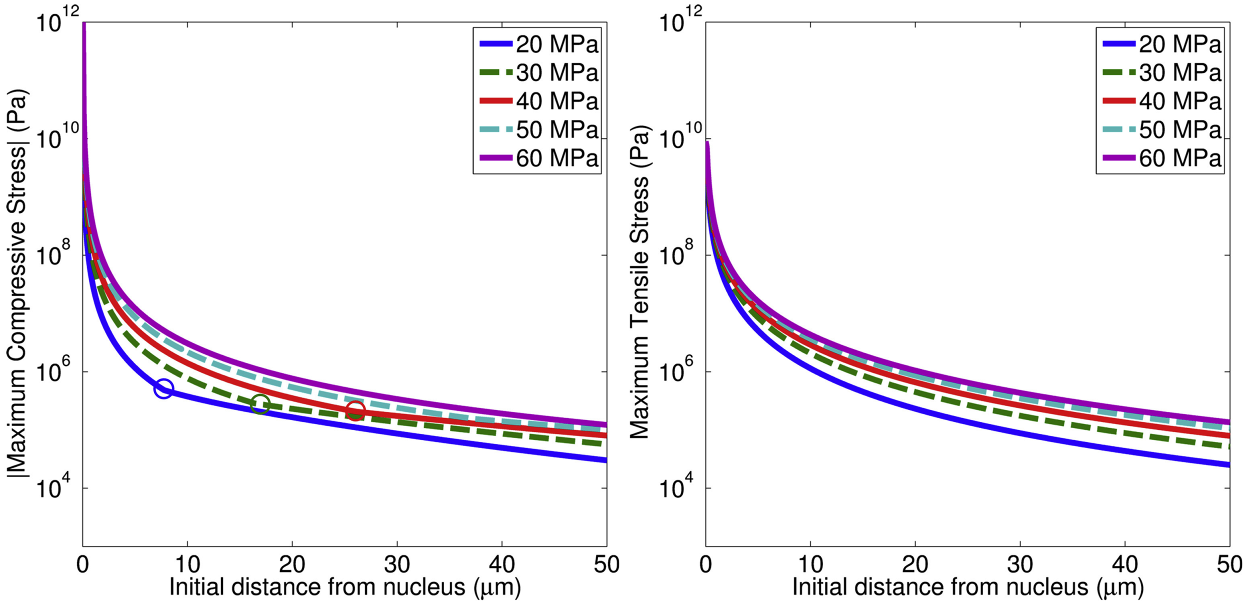

Figure 5.15: Maximum compressive (left) and tensile (right) stresses as a function of initial distance from the bubble nucleus for different peak negative pressures (p_A= 20, 30, 40, 50 and 60 MPa). Elastic-to-viscous transitions are circled on compressive stress traces.

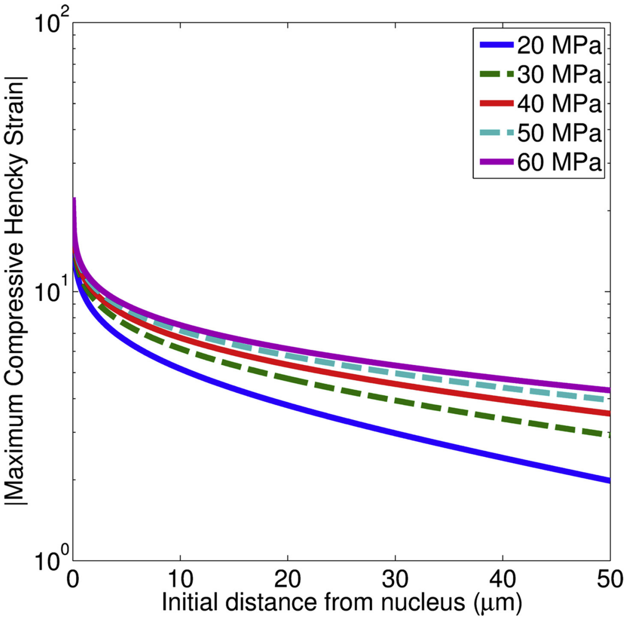

Figure 5.16: Maximum compressive Hencky strain as a function of distance from the bubble nucleus for different peak negative pressures (p_A= 20, 30, 40, 50 and 60 MPa).

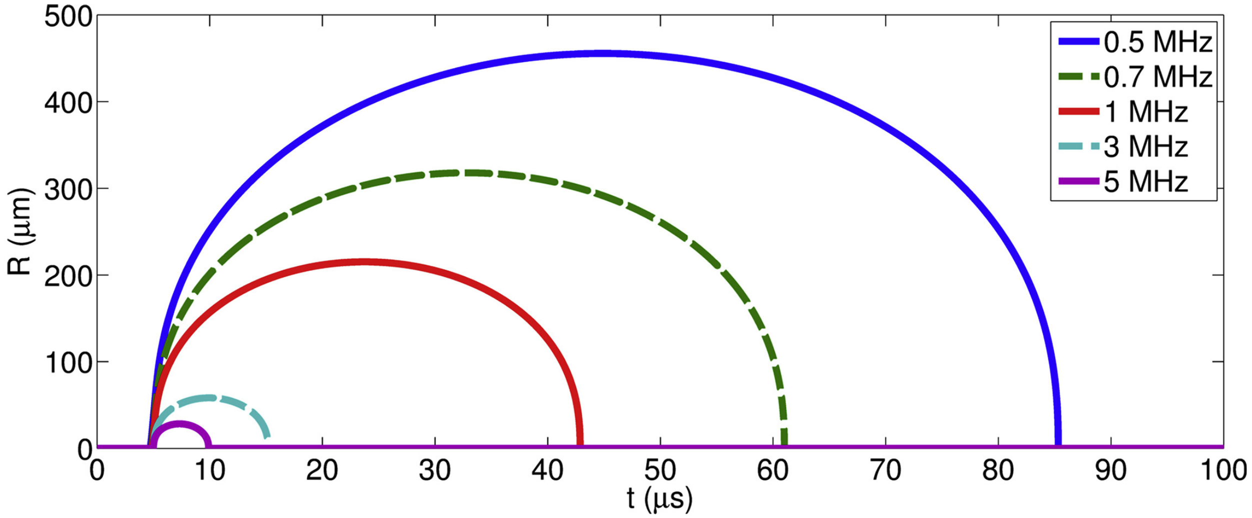

Figure 5.17: Time history of the bubble radius for different frequencies (ω = 0.5, 0.7, 1.0, 3.0 and 5.0 MHz)

5.5.0.4 Waveform Frequency

Figures 5.17, 5.18 and 5.19 show the time history of the bubble radius, maximum radial compressive/tensile stress and maximum radial compressible (Hencky) strain experienced by Lagrangian particles starting different distances away from the bubble for ω = 0.5, 0.7, 1.0, 3.0 and 5.0 MHz, holding all other properties constant. Equivalently, this corresponds to varying the dimensionless frequency holding all other dimensionless parameters fixed.

Decreased pulse frequency enhances bubble growth as the tension driving bubble growth acts for a longer time. As a result, larger maximum radii and collapse times (from R_{max} to R_{min}) are achieved with decreasing frequency. For the maximum tensile stress and compressive strain, these decreases are monotonic; at a given location, the stress and strain decrease with increasing frequency. As when previous parameters were varied, “kinks” are observed in the maximum compressive stress for ω = 0.7, 1.0, 3.0 and 5.0 MHz, marking the location at which the dominant stress contribution changes from elastic to viscous. As a result of the smaller R_{max}, elastic contributions decrease rapidly and are overwhelmed by viscous stresses closer to the bubble wall.

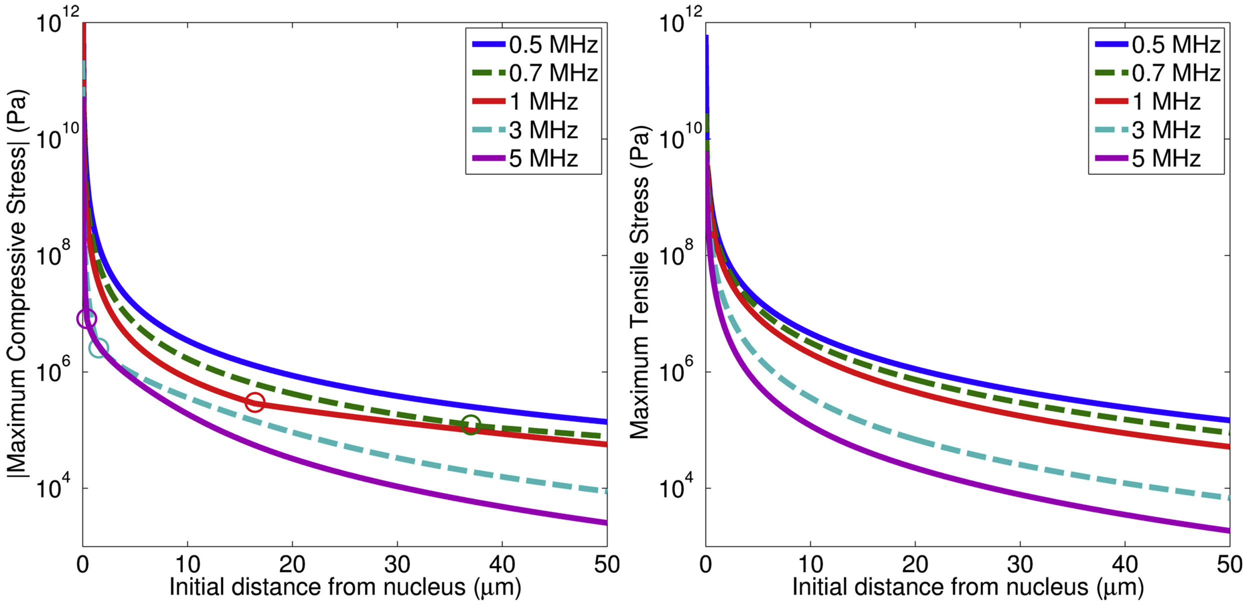

Figure 5.18: Maximum compressive (left) and tensile (right) stresses as a function of distance from the bubble nucleus for different frequencies ($\omega = 0.5, 0.7, 1.0, 3.0$ and 5.0 MHz). Elastic-to-viscous transitions are circled on compressive stress traces.

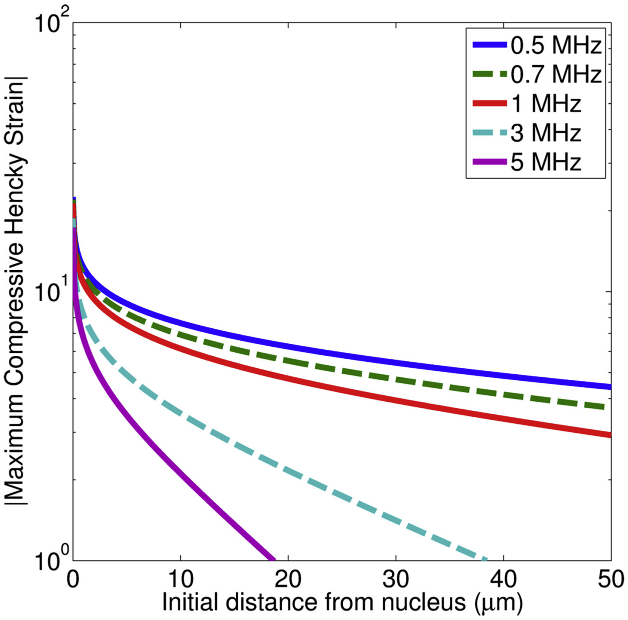

Figure 5.19: Maximum compressive Hencky strain as a function of distance from the bubble nucleus for different frequencies ($\omega = 0.5, 0.7, 1.0, 3.0$ and 5.0 MHz).

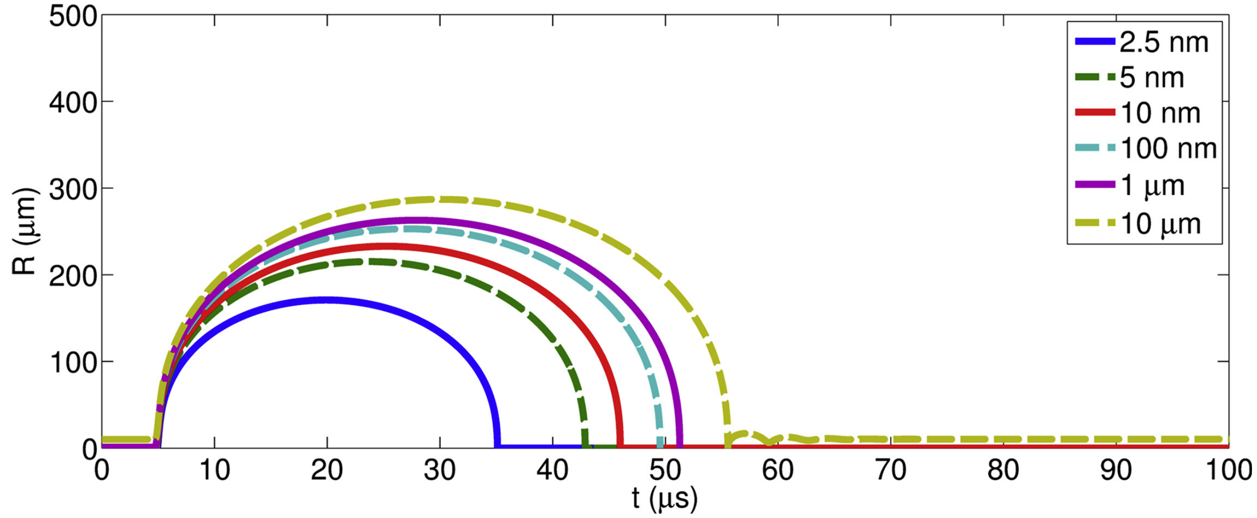

Figure 5.20: Time history of the bubble radius for different initial bubble radii (R_0 = 2.5, 5.0, 10, 100, 1000 and 10,000 nm).

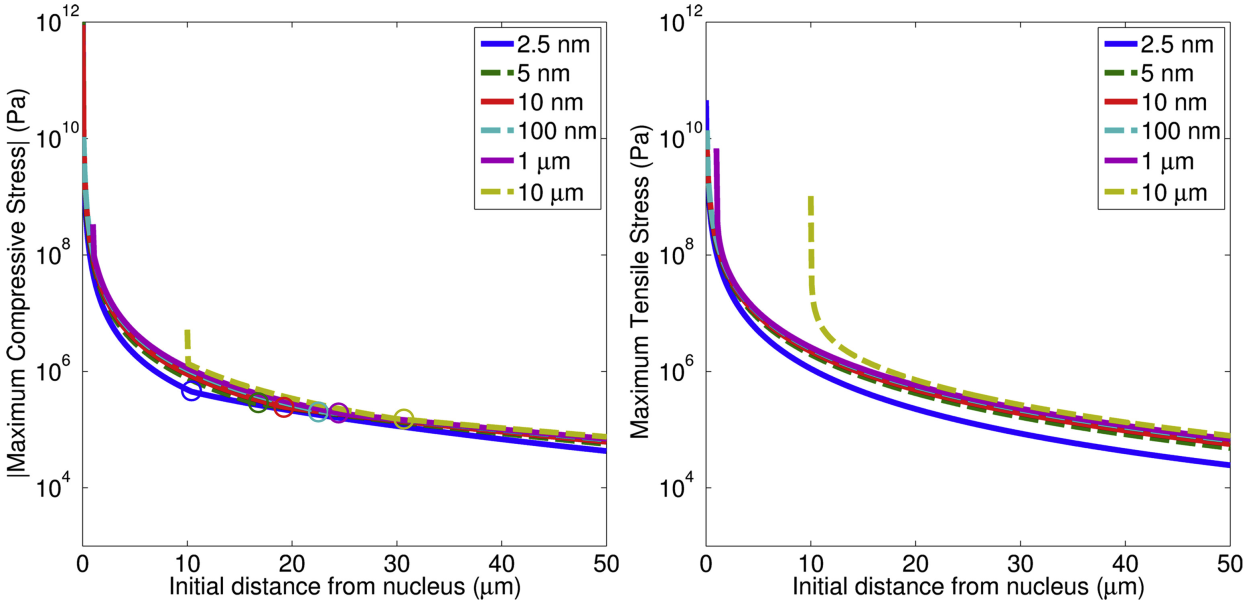

Figure 5.21: Maximum compressive (left) and tensile (right) stresses as a function of initial distance from the bubble nucleus for different initial bubble radii (R_0 = 2.5, 5.0, 10, 100, 1000 and 10,000 nm). Elastic-to-viscous transitions are circled on compressive stress traces.

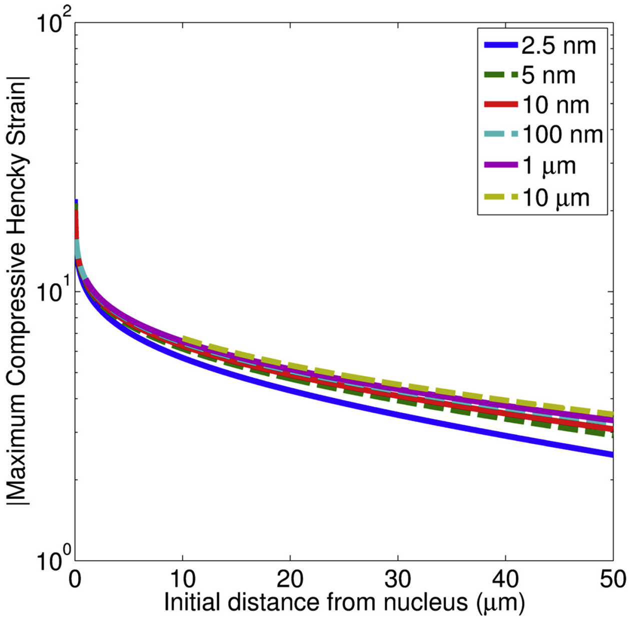

Figure 5.22: Maximum compressive Hencky strain as a function of distance from the bubble nucleus for different initial bubble radii (R_0 = 2.5, 5.0, 10, 100, 1000 and 10,000 nm).

5.5.0.5 Nucleus Size

Figures 5.20, 5.21 and 5.22 show the time history of the bubble radius, maximum radial compressive/tensile stress and maximum radial compressible (Hencky) strain experienced by Lagrangian particles starting different distances away from the bubble, for $R_0 = 2.5, 5.0, 10, 100, 1000$ and 10000 nm, holding other parameters at their values given in the *Baseline Case*. In terms of dimensionless parameters, varying the initial radius (nucleus size) modifies the Reynolds and Weber numbers, as well as the dimensionless frequency.

Increasing the initial nucleus size enhances bubble growth. As a result, larger maximum radii, minimum radii, and collapse times (from R_{max} to R_{min}) are achieved with increasing initial bubble radius. For smaller nuclei ($R_0 < 10$ nm), small increases in nuclei size can produce large increases in maximum bubble radius. When nuclei sizes are increased to 10 μm initial radius, the minimum bubble radius becomes sufficient to permit additional cycles of bubble growth and collapse. A more detailed consideration of bubble behavior at and following R_{min} is beyond the scope of the present study; however, experiments cannot rule out the possibility of additional bubble oscillations due to limitations in temporal resolution (Vlaisavljevich *et al.*, 2015a). Since the initial bubble radii vary, the initial distance from the radius starts from different locations on the graph. Except for the 2.5 nm case, which shows noticeably lower values, the maximum compressive/tensile stresses and the maximum compressive strain exhibit only a weak dependence on the initial radius. The stresses show different behavior close to the bubble wall for micron-sized initial radii. The higher tensile stresses are explained by the finding that elastic stress is no longer purely compressive and contributes a significant tensile component at collapse. The appearance of elastic tensile stress at larger initial nuclei sizes occurs because larger nuclei lead to smaller minimum radii. These observations can also be understood by considering the maximum values of each elastic term on the right side of Eq. 6.6: the first term is tensile while the second is compressive. Thus, for smaller initial nuclei, $R_{max}/R_0 > R_0/R_{min}$ and the dominant elastic contribution is compressive at maximum bubble radius, while for larger initial radii, $R_{max}/R_0 < R_0/R_{min}$ and the dominant elastic contribution is tensile at collapse. Although the relative contributions of compressive stress to total stress differs significantly in small vs. large nuclei sizes, the relationships between compressive elastic and compressive viscous stresses are similar to previous sections. Kinks indicating a transition from dominant elastic to dominant viscous compressive stress are again present in the maximum compressive stress plots and vary with maximum bubble radius; thus the smallest growth case (R_0 = 2.5 nm) has a kink located significantly closer to the bubble wall.

5.5.1 Elastic–to–Viscous Stress Transition

In each parameter variation study, the presence of “kinks” has been noted in certain compressive stress traces which indicate the distance of a Lagrangian particle from the bubble nucleus at which the viscous (rather than elastic) component becomes the dominant contribution to compressive stress. In other words, cells whose initial position is less than this distance experience elastic stress as an absolute maximum compressive stress, while cells whose initial position is greater than this distance experience viscous stress as the larger compressive stress. This elastic-to-viscous transition distance location, x_{EV}, could provide a means of identifying regions dominated by elastic vs. viscous effects in therapeutic ultrasound lesions – or strain magnitude vs. rate. The dependence of

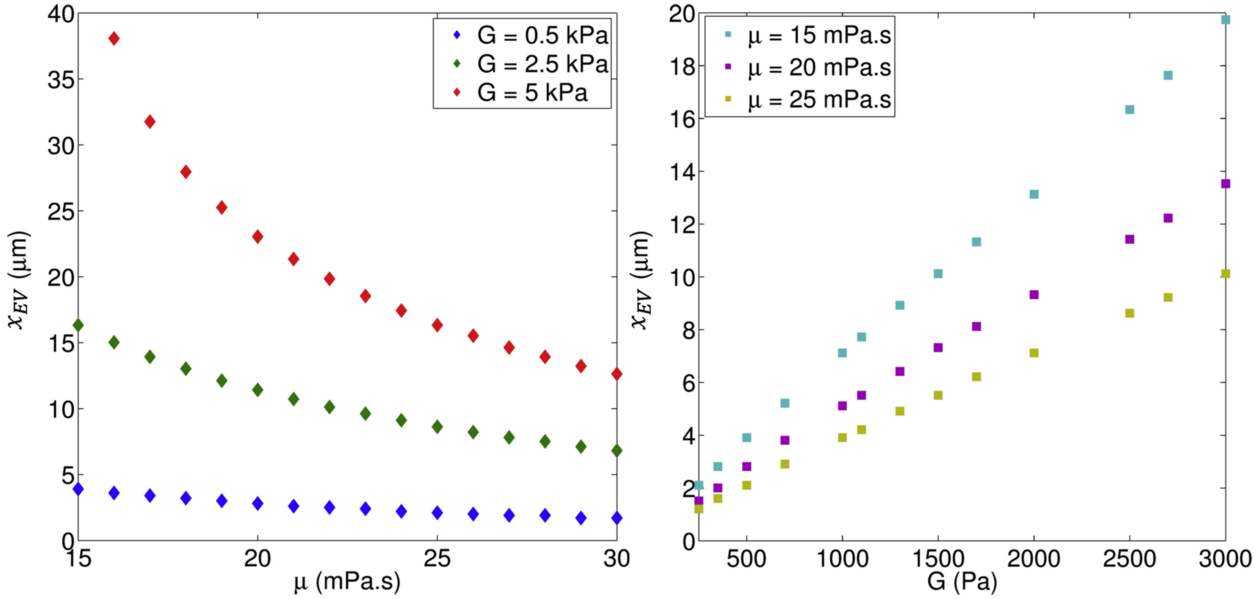

Figure 5.23: Elastic-to-viscous compressive stress transition distance x_{EV} as a function of viscosity for G = 0.5, 2.5 and 5 kPa (left) and of shear modulus for μ = 15, 20 and 25 mPas (right).

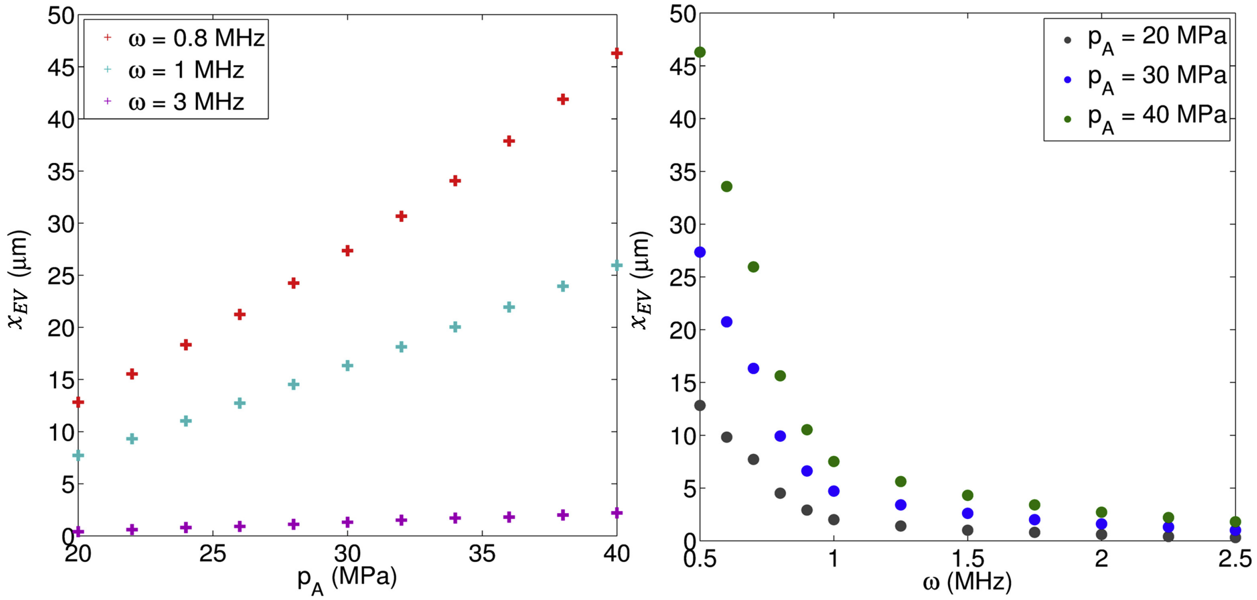

Figure 5.24: Elastic-to-viscous compressive stress transition distance xEV as a function of peak negative pressure for ω = 0.8, 1.0, and 3.0 MHz (left) and of waveform frequency for p_A = 20, 30 and 40 MPa (right).

Table 5.2: Mechanical damage mechanisms during a single cycle of bubble growth and collapse for nuclei sizes < 10 nm.

$R_1 = R_0$	$R_2 = R_{max}$	$R_3 = R_{min} < R_0$
• viscous effects dominate • maximum compressive stress (absolute maximum for $x > x_{EV}$) • maximum strain rate	• elastic effects dominate • maximum compressive stress (absolute maximum for $x < x_{EV}$) • maximum compressive strain (absolute)	• viscous effects dominate • maximum tensile stress • maximum tensile strain • maximum strain rate

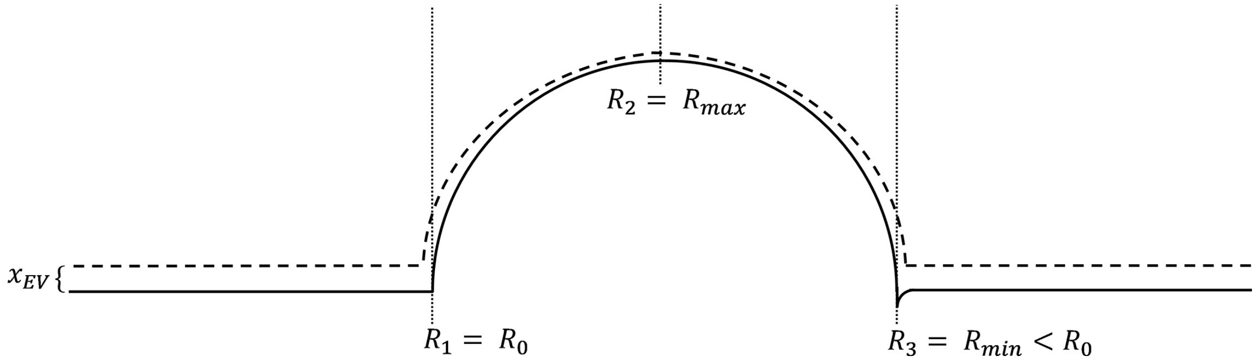

Figure 5.25: Schematic illustrating three likely time points for mechanical tissue damage during a single cycle of bubble growth and collapse. The dominant mechanisms acting at points R_1, R_2 and R_3 are given in Table 5.2.

x_{EV} on shear modulus and viscosity as well as on waveform peak negative pressure and frequency are shown in Figs. 23 and 24, respectively, where x_{EV} is determined by calculating the distance where the second spatial derivative of compressive stress becomes discontinuous. All parameters are varied about the baseline. The elastic-to-viscous transition distance strongly depends on μ and G, as it decreases with increasing viscosity but increases with increasing shear modulus; x_{EV} decreases with increasing frequency but increases (linearly) with increasing amplitude as expected based on the dependence of R_{max} on those properties.

5.6 Discussion

Experimental studies suggest that tissue properties play a key role in determining tissue susceptibility to cavitation generation and histotripsy-induced tissue damage (Vlaisavljevich *et al.*, 2013b). Our results highlight the importance of elasticity, viscosity, peak negative pressure, and waveform frequency to hypothesized mechanical tissue damage mechanisms. An improved understanding of cavitation damage mechanisms will help predict damage susceptibility of different tissues as well as differential damage responses within a focal region under different acoustic parameters. This knowledge can ultimately be used to guide safety considerations and enable treatment planning.

Figure 5.25 illustrates the relationships between the maxima in total stress, strain, and strain rate by highlighting three key points during a single cycle of bubble growth and collapse that correspond to relative or absolute maxima in these field quantities. First, a tensile histotripsy pulse drives the onset of explosive bubble growth when $R = R_0$. At this time, viscous effects predominate and both the strain rate and compressive stress achieve relative maxima. At distances greater than x_{EV} (the elastic-to-viscous transition point) this maximum in compressive viscous stress at the onset of bubble growth will also contribute the absolute maximum total compressive stress during the lifespan of the bubble. Next, bubble growth proceeds rapidly until viscous resistance and tissue stiffness limit growth to a maximum radius, $R = R_{max}$. Here, tissue elasticity has the dominant influence on bubble dynamics. Both the compressive stress and compressive strain are maximized, while the strain rate and viscous stress are negligible. At distances less than x_{EV}, this maximum in compressive elastic stress contributes the absolute maximum total compressive stress over the lifespan of the bubble. Finally, the bubble undergoes a violent collapse to a minimum radius $R_{min} < R_0$. At minimum radius, viscous effects again dominate, and tensile stress, tensile strain, and strain rate are all maximized. Tensile stress is purely viscous in origin and contributes the absolute maximum total stress when viscosity is sufficiently large.

These maxima in field quantities are also affected by waveform parameters that change the underlying bubble dynamics. Specifically, any change in waveform frequency or pressure amplitude that changes R_0, R_{max}, or R_{min} can also change the stresses and strains. First, increases in pressure amplitude permit greater bubble growth, increasing R_{max}. This will produce proportional increases in maximum compressive stress and strain as well as relatively smaller increases in tensile stress. In contrast, increases in frequency limit bubble growth and thus decrease the maximum compressive stress and strain. Waveform parameters can also affect x_{EV}. Increases in pressure amplitude and decreases in frequency result in smaller x_{EV} values, indicating that the elastic compressive stress at R_{max} is exceeded by viscous compressive stress at the onset of bubble growth closer to the bubble wall in these reduced growth cases. Additionally, tensile strains at bubble collapse far exceeded the ultimate fractional strains measured for soft tissue but were nearly instantaneous and more localized to the bubble wall than compressive strains. Further study is needed to clarify their relevance to strain-related tissue damage. More readily understood is the observation that maximum compressive strain occurs at maximum radius when the tissue is under greatest deformation and coincides with a maximum in compressive (purely elastic) stress, thus supporting the hypothesis that maximum radius is a relevant parameter for mechanical tissue damage.

5.6.1 Predicting the Elastic–to–Viscous Transition

Stress is hypothesized to play an important role in tissue damage produced by high-amplitude ultrasound therapies. In a study of tissue mechanical properties and susceptibility to perforation, undamaged tissues were observed to have higher ultimate tensile strength, thus suggesting that higher ultimate tensile stress was more predictive of tissue resistance to damage than high ultimate strain (Vlaisavljevich *et al.*, 2013b). These observations motivate further study of the relationship between stress and tissue damage; however, stress fields are difficult to measure under highly transient loading. A means of relating salient features of the stress field to more measurable parameters could improve understanding of stress-related damage mechanisms.

One potential means of characterizing stress fields is by the predominance of viscous vs. elastic stress characteristics. Fundamentally, the elastic stress depends on the tissue deformation (strain) and viscous stress is directly proportional to strain rate. Thus, the elastic-to-viscous stress transition distance, x_{EV}, introduces a spatial dependence on the relevance of strain vs. strain rates in observed tissue damage. Recent experimental studies suggest that strain and strain rate have different effects on cell injury (Bar-Kochba *et al.*, 2016): strain rate was found to affect injury morphology and the extent of cell death across a population while compressive strain determined the time to cell death. It is thus reasonable to expect that tissue regions dominated by either strain or strain rate effects will give rise to distinct patterns of injury. Prediction of x_{EV} could thus be used to predict the spatial extent of these distinct histopathologies – as long as the material models are sufficiently accurate. The monotonic results in Figs. 23 and 24 suggest that an analytical expression for x_{EV} may be achievable. One might expect that x_{EV}, properly scaled, should depend on the relative magnitude of elastic forces ($\sim G\delta^2$) to viscous forces ($\sim \mu v \delta$), where δ and v are characteristic lengths and velocities corresponding to the deformation magnitude and rate. The relevant length describing deformations is R_{max}, the point at which the tissue is under maximum deformation. The relevant velocity characterizing the growth is expected to depend on the pressure amplitude, e.g., $\sqrt{p_A/\rho_\infty}$. Thus, defining the dimensionless elastic to viscous forces ratio,

$$\xi = \frac{G R_{max}}{\mu \sqrt{p_A/\rho_\infty}}, \tag{5.10}$$

it is expected that the properly scaled transition location obeys the following relation:

$$\frac{x_{EV}}{R_{max}} = f(\xi), \tag{5.11}$$

where f is some function of ξ. To investigate this scaling, x_{EV}/R_{max} is plotted vs. ξ in Fig. 26 by including all of the data from Figs. 23 and 24.

The results are unambiguous: for the parameter range under consideration, all of the data collapse onto a single curve, thus verifying the validity of the scaling of Eq. (10). Moreover, for $\xi \in [0, 0.25]$, the relationship is linear, such that

$$\frac{x_{EV}}{R_{max}} = c\xi, \tag{5.12}$$

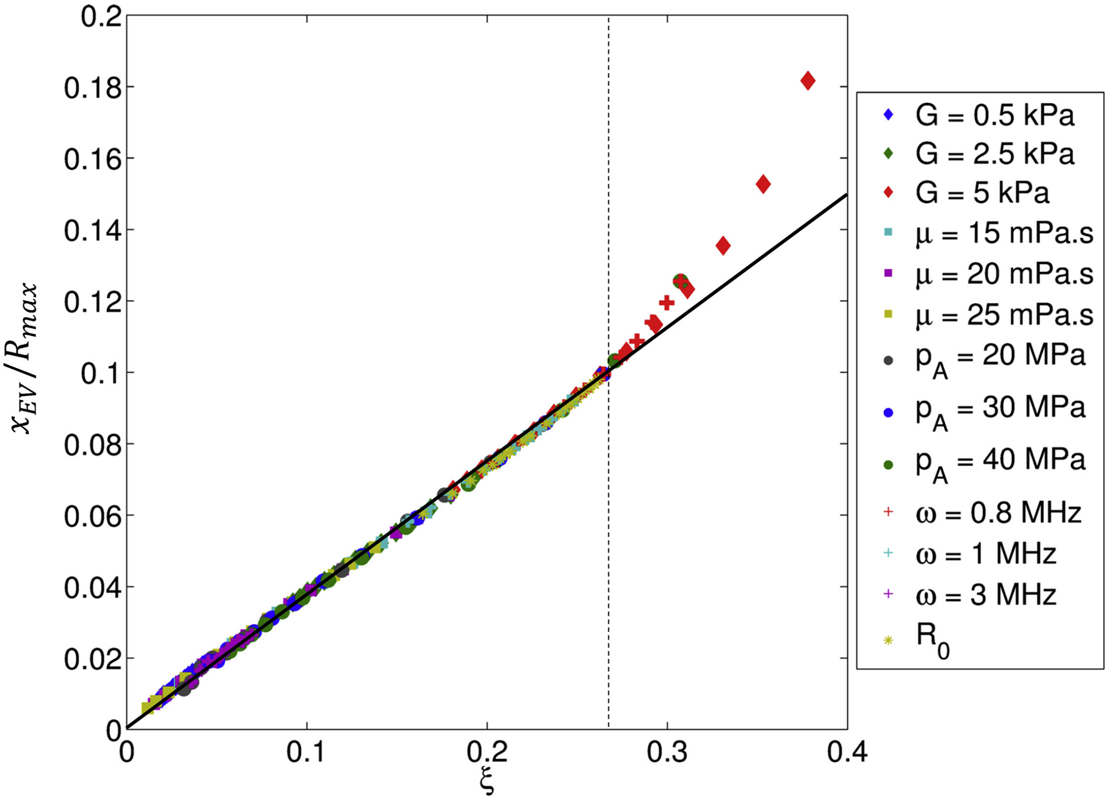

Figure 5.26: Scaled elastic–to–viscous compressive stress transition distance as a function of the dimensionless elastic–to–viscous forces ratio, ξ.

where $c \approx 0.4$ by data fit. Since ξ represents the ratio of elastic to viscous forces, the increase of x_{EV}/R_{max} with ξ is understandable: as the relative importance of elastic stresses increases compared to the viscous contribution (increasing ξ), e.g., due to increased shear modulus relative to viscosity, the region in which elastic effects dominate extends farther from the bubble wall. The linear dependence on ξ, and thus on R_{max}, in $[0, 0.25]$ indicates that the size of the region dominated by elastic stresses increases in a geometrically similar fashion.

For the larger shear modulus cases with low viscosity ($G = 5$ kPa and $\mu < 20$ mPa.s, red diamond in Fig. 5.26) as well as the lowest frequency ($\omega = 0.8$ MHz), the scaled transition location increases more rapidly with increasing ξ, such that x_{EV}/R_{max} no longer obeys a linear relationship; the data collapse is not as clear. These deviations reflect the predominance of elastic over viscous effects. For low frequency with equivalent viscoelastic parameters, the dominance of elasticity on overall dynamics occurs because bubble growth in these large deformation cases is limited more by tissue resistance to further deformation than by viscous dissipation. The authors recognize that for the scaling in Eq. 5.10 to be practically relevant, a corresponding scaling for R_{max} or perhaps R_{max}/R_0 is necessary, though it lies beyond the scope of the present study and has been investigated by others (Bader & Holland, 2016).

Conclusions

This work studied the effects of tissue properties (viscosity, shear modulus, nucleus size) and waveform parameters (peak negative pressure, frequency) on the bubble dynamics of a 5 nm nucleus subjected to a single negative histotripsy-relevant cycle. The resulting stress and strain fields in the surrounding medium, modeled via a Kelvin-Voigt viscoelastic constitutive relation with nonlinear elasticity, were examined in light of potential tissue injury. Overall, the largest radial stresses were experienced at the bubble wall and are due to different mechanisms: while the largest tensile stress was of viscous origin and occurs at collapse, two peaks in compressive stress occurred at initial growth (viscous) and maximum radius (elastic). The maximum stresses/strains depended on the tissue and waveform properties: in addition to affecting the stresses/strains via the bubble dynamics (as do the waveform properties and nucleus size), the viscosity and shear modulus also dictated the dependence on strain magnitude and rate. The stresses and strains decreased with depth into the tissue, though the viscous and elastic contributions decreased at different rates. Elastic stresses produced maximum compressive stress for cells initially near the bubble and viscous stresses dominated farther away. There was thus a critical initial distance from the nucleus beyond which the maximum compressive stress experienced by those cells is of viscous origin. Scaling analysis was used to show that a fundamental relationship exists between the scaled transition location and the dimensionless elastic to viscous forces ratio, which was linear for the majority of the parameter range. This result further indicated that the size of the region dominated by elastic stresses increases in a geometrically similar fashion. Thus, assuming that stresses/strains are the dominant mechanisms of cavitation-induced tissue damage, our results support the potential value of using maximum bubble radius as a metric for tissue damage, especially if this metric includes dependence on tissue viscosity, elasticity, and waveform parameters.

Given the fundamental nature of the present problem, our results can be generalized. However, they are limited to the material model under consideration. The chosen model accounts for important features of soft tissue mechanics (finite deformation, viscoelasticity), but the complex microstructure may require more sophisticated constitutive relations. Bubble-bubble interactions could also influence the damage mechanisms postulated in this study. Thermodynamics and transport phenomena in soft tissue are not well understood; mass transport inside (Barajas & Johnsen, 2017) and outside the bubble may affect bubble growth. Strategies to improve the fidelity of the models are underway and require experimental characterization of soft tissue.

CHAPTER 6

Modeling Tissue–Selective Cavitation Damage

This Chapter is adapted from Mancia *et al.* (2019).

6.1 Abstract

The destructive growth and collapse of cavitation bubbles are used for therapeutic purposes in focused ultrasound procedures and can contribute to tissue damage in traumatic injuries. Histotripsy is a focused ultrasound procedure that relies on controlled cavitation to homogenize soft tissue. Experimental studies of histotripsy cavitation have shown that the extent of ablation in different tissues depends on tissue mechanical properties and waveform parameters. Variable tissue susceptibility to the large stresses, strains, and strain rates developed by cavitation bubbles has been suggested as a basis for localized liver tumor treatments that spare large vessels and bile ducts. However, field quantities developed within microns of cavitation bubbles are too localized and transient to measure in experiments. Previous numerical studies have attempted to circumvent this challenge but made limited use of realistic tissue property data. In this study, numerical simulations are used to calculate stress, strain, and strain rate fields produced by bubble oscillation under histotripsy forcing in a variety of tissues with literature-sourced viscoelastic and acoustic properties. Strain field calculations are then used to predict a theoretical damage radius using tissue ultimate strain data. Simulation results support the hypothesis that differential tissue responses could be used to design tissue–selective treatments. Results agree with studies correlating tissue

ultimate fractional strain with resistance to histotripsy ablation and are also consistent with experiments demonstrating smaller lesion size under exposure to higher frequency waveforms. Methods presented in this study provide an approach for modeling tissue–selective cavitation damage in general.

6.2 Introduction

Cavitation occurs when a sufficient pressure rarefaction causes microscopic nuclei in a fluid or solid to rapidly grow into macroscopic bubbles (Brennen, 2014). These bubbles can mechanically damage surrounding material by inducing large stresses, strains, and strain rates in their surroundings as they grow and collapse. Cavitation has been studied extensively for hydrodynamic applications and is known to erode even the hardest steels (Richman *et al.*, 1995). Recently, interest has grown in cavitation damage to biological materials including tissue (Mancia *et al.*, 2017; Pahk *et al.*, 2019) and surgical mesh (Bigelow *et al.*, 2019) given its relevance to therapeutic ultrasound and traumatic injuries. Cavitation is a potential source of neuron damage in blast traumatic brain injury (Goeller *et al.*, 2012; Estrada *et al.*, 2017; Franck, 2017), and it has also been proposed as a useful context in which to study tissue damage incurred through high–strain–rate injuries (Estrada *et al.*, 2018). Laser surgery (Brujan & Vogel, 2006) and therapeutic ultrasound (Brujan, 2004) also motivate studies of controlled cavitation damage. In particular, cavitation contributes to kidney stone fractionation in shock wave lithotripsy (Coleman *et al.*, 1987), and histotripsy is a noninvasive, nonthermal focused ultrasound procedure that uses targeted groups of microscopic bubbles to homogenize soft tissue into acellular debris. Histotripsy has been investigated as a potential treatment for benign prostate hyperplasia, thrombolysis, and solid tumors (Khokhlova *et al.*, 2015).

Cavitation damage mechanisms are challenging to study because stresses and strains developed in surrounding tissue by individual cavitation bubbles are too localized and transient to measure experimentally (Mancia *et al.*, 2017; Vlaisavljevich *et al.*, 2016c). The opacity of tissues also limits optical access. Computational modeling can circumvent these experimental limitations and quantify stress, strain, and strain rate fields in tissue. Previous studies have modeled deformations produced by single cavitation bubbles in viscoelastic materials under harmonic (Church & Yang, 2006) and High Intensity Focused Ultrasound (HIFU) (Pahk *et al.*, 2019) forcing. Although HIFU can still involve cavitation as a secondary damage mechanism (Rabkin *et al.*, 2005), it is a predominantly thermal therapy. Histotripsy ablation is more dependent on the mechanical effects of inertial cavitation, which occurs when applied tension causes nanoscale nuclei to grow into cavities that subsequently collapse under the inertia of the surrounding medium (Miller *et al.*, 1996). Bubble growth subjects tissue to high strain rates and induces large compressive radial stress and strain components in the tissue that are maximized at maximum bubble radius. Bubble collapse is also a high–strain–rate phenomenon and generates large tensile radial stress and strain components in the tissue (Mancia *et al.*, 2017). These damage mechanisms are common to cavitation injury in other settings (Estrada *et al.*, 2018), making histotripsy a useful model for studying cavitation–induced tissue damage in general. Previous work has considered stresses and strains induced by bubbles under histotripsy forcing (Mancia *et al.*, 2017; Vlaisavljevich *et al.*, 2016c). These studies calculated the spatiotemporal evolution of stress and strain fields around a single cavitation bubble in a general viscoelastic medium exposed to different forcing conditions. However, consideration of more specific and relevant tissue types is needed to fully explain observations of tissue–selective cavitation damage. Furthermore, recent observations suggest that strain rate plays a unique role in cell injury (Bar-Kochba *et al.*, 2016) and thus deserves a more detailed investigation. Prior modeling work has used maximum bubble radius as a cavitation damage metric for histotripsy (Bader & Holland, 2016), but correlations between damage extent and physical damage mechanisms have been limited.

Experimental studies of histotripsy applied to different tissues suggest that differential tissue responses to cavitation can be used to design treatments that are self–limiting and vessel–sparing, preventing damage to critical anatomical structures (Vlaisavljevich *et al.*, 2013a). Figure 6.1 shows MRI images and histopathology slides illustrating the preservation of bile ducts and hepatic arteries in treated porcine liver. It was hypothesized that differences in tissue mechanical properties were

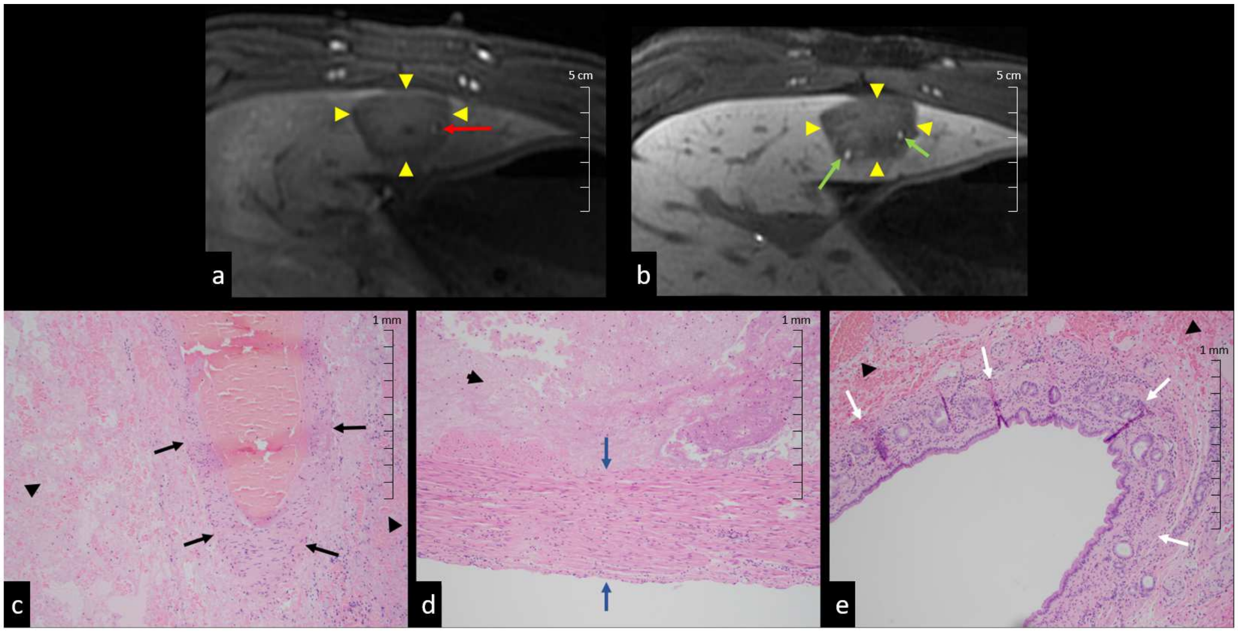

Figure 6.1: Histotripsy liver lesions with preserved vessels (a,c,d) and bile ducts (b,e). Results show (a) arterial phase MR image of patent artery (red arrow) in ablation zone (arrow heads), (b) liver-specific contrast MR image with patent bile ducts (green arrows) in ablation zone (arrow heads). H&E slides of (c) portal vein (black arrows), (d) intact artery wall (blue arrows), and (e) bile ducts (white arrows) with adjacent necrosis (arrow heads) in ablation zone.

responsible for these effects, and examination of gross lesions revealed that tissues with higher ultimate stress and ultimate fractional strain were more resistant to histotripsy-generated cavitation. These findings suggest that mechanical stress and strain in particular could play important roles in cavitation damage. There is also evidence that lesion size correlates with waveform amplitude (Lin *et al.*, 2014) and that higher frequency histotripsy waveforms produce smaller lesions (Lin *et al.*, 2014b). The objective of this study is therefore to model bubble behavior and proposed damage mechanisms in different tissue types in order to provide an understanding of observed tissue–selective cavitation effects. Tissues in this study are most relevant to a liver tumor ablation application given recent experimental interest (Smolock *et al.*, 2018; Vlaisavljevich *et al.*, 2016b) and the variety of tissues involved. The methods presented in this study could potentially be applied to estimate cavitation–induced tissue damage for treatment planning and injury diagnostics.

This study uses a spherical bubble dynamics model with viscoelasticity to quantify mechanical stress, strain, and strain rates produced by single cavitation bubbles exposed to histotripsy forcing at different frequencies in specific tissues whose viscoelastic and acoustic properties are obtained from the literature. First, the theoretical model for bubble dynamics in viscoelastic media which has been applied to experiments in polyacrylamide gels (Estrada *et al.*, 2018) is presented. Subsequently, a literature review is provided summarizing data from viscoelastic and acoustic parameter measurements for our tissues of interest. We then discuss the problem setup and numerical methods used to perform the simulations. Equations for mechanical stress, strain, and strain rate fields in tissue are provided. Results are presented showing radial dynamics and field quantities for each tissue at three relevant waveform frequencies (0.5 MHz, 1 MHz, and 3 MHz). Calculated strain fields are then compared to ultimate fractional (tensile) strain measurements to estimate damage radii in tissues of interest.

6.3 Methods

6.3.1 Theoretical Model

Simulations model a single, spherical, homobaric bubble in a homogenous viscoelastic medium exposed to a histotripsy waveform. Previous computational studies of histotripsy cavitation have used a similar model to study bubble dynamics in water (Vlaisavljevich *et al.*, 2016a) and agarose tissue phantoms (Vlaisavljevich *et al.*, 2014, 2015b, 2016c; Mancia *et al.*, 2017). Table 6.1 lists viscoelastic and acoustic properties of each model tissue, and Table 6.2 gives the constant initial conditions and thermodynamic properties used in all simulations. Radial bubble dynamics are described by the Keller-Miksis equation (Keller & Miksis, 1980):

$$\left(1-\frac{\dot{R}}{c_\infty}\right)R\ddot{R}+\frac{3}{2}\left(1-\frac{\dot{R}}{3c_\infty}\right)\dot{R}^2=\frac{1}{\rho_\infty}\left(1+\frac{\dot{R}}{c_\infty}+\frac{R}{c_\infty}\frac{d}{dt}\right)\left[p_B-\left(p_\infty+p_f(t)\right)-\frac{2S}{R}+J\right], \tag{6.1}$$

where R is the bubble radius, and c_∞ and ρ_∞ are the constant sound speed and density of each tissue (Table 6.1). The pressure of air inside the bubble is p_B, and pressure in the surrounding tissue is the sum of the ambient pressure, p_∞, and the acoustic forcing pressure, $p_f(t)$. The variables S and J are the tissue surface tension and integral of the deviatoric stresses, respectively. Although the chosen Keller-Miksis model risks under–predicting the minimum bubble radius and maximum wall velocity at bubble collapse (Prosperetti & Lezzi, 1986), precise dynamics at bubble collapse are beyond the scope of the present study. Histotripsy bubbles undergo more complex behavior at collapse, including breakup into smaller bubbles (Duryea *et al.*, 2015), so this work primarily concerns bubble dynamics until the point of collapse. Due to a lack of surface tension data for various tissues, surface tension is assumed equal to that of water at 25°C for all simulations: $S = 0.072$ N/m. This is a reasonable assumption given the high water content of tissues considered in this study, and the limited effect surface tension is expected to have on the bubble dynamics.

Tissue is modeled using a finite deformation Kelvin–Voigt constitutive equation (Gaudron *et al.*, 2015), resulting in the following integral of the deviatoric contribution of the stresses in the surrounding medium:

$$J = -\frac{4\mu\dot{R}}{R} - \frac{G}{2}\left[5 - 4\left(\frac{R_0}{R}\right) - \left(\frac{R_0}{R}\right)^4\right], \tag{6.2}$$

where R_0, the bubble radius in stress-free surroundings, is equal to the initial bubble radius. As in a previous studies (Vlaisavljevich *et al.*, 2014, 2015b, 2016c,a; Mancia *et al.*, 2017), all simulations are initialized with $R_0 = 5$ nm. This assumption is in accordance with previous experimental studies that inferred nuclei sizes in the range of nanometers (Maxwell *et al.*, 2013); however, it can have significant consequences for subsequent field calculations and is discussed further in Section 4.2. All simulations also use a fixed tissue viscosity, $\mu = 0.01$ Pa.s, given the lack of tissue viscosity data at relevant frequencies and the dependence of viscosity measurements on the assumed viscoelastic constitutive equation. This viscosity value for liver has also been used previously in cavitation modeling (Webb *et al.*, 2011) and was justified by expected shear–thinning behavior of tissue. Tissue shear modulus, G is selected for each tissue (Table 6.1) according to reference values from the literature. Tissue acoustic parameters are also literature–sourced and are discussed further in

Section 2.2.

Changes in internal bubble temperature are considered following the approaches described in (Prosperetti *et al.*, 1988; Kamath *et al.*, 1993; Warnez & Johnsen, 2015). Previous authors (Estrada *et al.*, 2018; Barajas & Johnsen, 2017) have also considered mass transfer effects, but in this study the tissue–bubble boundary is assumed to be impervious to gas, and vapor inside the bubble is neglected. Although these simplifications could underpredict the lifespan of the bubble and distort subsequent rebounds (Bader, 2018a), such effects are likely negligible in the single collapse case considered here. The mass boundary layer thickness is also expected to be small relative to the bubble radius during expansion, so mass transfer effects can be safely neglected during bubble growth (Barajas & Johnsen, 2017; Mancia *et al.*, 2017).

The energy equation for air inside the bubble is coupled to the Keller–Miksis equation (Eq. 6.1) by the internal bubble pressure, p_B:

$$\dot{p}_B = \frac{3}{R}\left((\kappa - 1)K\frac{\partial T}{\partial r}\bigg|_R - \kappa p_B \dot{R}\right) \tag{6.3}$$

$$\frac{\kappa}{\kappa - 1}\frac{p_B}{T}\left[\frac{\partial T}{\partial t} + \frac{1}{\kappa p_B}\left((\kappa - 1)K\frac{\partial T}{\partial r} - \frac{r\dot{p}_B}{3}\right)\frac{\partial T}{\partial r}\right] = \dot{p}_B + \frac{1}{r^2}\frac{\partial}{\partial r}\left(r^2 K\frac{\partial T}{\partial r}\right), \tag{6.4}$$

where $T(r,t)$ is the temperature field of air inside the bubble, which has a ratio of specific heats κ, and its thermal conductivity is given by $K = K_A T + K_B$, where constants K_A and K_B were determined empirically for air (Prosperetti *et al.*, 1988). The initial pressure inside the bubble is $p_B(0) = p_\infty + 2S/R$. A boundary condition is prescribed for the center of the bubble: $\nabla T = 0$ at $r = 0$. Following (Prosperetti, 1991; Estrada *et al.*, 2018), the bubble wall boundary condition is simplified to $T(R) = T_\infty$ under the assumption that the surrounding tissue remains at its constant ambient temperature through this single cycle of growth and collapse.

The far-field pressure equals the sum of the ambient pressure in surrounding tissue, p_∞, and

Table 6.1: Tissue viscoelastic and acoustic properties, taken from the literature

Tissue	Shear Modulus (kPa)	Density (kg/m^3)	Sound Speed (m/s)	UTS (MPa)	Ultimate True Strain
Liver	1.8 ± 0.4	1060	1577 ± 11	0.27	0.38
HCC	23.4	1060	1555 ± 15	-	-
Diseased Liver	19.8	1060	1559 ± 4	-	-
Hepatic Artery	210 ± 47	1050	1616 ± 25	1.4	0.63
Gallbladder	85 ± 8.2	1060	1584	2.5	0.43 ± 0.3
Bile Duct	166 ± 67	1060	1600	-	-
Stomach	0.637	1058	1619.4 ± 21	0.43	0.66

Tissue viscosity is assumed to be 0.01 Pa-s, and all viscoelastic properties were measured under quasistatic conditions for all tissues. Additional assumptions discussed in Sect. 2.2. References: General ((Duck, 2013)); Liver, HCC, and Diseased Liver ((Webb *et al.*, 2011);(Palmeri *et al.*, 2008);(Bamber & Hill, 1981);(Honjo *et al.*, 2014)); Hepatic Artery ((Deng *et al.*, 1994);(Holzapfel *et al.*, 2005)); Gallbladder ((Karimi *et al.*, 2017)); Bile Duct ((Duch *et al.*, 2004)); Stomach ((Lim *et al.*, 2009);(Saijo *et al.*, 1991)).

the time-varying histotripsy pulse, $p_f(t)$:

$$p_f(t) = \begin{cases} p_A \left(\frac{1+\cos[\omega(t-\delta)]}{2}\right)^n, & |t-\delta| \leq \frac{\pi}{\omega}, \\ 0, & |t-\delta| > \frac{\pi}{\omega}. \end{cases} \tag{6.5}$$

The “frequency,” f of this half-cycle pulse ($\omega = 2\pi f$) is varied between 0.5 – 3 MHz. In particular, the frequencies 0.5, 1, and 3 MHz have been chosen to encompass the frequency range in use for the widest variety of potential clinical applications (Vlaisavljevich *et al.*, 2015b,d; Lin *et al.*, 2014b). The peak tensile pressure, $p_A = -30$ MPa, time delay, $\delta = 5$ μs, and fitting parameter, $n = 3.7$, are chosen to be representative of an experimental histotripsy pulse (Vlaisavljevich *et al.*, 2014, 2015b, 2016c,a; Mancia *et al.*, 2017) and are constant for all simulations (Table 6.2). Figure 2 shows the 1 MHz analytic waveform (black dotted trace) over a representative experimental waveform of the same frequency (solid blue trace). Although the analytic waveform is a simplification, its use is supported by previous work showing that bubbles produced via intrinsic threshold histotripsy are generated directly from the negative pressure of the incident waveform and are not dependent on the positive portion of the waveform (Lin *et al.*, 2014; Maxwell *et al.*, 2013).

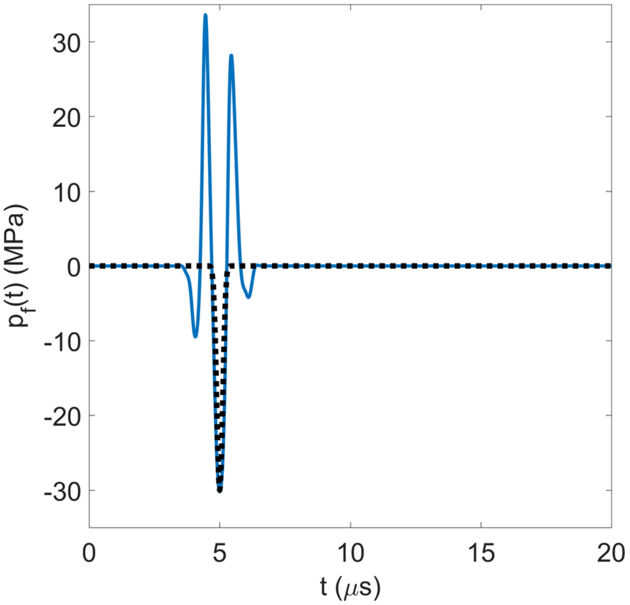

Figure 6.2: Analytic waveform (black dotted trace) over a representative experimental waveform (solid blue trace); both have a frequency of 1 MHz.

6.3.2 Viscoelastic and Acoustic Parameters

Viscoelastic and acoustic properties representative of healthy liver, hepatocellular carcinoma (HCC), diseased liver, hepatic artery, gallbladder, bile duct and stomach are given in Table 6.1. In the table, 'HCC' refers to samples that consist entirely of tumor while 'Diseased Liver' includes only liver tissue adjacent to tumors. Given the lack of tissue viscosity data in the MHz frequency range, viscosity is taken to be 0.01 Pa-s for all tissues. This value is near Webb et al's estimate for liver at 1 MHz (Webb *et al.*, 2011) and accounts for expected shear–thinning behavior of soft tissues at this frequency (Madsen *et al.*, 1983; Yang & Church, 2006). All viscoelastic properties were measured under quasistatic conditions.

The shear modulus of healthy liver is taken to be 1.8 kPa, corresponding to a mean *in vivo* measurement of a healthy human volunteer based on acoustic radiation force (Palmeri *et al.*, 2008). Shear moduli for HCC and diseased liver are taken to be the mean of their respective shear wave elastography measurements made in liver tumor patients with chronic liver disease due to NASH (1 sample), alcohol (4 samples), and HBV (2 samples) (Honjo *et al.*, 2014). Hepatic artery shear modulus is the lower bound of the right coronary artery shear modulus measured by (Deng *et al.*, 1994) given the similar luminal diameters of hepatic and coronary arteries (Silveira *et al.*, 2009; Holzapfel *et al.*, 2005). Assuming all tissues are incompressible (Poisson's ratio, $\nu = 0.5$), the shear moduli of gallbladder, bile duct, and stomach are taken to be 1/3 the value of their measured Young's moduli. A gallbladder shear modulus of 85 ± 8.2 kPa is used, which was measured in the transverse direction (Karimi *et al.*, 2017). A bile duct shear modulus of approximately 166 ± 67 kPa is obtained from the average of 10 porcine bile ducts measured under circumferential (cross-sectional) strain (Duch *et al.*, 2004). The mean shear modulus of stomach obtained from measurements under different indentation depths is estimated to be 0.637 kPa (Lim *et al.*, 2009).

The density of liver and stomach tissues were found in (Duck, 2013). The density of hepatic artery is taken to be the lower bound of a mixed sample of arteries from the same reference. Tissue density data was not available for gallbladder, bile duct, diseased liver, and HCC, so these were taken to have the same density as liver ($1060\,\mathrm{kg/m^3}$). The sound speed in liver, HCC, and diseased liver are taken to be the mean values given for 15 healthy liver specimens, 7 liver tumor samples, and 4 liver specimens with tumor present (Bamber & Hill, 1981). Sound speed in hepatic artery is assumed equal to the mean of whole healthy artery (including intima, media, and adventitia) given in (Duck, 2013) and used as a reference value in studies of diseased arteries (Hoskins, 2007). No sound speed data was available for bile duct, so simulations use a velocity that is intermediate between that of hepatic artery and gallbaldder: 1600 m/s. Sound speed of stomach was taken to be the value measured for "normal mucosa" (Saijo *et al.*, 1991).

Ultimate tensile strength (UTS) is defined as the tensile stress needed to produce rupture of a gross tissue sample. The UTS values for human liver, gallbladder, and stomach are given in (Duck, 2013). A specific UTS for hepatic artery was not found in the literature, so the mean UTS for a mixed sample of arteries subjected to tension in the transverse (cross-sectional) orientation is used: 1.4 MPa. This value is close to the UTS of coronary artery adventitia given by (Holzapfel *et al.*, 2005): 1.43 MPa. Ultimate (tensile) strain values for liver, a mixed sample of arteries, gallbladder, and stomach were obtained from (Yamada *et al.*, 1970). These values were measured with respect

Table 6.2: Parameters fixed for all simulations

Parameter	Value
R_0	5 nm
p_A	30 MPa
n	3.7
δ	5 seconds
p_∞	101.325 kPa
T_∞	25 °C
κ	1.4
K_A	5.28×10^{-5} W/mK^2
K_B	1.165×10^{-2} W/mK

to the original length of the specimens and are thus engineering strains. Before inclusion in Table 6.1, these engineering strains, e, are converted to equivalent true strains, ϵ, using the expression: $\epsilon = \ln(1 + e)$.

6.3.3 Problem Setup

The equations are nondimensionalized (Barajas & Johnsen, 2017) using the initial bubble radius, R_0, atmospheric pressure, p_∞, tissue density, ρ_∞, and far-field temperature, T_∞ to define a characteristic velocity, $U_c = \sqrt{p_\infty/\rho_\infty}$ and dimensionless parameters: Reynolds number, Re $= \rho_\infty U_c R_0/\mu$, Cauchy number, Ca $= p_\infty/G$, Weber number, We $= p_\infty R_0/2S$, dimensionless sound speed, $C = c_\infty/U_c$, and $\chi = T_\infty K(T_\infty)/p_\infty R_0 U_c$. A variable–step, variable–order solver based on numerical differentiation formulas (MATLAB *ode15s*) is used for numerical time marching (Shampine & Reichelt, 1997; Shampine *et al.*, 1999). Equations are integrated over a dimensional time span of $t = [0, 100]$ in microseconds. The maximum step size is 1.0 μs. Using numerical methods described by (Barajas & Johnsen, 2017; Estrada *et al.*, 2018), the PDE is spatially discretized on a mesh of $N_s + 1$ points in r-space (Prosperetti *et al.*, 1988) inside the bubble and solved via second-order central differences. Simulations use $N_s = 30$ points inside the bubble, for which results are sufficiently converged. Each stress and strain trace contains 10,000 points.

6.3.4 Stress and Strain Fields

A Kelvin–Voigt–based Neo–Hookean constitutive model relates the deviatoric stress, $\boldsymbol{\tau}$, and strain, $\mathbf{E}$, tensors in the surrounding tissue whose coordinates span $r \in [R, L]$, where R is the time-dependent bubble radius and $L \gg R$ is the arbitrary size of the domain. The radial and hoop stresses at any field coordinate r in the surroundings are given by,

$$\tau_{rr} = -4\mu \frac{R^2 \dot{R}}{r^3} + \frac{2G}{3}\left[\left(\frac{r_0}{r}\right)^4 - \left(\frac{r}{r_0}\right)^2\right] = -2\tau_{\theta\theta}, \tag{6.6}$$

which is derived from finite deformation theory (Gaudron *et al.*, 2015). In Equation (6.6), the original and current radial coordinates are related by:

$$r_0(r,t) = \sqrt[3]{r^3 - R^3 + R_0^3}. \tag{6.7}$$

This model has been used to represent the significant nanometer–to–micron–scale growth that occurs in histotripsy (Mancia *et al.*, 2017) and was applied to laser-induced cavitation experiments in polyacrylamide gels (Estrada *et al.*, 2018). Applicability of the Neo–Hookean model can be challenged given these extremely large deformations; however, it remains superior to commonly used models assuming infinitesimal deformations. Furthermore, results obtained with a Neo-Hookean constitutive model for single, attached murine myoblasts achieved excellent agreement with measured force–deformation curves (Peeters *et al.*, 2005). The cells in that study were also modeled as homogeneous and isotropic incompressible elastic solids.

Strain fields in the surrounding tissue are computed using the Hencky (or true) strain definition used previously in models of histotripsy (Mancia *et al.*, 2017) and laser–induced (Estrada *et al.*, 2017) cavitation:

$$E_{rr} = -2\ln\left(\frac{r}{r_0}\right) = -2E_{\theta\theta}. \tag{6.8}$$

It is expected that tissue will behave differently under tension and compression; however, the distinct damage consequences of either mode of deformation require further experimental study. For example, despite observations of tensile stress wave emission at optical breakdown in laser cavitation and the known greater susceptibility of cells to damage under tension vs. compression (Brujan & Vogel, 2006), experiments to date have been unable to separate the damage effects due to an emitted stress wave from those due to bubble expansion (Cherian & Rau, 2008). Given these uncertainties and our present interest in general tissue failure, radial and hoop stresses and strains are converted into their von Mises equivalent invariants as in (Estrada, 2017; von Mises, 1913):

$$\bar{\tau} = \sqrt{\frac{3}{2}\tau_{ij}\tau_{ij}} = \sqrt{\frac{3}{2}\left[\tau_{rr}^2 + 2\left(-\frac{1}{2}\tau_{rr}\right)^2\right]} = \frac{3}{2}|\tau_{rr}|, \tag{6.9}$$

$$\bar{E} = \sqrt{\frac{2}{3}E_{ij}E_{ij}} = \sqrt{\frac{2}{3}\left[E_{rr}^2 + 2\left(-\frac{1}{2}E_{rr}\right)^2\right]} = |E_{rr}| \tag{6.10}$$

6.4 Results

6.4.1 Radial Dynamics

Radial dynamics for each tissue are modeled at waveform frequencies of 0.5 MHz, 1 MHz, and 3 MHz as shown in Figure 6.3. The bubbles grow and collapse with no visible rebounds, as expected from experiments in tissue–mimicking gels (Wilson *et al.*, 2019). Bubble growth is restricted in tissues with the highest shear moduli. In particular, the smallest maximum radius is achieved in stiff hepatic artery and the largest maximum radii occur in liver and stomach. There is also notable similarity in the radius vs. time behavior for tissues that have similar shear moduli such as diseased liver and HCC tumor. Bubble growth in all tissues is responsive to waveform frequency with smaller bubble growth observed in all tissues exposed to higher frequency waveforms.

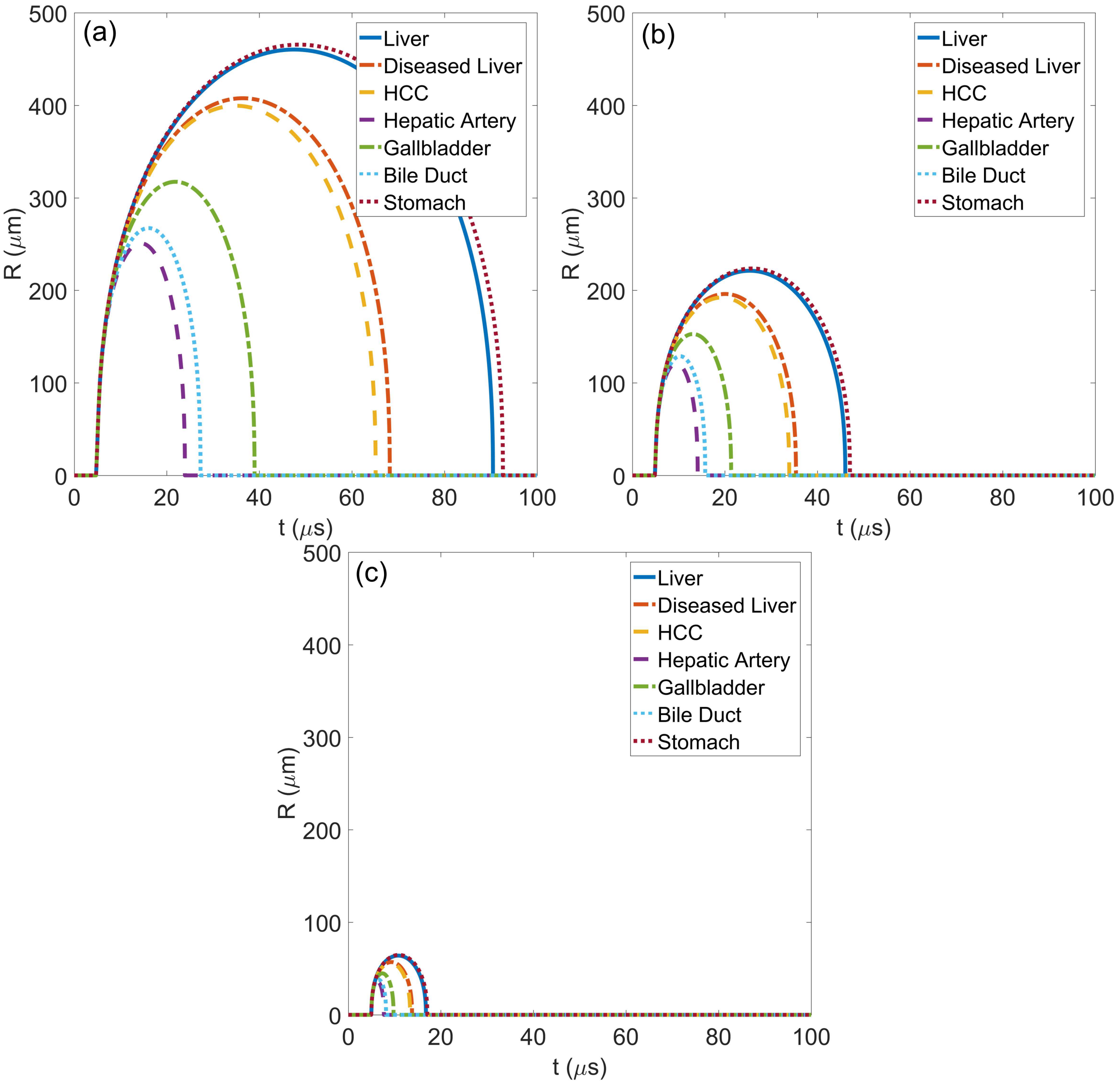

Figure 6.3: Simulated radius as a function of time traces for (a) 0.5 MHz, (b) 1 MHz, and (c) 3 MHz waveforms in tissues with properties given in Table 1.

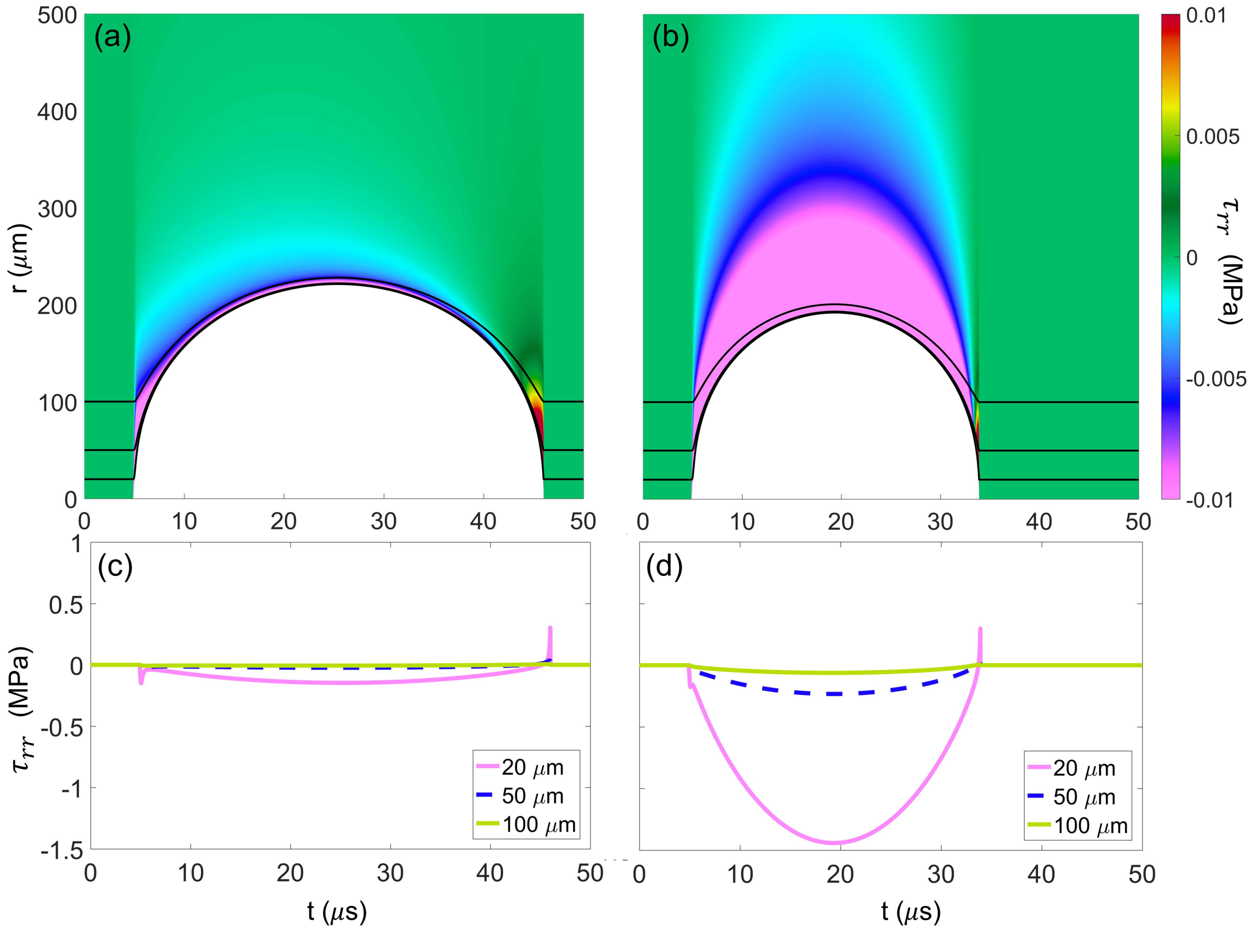

Figure 6.4: Total deviatoric radial stress fields developed in liver (a) and HCC (b) exposed to 1 MHz waveform. White region corresponds to tissue deformation with respect to distance from the bubble nucleus as a function of time. Black lines correspond to Lagrangian paths taken by particles starting 20, 50, and 100 μm from the bubble nucleus. Plots (c) and (d) show the numerical magnitudes of total stress along the Lagrangian paths shown in (a) and (b), respectively.

6.4.2 Stress Fields

Stress fields are calculated using Equations (6.6) and (6.9) with the constant parameters given in Tables 6.1 and 6.2. To determine the loads experienced by cells in the vicinity of the bubble, stresses with respect to starting distance from the bubble center are determined by following a (Lagrangian) particle starting at some initial distance from the bubble nucleus in the undeformed tissue. The particle then moves with the tissue as the tissue is deformed by the bubble. Stresses experienced by the particle can be calculated for different starting distances, r_0, from the center of

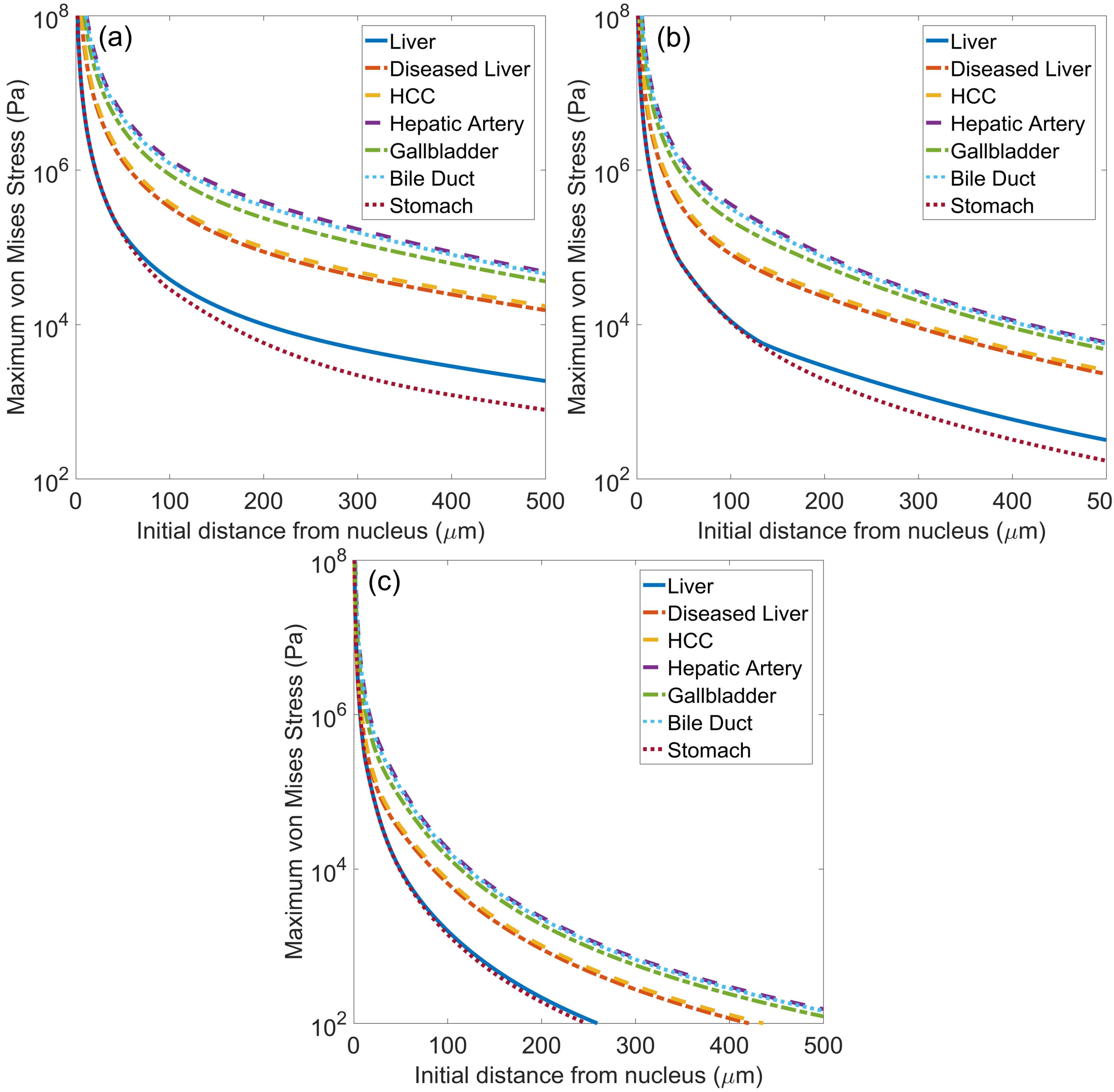

Figure 6.5: Maximum von Mises stress surrounding bubble as a function of initial distance from the bubble nucleus for different tissues exposed to (a) 0.5 MHz, (b) 1 MHz, and (c) 3 MHz waveforms.

the nucleus, starting at the nucleus wall ($r_0 = R_0$).

Figure 6.4 shows the total deviatoric radial stress (Equation 6.6) developed in (a) liver and (b) HCC tumor exposed to a 1 MHz waveform as each tissue is deformed by a bubble (shown in white). Black lines correspond to Lagrangian paths for particles starting at 20, 50, and 100 μm from the bubble nucleus. Total stress is quantified along each Lagrangian trajectory as a function of time below each respective tissue in (c) and (d), showing larger stress magnitudes in the higher shear modulus tissue (HCC) at all starting distances. Radial stresses are seen to be predominantly compressive (negative) during bubble growth and early collapse with a brief, localized maximum in tensile (positive) stress when the bubble reaches its minimum radius.

Figure 6.5 shows traces of maximum von Mises stress (Equation 6.9) in each tissue as a function of initial distance from the bubble nucleus (r_0) under waveform frequencies of (a) 0.5, (b) 1, and (c) 3 MHz. The ultimate tensile strength (UTS) values of liver, stomach, hepatic artery, and gallbladder are given in Table 6.1. Under all forcing conditions, stresses in these tissues attenuate below the UTS within 100 microns from the bubble wall. Distances before attenuation below UTS are greatest for hepatic artery and gallbladder while attenuation below UTS occurs closest to the bubble wall for liver and stomach.

Stress is higher at all distances from the bubble in tissues with higher shear moduli such as hepatic artery and bile duct. In tissues with lower shear moduli (e.g. stomach and liver), stresses are consistently smaller. Additionally, stress traces for these low shear moduli cases exhibit an abrupt change in slope or discontinuous second derivative that is most prominent in Figure 6.5 (b). These points correspond to the distance at which the viscous stress component in Equation (6.6) first exceeds the elastic component. This ‘elastic-to-viscous’ transition point is dependent on the relative magnitudes of viscosity and shear modulus. It can be predicted for a range of tissue and waveform parameters (Mancia *et al.*, 2017). A transition from dynamics dominated by tissue elasticity to more prominent viscous effects farther from the bubble has also been noted to occur in laser cavitation (Estrada *et al.*, 2018). Stresses attenuate more rapidly in the high forcing frequency cases, reflecting the significantly smaller bubble growth in these cases.

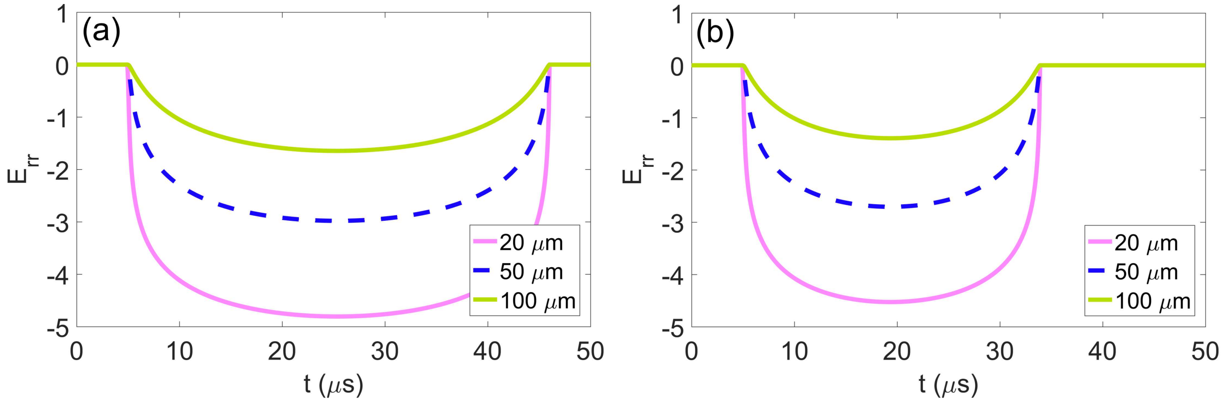

Figure 6.6: Total radial strain along the Lagrangian paths starting 20, 50, and 100 μm from the bubble nucleus in (a) liver and (b) HCC exposed to a 1 MHz waveform.

6.4.3 Strain Fields

Strain fields are calculated using Equations (6.8) and (6.10). As with stresses, strains are determined with respect to starting distance from the bubble nucleus in the undeformed tissue using a Lagrangian framework. Figure 6.6 quantifies total radial strain along Lagrangian trajectories starting 20, 50, and 100 μm from the nucleus as a function of time for (a) liver and (b) HCC. Radial strains are compressive and maximized at maximum bubble radius at all distances. Maximum von Mises strain as a function of initial distance from the bubble nucleus is shown in Figure 6.7 for each tissue under waveform frequencies of (a) 0.5, (b) 1, and (c) 3 MHz. Vertical lines correspond to the distance at which the strain first attenuates below the ultimate fractional (tensile) strain of liver, stomach, hepatic artery, and gallbladder (ultimate strain values are given in Table 6.1). At each forcing frequency, distances for which strain is larger than its ultimate value are greatest for liver and stomach while attenuation below ultimate strain occurs closest to the bubble for hepatic artery and gallbladder. A comparison of the distance to attenuation below ultimate strain and the maximum bubble radius achieved in each case is presented in Table 6.3. Von Mises strain is highest at all starting distances in low shear moduli tissues such as liver and stomach. In contrast, tissues with higher shear moduli such as hepatic artery and bile duct experience smaller deformations. Strains also attenuate more rapidly in all tissues as waveform frequency increases. The extremely high strains observed near the bubble wall are discussed further in Section 4.2.

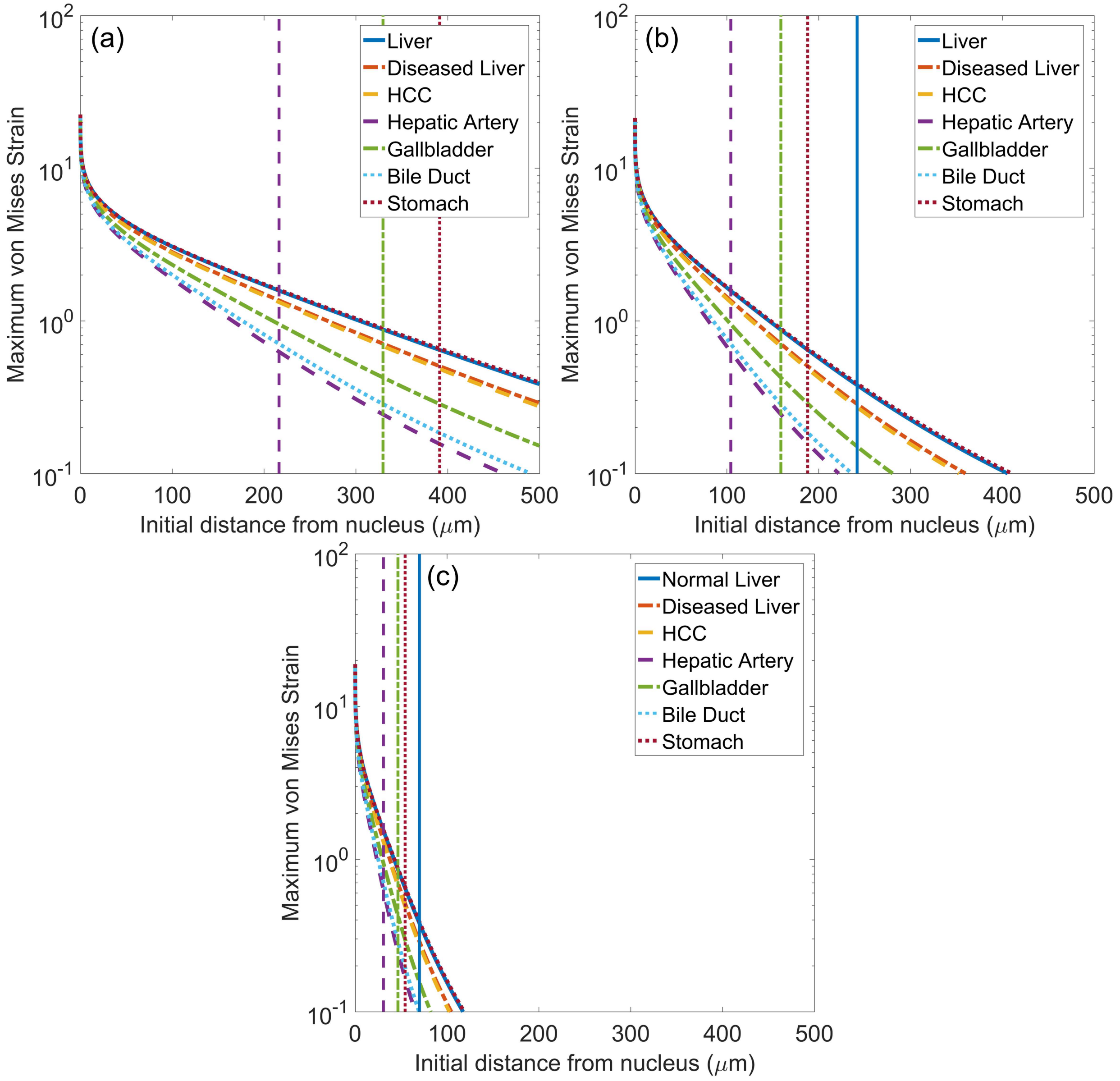

Figure 6.7: Maximum von Mises strain surrounding bubble as a function of initial distance from the bubble nucleus for different tissues exposed to (a) 0.5 MHz, (b) 1 MHz, and (c) 3 MHz waveforms. Vertical lines indicate the distance at which strain first attenuates below the ultimate true strain of liver, hepatic artery, gallbladder, and stomach.

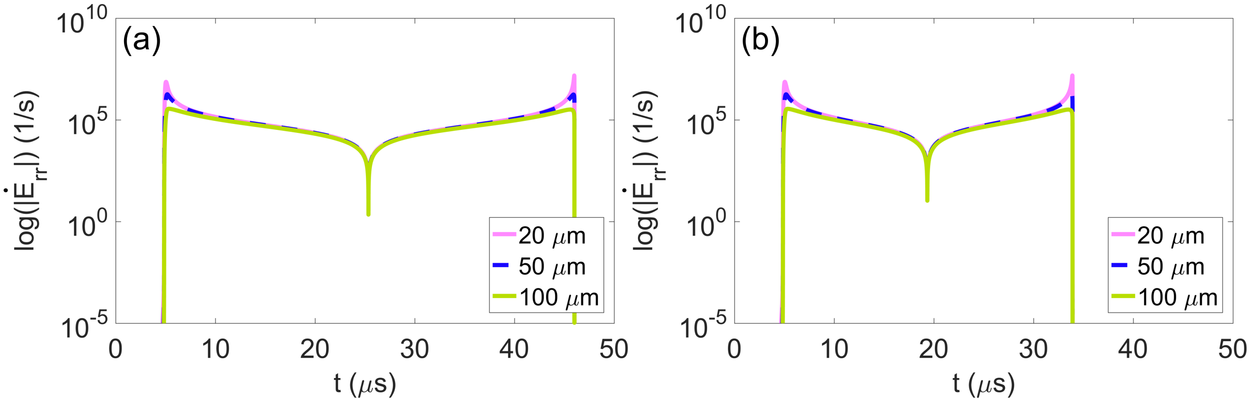

Figure 6.8: Total radial strain rate along the Lagrangian paths starting 20, 50, and 100 μm from the bubble nucleus in (a) liver and (b) HCC exposed to a 1 MHz waveform.

6.4.4 Strain Rate Fields

Radial strain rate fields and von Mises strain rate fields are calculated from the time derivatives of Equations (6.8) and (6.10), respectively. Maximum strain rates are determined with respect to starting distance from the bubble nucleus and are plotted for each tissue. Figure 6.8 shows radial strain rate histories along Lagrangian trajectories starting 20, 50, and 100 μm from the nucleus as a function of time for (a) liver and (b) HCC. Strain rates are spatially localized to the bubble wall with nearly symmetric local maxima at the onset of bubble growth and at collapse to minimum radius (Mancia *et al.*, 2017). The largest strain rates occur at the onset of bubble growth and when the bubble reaches its minimum radius. Figure 6.9 shows traces of maximum strain rates for waveform frequencies of (a) 0.5, (b) 1, and (c) 3 MHz. Given the similar magnitude of strain rates in different tissues, inset figures showing maximum strain rate magnitude at starting distances of 450 – 455 μm from the nucleus (boxed region of traces) are included. Vertical lines indicating the point of strain attenuation below ultimate true strain of select tissues are reproduced from Figure 6.7.

Of note, strain rates achieve extremely high values near the bubble wall. This is a consequence of taking the equilibrium bubble radius to be on the order of nanometers. The chosen nucleus size is based on present knowledge of nucleation in water and can be refined with future experiments to obtain more accurate estimates of strain rate within microns from the bubble wall. For an arbitrary

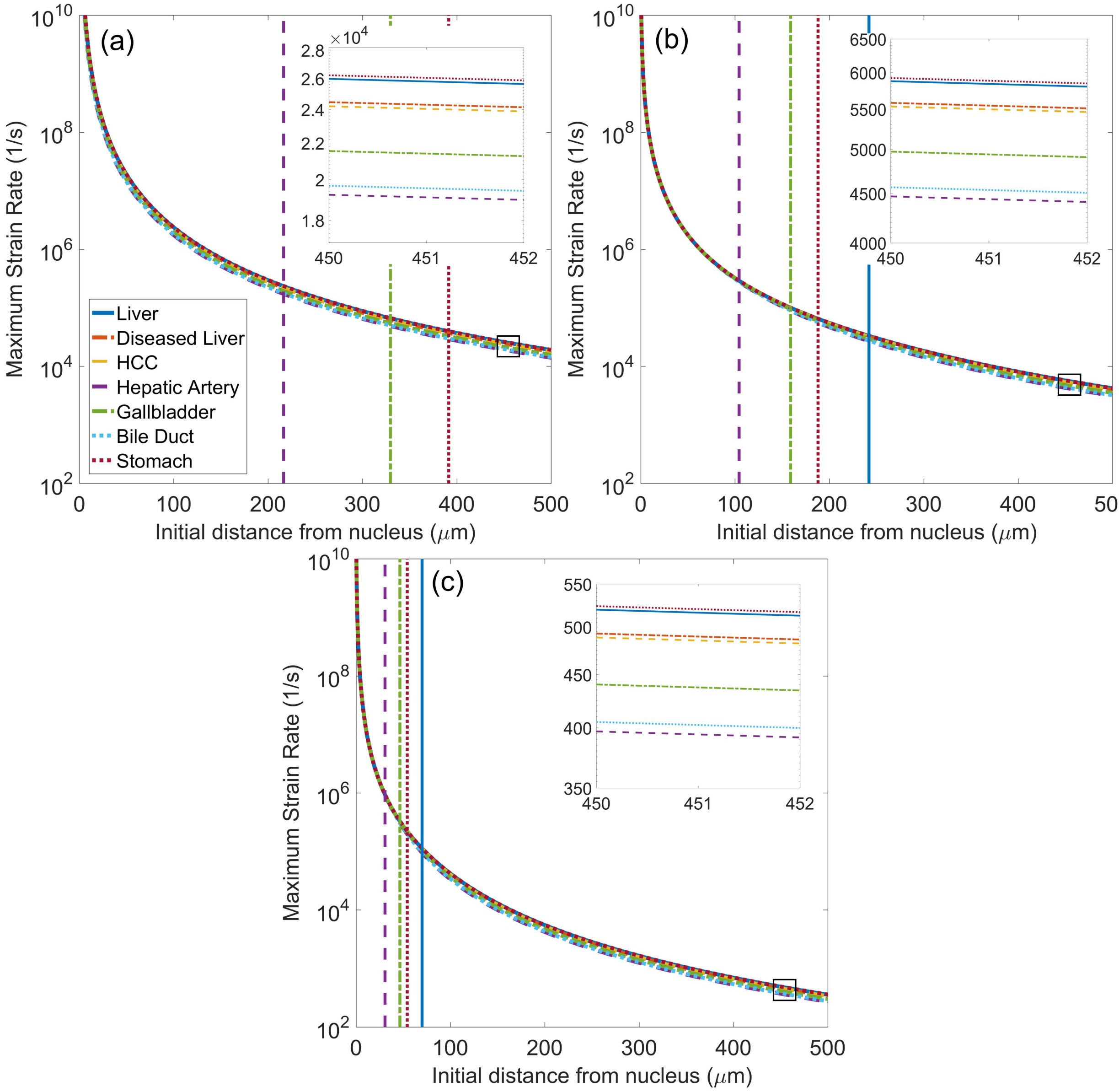

Figure 6.9: Maximum von Mises strain rate surrounding bubble as a function of initial distance from the bubble nucleus for different tissues exposed to (a) 0.5 MHz, (b) 1 MHz, and (c) 3 MHz waveforms. Inset figures show enlargement of strain rate traces in the boxed region. Vertical lines indicate the distance at which strain first attenuates below the ultimate true strain of liver, hepatic artery, gallbladder, and stomach.

nucleus size, strain rates approach a decay proportional to r^{-3}. The specific rates of attenuation in each tissue are proportional to the extent of deformation, and the separation between traces in the inset figures parallels variations in maximum radius. As waveform frequency increases, strain–rate magnitude decreases. As shown in the inset figures, strain rates are approximately an order of magnitude lower for each incremental increase in forcing frequency.

6.5 Discussion

Observed differences in histotripsy ablation of tissues with different mechanical properties (Vlaisavljevich *et al.*, 2014, 2015b, 2016c,a) prompted the hypothesis that mechanical stress, strain, and strain rate are predominant mechanisms of cavitation– induced tissue damage. Although histotripsy treatments involve bubble clouds, a thorough understanding of single–bubble damage will ultimately be needed to guide the development of bubble cloud damage models. This study aims to identify how mechanical cavitation damage mechanisms depend on tissue properties in the context of a histotripsy liver ablation application. First a summary of results for each hypothesized damage mechanism considered in this study is provided. We then use strain data and ultimate strain measurements to predict the spatial extent of mechanical cavitation damage.

6.5.1 Mechanical Damage Mechanisms

Given the uncertain consequences of radial vs. hoop components of stress and strain, their scalar von Mises equivalents permit comparisons with measured ultimate strain and stress values. Stress is smaller at all distances from the bubble wall in tissues with lower shear moduli and in all tissues exposed to higher frequency waveforms. The rate of stress attenuation is also greater in these cases. The increased rate of stress attenuation at high waveform frequency is likely explained by reduced bubble growth. However, at a given forcing frequency, stress attenuates more rapidly in low–shear–modulus tissues despite larger bubble growth. This is a consequence of differences in shear modulus, which is two orders of magnitude smaller in liver than in hepatic artery. From the UTS data in Table 6.1, it is expected that stresses capable of gross tissue rupture are localized to within 100 microns from the bubble wall at all forcing frequencies. This suggests that stress–induced effects could be localized to a single cell. Studies of laser cavitation in an elastic medium have also noted that stress effects are typically confined to the cellular and subcellular level (Brujan & Vogel, 2006).

Maximum strain is largest at maximum bubble radius when the tissue is maximally deformed. Consequently, strain is highest at all starting distances in tissues in which bubbles achieve larger maximum radii. Strain also decreases more rapidly as waveform frequency increases, again as a consequence of the smaller maximum radii reached as frequency is increased. The close relationship of strain to maximum bubble radius makes it an attractive quantity for potential damage extent predictions. For example, observations of single bubbles in the periphery of a bubble cloud have noted that damage appears proportional to maximum bubble diameter (Vlaisavljevich *et al.*, 2016c). Furthermore, studies of cavitation damage to neurons found that cell fragmentation correlates with maximum bubble radius (Estrada *et al.*, 2017). At present, strain is also a more experimentally accessible quantity than either stress or strain rate. For these reasons, this study compares calculated strain to literature–sourced ultimate strain measurements to estimate the single–bubble damage extent in different tissues.

Studies of neurons under compression found that strain magnitude was related to time to cell death while strain rate affected injury morphology and the extent of cell death across a population (Bar-Kochba *et al.*, 2016). Thus, strain rates in addition to strain are considered given the potential for distinct contributions to tissue damage. In contrast to stresses and strains, strain rates attain large magnitudes that remain large ($\sim 10^3$ 1/s) even 500 μm away from the bubble wall. This is consistent with previous theoretical and experimental studies suggesting that the effects of viscosity and strain rate tend to dominate farther from the bubble (Mancia *et al.*, 2017; Estrada *et al.*, 2018). Strain rate magnitude parallels bubble expansion, a consequence of the nearly symmetric phases of bubble growth and collapse in all tissues and at all forcing frequencies considered in the present study. Asymmetry of growth and collapse phases that could give rise to significant differ-

Table 6.3: Strain–related damage extent, x_D and maximum radii, R_{max} in microns for different waveform frequencies

	0.5 MHz		1 MHz		3 MHz	
Tissue	x_D	R_{max}	x_D	R_{max}	x_D	R_{max}
Liver	503	460	242	221	70.0	64.0
Stomach	391	466	188	224	54.3	64.7
Gallbladder	330	317	159	153	46.6	44.8
Hepatic Artery	216	251	104	121	30.8	35.7

ences in strain rate behavior has been noted in tissues with wider variation in viscosity (Mancia *et al.*, 2017). That study also found that strain rate, while typically more significant farther from the bubble, dominated tissue response closer to the bubble wall in tissues with larger viscosity to shear modulus ratios. In the present study, low–shear–modulus tissues (i.e., those with a larger viscosity to shear modulus ratio) exhibit the highest strain rates at all forcing frequencies. Minimal distinction between strain rate traces in different tissues suggests strain rate is not a significant mechanism for tissue–selective effects; however, this could change if needed viscosity measurements are obtained for these tissues.

6.5.2 Extent of Tissue Damage

Measurements of ultimate true strain are used for comparisons of the approximate extent of the damaged region, x_D, in different tissues. We define the "damaged region" as the spatial region extending from the bubble nucleus to where strains first attenuate below the ultimate true strain of a given tissue. Table 6.3 shows the damage radius in each tissue for a given forcing condition alongside the associated maximum bubble radius obtained from simulations. As tissue shear modulus increases, there is a decrease in damage radius at all frequencies. This general trend agrees with experimental observations (Vlaisavljevich *et al.*, 2013a; Cherian & Rau, 2008) and suggests mechanical strain plays a key role in tissue–selective effects, particularly given the significant difference in damage radii between liver and hepatic artery (Vlaisavljevich *et al.*, 2013a). Damage radii shift to proportionally lower values as waveform frequency increases from 0.5 to 3 MHz, a finding consistent with experimental observations of smaller lesion size at higher waveform frequencies (Lin *et al.*, 2014b).

Table 6.3 also includes the maximum bubble radii achieved in each simulation. As expected, high–shear–modulus tissues exhibit stronger resistance to deformation and have reduced maximum bubble radii. Reduced bubble growth is also seen at higher frequencies due to decreased exposure to the driving tensile pulse. The predicted damage radius is smaller than the maximum bubble radius in stomach and hepatic artery under all forcing conditions. This behavior is consistent with trends seen in laser–induced cavitation damage to rat corneas (Cherian & Rau, 2008). Liver tissue and, to a smaller degree, gallbladder have damage radii that are slightly larger than maximum radius at all frequencies. This behavior is a consequence of the lower ultimate strains of these tissues. In general, the proportional relationship between predicted damage radius and maximum bubble radius supports the proposed use of maximum bubble radius as a damage metric for histotripsy (Mancia *et al.*, 2017; Bader & Holland, 2016). Correlations between maximum bubble radius and damage extent have also been observed experimentally in histotripsy (Vlaisavljevich *et al.*, 2016c) and laser–induced cavitation in hydrogels (Estrada *et al.*, 2017). In general, predictions of damage radii that are comparable to the maximum bubble radius are supported by observations of highly localized cavitation damage and the sharply demarcated boundaries of histotripsy lesions (Parsons *et al.*, 2006a; Vlaisavljevich *et al.*, 2016c).

The proportional relationship between damage radius and maximum bubble radius can be shown to depend on the ultimate true strain of a given tissue. The Keller-Miksis equation (Eq. 6.1) includes only first–order compressibility effects, so tissues in this study are nearly incompressible. It follows that strain fields are entirely determined by R through Equations 6.7 and 6.8. Given the further assumption that $R_0 \ll R_{max}$, an expression can be derived for the ratio x_D/R_{max} in terms of the ultimate true strain, ϵ, that is constant for a given tissue under all forcing conditions:

$$\frac{x_D}{R_{max}} = \left[\exp\left(\frac{3}{2}\epsilon\right) - 1\right]^{-1/3} \tag{6.11}$$

For tissues with an ultimate strain larger than a critical value $\epsilon^* = \frac{2\ln 2}{3} = 0.46$, the damage radius will be less than the maximum bubble radius. This is clearly true for stomach ($\epsilon = 0.66$) and hepatic artery ($\epsilon = 0.63$) while gallbladder has an ultimate strain ($\epsilon = 0.43$) only slightly below the critical value. In contrast, liver ($\epsilon = 0.38$) has the smallest ultimate strain and demonstrates $x_D > R_{max}$ behavior at all waveform frequencies. Previous authors have developed metrics to predict R_{max} in histotripsy for given forcing conditions and tissue parameters (Bader & Holland, 2016), so these methods and Eq. 6.11 can be used to predict the single–bubble damage radius. Of note, use of Eq. 6.11 permits substitution of an ultimate strain measured at an elevated strain rate.

The proposed strain–based damage metric and maximum bubble radius show good qualitative agreement with experimental observations and thus provide direction for future treatment planning algorithms. However, it should be noted that model assumptions tend towards an upper–bound estimation of the single–bubble damage radius. In particular, the spherical symmetry and first–order compressibility assumed by the Keller–Miksis equation lead to higher pressures, stresses, and strains developed at bubble collapse. Since maximum stresses and strains tend to occur at maximum bubble radius and at collapse, these assumptions could overestimate the predicted damage radius. Additionally, this study bases damage radii predictions on quasistatic measurements of ultimate true strain in each tissue. The vast majority of tissue measurements to date have been performed under quasistatic conditions not applicable to the ultra–high strain rates ($>10^8$ 1/s) generated during cavitation bubble growth and collapse. However, the ultimate strength or strain of a gross tissue sample as well as its shear modulus should be measured at more relevant strain rates (Brujan & Vogel, 2006). For example, studies of ballistic gelatin, the closest tissue surrogate studied under high strain rates, found that the gel's compressive strength increased from 3 kPa at a strain rate of ~0.001/s to 6 MPa at a strain rate of ~3200/s (Kwon & Subhash, 2010). This again suggests the damage radii predicted here could over–estimate the true damage extent. New approaches for determining tissue properties under high strain rate stand to improve the accuracy of stress, strain, and strain rate calculations in this study (Estrada *et al.*, 2018) or treatment planning applications seeking to avoid collateral damage.

Cavitation–induced damage most likely involves a combination of direct mechanical destruction of cells and changes in cell microenvironment that induce apoptosis. Thus, a more rigorous definition of tissue 'damage' is needed. Relating stress, strain, and strain rate calculations to the spatial extent of tissue damage is challenging given the limited measurements that can be made at time and length scales relevant to cavitation. Future work applying the methods of a recent study correlating cellular changes with cavitation damage extent will be valuable for this purpose (Estrada, 2017). Furthermore, the mechanics of cavitation in soft matter are likely more complex than current theories can represent. For example, no known material can tolerate the extremely high stresses and strains calculated at the bubble without immediate rupture. The assumption of continuous stretching of tissue from a nanometer–sized nucleus is likely an oversimplification, and this work motivates the need for future experiments clarifying the sequence of events producing cavitation damage. The choice of a 5 nm nucleus in this study was based on experimental predictions of nucleus size in water and other fluids calculated to match experimentally observed cavitation thresholds using intrinsic threshold histotripsy (Maxwell *et al.*, 2013). More likely, however, the ultra–high strain rates generated at cavitation inception would immediately rupture tissue. This early tissue rupture could then briefly give rise to a larger 'stress–free' or equilibrium radius that acts as an effective initial radius for calculations of stress and strain fields. This process would then repeat until the bubble reaches its maximum size. Alternatively, bubble nuclei present in extracellular fluid might fail to exert significant stress and strain on surrounding cells until they reach a large enough size. The consequences that a larger effective initial radius could have for stress magnitudes are illustrated in Figure 6.10. This figure shows von Mises stress as a function of scaled distance from the maximum bubble radius in (a) liver and (b) hepatic artery for four different initial radii. Relative to the assumed case of bubble growth from a 5 nm nucleus (solid blue trace), the larger initial radii lead to significantly smaller stresses at the bubble wall ($r = R_{max}$). However, notably, the rates of stress attenuation in all traces are unaffected, and the stress traces for each R_0 are self–similar. While experiments would ultimately be needed to inform the choice of initial radius, this presently assumed parameter is unlikely to significantly affect the predicted

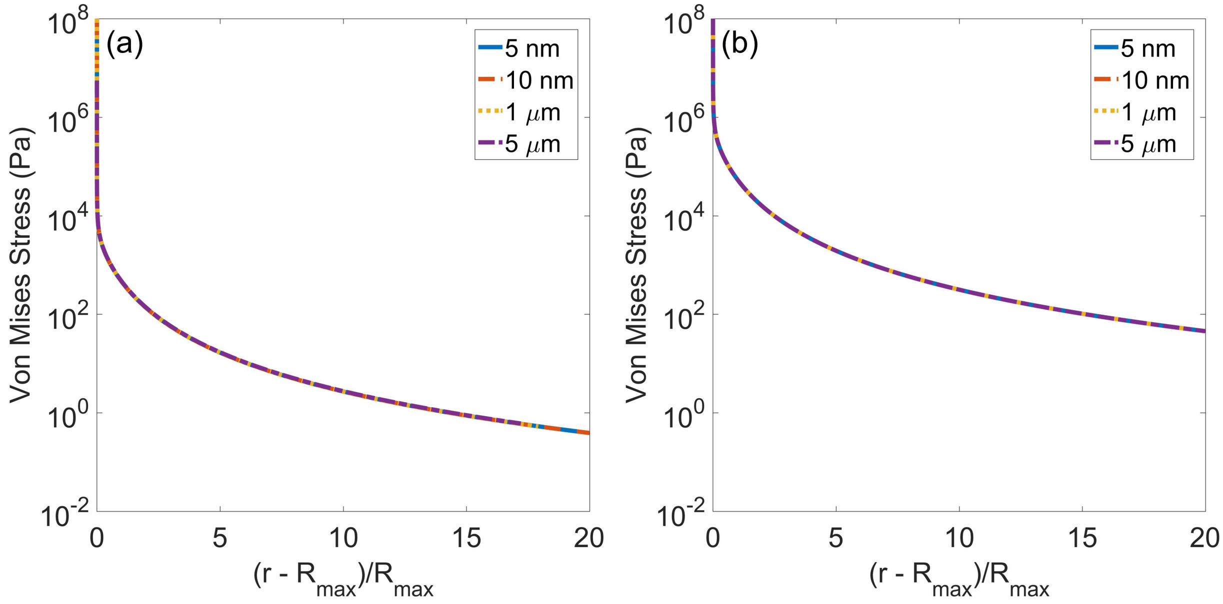

Figure 6.10: Von Mises stress as a function of scaled distance from maximum bubble radius for different initial radii in (a) liver ($R_{max}/R_0 = 4.4 \times 10^4, 2.4 \times 10^4, 264, 55$) and (b) hepatic artery ($R_{max}/R_0 = 2.4 \times 10^4, 1.3 \times 10^4, 140, 31$) under 1 MHz forcing.

damage radii in this study given the relatively weak dependence of R_{max} on R_0. For example, in Figure 6.10(a) for liver, the R_{max} values are 220, 240, 264, and 275 microns. Thus by Equation 6.11, the x_D values are 241, 263, 289, and 301 microns. Similarly, for Figure 6.10(b) for hepatic artery, the R_{max} values are 120, 130, 140, and 155 microns, and the x_D values are 103, 112, 121, and 133 microns.

6.6 Conclusions

This study models bubble dynamics in a variety of tissues with literature–sourced viscoelastic and acoustic properties to investigate potential mechanisms responsible for experimental observations of tissue–selective cavitation damage. Results are presented showing radial dynamics, stress, strain, and strain rate fields for different tissues at three waveform frequencies (0.5 MHz, 1 MHz, and 3 MHz) relevant to focused ultrasound applications. Calculated von Mises equivalent tensile strain fields are then compared to available ultimate true strain data to compare predicted strain–related damage extent in different tissues. The distinct viscoelastic properties of each tissue affect the magnitudes of stress, strain, and strain rate more significantly with increasing distance from the bubble. Findings support the hypothesis that differential tissue mechanical responses could be used to design tissue–selective treatments and are also consistent with experiments demonstrating resistance to ablation in stiffer tissues (Vlaisavljevich *et al.*, 2013a), smaller lesion size associated with higher frequency waveforms (Lin *et al.*, 2014b), and sharp boundaries of the histotripsy ablation zone (Parsons *et al.*, 2006a).

This work is limited by the available viscoelastic and acoustic property measurements in each tissue. Strain rate trends, in particular, are dependent on tissue viscosity; however, measurements of viscosity in the same tissue vary widely based on testing method and assumed constitutive relationship. The applicability of results in this study could be strengthened by recent advances in measurement techniques for the mechanical properties of inhomogeneous soft tissue (Margueritat *et al.*, 2019). Further study of tissue failure under compression and in response to high strain rates could also improve damage predictions.

CHAPTER 7

Conclusion

We provide a summary of thesis objectives and conclusions then describe potential directions for future research.

7.1 Summary

The primary objectives of this thesis are to use validated single–bubble numerical simulations for material characterization under cavitation conditions and for the study of cavitation damage mechanisms. In pursuit of these objectives, we make several contributions to the field. These contributions are described in Chapters 2 – 6 and are summarized below.

1. We presented a novel approach for using single–bubble experiments and numerical simulations to measure the size distribution of nanoscale cavitation nucleii present at the acoustic threshold (Mancia *et al.*, 2020).

2. We provided a quantitative comparison of different histotripsy modeling approaches to experimental radius vs. time data obtained from single–bubble nucleation events in water (Mancia *et al.*, 2020b). A common analytic approximation for histotripsy waveforms was validated by making direct use of experimental data. We evaluated select models for radial dynamics and bubble contents assuming that the primary parametric uncertainty in water lies in the initial radius or nucleus size. We also presented a quantitative summary of ini-

tial radius statistics and validation metrics for each treatment of radial dynamics and bubble contents.

3. We provided a demonstration of the IMR method with acoustic– rather than laser–induced cavitation data and used it to infer material properties of 0.3% and 1% agarose gel specimens (Mancia *et al.*, 2020c). Distributions for agarose properties including pore size, shear modulus, and viscosity were inferred using a combination of ultrasound–induced cavitation radius vs. time measurements and bubble dynamics in a finite–deformation Kelvin–Voigt material.

4. We used a validated single–bubble model to study the effects of tissue properties and waveform parameters on the bubble dynamics of a nucleus subjected to a single negative histotripsy-relevant cycle and calculated stress, strain, and strain rate fields in a tissue–like viscoelastic medium (Mancia *et al.*, 2017). A relationship was identified between the dominant contribution to viscous vs. elastic stress and distance from the bubble nucleus.

5. We modeled bubble dynamics in a variety of tissues with literature–sourced viscoelastic and acoustic properties to investigate potential mechanisms for tissue–selective cavitation damage (Mancia *et al.*, 2019). For each tissue, we presented results showing radial dynamics and field quantities at three relevant waveform frequencies (0.5 MHz, 1 MHz, and 3 MHz). Calculated strain fields were compared to ultimate fractional (tensile) strain measurements to estimate damage radii in each tissue.

7.2 Conclusions

The following conclusions are drawn from the work presented in Chapters 2 – 6:

1. We presented a novel approach for using single–bubble experiments and simulations to measure the size distribution of nanoscale cavitation nucleii present at the acoustic threshold (Mancia *et al.*, 2020). It was shown that variation between individual experiments performed under identical conditions can be fully explained by a quantifiable uncertainty in nucleus

size. We distinguished cavitation at the acoustic threshold as a subtype of heterogeneous cavitation that is nevertheless intrinsic to a given medium. Nuclei were shown to follow a lognormal size distribution typical of heterogeneous cavitation in other contexts and with a mean radius consistent with first principles estimates for ion-stabilized nanoscale nuclei. Our work supports a previous hypothesis that self–ionization explains the persistent difference between acoustic measurements and theoretical estimates of the cavitation threshold in water. We also demonstrated the value of the acoustic cavitation threshold and associated nucleus size distribution as intrinsic material properties that are useful for the characterization of liquids and soft matter.

2. Radius vs. time measurements for single historipsy–nucleated bubbles in water were used to objectively compare a variety of bubble dynamics modeling assumptions (Chapter 3). We justified a popular analytic approximation of the histotripsy waveform. Notably, we found that even modeling approaches with significant assumptions regarding compressibility and thermal effects are adequate for simulating the majority of histotripsy single–bubble behavior. In particular, we showed that all models are applicable at maximum bubble radius, which is considered a key damage metric. Our validation of these simplified models stands to improve the computational efficiency of bubble cloud models.

3. We demonstrated the inertial microcavitation–based high strain–rate rheometry (IMR) method for characterization of agarose gel using acoustic cavitation data (Chapter 4). Our approach inferred material properties such as pore size, shear modulus, and viscosity for the 0.3% and 1% agarose gel specimens in an efficient and cost–effective manner. This work justified the use of a new source of cavitation data: Radius vs. time measurements from acoustic rather than laser–induced cavitation experiments. In comparing the optimized initial radius and associated normalized rms error distributions obtained with various models applied to 88 experimental data sets, we found minimal distinction (< 1%) among these modeling approaches. Our findings are valuable because acoustic cavitation experiments are less likely to

alter material properties than laser–induced cavitation experiments, and acoustic cavitation is a closer analogue to blast injuries. We also show that cavitation–based material characterization can be applied to agarose, a more complex material than polyacrylamide that is more widely used as a tissue phantom.

4. We used a validated single–bubble model to study the effects of tissue properties and waveform parameters on the bubble dynamics of a nucleus subjected to a single negative histotripsy-relevant cycle and calculated stress, strain, and strain rate fields in a tissue–like viscoelastic medium (Mancia *et al.*, 2017). We found that all field quantities are maximized at the bubble wall and attenuate with increasing distance from the bubble, a result consistent with observed sharp boundaries of the histotripsy ablation zone. Furthermore, stress was found to be of two distinct origins: viscous and elastic. Stress contributions attenuate at different rates with elastic stresses dominating near the bubble wall and viscous stresses dominating farther away. We identify the critical distance beyond which the maximum compressive stress is of viscous rather than elastic origin. Our scaling analysis demonstrates that a fundamental relationship exists between the scaled transition location and the dimensionless elastic–to–viscous forces ratio.

5. We modeled bubble dynamics in a variety of tissues with literature–sourced viscoelastic and acoustic properties to investigate potential mechanisms for tissue–selective cavitation damage (Mancia *et al.*, 2019). We compared calculated von Mises strain fields to available ultimate true strain data and estimated the predicted strain–related damage extent in different tissues relevant to a liver tumor ablation application. We showed that the distinct viscoelastic properties of each tissue affect the magnitudes of stress, strain, and strain rate more significantly with increasing distance from the bubble. Our findings support the hypothesis that differential tissue mechanical responses could be used to design tissue–selective treatments. Modeling results were consistent with experiments demonstrating resistance to ablation in stiffer tissues, smaller lesion size associated with higher frequency waveforms, and sharp

boundaries of the histotripsy ablation zone. Our approach to quantifying damage extent can inform the design of treatments that are selective to pathological tissue and spare critical anatomic structures.

7.3 Future Research Directions

This work motivates multiple avenues for future research. We categorize suggested future studies based on their relevance to the broader themes of (i) nucleation, (ii) bubble dynamics in water and soft matter, and (iii) cavitation damage mechanisms.

7.3.1 Nucleation

We presented a novel approach for using single–bubble experiments and simulations to measure the size distribution of nanoscale cavitation nuclei present at the acoustic threshold (Mancia *et al.*, 2020). The nucleus size distribution had a mean radius consistent with first principles estimates for ion–stabilized nuclei ("bubbstons") that arise spontaneously during self–ionization of water (Bunkin & Bunkin, 1992). Our work focused on water given its well–characterized physical properties. Future studies could examine the effects of ion concentration, pH, and gas content of water on the nucleus size distribution. A more thorough investigation of surface tension is also needed as the local value for a nanoscale nucleus differs from that of the bulk liquid. This work could also inform the development of molecular dynamics simulations capable of modeling the earliest stages of nucleation and bubbston formation. Furthermore, these methods could be extended to determine threshold nucleus size distributions in other liquids and viscoelastic media such as those considered in previous acoustic cavitation threshold studies (Maxwell *et al.*, 2013). Although the acoustic cavitation thresholds of water and water–based tissues are comparable, the measured acoustic cavitation thresholds of adipose tissue, 1,3–butenadiol, and olive oil are significantly different (Bader *et al.*, 2019), suggesting that a distinct nucleation mechanism is at work or that an alternative source of preexisting nuclei is present in these cases.

7.3.2 Bubble Dynamics in Water and Soft Matter

We showed that even modeling approaches with significant assumptions regarding liquid compressibility and thermal effects are adequate for simulating the majority of histotripsy single–bubble behavior in water. These results could inform the development of computationally efficient bubble cloud models that permit real–time treatment monitoring for histotripsy. We justified an analytic approximation of the histotripsy waveform for this nearly ideal case of inertial cavitation with reference to experimental data, and the numerical results obtained by using our approximate waveform were in excellent agreement with experiments. However, the limits of this approximation should be explored in future work because the precise acoustic forcing experienced by a bubble at its point of inception cannot be directly measured due to damaging cavitation at the hydrophone tip. A more precise characterization of acoustic forcing experienced by a bubble, particularly in the presence of multiple bubbles and other confounding factors, is especially important in applications that involve continuous forcing such as cavitation–mediated HIFU and diagnostic ultrasound. Furthermore, improvements in the spatial and temporal resolution of experiments could enable more data collection immediately after the onset of bubble growth and immediately before collapse to minimum radius. Such additional data could further distinguish the accuracy of models we have used.

We demonstrated the inertial microcavitation–based high strain–rate rheometry (IMR) method for characterization of agarose gels using radius vs. time measurements from acoustic cavitation experiments. Our method determined parameter distributions for agarose pore size, gel viscosity, and gel shear modulus. Future work considering additional parameter and model uncertainties could improve the approach and extend it to more complex materials. For instance, our resulting parameter distributions are ultimately dependent on the constitutive model assumed for the gel. Since our approach is general, one could apply it using alternative viscoelastic constitutive models such as the standard nonlinear solid model proposed by Estrada *et al.* (Estrada *et al.*, 2018). Due to resolution limitations, less data can be obtained for smaller bubbles (e.g. maximum radii

< 10 microns). Relative to water data, gel radius vs. time measurements have fewer data points per experiment in part due to restricted bubble growth in gel media. Improvements in spatial resolution could increase the applicability of our methods to stiffer gels.

7.3.3 Cavitation Damage Mechanisms

We used a validated single–bubble model to study the effects of tissue properties and waveform parameters on the bubble dynamics of a nucleus subjected to a single negative histotripsy-relevant cycle and calculated stress, strain, and strain rate fields in a tissue–like viscoelastic medium (Mancia *et al.*, 2017). We identified the critical distance beyond which the maximum compressive stress is of viscous rather than elastic origin. Although we identified a scaling between the between this critical distance and the dimensionless elastic–to–viscous forces ratio, our scaling depends on maximum bubble radius in addition to known tissue and waveform parameters. Future work could identify a scaling for maximum bubble radius that depends only on known quantities. An analytic expression for maximum radius has been proposed (Bader & Holland, 2016), but requires validation with single–bubble experimental data. We modeled bubble dynamics in a variety of tissues with literature–sourced viscoelastic and acoustic properties to study tissue–selective cavitation damage (Mancia *et al.*, 2019). Our method for estimating damage extent in each tissue could be applied using different constitutive models and different tissue properties. For example, the IMR method could be used to determine the most realistic constitutive model and tissue properties for each tissue under cavitation–relevant conditions. Novel tissue property measurement techniques that account for inhomogeneities (Margueritat *et al.*, 2019) or for cellular microstructure could also be used for damage extent predictions.

BIBLIOGRAPHY

Adams, Matthew T, Cleveland, Robin O, & Roy, Ronald A. 2017. Modeling-based design and assessment of an acousto-optic guided high-intensity focused ultrasound system. *Journal of biomedical optics*, **22**(1), 017001.

Akulichev, VA. 1967. Pulsations of cavitation bubbles in the field of an ultrasonic wave. *Soviet Physics Acoustics*, **13**(2), 149.

Allen, John S, & Roy, Ronald A. 2000a. Dynamics of gas bubbles in viscoelastic fluids. I. Linear viscoelasticity. *J Acoust Soc Am*, **107**(6), 3167–3178.

Allen, John S, & Roy, Ronald A. 2000b. Dynamics of gas bubbles in viscoelastic fluids. II. Nonlinear viscoelasticity. *J Acoust Soc Am*, **108**(4), 1640–1650.

Ando, Keita, Colonius, Tim, & Brennen, Christopher E. 2011. Numerical simulation of shock propagation in a polydisperse bubbly liquid. *Int. J. Multiph. Flow*, **37**(6), 596–608.

Ando, Keita, Liu, Ai-Qun, & Ohl, Claus-Dieter. 2012. Homogeneous nucleation in water in microfluidic channels. *Phys. Rev. Lett.*, **109**(4), 044501.

Apfel, RE. 1981. Acoustic cavitation prediction. *The Journal of the Acoustical Society of America*, **69**(6), 1624–1633.

Apfel, Robert E, & Holland, Christy K. 1991. Gauging the likelihood of cavitation from short-pulse, low-duty cycle diagnostic ultrasound. *Ultrasound in medicine & biology*, **17**(2), 179–185.

Arora, Pamela D, Narani, Nazanin, & McCulloch, Christopher AG. 1999. The compliance of collagen gels regulates transforming growth factor-β induction of α-smooth muscle actin in fibroblasts. *The American journal of pathology*, **154**(3), 871–882.

Azouzi, Mouna El Mekki, Ramboz, Claire, Lenain, Jean-François, & Caupin, Frederic. 2013. A coherent picture of water at extreme negative pressure. *Nat. Phys.*, **9**(1), 38.

Bader, Kenneth B. 2018a. The influence of medium elasticity on the prediction of histotripsy-induced bubble expansion and erythrocyte viability. *Physics in Medicine & Biology*, **63**(9), 095010.

Bader, Kenneth B. 2018b. The influence of medium elasticity on the prediction of histotripsy-induced bubble expansion and erythrocyte viability. *Physics in Medicine & Biology*, **63**(9), 095010.

Bader, Kenneth B, & Holland, Christy K. 2016. Predicting the growth of nanoscale nuclei by histotripsy pulses. *Physics in Medicine & Biology*, **61**(7), 2947.

Bader, Kenneth B, Vlaisavljevich, Eli, & Maxwell, Adam D. 2019. For whom the bubble grows: physical principles of bubble nucleation and dynamics in histotripsy ultrasound therapy. *Ultrasound Med. Biol.*

Bailey, M.R., Cleveland, R.O., Colonius, T., Crum, L.A., Evan, A.P., Lingeman, J.E., McAteer, James A., Sapozhnikov, O.A., & Williams, J.C., Jr. 2003a (Oct). Cavitation in shock wave lithotripsy: the critical role of bubble activity in stone breakage and kidney trauma. *Pages 724–727 of: 2003 IEEE Symposium on Ultrasonics*, vol. 1.

Bailey, MR, Khokhlova, VA, Sapozhnikov, OA, Kargl, SG, & Crum, LA. 2003b. Physical mechanisms of the therapeutic effect of ultrasound (a review). *Acoustical Physics*, **49**(4), 369–388.

Bamber, JC, & Hill, CR. 1981. Acoustic properties of normal and cancerous human liveri. dependence on pathological condition. *Ultrasound in Medicine and Biology*, **7**(2), 121–133.

Bar-Kochba, Eyal, Scimone, Mark T, Estrada, Jonathan B, & Franck, Christian. 2016. Strain and rate-dependent neuronal injury in a 3d in vitro compression model of traumatic brain injury. *Scientific reports*, **6**, 30550.

Barajas, Carlos, & Johnsen, Eric. 2017. The effects of heat and mass diffusion on freely oscillating bubbles in a viscoelastic, tissue-like medium. *The Journal of the Acoustical Society of America*, **141**(2), 908–918.

Ben-Yosef, N, Ginio, O, Mahlab, D, & Weitz, A. 1975. Bubble size distribution measurement by doppler velocimeter. *J. Appl. Phys.*, **46**(2), 738–740.

Benson, Sidney W, & Gerjuoy, Edward. 1949. The tensile strengths of liquids. i. thermodynamic considerations. *The Journal of Chemical Physics*, **17**(10), 914–918.

Bentz, Kyle C, Walley, Susan E, & Savin, Daniel A. 2016. Solvent effects on modulus of poly (propylene oxide)-based organogels as measured by cavitation rheology. *Soft Matter*, **12**(22), 4991–5001.

Bigelow, Timothy A, Thomas, Clayton L, Wu, Huaiqing, & Itani, Kamal MF. 2018. Histotripsy treatment of s. aureus biofilms on surgical mesh samples under varying scan parameters. *IEEE transactions on ultrasonics, ferroelectrics, and frequency control*, **65**(6), 1017–1024.

Bigelow, Timothy A, Thomas, Clayton L, Wu, Huaiqing, & Itani, Kamal MF. 2019. Impact of high-intensity ultrasound on strength of surgical mesh when treating biofilm infections. *IEEE transactions on ultrasonics, ferroelectrics, and frequency control*, **66**(1), 38–44.

Billet, ML. 1986. Cavitation nuclei measurements with an optical system. *J. Fluids Eng.*, **108**(3), 366–372.

Blomley, Martin JK, Cooke, Jennifer C, Unger, Evan C, Monaghan, Mark J, & Cosgrove, David O. 2001. Microbubble contrast agents: a new era in ultrasound. *Bmj*, **322**(7296), 1222–1225.

Borkent, Bram M, Arora, Manish, & Ohl, Claus-Dieter. 2007. Reproducible cavitation activity in water-particle suspensions. *J. Acoust. Soc. Am.*, **121**(3), 1406–1412.

Brennen, Christopher E. 2014. *Cavitation and bubble dynamics*. Cambridge University Press.

Brennen, Christopher Earls. 2015. Cavitation in medicine. *Interface focus*, **5**(5), 20150022.

Brotchie, Adam, Grieser, Franz, & Ashokkumar, Muthupandian. 2009. Effect of power and frequency on bubble-size distributions in acoustic cavitation. *Phys. Rev. Letters*, **102**(8), 084302.

Brujan, EA. 2004. The role of cavitation microjets in the therapeutic applications of ultrasound. *Ultrasound in medicine & biology*, **30**(3), 381–387.

Brujan, Emil. 2010. *Cavitation in non-newtonian fluids: With biomedical and bioengineering applications*. Springer Science & Business Media.

Brujan, Emil-Alexandru, & Vogel, Alfred. 2006. Stress wave emission and cavitation bubble dynamics by nanosecond optical breakdown in a tissue phantom. *Journal of Fluid Mechanics*, **558**, 281–308.

Bunkin, NF, & Bunkin, FV. 1992. Bubbstons: stable microscopic gas bubbles in very dilute electrolytic solutions. *J. Exp. Theor. Phys.*, **74**(2), 271–276.

Canchi, Saranya, Kelly, Karen, Hong, Yu, King, Michael A, Subhash, Ghatu, & Sarntinoranont, Malisa. 2017. Controlled single bubble cavitation collapse results in jet-induced injury in brain tissue. *Journal of the mechanical behavior of biomedical materials*, **74**, 261–273.

Catheline, S, Gennisson, J-L, Delon, G, Fink, M, Sinkus, R, Abouelkaram, S, & Culioli, J. 2004. Measurement of viscoelastic properties of homogeneous soft solid using transient elastography: An inverse problem approach. *The Journal of the Acoustical Society of America*, **116**(6), 3734–3741.

Chatterjee, Dhiman, & Arakeri, Vijay H. 1997. Towards the concept of hydrodynamic cavitation control. *J. Fluid Mech.*, **332**, 377–394.

Chaudhuri, Ovijit, Gu, Luo, Klumpers, Darinka, Darnell, Max, Bencherif, Sidi A, Weaver, James C, Huebsch, Nathaniel, Lee, Hong-pyo, Lippens, Evi, Duda, Georg N, *et al.*. 2016. Hydrogels with tunable stress relaxation regulate stem cell fate and activity. *Nature materials*, **15**(3), 326–334.

Cherian, Anoop V, & Rau, Kaustubh R. 2008. Pulsed-laser-induced damage in rat corneas: time-resolved imaging of physical effects and acute biological response. *Journal of Biomedical Optics*, **13**(2), 024009.

Chikina, Ioulia, & Gay, Cyprien. 2000. Cavitation in adhesives. *Phys. Rev. Letters*, **85**(21), 4546.

Chin, Michael S, Freniere, Brian B, Fakhouri, Sami, Harris, John E, Lalikos, Janice F, & Crosby, Alfred J. 2013. Cavitation rheology as a potential method for in vivo assessment of skin biomechanics. *Plastic and reconstructive surgery*, **131**(2), 303e.

Church, Charles C. 1989. A theoretical study of cavitation generated by an extracorporeal shock wave lithotripter. *The Journal of the Acoustical Society of America*, **86**(1), 215–227.

Church, Charles C. 2002. Spontaneous homogeneous nucleation, inertial cavitation and the safety of diagnostic ultrasound. *Ultrasound in medicine & biology*, **28**(10), 1349–1364.

Church, Charles C, & Yang, Xinmai. 2006. A theoretical study of gas bubble dynamics in tissue. *Pages 217–224 of: Innovations in nonlinear acoustics: ISNA17-17th international symposium on nonlinear acoustics including the international Sonic Boom Forum*, vol. 838. AIP Publishing.

Coleman, AJ, & Saunders, JE. 1993. A review of the physical properties and biological effects of the high amplitude acoustic fields used in extracorporeal lithotripsy. *Ultrasonics*, **31**(2), 75–89.

Coleman, Andrew J, Saunders, John E, Crum, Lawrence A, & Dyson, Mary. 1987. Acoustic cavitation generated by an extracorporeal shockwave lithotripter. *Ultrasound in medicine and biology*, **13**(2), 69–76.

Cooper, Michol, Xu, Zhen, Rothman, Edward D, Levin, Albert M, Advincula, Arnold P, Fowlkes, J Brian, & Cain, Charles A. 2004. Controlled ultrasound tissue erosion: the effects of tissue type, exposure parameters and the role of dynamic microbubble activity. *Pages 1808–1811 of: IEEE Ultrasonics Symposium, 2004*, vol. 3. IEEE.

Córdoba, Andrés, Indei, Tsutomu, & Schieber, Jay D. 2012. Elimination of inertia from a generalized langevin equation: Applications to microbead rheology modeling and data analysis. *Journal of Rheology*, **56**(1), 185–212.

Coussios, ¿ CC, Farny, CH, Ter Haar, G, & Roy, RA. 2007. Role of acoustic cavitation in the delivery and monitoring of cancer treatment by high-intensity focused ultrasound (hifu). *International journal of hyperthermia*, **23**(2), 105–120.

Crum, Lawrence, Bailey, Michael, Hwang, Joo Ha, Khokhlova, Vera, & Sapozhnikov, Oleg. 2010. Therapeutic ultrasound: Recent trends and future perspectives. *Physics Procedia*, **3**(1), 25–34.

Crum, Lawrence A. 1979. Tensile strength of water. *Nature*, **278**(5700), 148–149.

Cui, Jun, Lee, Cheol Hee, Delbos, Aline, McManus, Jennifer J, & Crosby, Alfred J. 2011. Cavitation rheology of the eye lens. *Soft Matter*, **7**(17), 7827–7831.

Culjat, Martin O, Goldenberg, David, Tewari, Priyamvada, & Singh, Rahul S. 2010. A review of tissue substitutes for ultrasound imaging. *Ultrasound in medicine & biology*, **36**(6), 861–873.

Davitt, Kristina, Arvengas, Arnaud, & Caupin, Frédéric. 2010. Water at the cavitation limit: Density of the metastable liquid and size of the critical bubble. *EPL*, **90**(1), 16002.

De, Smita, Rosen, Jacob, Dagan, Aylon, Hannaford, Blake, Swanson, Paul, & Sinanan, Mika. 2007. Assessment of tissue damage due to mechanical stresses. *Int J Robot Res*, **26**(11-12), 1159–1171.

Debenedetti, Pablo G. 1996. *Metastable liquids: concepts and principles*. Princeton University Press.

Deng, SX, Tomioka, J, Debes, JC, & Fung, YC. 1994. New experiments on shear modulus of elasticity of arteries. *American Journal of Physiology-Heart and Circulatory Physiology*, **266**(1), H1–H10.

DePalma, Ralph G, Burris, David G, Champion, Howard R, & Hodgson, Michael J. 2005. Blast injuries. *New England Journal of Medicine*, **352**(13), 1335–1342.

Diamond, Scott L. 1999. Engineering design of optimal strategies for blood clot dissolution. *Annu Rev Biomed Eng*, **1**(1), 427–461.

Donaldson, James F, Lardas, Michael, Scrimgeour, Duncan, Stewart, Fiona, MacLennan, Steven, Lam, Thomas BL, & McClinton, Samuel. 2015. Systematic review and meta-analysis of the clinical effectiveness of shock wave lithotripsy, retrograde intrarenal surgery, and percutaneous nephrolithotomy for lower-pole renal stones. *European urology*, **67**(4), 612–616.

Dubinsky, Theodore J, Cuevas, Carlos, Dighe, Manjiri K, Kolokythas, Orpheus, & Hwang, Joo Ha. 2008. High-intensity focused ultrasound: current potential and oncologic applications. *American journal of roentgenology*, **190**(1), 191–199.

Duch, Birgitte U, Andersen, Helle, & Gregersen, Hans. 2004. Mechanical properties of the porcine bile duct wall. *BioMedical Engineering OnLine*, **3**(1), 23.

Duck, Francis A. 2013. *Physical properties of tissues: a comprehensive reference book*. Academic press.

Duryea, Alexander P, Cain, Charles A, Roberts, William W, & Hall, Timothy L. 2015. Removal of residual cavitation nuclei to enhance histotripsy fractionation of soft tissue. *IEEE Trans Ultrason Ferroelectr Freq Control*, **62**(12), 2068–2078.

Eskridge, Susan L, Macera, Caroline A, Galarneau, Michael R, Holbrook, Troy L, Woodruff, Susan I, MacGregor, Andrew J, Morton, Deborah J, & Shaffer, Richard A. 2012. Injuries from combat explosions in iraq: injury type, location, and severity. *Injury*, **43**(10), 1678–1682.

Estrada, Jonathan B. 2017 (May). *Microcavitation as a neural cell damage mechanism in an in vitro model of blast traumatic brain injury*. Ph.D. thesis, Brown University.

Estrada, Jonathan B, Scimone, Mark T, Cramer, Harry C, Mancia, Lauren, Johnsen, Eric, & Franck, Christian. 2017. Microcavitation as a neuronal damage mechanism in an in vitro model of blast traumatic brain injury. *Biophysical journal*, **112**(3), 159a.

Estrada, Jonathan B, Barajas, Carlos, Henann, David L, Johnsen, Eric, & Franck, Christian. 2018. High strain-rate soft material characterization via inertial cavitation. *Journal of the Mechanics and Physics of Solids*, **112**, 291–317.

Fisher, John C. 1948. The fracture of liquids. *J. Appl. Phys.*, **19**(11), 1062–1067.

Franck, Christian. 2017. Microcavitation: the key to modeling blast traumatic brain injury? *Concussion*, **2**(3).

Fuster, Daniel, & Colonius, Tim. 2011. Modelling bubble clusters in compressible liquids. *Journal of Fluid Mechanics*, **688**, 352–389.

Gaudron, R, Warnez, MT, & Johnsen, E. 2015. Bubble dynamics in a viscoelastic medium with nonlinear elasticity. *Journal of Fluid Mechanics*, **766**, 54–75.

Gilmore, Forrest R. 1952. The growth or collapse of a spherical bubble in a viscous compressible liquid.

Goeller, Jacques, Wardlaw, Andrew, Treichler, Derrick, O'Bruba, Joseph, & Weiss, Greg. 2012. Investigation of cavitation as a possible damage mechanism in blast-induced traumatic brain injury. *Journal of neurotrauma*, **29**(10), 1970–1981.

Greenspan, Martin. 1967. Radiation-induced acoustic cavitation; apparatus and some results. *J. Res. Nat. Bur. Stand., C*, **71**, 299–312.

Greenspan, Martin, & Tschiegg, Carl E. 1982. Radiation-induced acoustic cavitation; threshold versus temperature for some liquids. *J. Acoust. Soc. Am.*, **72**(4), 1327–1331.

Guan, Pengfei, Lu, Shuo, Spector, Michael JB, Valavala, Pavan K, & Falk, Michael L. 2013. Cavitation in amorphous solids. *Phys. Rev. Letters*, **110**(18), 185502.

Gupta, Raj K, & Przekwas, Andrzej J. 2015. A framework for multiscale modeling of warfighter blast injury protection. *In: Proceedings of the International Conference on Computational Methods*, vol. 2.

Harvey, E Newton, Barnes, DK, McElroy, Wm D, Whiteley, AH, Pease, DC, & Cooper, KW. 1944. Bubble formation in animals. I. Physical factors. *Journal of Cellular and Comparative Physiology*, **24**(1), 1–22.

Herbert, Eric, Balibar, Sébastien, & Caupin, Frédéric. 2006. Cavitation pressure in water. *Phys. Rev. E*, **74**(4), 041603.

Herring, Conyers. 1941. *Theory of the pulsations of the gas bubble produced by an underwater explosion*. Columbia Univ., Division of National Defense Research.

Holzapfel, Gerhard A, Sommer, Gerhard, Gasser, Christian T, & Regitnig, Peter. 2005. Determination of layer-specific mechanical properties of human coronary arteries with nonatherosclerotic intimal thickening and related constitutive modeling. *American Journal of Physiology-Heart and Circulatory Physiology*, **289**(5), H2048–H2058.

Honjo, Mitsuyoshi, Moriyasu, Fuminori, Sugimoto, Katsutoshi, Oshiro, Hisashi, Sakamaki, Kentaro, Kasuya, Kazuhiko, Nagai, Takeshi, Tsuchida, Akihiko, & Imai, Yasuharu. 2014. Relationship between the liver tissue shear modulus and histopathologic findings analyzed by intraoperative shear wave elastography and digital microscopically assisted morphometry in patients with hepatocellular carcinoma. *Journal of Ultrasound in Medicine*, **33**(1), 61–71.

Hoskins, Peter R. 2007. Physical properties of tissues relevant to arterial ultrasound imaging and blood velocity measurement. *Ultrasound in medicine & biology*, **33**(10), 1527–1539.

Hu, Yuhang, Zhao, Xuanhe, Vlassak, Joost J, & Suo, Zhigang. 2010. Using indentation to characterize the poroelasticity of gels. *Applied Physics Letters*, **96**(12), 121904.

Hu, Yuhang, You, Jin-Oh, Auguste, Debra T, Suo, Zhigang, & Vlassak, Joost J. 2012. Indentation: A simple, nondestructive method for characterizing the mechanical and transport properties of ph-sensitive hydrogels. *Journal of Materials Research*, **27**(1), 152–160.

Hua, Chengyun, & Johnsen, Eric. 2013. Nonlinear oscillations following the rayleigh collapse of a gas bubble in a linear viscoelastic (tissue-like) medium. *Phys Fluids*, **25**(8), 083101.

Kamath, V, Prosperetti, A, & Egolfopoulos, FN. 1993. A theoretical study of sonoluminescence. *The Journal of the Acoustical Society of America*, **94**(1), 248–260.

Karimi, Alireza, Shojaei, Ahmad, & Tehrani, Pedram. 2017. Measurement of the mechanical properties of the human gallbladder. *Journal of medical engineering & technology*, **41**(7), 541–545.

Keller, Joseph B, & Miksis, Michael. 1980. Bubble oscillations of large amplitude. *The Journal of the Acoustical Society of America*, **68**(2), 628–633.

Ketterling, Jeffrey A, & Apfel, Robert E. 1998. Experimental validation of the dissociation hypothesis for single bubble sonoluminescence. *Physical review letters*, **81**(22), 4991.

Khanafer, K, Schlicht, MS, & Berguer, R. 2013. How should we measure and report elasticity in aortic tissue? *European Journal of Vascular and Endovascular Surgery*, **45**(4), 332–339.

Khokhlova, Vera A, Fowlkes, J Brian, Roberts, William W, Schade, George R, Xu, Zhen, Khokhlova, Tatiana D, Hall, Timothy L, Maxwell, Adam D, Wang, Yak-Nam, & Cain, Charles A. 2015. Histotripsy methods in mechanical disintegration of tissue: Towards clinical applications. *International journal of hyperthermia*, **31**(2), 145–162.

Kinoshita, Manabu, McDannold, Nathan, Jolesz, Ferenc A, & Hynynen, Kullervo. 2006. Noninvasive localized delivery of herceptin to the mouse brain by mri-guided focused ultrasound-induced blood–brain barrier disruption. *Proceedings of the National Academy of Sciences*, **103**(31), 11719–11723.

Kwon, Jiwoon, & Subhash, Ghatu. 2010. Compressive strain rate sensitivity of ballistic gelatin. *Journal of biomechanics*, **43**(3), 420–425.

Lam, Julien, Lombard, Julien, Dujardin, Christophe, Ledoux, Gilles, Merabia, Samy, & Amans, David. 2016. Dynamical study of bubble expansion following laser ablation in liquids. *Applied Physics Letters*, **108**(7), 074104.

Lancellotti, Patrizio, Pibarot, Philippe, Chambers, John, Edvardsen, Thor, Delgado, Victoria, Dulgheru, Raluca, Pepi, Mauro, Cosyns, Bernard, Dweck, Mark R, Garbi, Madalina, *et al.*. 2016. Recommendations for the imaging assessment of prosthetic heart valves: a report from the european association of cardiovascular imaging endorsed by the chinese society of echocardiography, the inter-american society of echocardiography, and the brazilian department of cardiovascular imaging. *European Heart Journal–Cardiovascular Imaging*, **17**(6), 589–590.

Lee, Kuen Yong, & Mooney, David J. 2012. Alginate: properties and biomedical applications. *Progress in polymer science*, **37**(1), 106–126.

Leighton, Timothy. 2012. *The acoustic bubble*. Academic press.

Lim, Yi-Je, Deo, Dhanannjay, Singh, Tejinder P, Jones, Daniel B, & De, Suvranu. 2009. In situ measurement and modeling of biomechanical response of human cadaveric soft tissues for physics-based surgical simulation. *Surgical endoscopy*, **23**(6), 1298.

Lin, Kuang-Wei, Kim, Yohan, Maxwell, Adam D, Wang, Tzu-Yin, Hall, Timothy L, Xu, Zhen, Fowlkes, J Brian, & Cain, Charles A. 2014. Histotripsy beyond the intrinsic cavitation threshold using very short ultrasound pulses: microtripsy. *IEEE Trans Ultrason Ferroelectr Freq Control*, **61**(2), 251–265.

Lin, Kuang-Wei, Duryea, Alexander, Kim, Yohan, Hall, Timothy, Xu, Zhen, & Cain, Charles. 2014b. Dual-beam histotripsy: A low-frequency pump enabling a high-frequency probe for precise lesion formation. *IEEE transactions on ultrasonics, ferroelectrics, and frequency control*, **61**(2), 325–340.

Liu, Li, Fan, Yurun, & Li, Wei. 2014. Viscoelastic shock wave in ballistic gelatin behind soft body armor. *Journal of the mechanical behavior of biomedical materials*, **34**, 199–207.

Liu, Zhenhuan, & Brennen, Christopher E. 1998. Cavitation nuclei population and event rates. *J. Fluids Eng.*, **120**(4), 728–737.

Ma, Jingsen, Hsiao, Chao-Tsung, & Chahine, Georges L. 2018. Numerical study of acoustically driven bubble cloud dynamics near a rigid wall. *Ultrasonics sonochemistry*, **40**, 944–954.

Madsen, Ernest L, Sathoff, H John, & Zagzebski, James A. 1983. Ultrasonic shear wave properties of soft tissues and tissuelike materials. *The Journal of the Acoustical Society of America*, **74**(5), 1346–1355.

Maeda, Kazuki, & Colonius, Tim. 2019. Bubble cloud dynamics in an ultrasound field. *Journal of fluid mechanics*, **862**, 1105.

Mancia, Lauren, Vlaisavljevich, Eli, Xu, Zhen, & Johnsen, Eric. 2017. Predicting tissue susceptibility to mechanical cavitation damage in therapeutic ultrasound. *Ultrasound in medicine & biology*, **43**(7), 1421–1440.

Mancia, Lauren, Vlaisavljevich, Eli, Yousefi, Nyousha, Rodriguez, Mauro, Ziemlewicz, Timothy J, Lee, Fred T, Henann, David, Franck, Christian, Xu, Zhen, & Johnsen, Eric. 2019. Modeling tissue-selective cavitation damage. *Physics in Medicine & Biology*, **64**(22), 225001.

Mancia, Lauren, Rodriguez, Mauro, Sukovich, Jonathan, Haskell, Scott, Xu, Zhen, & Johnsen, Eric. 2020, Under Review. Acoustic measurements of nucleus size distribution at the cavitation threshold. *Physical Review Letters*.

Mancia, Lauren, Rodriguez, Mauro, Sukovich, Jonathan, Xu, Zhen, & Johnsen, Eric. 2020b, In Preparation. Validation of single-bubble dynamics models for histotripsy. *Phys. Med. Biol.*

Mancia, Lauren, Sukovich, Jonathan, Xu, Zhen, & Johnsen, Eric. 2020c, In Preparation. Acoustic cavitation rheology. *Soft Matter*.

Margueritat, Jérémie, Virgone-Carlotta, Angélique, Monnier, Sylvain, Delanoë-Ayari, Hélène, Mertani, Hichem C, Berthelot, Alice, Martinet, Quentin, Dagany, Xavier, Rivière, Charlotte, Rieu, Jean-Paul, *et al.*. 2019. High-frequency mechanical properties of tumors measured by brillouin light scattering. *Physical Review Letters*, **122**(1), 018101.

Mason, Thomas G, & Weitz, DA. 1995. Optical measurements of frequency-dependent linear viscoelastic moduli of complex fluids. *Physical review letters*, **74**(7), 1250.

Maxwell, Adam D, Cain, Charles A, Hall, Timothy L, Fowlkes, J Brian, & Xu, Zhen. 2013. Probability of cavitation for single ultrasound pulses applied to tissues and tissue-mimicking materials. *Ultrasound in medicine & biology*, **39**(3), 449–465.

Miller, Douglas L, & Song, Jianming. 2003. Tumor growth reduction and dna transfer by cavitation-enhanced high-intensity focused ultrasound in vivo. *Ultrasound in medicine & biology*, **29**(6), 887–893.

Miller, Douglas L, Smith, Nadine B, Bailey, Michael R, Czarnota, Gregory J, Hynynen, Kullervo, Makin, Inder Raj S, & of the American Institute of Ultrasound in Medicine, Bioeffects Committee. 2012. Overview of therapeutic ultrasound applications and safety considerations. *Journal of Ultrasound in Medicine*, **31**(4), 623–634.

Miller, Morton W, Miller, Douglas L, & Brayman, Andrew A. 1996. A review of in vitro bioeffects of inertial ultrasonic cavitation from a mechanistic perspective. *Ultrasound in medicine & biology*, **22**(9), 1131–1154.

Milner, Matt P, & Hutchens, Shelby B. 2019. A device to fracture soft solids at high speeds. *Extreme Mechanics Letters*, **28**, 69–75.

Mørch, Knud Aage. 2007. Reflections on cavitation nuclei in water. *Physics of Fluids*, **19**(7), 072104.

Movahed, Pooya, Kreider, Wayne, Maxwell, Adam D, Hutchens, Shelby B, & Freund, Jonathan B. 2016. Cavitation-induced damage of soft materials by focused ultrasound bursts: A fracture-based bubble dynamics model. *The Journal of the Acoustical Society of America*, **140**(2), 1374–1386.

Narayanan, Janaky, Xiong, Jun-Ying, & Liu, Xiang-Yang. 2006. Determination of agarose gel pore size: Absorbance measurements vis a vis other techniques. *Page 83 of: Journal of Physics: Conference Series*, vol. 28. IOP Publishing.

Nayar, VT, Weiland, JD, Nelson, CS, & Hodge, AM. 2012. Elastic and viscoelastic characterization of agar. *Journal of the mechanical behavior of biomedical materials*, **7**, 60–68.

Noltingk, B E, & Neppiras, E A. 1950a. Cavitation produced by ultrasonics. *Proceedings of the Physical Society. Section B*, **63**(9), 674.

Noltingk, B Eo, & Neppiras, Eo A. 1950b. Cavitation produced by ultrasonics. *Proceedings of the Physical Society. Section B*, **63**(9), 674.

Normand, Valéry, Lootens, Didier L, Amici, Eleonora, Plucknett, Kevin P, & Aymard, Pierre. 2000. New insight into agarose gel mechanical properties. *Biomacromolecules*, **1**(4), 730–738.

Nyborg, WL, Carson, PL, Carstensen, EL, Dunn, F, Miller, DL, Miller, M, Thompson, HE, & Ziskin, MC. 2002. Exposure criteria for medical diagnostic ultrasound: II. Criteria based on all known mechanisms. *Bethesda, MD: National Council on Radiation Protection and Measurements*.

Nyein, Michelle K, Jason, Amanda M, Yu, Li, Pita, Claudio M, Joannopoulos, John D, Moore, David F, & Radovitzky, Raul A. 2010. In silico investigation of intracranial blast mitigation with relevance to military traumatic brain injury. *Proceedings of the National Academy of Sciences*, **107**(48), 20703–20708.

Ohl, Claus-Dieter, Lindau, Olgert, & Lauterborn, Werner. 1998. Luminescence from spherically and aspherically collapsing laser induced bubbles. *Physical Review Letters*, **80**(2), 393.

Pahk, Ki Joo, de Andrade, Matheus Oliveira, Gélat, Pierre, Kim, Hyungmin, & Saffari, Nader. 2019. Mechanical damage induced by the appearance of rectified bubble growth in a viscoelastic medium during boiling histotripsy exposure. *Ultrasonics Sonochemistry*.

Paliwal, Sumit, & Mitragotri, Samir. 2006. Ultrasound-induced cavitation: applications in drug and gene delivery. *Expert opinion on drug delivery*, **3**(6), 713–726.

Palmeri, Mark L, Wang, Michael H, Dahl, Jeremy J, Frinkley, Kristin D, & Nightingale, Kathryn R. 2008. Quantifying hepatic shear modulus in vivo using acoustic radiation force. *Ultrasound in medicine & biology*, **34**(4), 546–558.

Parsons, Jessica E, Cain, Charles A, Abrams, Gerald D, & Fowlkes, J Brian. 2006a. Pulsed cavitational ultrasound therapy for controlled tissue homogenization. *Ultrasound in medicine & biology*, **32**(1), 115–129.

Parsons, Jessica E., Cain, Charles A., Abrams, Gerald D., & Fowlkes, J. Brian. 2006b. Pulsed cavitational ultrasound therapy for controlled tissue homogenization. *Ultrasound Med Biol*, **32**(1), 115–129.

Parsons, Jessica E, Cain, Charles A, & Fowlkes, J Brian. 2007. Spatial variability in acoustic backscatter as an indicator of tissue homogenate production in pulsed cavitational ultrasound therapy. *IEEE transactions on ultrasonics, ferroelectrics, and frequency control*, **54**(3), 576–590.

Peeters, EAG, Oomens, CWJ, Bouten, CVC, Bader, DL, & Baaijens, FPT. 2005. Mechanical and failure properties of single attached cells under compression. *Journal of biomechanics*, **38**(8), 1685–1693.

Pernodet, Nadine, Maaloum, Mounir, & Tinland, Bernard. 1997. Pore size of agarose gels by atomic force microscopy. *Electrophoresis*, **18**(1), 55–58.

Plesset, MS. 1949. The dynamics of cavitation bubbles. *J Appl Mech*, **16**, 277–282.

Prosperetti, A. 1984. Bubble phenomena in sound fields: part one. *Ultrasonics*, **22**(2), 69–77.

Prosperetti, A, & Lezzi, A. 1986. Bubble dynamics in a compressible liquid. part 1. first-order theory. *Journal of Fluid Mechanics*, **168**, 457–478.

Prosperetti, Andrea. 1977. Thermal effects and damping mechanisms in the forced radial oscillations of gas bubbles in liquids. *The Journal of the Acoustical Society of America*, **61**(1), 17–27.

Prosperetti, Andrea. 1991. The thermal behaviour of oscillating gas bubbles. *Journal of Fluid Mechanics*, **222**, 587–616.

Prosperetti, Andrea, Crum, Lawrence A, & Commander, Kerry W. 1988. Nonlinear bubble dynamics. *The Journal of the Acoustical Society of America*, **83**(2), 502–514.

Rabkin, Brian A, Zderic, Vesna, & Vaezy, Shahram. 2005. Hyperecho in ultrasound images of hifu therapy: involvement of cavitation. *Ultrasound in medicine & biology*, **31**(7), 947–956.

Ramasamy, Arul, Hill, Adam M, Masouros, Spyros, Gibb, Iain, Bull, Anthony MJ, & Clasper, Jon C. 2011. Blast-related fracture patterns: a forensic biomechanical approach. *Journal of the Royal Society Interface*, **8**(58), 689–698.

Rambod, Edmond, Beizaie, Masoud, Shusser, Michael, Milo, Simcha, & Gharib, Morteza. 1999. A physical model describing the mechanism for formation of gas microbubbles in patients with mitral mechanical heart valves. *Annals of biomedical engineering*, **27**(6), 774–792.

Rayleigh, Lord. 1917. Viii. on the pressure developed in a liquid during the collapse of a spherical cavity. *The London, Edinburgh, and Dublin Philosophical Magazine and Journal of Science*, **34**(200), 94–98.

Reuter, Fabian, Lesnik, Sergey, Ayaz-Bustami, Khadija, Brenner, Gunther, & Mettin, Robert. 2019. Bubble size measurements in different acoustic cavitation structures: filaments, clusters, and the acoustically cavitated jet. *Ultrason. Sonochem.*, **55**, 383–394.

Richman, RH, Rao, AS, & Kung, D. 1995. Cavitation erosion of niti explosively welded to steel. *Wear*, **181**, 80–85.

Riesz, Peter, & Kondo, Takashi. 1992. Free radical formation induced by ultrasound and its biological implications. *Free Radical Biology and Medicine*, **13**(3), 247–270.

Roberts, William W. 2014. Development and translation of histotripsy: current status and future directions. *Current opinion in urology*, **24**(1), 104.

Roberts, William W, Hall, Timothy L, Ives, Kimberly, Wolf, J Stuart, Fowlkes, J Brian, & Cain, Charles A. 2006. Pulsed cavitational ultrasound: a noninvasive technology for controlled tissue ablation (histotripsy) in the rabbit kidney. *J Urol*, **175**(2), 734–738.

Rodriguez, Mauro, & Johnsen, Eric. 2019. A high-order accurate five-equations compressible multiphase approach for viscoelastic fluids and solids with relaxation and elasticity. *Journal of Computational Physics*, **379**, 70–90.

Rosenfeld, Jeffrey V, McFarlane, Alexander C, Bragge, Peter, Armonda, Rocco A, Grimes, Jamie B, & Ling, Geoffrey S. 2013. Blast-related traumatic brain injury. *The Lancet Neurology*, **12**(9), 882–893.

Rossinelli, Diego, Hejazialhosseini, Babak, Hadjidoukas, Panagiotis, Bekas, Costas, Curioni, Alessandro, Bertsch, Adam, Futral, Scott, Schmidt, Steffen J, Adams, Nikolaus A, & Koumoutsakos, Petros. 2013. 11 pflop/s simulations of cloud cavitation collapse. *Pages 1–13 of: SC'13: Proceedings of the International Conference on High Performance Computing, Networking, Storage and Analysis*. IEEE.

Russell, Rob, Clasper, Jon, Jenner, Bruce, Hodgetts, Timothy J, & Mahoney, Peter F. 2014. Ballistic injury. *BMJ*, **348**, bmj–g1143.

Saijo, Yoshifumi, Tanaka, Motonao, Okawai, Hiroaki, & Dunn, Floyd. 1991. The ultrasonic properties of gastric cancer tissues obtained with a scanning acoustic microscope system. *Ultrasound in Medicine and Biology*, **17**(7), 709–714.

Salzar, Robert S, Treichler, Derrick, Wardlaw, Andrew, Weiss, Greg, & Goeller, Jacques. 2017. Experimental investigation of cavitation as a possible damage mechanism in blast-induced traumatic brain injury in post-mortem human subject heads. *J. Neurotrauma*, **34**(8), 1589–1602.

Sankin, GN, & Teslenko, VS. 2003. Two-threshold cavitation regime. *Dokl. Phys.*, **48**(12), 665–668.

Schroeder, Avi, Kost, Joseph, & Barenholz, Yechezkel. 2009. Ultrasound, liposomes, and drug delivery: principles for using ultrasound to control the release of drugs from liposomes. *Chemistry and physics of lipids*, **162**(1-2), 1–16.

Shampine, Lawrence F, & Reichelt, Mark W. 1997. The matlab ode suite. *SIAM journal on scientific computing*, **18**(1), 1–22.

Shampine, Lawrence F, Reichelt, Mark W, & Kierzenka, Jacek A. 1999. Solving index-1 daes in matlab and simulink. *SIAM Rev.*, **41**(3), 538–552.

Shima, A, & Tsujino, T. 1982. On the dynamics of bubbles in polymer aqueous solutions. *Appl Sci Res*, **38**(1), 255–263.

Shunmugasamy, Vasanth Chakravarthy, Gupta, Nikhil, & Coelho, Paulo G. 2010. High strain rate response of rabbit femur bones. *Journal of biomechanics*, **43**(15), 3044–3050.

Silveira, Luís Augusto da, Silveira, Fernando Braga Cassiano, & Fazan, Valéria Paula Sassoli. 2009. Arterial diameter of the celiac trunk and its branches: anatomical study. *Acta cirurgica brasileira*, **24**(1), 43–47.

Singh, I, Narasimhan, R, & Ramamurty, Upadrasta. 2016. Cavitation-induced fracture causes nanocorrugations in brittle metallic glasses. *Phys. Rev. Letters*, **117**(4), 044302.

Smolock, Amanda R, Cristescu, Mircea M, Vlaisavljevich, Eli, Gendron-Fitzpatrick, Annette, Green, Chelsey, Cannata, Jonathan, Ziemlewicz, Timothy J, & Lee Jr, Fred T. 2018. Robotically assisted sonic therapy as a noninvasive nonthermal ablation modality: Proof of concept in a porcine liver model. *Radiology*, **287**(2), 485–493.

Solomon, WK, & Jindal, VK. 2007. Modeling changes in rheological properties of potatoes during storage under constant and variable conditions. *LWT-Food Science and Technology*, **40**(1), 170–178.

Storrie, Hannah, & Mooney, David J. 2006. Sustained delivery of plasmid dna from polymeric scaffolds for tissue engineering. *Advanced drug delivery reviews*, **58**(4), 500–514.

Stuhmiller, James H, Ho, Kevin H-H, Vander Vorst, Michael J, Dodd, Kenneth T, Fitzpatrick, Thomas, & Mayorga, Maria. 1996. A model of blast overpressure injury to the lung. *Journal of biomechanics*, **29**(2), 227–234.

Sukop, Michael C, & Or, Dani. 2005. Lattice boltzmann method for homogeneous and heterogeneous cavitation. *Physical Review E*, **71**(4), 046703.

Sukovich, Jonathan R, Haskell, Scott C, Xu, Zhen, & Hall, Timothy L. 2020. A cost-effective, multi-flash,ghost imaging technique for high temporal and spatial resolution imaging of cavitation using still-frame cameras. *The Journal of the Acoustical Society of America*, **147**(3), 1339–1343.

Sundaramurthy, Aravind, Alai, Aaron, Ganpule, Shailesh, Holmberg, Aaron, Plougonven, Erwan, & Chandra, Namas. 2012. Blast-induced biomechanical loading of the rat: an experimental and anatomically accurate computational blast injury model. *Journal of neurotrauma*, **29**(13), 2352–2364.

Vlaisavljevich, Eli, Kim, Yohan, Owens, Gabe, Roberts, William, Cain, Charles, & Xu, Zhen. 2013a. Effects of tissue mechanical properties on susceptibility to histotripsy-induced tissue damage. *Physics in Medicine & Biology*, **59**(2), 253.

Vlaisavljevich, Eli, Kim, Yohan, Owens, Gabe, Roberts, William, Cain, Charles, & Xu, Zhen. 2013b. Effects of tissue mechanical properties on susceptibility to histotripsy-induced tissue damage. *Phys Med Biol*, **59**(2), 253.

Vlaisavljevich, Eli, Kim, Yohan, Allen, Steven, Owens, Gabe, Pelletier, Shawn, Cain, Charles, Ives, Kimberly, & Xu, Zhen. 2013c. Image-guided non-invasive ultrasound liver ablation using histotripsy: Feasibility study in an in vivo porcine model. *Ultrasound in medicine & biology*, **39**(8), 1398–1409.

Vlaisavljevich, Eli, Maxwell, Adam, Warnez, Matthew, Johnsen, Eric, Cain, Charles, & Xu, Zhen. 2014. Histotripsy-induced cavitation cloud initiation thresholds in tissues of different mechanical properties. *IEEE Trans. Ultrason. Ferroelectr. Freq. Control*, **61**(2), 341–352.

Vlaisavljevich, Eli, Lin, Kuang-Wei, Warnez, Matthew T, Singh, Rahul, Mancia, Lauren, Putnam, Andrew J, Johnsen, Eric, Cain, Charles, & Xu, Zhen. 2015a. Effects of tissue stiffness, ultrasound frequency, and pressure on histotripsy-induced cavitation bubble behavior. *Physics in Medicine & Biology*, **60**(6), 2271.

Vlaisavljevich, Eli, Lin, Kuang-Wei, Maxwell, Adam, Warnez, Matthew T, Mancia, Lauren, Singh, Rahul, Putnam, Andrew J, Fowlkes, Brian, Johnsen, Eric, Cain, Charles, *et al.*. 2015b. Effects of ultrasound frequency and tissue stiffness on the histotripsy intrinsic threshold for cavitation. *Ultrasound in medicine & biology*, **41**(6), 1651–1667.

Vlaisavljevich, Eli, Aydin, Omer, Lin, Kuang-Wei, Durmaz, Yasemin Yuksel, Fowlkes, Brian, ElSayed, Mohamed, & Xu, Zhen. 2015c. The role of positive and negative pressure on cavitation nucleation in nanodroplet-mediated histotripsy. *Phys Med Biol*, **61**(2), 663.

Vlaisavljevich, Eli, Aydin, Omer, Durmaz, Yasemin Yuksel, Lin, Kuang-Wei, Fowlkes, Brian, El-Sayed, Mohamed, & Xu, Zhen. 2015d. Effects of ultrasound frequency on nanodroplet-mediated histotripsy. *Ultrasound in medicine & biology*, **41**(8), 2135–2147.

Vlaisavljevich, Eli, Xu, Zhen, Maxwell, Adam D, Mancia, Lauren, Zhang, Xi, Lin, Kuang-Wei, Duryea, Alexander P, Sukovich, Jonathan R, Hall, Timothy L, Johnsen, Eric, *et al.*. 2016a. Effects of temperature on the histotripsy intrinsic threshold for cavitation. *IEEE transactions on ultrasonics, ferroelectrics, and frequency control*, **63**(8), 1064–1077.

Vlaisavljevich, Eli, Greve, Joan, Cheng, Xu, Ives, Kimberly, Shi, Jiaqi, Jin, Lifang, Arvidson, Alexa, Hall, Tim, Welling, Theodore H, Owens, Gabe, *et al.*. 2016b. Non-invasive ultrasound liver ablation using histotripsy: Chronic study in an in vivo rodent model. *Ultrasound Med Biol*.

Vlaisavljevich, Eli, Maxwell, Adam, Mancia, Lauren, Johnsen, Eric, Cain, Charles, & Xu, Zhen. 2016c. Visualizing the histotripsy process: Bubble cloud–cancer cell interactions in a tissue-mimicking environment. *Ultrasound in medicine & biology*, **42**(10), 2466–2477.

Vogel, Alfred, Busch, S, & Parlitz, U. 1996. Shock wave emission and cavitation bubble generation by picosecond and nanosecond optical breakdown in water. *The Journal of the Acoustical Society of America*, **100**(1), 148–165.

Vogel, Alfred, Linz, Norbert, Freidank, Sebastian, & Paltauf, Günther. 2008. Femtosecond-laser-induced nanocavitation in water: implications for optical breakdown threshold and cell surgery. *Physical review letters*, **100**(3), 038102.

Vokurka, K. 1986. Comparison of rayleigh's, herring's, and gilmore's models of gas bubbles. *Acta Acustica united with Acustica*, **59**(3), 214–219.

von Mises, R. 1913. Mechanik der festen körper im plastisch-deformablen zustand. *Nachrichten von der Gesellschaft der Wissenschaften zu Göttingen, Mathematisch-Physikalische Klasse*, **1913**, 582–592.

Walton, Alan J, & Reynolds, Geo T. 1984. Sonoluminescence. *Adv. Phys.*, **33**(6), 595–660.

Wang, Yi-Chun. 1999. Effects of nuclei size distribution on the dynamics of a spherical cloud of cavitation bubbles. *J. Fluids Eng.*, **121**(4), 881–886.

Wang, Yunpeng, Wang, Sheng, Xu, Chenhui, Xuan, Shouhu, Jiang, Wanquan, & Gong, Xinglong. 2016. Dynamic behavior of magnetically responsive shear-stiffening gel under high strain rate. *Composites Science and Technology*, **127**, 169–176.

Warnez, MT, & Johnsen, E. 2015. Numerical modeling of bubble dynamics in viscoelastic media with relaxation. *Physics of Fluids*, **27**(6), 063103.

Watson, Tim. 2008. Ultrasound in contemporary physiotherapy practice. *Ultrasonics*, **48**(4), 321–329.

Webb, Ian R, Payne, Stephen J, & Coussios, Constantin-C. 2011. The effect of temperature and viscoelasticity on cavitation dynamics during ultrasonic ablation. *The Journal of the Acoustical Society of America*, **130**(5), 3458–3466.

Wells Jr, Roe E, & Merrill, Edward W. 1962. Influence of flow properties of blood upon viscosity-hematocrit relationships. *Journal of Clinical Investigation*, **41**(8), 1591.

Wienken, W, Stiller, J, & Keller, A. 2006. A method to predict cavitation inception using large-eddy simulation and its application to the flow past a square cylinder. *J. Fluids Eng.*, **128**(2), 316–325.

Wilkerson, JW, & Ramesh, KT. 2016. Unraveling the anomalous grain size dependence of cavitation. *Phys. Rev. Letters*, **117**(21), 215503.

Wilson, Chad T, Hall, Timothy L, Johnsen, Eric, Mancia, Lauren, Rodriguez, Mauro, Lundt, Jonathan E, Colonius, Tim, Henann, David L, Franck, Christian, Xu, Zhen, *et al.*. 2019. Comparative study of the dynamics of laser and acoustically generated bubbles in viscoelastic media. *Phys. Rev. E*, **99**(4), 043103.

Wurster, Clemens, Staudenraus, Joachim, & Eisenmenger, Wolfgang. 1994. The fiber optic probe hydrophone. *Pages 941–944 of: 1994 Proceedings of IEEE Ultrasonics Symposium*, vol. 2. IEEE.

Xiao, H. 2005. Hencky strain and hencky model: extending history and ongoing tradition. *Multidiscipline Modeling in Materials and Structures*, **1**(1), 1–52.

Xu, Jin, & Bigelow, Timothy A. 2011. Experimental investigation of the effect of stiffness, exposure time and scan direction on the dimension of ultrasound histotripsy lesions. *Ultrasound in medicine & biology*, **37**(11), 1865–1873.

Xu, Zhen, Ludomirsky, Achiau, Eun, Lucy Y, Hall, Timothy L, Tran, Binh C, Fowlkes, J Brian, & Cain, Charles A. 2004. Controlled ultrasound tissue erosion. *IEEE transactions on ultrasonics, ferroelectrics, and frequency control*, **51**(6), 726–736.

Xu, Zhen, Fowlkes, J Brian, Rothman, Edward D, Levin, Albert M, & Cain, Charles A. 2005a. Controlled ultrasound tissue erosion: The role of dynamic interaction between insonation and microbubble activity. *The Journal of the Acoustical Society of America*, **117**(1), 424–435.

Xu, Zhen, Fowlkes, J. Brian, Rothman, Edward D., Levin, Albert M., & Cain, Charles A. 2005b. Controlled ultrasound tissue erosion: The role of dynamic interaction between insonation and microbubble activity. *J Acoust Soc Am*, **117**(1), 424–435.

Yamada, Hiroshi, Evans, F Gaynor, *et al.*. 1970. Strength of biological materials.

Yang, Xinmai, & Church, Charles C. 2005. A model for the dynamics of gas bubbles in soft tissue. *The Journal of the Acoustical Society of America*, **118**(6), 3595–3606.

Yang, Xinmai, & Church, Charles C. 2006. A simple viscoelastic model for soft tissues the frequency range 6-20 mhz. *IEEE transactions on ultrasonics, ferroelectrics, and frequency control*, **53**(8), 1404–1411.

Zheng, Q, Durben, DJ, Wolf, GH, & Angell, CA. 1991. Liquids at large negative pressures: water at the homogeneous nucleation limit. *Science*, **254**(5033), 829–832.

Zhou, Yufeng. 2015. *Principles and applications of therapeutic ultrasound in healthcare*. CRC press.

Zilonova, E, Solovchuk, M, & Sheu, TWH. 2018. Bubble dynamics in viscoelastic soft tissue in high-intensity focal ultrasound thermal therapy. *Ultrasonics sonochemistry*, **40**, 900–911.

Zimberlin, Jessica A., Sanabria-DeLong, Naomi, Tew, Gregory N., & Crosby, Alfred J. 2007. Cavitation rheology for soft materials. *Soft Matter*, **3**, 763–767.

Zimberlin, Jessica A, McManus, Jennifer J, & Crosby, Alfred J. 2010. Cavitation rheology of the vitreous: mechanical properties of biological tissue. *Soft Matter*, **6**(15), 3632–3635.